Power
Electronics
and Electrical
Drives

RWTH AACHEN UNIVERSITY

Bernhard Burkhart

Switched Reluctance Generator for Range Extender Applications

Design, Control and Evaluation

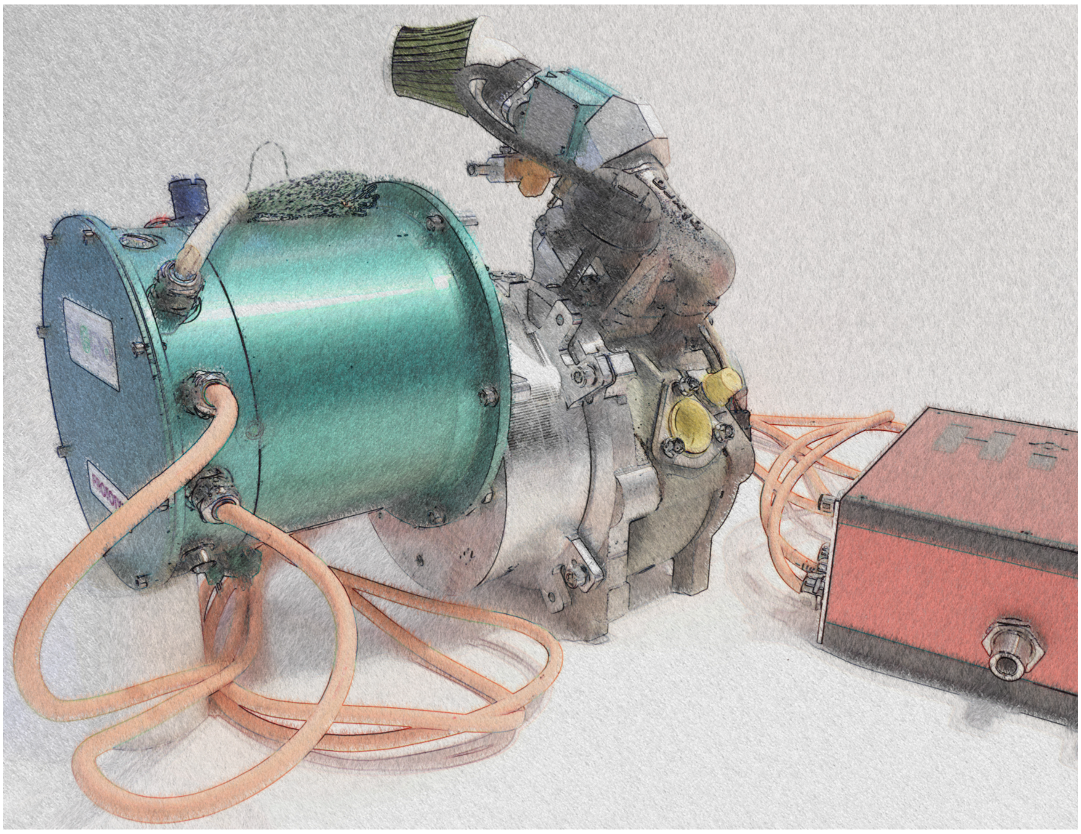

Aachener Beiträge des ISEA Band 116

Bernhard Burkhart

Switched Reluctance Generator for Range Extender Applications

Design, Control and Evaluation

Switched Reluctance Generator for Range Extender Applications

Design, Control and Evaluation

Von der Fakultät für Elektrotechnik und Informationstechnik der Rheinisch-Westfälischen Technischen Hochschule Aachen zur Erlangung des akademischen Grades eines Doktors der Ingenieurwissenschaften genehmigte Dissertation

vorgelegt von
Diplom-Ingenieur
Bernhard Burkhart
aus
Göppingen

Berichter:
Univ.-Prof. Dr. Ir. Dr. h. c. Rik W. De Doncker
Univ.-Prof. Barrie C. Mecrow

Tag der mündlichen Prüfung:
13. Juli 2018

Electronic version
This dissertation is available online on the website of the university library (https://publications.rwth-aachen.de/).

AACHENER BEITRÄGE DES ISEA
Vol. 116

Editor:
Univ.-Prof. Dr. ir. h. c. Rik W. De Doncker
Director of the Institute for Power Electronics and Electrical Drives (ISEA)
RWTH Aachen University

ISSN 1437-675X

Institute for Power Electronics and Electrical Drives (ISEA)
Jägerstr. 17/19 ▪ 52066 Aachen ▪ Germany
Tel: +49 (0)241 80-96920
Fax: +49 (0)241 80-92203
post@isea.rwth-aachen.de

Preface

Seit meinem Start am ISEA sind mittlerweile über 11 Jahre vergangen. Während dieser Zeit als Student, wissenschaftlicher Mitarbeiter, Gruppenleiter und schlussendlich Oberingenieur haben mich viele Menschen begleitet, geprägt und bei der Verfassung dieser Arbeit unterstützt. Mein Dank gilt generell allen Wegbegleitern, die das ISEA immer wieder aufs Neue erfinden und dieses einzigartige Arbeitsklima ermöglichen. Einigen davon möchte ich hier namentlich danken.

An erster Stelle danke ich Professor De Doncker für die Möglichkeit am ISEA zu promovieren sowie das mir übertragene Vertrauen, neben der wissenschaftlichen Arbeit auch Verwaltungsaufgaben als Gruppenleiter und Oberingenieur übernehmen zu dürfen. Dieses Vertrauen hat mich immer sehr motiviert. Professor Mecrow danke ich für die Übernahme des Koreferats sowie die interessanten Gespräche im Rahmen der Prüfung. Neben den Prüfern gilt mein Dank auch Allen die diese Arbeit finanziell ermöglicht haben. Hier ist zum einen das Bundesministerium für Wirtschaft und Energie (BMWi) für die Förderung des Projekts HiREX zu nennen, aber auch die Projektpartner AixControl, Daimler, ENGIRO sowie Isar Getriebetechnik. Insbesondere den Firmen Daimler sowie ENGIRO danke ich für den Bau der vielen Prototypen im Rahmen der Arbeit. Helge Brauer gilt mein Dank für den großen Korrektur-Einsatz zu jeder Tages- und Nachtzeit während des Endspurts. Auch für die wertvollen Anmerkungen von Artur Mittelstedt und Claude Weiß möchte ich mich bedanken.

Mein Dank gilt ebenso allen Kollegen der Antriebsgruppe für den intensiven fachlichen Austausch, die ehrlichen Diskussionen und die gegenseitige Unterstützung bei Problemen. Bei Annegret Klein-Heßling möchte ich mich ganz besonders für die lange Projektzusammenarbeit und das Bauen der vielen Antriebsumrichter bedanken. Tobias Lange, Stefan Koschik und Andreas Bubert gilt mein Dank für den Einsatz an den Antriebsprüfständen. Bei Claude Weiß, Iliya Ralev und Tetsuya Kojima möchte ich mich für die gemeinsame Büro-Zeit und die vielen Diskussionen über die SRM bedanken. Zum Glück habt ihr den Kühlschrank erst abgetaut als ich bereits ausgezogen war. Michael Schubert gilt mein Dank für die vielen fachlichen und administrativen Diskussionen, während im Hintergrund das Wasser rauschte. Auch Jan Gottschlich darf als Leistungselektroniker hier nicht fehlen, der quasi bei jeder Elektronik die Finger mit im Spiel hatte, und ohne den die Regelung nie so strukturiert aufgebaut worden wäre. Nicht zuletzt gilt allen Antrieblern mein Dank für die vielen wissenschaftlichen Getränke- und Fleischstudien die im Laufe der Jahre durchgeführt wurden.

Neben den wissenschaftlichen Mitarbeitern möchte ich mich auch bei allen Werkstätten und der gesamten Institutsverwaltung für die Unterstützung und die gute Zusammenarbeit bedanken. Mein Dank gilt allen Gruppenleiter-Kollegen für die humorvollen wöchentlichen Meetings, ohne die man vielleicht doch das eine oder andere Mal den Kopf verloren hätte. Insbesondere möchte ich mich bei Stefan Engel und Hauke van Hoek für das entgegen ge-

brachte Vertrauen, die Aufmunterungen und den Einsatz für das Institut bedanken. Ebenso muss ich mich bei allen „Verrückten“ bedanken, die Ende 2017 positiven Druck aufgebaut haben um die Arbeit endlich abzugeben.

Während meiner Zeit am ISEA hatte ich das Glück Studenten mitbetreuen zu dürfen, von denen ich einigen namentlich danken möchte. Muneer Al Sabbagh für die ersten Simulationen der 2-phasigen Reluktanzgeneratoren. Artur Mittelstedt für die Betrachtungen des DC/DC-Wandlers in seiner Bachelorarbeit, sowie den Grundstein des Vorauslegungstools in der Masterarbeit. Alexander Stippich für die Getriebeuntersuchung, die bereits früh den Keim für HIREX gesät hat. Xuan Zhang für das akustische Hoch- und Runtersimulieren der Generatoren. Christoph Coenen, für die Bändigung des 6-phasigen Außenläufermonsters mit skalierbarem FPGA-Code. Daniel Scharfenstein für die Unterstützung beim Programmieren und das aktive Rauschen. Syed Hafeez und Russell Sabir für viele Simulationen und gemeinsame Paper. Richard Stelzer, Martin Kramer, Lukas Hüssen und Christian Monissen für das Portieren von Code und Aufarbeiten von so einigen Simulationsideen und -modellen zum Ende der Arbeit hin. Ohne diese Unterstützung wäre die Arbeit in diesem Umfang nicht durchführbar gewesen.

Danken möchte ich ebenso meiner Familie und Freunden für den steten Rückhalt und die Ermunterung. Meinen drei Kindern Emilien, Victor und Arthur danke ich für die Ablenkung von der Arbeit. Mein Größter Dank gilt schlussendlich meiner Frau Elodie. Ohne dein Verständnis und deine Unterstützung wäre diese Dissertation nicht möglich gewesen. Gerade in der Schlussphase hast du mir den Rücken freigehalten und auch die Situation mit plötzlich drei Kindern fast im Alleingang gemeistert.

Aachen, im Dezember 2018 *Bernhard Burkhart*

Contents

1 Introduction

Road transportation is responsible for about 19 % of the German CO_2 emissions in 2017, with approximately 170 Mio. t [Umw18]. Beginning of 2018, about 99 % of the 46 million passenger cars in Germany run on fossil fuel, such as gasoline or diesel [Kra18]. These cars emit greenhouse and additional toxic gases, such as NO_x. Electrification of the transportation sector, in particular passenger cars, is a viable solution for de-carbonization and the reduction of local emissions. However, the energy density of current battery technology as well as the cost, make it not always desirable to cover the total required energy with a battery storage system. To electrify the fleet of passenger cars, one possible solution are range extender (REX). Present day range extender (REX) comprise a small internal combustion engine (ICE) combined with an electrical generator. The REX technology makes use of the high power density of fossil or synthetic fuel and converts it into electrical energy. Especially for continuous long trips or when the distance between charging stations is large, REX offer a compact solution compared to large battery packs or fuel cells. REX offer some significant advantages over more complex hybrid drive trains. If the REX is activated before complete battery depletion, only the average vehicle power needs to be installed. As no direct connection to the tires exists, the REX can run at energy efficient operation points and, therefore, achieve a higher system efficiency compared to a traction drive. As the energy density of fossil fuel is by a magnitude higher than current battery storage systems, with a comparable small fuel tank a large range extension can be achieved. Finally, refilling can be done within a few minutes at widely available infrastructure.

To be competitive REX need to be cost effective, compact and very reliable as in an optimal use case they are rarely activated. These targets, combined with the fact that the system shall mainly run at nominal power, lead to the switched reluctance generator (SRG)[(i)] as one potential electric generator candidate. Within this thesis, possible SRG solutions regarding machine design and control for REX applications are discussed.

To assess the potential of SRG technology for REX, two drive configurations, a low- and a high-speed scenario, with an input power $P_{\mathrm{m,sh}}$ of 20 kW are considered and analyzed. To select a suitable machine design, a solution space based pre-design (SSBPD) approach is introduced in this thesis. In contrast to existing design tools, which focus on the optimization of a certain design or configuration, this approach enables the comparison of a vast number of potential machine configurations in a very short time without analytical tuning factors or expert knowledge. This comprises a variation of the number of phases N_{ph} and pole pairs n_{p} as well as the stator outer diameter D_{st} and, consequently, the machine stack length L_{stk}. Three machine designs are derived for a more detailed analysis of the machine performance, concerning efficiency, power density, acoustic behavior as well as material cost and torque profile. This analysis is not based only on finite element analysis (FEA) simulation results,

(i) As this thesis is dealing with a generator in particular, for the sake of readability only the term SRG will be used, including the general switched reluctance machine but also on full-scale prototype measurements of the chosen machines. From the analysis at nominal operation point, a recommendation on the most suitable machine configuration for REX is derived. Finally, the influence of the control parameter and power variation on the machine efficiency and the acoustic behavior is analyzed, even if REX should mainly be operated at nominal operation point. From the analysis of the partial load operation points, a recommendation for the power variation in terms of efficiency is derived. In addition, implications of the chosen machine configurations on power electronics and system design are presented. All together, the thesis offers guidance in the choice of an appropriate SRG configuration as well as its operational speed for REX applications. Therefore, the thesis is subdivided in the following chapters:

Chapter 2 - Fundamentals

The first part gives a short introduction to the REX application as well as an overview on existing products and prototypes. Requirements of the REX are combined with a brief discussion of potential electric generator solutions and the specifications of the two mentioned drive configurations. The second part covers essential fundamentals of SRG, including control and power electronic basics as well as employed system models.

Chapter 3 - Solution Space Based Pre-Design

Firstly, the fundamental idea of the SSBPD approach is introduced and compared to existing design approaches. Secondly, the design rules and the setup of the underlying solution database with the help of FEA based machine characteristics are presented together with a discussion of the obtained results. As the solution database comprises strongly differing machine configurations, a fast approach to compare application dependent thermal, electrical and mechanical aspects based only on available geometric parameters and comprehensible boundaries, such as the maximal coil temperature $\vartheta_{\text{coil,max}}$, is presented. This approach is compared to design results obtained with literature recommendations. Finally, prototype machine designs for the two drive configurations are assessed and selected.

Chapter 4 - Generator Design and Discussion

The machine designs for the low- and high-speed scenario are discussed and compared in detail based on simulations and measurements. In addition, a comparison between two- and three-phase SRGs is performed. The detailed evaluation of all relevant losses includes ac copper losses, iron core losses and mechanical losses. Based on the derived machine efficiency, a thermal analysis of the different solutions and an evaluation of the achievable power density is conducted. Besides, the acoustic behavior, the material cost and the torque profile of the various solutions are analyzed. The chapter concludes with a recommendation of machine configurations for REX.

Chapter 5 - Control and Power Variation

The potential of a converter freewheeling period on the system efficiency, including the source losses, is investigated. In addition, the influence on the eddy-current copper losses $P_{\text{l,cu,eddy}}$ is analyzed and a fast empirical prediction method is derived from the performed FEAs. The chapter includes a discussion of acoustic behavior at variable speed operation and in combination with an ICE. Finally, the additional findings are aligned with the results from chapter 4, to give an overall recommendation on SRG configurations for REX.

Chapter 6 - Summary and Conclusion

Chapter 6 summarizes the thesis, presents the main findings and gives an outlook on possible future work.

2 Fundamentals

This chapter introduces the basics of a REX application, including an overview of existing products and prototypes in section 2.1. From this discussion, two drive configurations are derived in section 2.1.2 to assess the potential of the SRG technology. The second part in section 2.2 introduces relevant SRG fundamentals. This includes a discussion of SRG losses as well as prototype solutions found in literature. Finally, the system models employed for further analysis in chapter 4 and 5 are introduced in section 2.3.

2.1 Range Extender System

Different configurations of hybrid drive trains exist for long time [Ema+05; Hof14]. In the world of hybrid electric vehicles (HEVs), vehicles with a REX can be categorized as serial HEV. A serial HEV as shown in fig. 2.1 combines a full electric drive-train, consisting of a battery, one or more inverters and electric traction machines, with an alternative power source. This alternative power source has no mechanical connection to the propulsion system. The alternative power source is only meant to recharge the battery during operation, when a wider operation range is required [AK11]. In the scope of this thesis, the alternative power source is based on an ICE combined with a generator and a power electronic inverter.

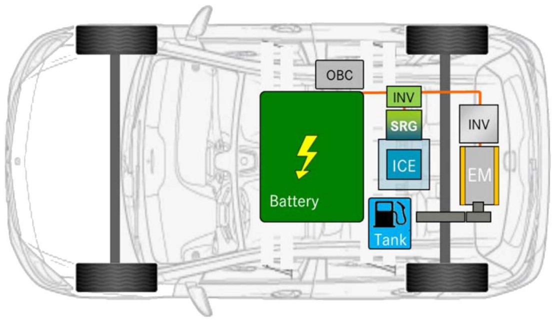

Fig. 2.1: Exemplary drive-train of an HEV with REX (taken from [Ind+16]).

The design of a REX can be simplified as it is only installed as a backup system for the primary battery. Therefore, the REX only needs to cover the continuous power of the HEV instead of the peak power [GN11]. This allows for a downsizing of the individual components. Also the operation point of the system can be freely chosen, allowing an optimization regarding system efficiency or acoustic behavior. While most control strategies simply operate the REX to guarantee a certain state-of-charge of the electric power source [And+12], more advanced strategies take the driving cycle or the cabin heat management into consideration [Gis+15]. Finally, the reduced number of operation points simplifies the exhaust treatment of the ICE [MST12]. Compared to more complex parallel HEVs, which have to be operated in various operation points, the combustion and exhaust treatment can be optimized for a small amount of operation points.

To supply the shaft input power $P_{\mathrm{m,sh}}$ to the generator, a large variety of power sources can be found in [Fer+12; HQD14]. Four-stroke gasoline piston engines offer a good compromise between efficiency, power density, acoustic behavior and emissions. Due to the small required mechanical input power $P_{\mathrm{m,sh}}$, mainly piston engines with less than three cylinders are considered [Pis+12; And+12; BMW17; Ind+16]. Another promising solution with a high power density are rotary wankel engines [Fis+09; Eng18]. The compact design and low vibrations make this engine type an interesting candidate, also for aircraft applications [Sig18]. The efficiency is reported to be slightly lower than in four-stroke gasoline piston engines [HQD14] and only a limited number of manufacturers of rotary wankel engines are available. All piston engines have in common that their rotational speed n_{ICE} is below 10 krpm, while a large variety of shaft power $P_{\mathrm{m,sh}}$ is available.

The before mentioned piston engines are mainly based on derivatives of available series ICEs for traction applications. For larger shaft power $P_{\mathrm{m,sh}}$ as well as higher power density, micro gas turbines [gre10; cap18; gre18] are proposed. While for the stationary power and gas markets these solutions are already widely in use [Ben13], for mobile applications only prototypes and press releases are available up to now. Especially at low power of several 10 kW the efficiency of these turbines is reported lower than piston engines [Ben13]. Another solution discussed in literature are free piston linear motors [HL16]. While many mechanical parts in the ICE are eliminated by this concept, a linear electric generator is required to transform the created thrust into electrical energy. Up to now, only laboratory prototypes of this technology were presented.

In the automotive industry, the REX research was initially driven by cost and volume issues of the available battery packs. With the development of electric vehicles with large battery packs covering sufficiently large operation ranges, interest in REX cooled off. The only large series REX available on the market is the `BMW i3` [BMW17] and the `Voltec` system of GM [Pis14] in the first Chevrolet Volt edition. The latter is not a pure REX as the ICE is able to directly drive the wheels through a complex gearbox.

In applications, such as aircraft and heavy-duty vehicles, the current battery technology still does not reach the required gravimetric energy density for long operation ranges. Also the total cost of ownership and environmental impact of large battery packs, which are rarely used for everyday driving cycles, have to be kept in mind [Pis14]. In such applications, REX can offer an interesting alternative to large battery storage systems.

System Voltage

Most electric passenger vehicles available on the market today, are equipped with a lithium-ion based energy storage system. The chosen energy storage system not only defines the nominal system voltage $U_{\mathrm{src,nom}}$, but also the losses. Fig. 2.2 depicts the internal resistances $R_{\mathrm{i,src}}$ of several vehicles over $U_{\mathrm{src,nom}}$, which were characterized over their lifetime in an extensive field test by the US Department of Energy [Ida17]. The relevant $R_{\mathrm{i,src}}$ for charging is in the range of 65 up to 180 mΩ, while $U_{\mathrm{src,nom}}$ ranges from 300 up to 360 V.

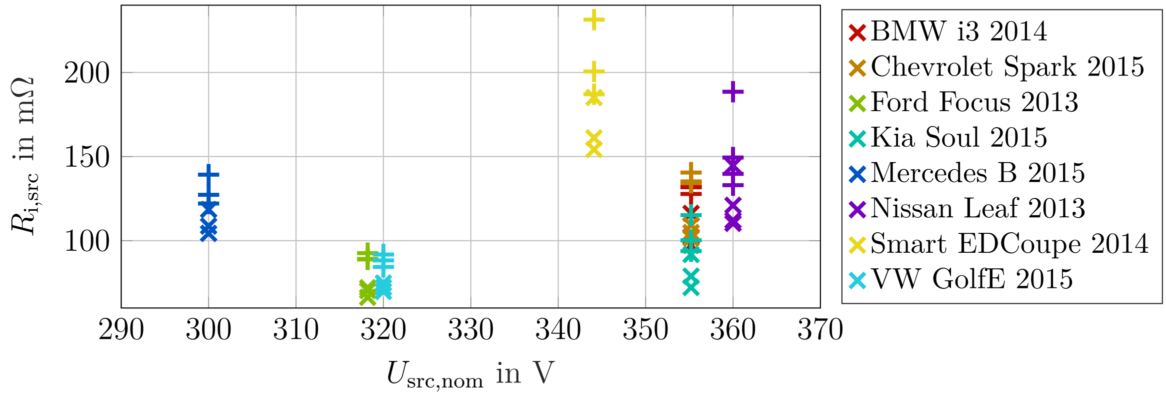

Fig. 2.2: $R_{\mathrm{i,src}}$ of exemplary electric vehicles over $U_{\mathrm{src,nom}}$. Each data point signifies a specific charging (x) or discharging (+) measurement [Ida17].

2.1.1 Generator Choice

Currently, available REX are mainly based on permanent magnet synchronous machines (PMSMs). However, the choice of a specific electric machine type as generator strongly depends on the application. In [Bur+17], an overview on advantages and disadvantages of various electric machine types can be found.

The major advantage of SRGs over conventional PMSMs is the lack of permanent magnets in the rotor. [KF17] exemplary shows the cost advantage for a small 250 W SRG over a PMSM. Beside the absolute cost advantage, which strongly depends on the raw material prices, availability of raw materials is of high importance for large-scale producers. An SRG mainly requires iron core material, shaft steel and copper, available from a large number of suppliers. In contrast, the rare earth magnet material supply is currently nearly completely controlled by one single country [Yat17]. The high generator speeds n_{SRG} possible with SRGs, are of interest in extreme applications, such as direct attachment to high-speed turbines [gre10]. Additional advantages, such as wide field weakening region and high overload potential, are of secondary interest for a REX application.

Concerning SRG disadvantages, the operation mode of a REX mitigates them partially. ICEs show highest efficiency at high torque levels [MST12], at which also SRGs show highest machine efficiency η_{mach} [Ral+17; Tak+12]. Therefore, the efficiency disadvantage compared to a PMSM is reduced. Also the complete system efficiency from fuel to battery is much less influenced by the electric generator, due to realistic ICE efficiencies η_{ICE} between 20 and 40 % [Fer+12]. High vibration amplitudes and torque ripple are expected to be partially covered by similar behavior of the ICE. Also, they can be influenced by the choice of operation point (generator speed n_{SRG}, total output torque T_{tot}), as the system behavior is detached from the current driving situation of the HEV.

2.1.2 Drive Configuration

To assess the potential of the SRG technology for REX applications, two scenarios with different drive configurations are considered in this thesis. The low-speed scenario generator is directly linked to an ICE with $n_{\mathrm{ICE}} = 7500\,\mathrm{rpm}$. In the high-speed scenario, the SRG is

System parameter	low-speed	high-speed
input power $P_{\mathrm{m,sh}}$	20 kW	
generator speed $n_{\mathrm{SRG,nom}}$	7500 rpm	free
total machine torque T_{tot}	25.5 Nm	free
stator outer diameter D_{st}	220 mm	free
stator stack length L_{stk}	60 mm	free
dc-link voltage u_{dc}	300 V	400 V

Table 2.1: Scenario specifications.

linked by a gearbox to a rotary wankel engine with $n_{\mathrm{ICE}} = 6000\,\mathrm{rpm}$. Table 2.1 lists the requirements for the two scenarios. The mechanical input power $P_{\mathrm{m,sh}}$ was set to 20 kW in the range of current prototypes and available products for compact HEVs. The corresponding generators for the two scenarios are chosen in section 3.4.

2.1.2.1 Low-Speed Scenario

Generator torque ripple and acoustic behavior play a secondary role for this scenario, because a single cylinder combustion engine with a low frequency torque ripple [MST12; Ind+16] is employed. The main target of this scenario is to obtain a cost-effective solution to replace current PMSM technology. To reduce the required cables between generator and inverter and the number of power electronic devices, machines with a low number of phases $N_{\mathrm{ph}} < 3$ are of interest for this scenario. The high compression ratio and the dead center of the single cylinder ICE require a quite large peak torque [Mül10; Gv15]. As single phase machines provide very limited starting torque, even with special rotor designs [Hen+11], an external starting device would be required. Configurations with a higher number of phases $N_{\mathrm{ph}} = 2$ are able to supply sufficient torque with a simple asymmetric rotor design, which will be discussed in section 4.4.2. From these considerations, 2-phase machines are of main interest for the low-speed scenario. This scenario is also an example for an application, in which the generator has to fit in a given envelope volume of a compact car [Ind+16]. The source voltage u_{src} of the available prototype battery system is 300 V.

2.1.2.2 High-Speed Scenario

A decoupling of the SRG nominal speed $n_{\mathrm{SRG,nom}}$ from the ICE speed n_{ICE} offers the potential to increase the generator power density $\phi_{\mathrm{P,tot}}$, as the required generator output torque T_{tot} is reduced by an increased $n_{\mathrm{SRG,nom}}$. This is especially important for applications where the weight and volume of the system is of high importance, such as small aircraft. The envelope volume is not pre-defined and can be chosen to maximize the generator power density $\phi_{\mathrm{P,tot}}$. In the high-speed scenario, the high torque ripple of 2-phase machines (see section 4.4.2) might cause acoustic issues in the gearbox [FNP16]. Therefore, 3-phase machines with a reduced torque ripple need to be considered for this scenario. Within this constraints, the number of phases N_{ph} and number of pole pairs n_{p} can be freely chosen to optimize machine efficiency η_{mach}, generator power density $\phi_{\mathrm{P,tot}}$ and acoustic behavior. As current battery packs have a nominal source voltage u_{src} up to 360 V and the internal source resistance $R_{i,src}$ increases the dc-link voltage u_{dc} during charging, u_{dc} is set to 400 V for this scenario.

2.1.3 Bearing Configuration

For the two scenarios, different bearing configurations are used (see fig. 2.3). For the low-speed scenario, two grease-lubricated grooved ball bearings are employed. For the high-speed scenario in addition to one grease-lubricated grooved ball bearing (B4 in fig. 2.3b) in the generator, three oil-lubricated grooved ball bearings are required in the gearbox. Two on the low-speed side (B1 and B2) and one on the high-speed side (B3).

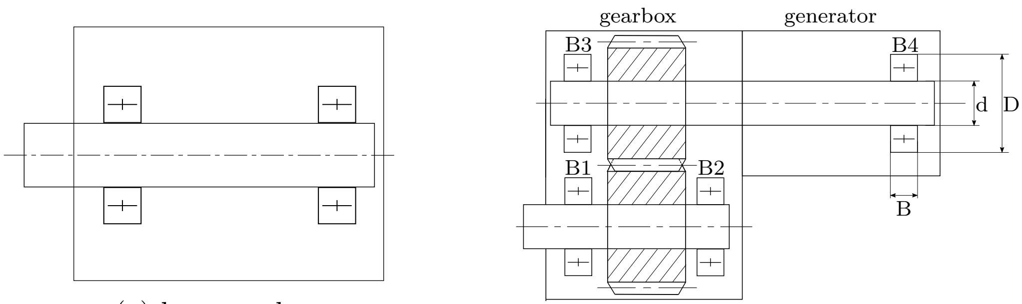

(a) low-speed

(b) high-speed

Fig. 2.3: Bearing configuration for low- and high-speed scenarios.

2.2 Switched Reluctance Generator

SRGs were first proposed by Taylor in 1840 [Tay]. With the development of modern power electronics, this machine type got more attention by scientists starting in the 1980's [Law+80]. Since then, the working principle and control of SRGs was described in detail in [Mil93; DPV11]. An overview of current research activities can be found in [Bur+17]. In this section, the most important fundamentals of SRGs are introduced.

Radial flux SRGs, as exemplary shown in fig. 2.4a, consist of a salient stator and rotor defined by the number of stator poles N_s and rotor poles N_r. The number of stator poles N_s are calculated from the number of phases N_{ph} and the number of pole pairs n_p by (2.1). Two stator poles form one pole pair of a specific phase. In case of machines with more than one phase, the number of rotor poles N_r has to be chosen different from the number of stator poles N_s to create a contiguous torque. As $N_r > N_s$ negatively influences the machine efficiency [Mil93], in this thesis only the case $N_r < N_s$, defined by (2.2), is considered. Table 2.2 lists the pole configurations investigated in this thesis in chapter 3. The naming convention of machine configurations can be found in section A.2.1.

$$N_s = 2 \cdot n_p \cdot N_{ph} \tag{2.1}$$

$$N_r = 2 \cdot n_p \cdot (N_{ph} - 1), N_{ph} > 1 \tag{2.2}$$

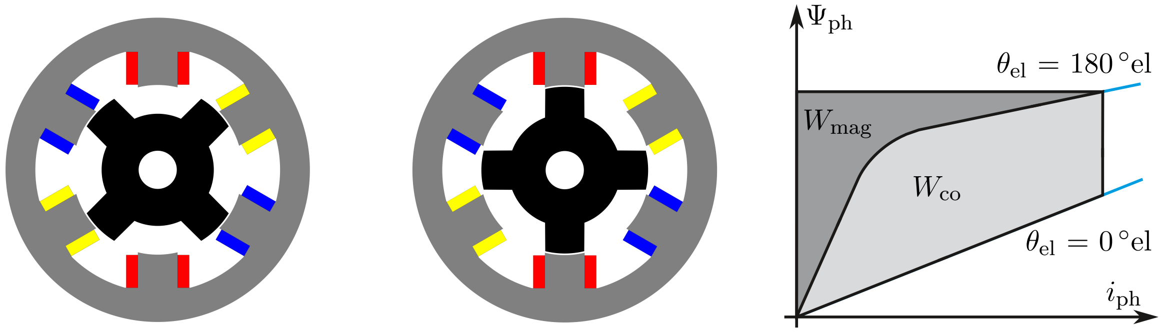

(a) $\theta_{\mathrm{el}} = 0\,°\mathrm{el}$, unaligned (b) $\theta_{\mathrm{el}} = 180\,°\mathrm{el}$, aligned (c) coenergy W_{co} of one phase

Fig. 2.4: Characteristic positions of a (3,1) SRG in relation to the red phase and definition of coenergy loop W_{co}. stator: gray, rotor: black, windings: colored

parameter	configuration					
number of phases N_{ph}	2			3		4
number of pole pairs n_{p}	1	2	3	1	2	1
number of stator poles N_{s}	4	8	12	6	12	8
number of rotor poles N_{r}	2	4	6	4	8	6

Table 2.2: Considered SRG configurations in this thesis.

In fig. 2.4a and 2.4b, the characteristic unaligned and aligned rotor position in relation to the red machine phase are depicted, respectively. By exciting the red phase close to the unaligned position, a magnetic flux Φ_{pl} is created, which tends to minimize the magnetic resistance, or reluctance, of the magnetic path through stator and rotor. The resulting tangential force pulls the rotor towards the aligned position. This procedure is repeated for all phases and rotor poles to create a continuous rotation. Therefore, one electric period is defined by the mechanical angle θ_{m} of one rotor pole. The electrical angle θ_{el}, periodic to $360\,°\mathrm{el}$, is then defined by the mechanical angle θ_{m} and the number or rotor poles N_{r} by (2.3). The electric base frequency f_{el} is calculated from the rotational speed of the shaft n_{SRG} and the number of rotor poles N_{r} by (2.4).

$$\theta_{\mathrm{el}} = N_{\mathrm{r}} \cdot \theta_{\mathrm{m}} \tag{2.3}$$

$$f_{\mathrm{el}} = N_{\mathrm{r}} \cdot \frac{n_{\mathrm{SRG}}}{60} \tag{2.4}$$

The resulting torque T_{tot} can be calculated with the help of the coenergy loop W_{co} enclosed by the characteristic unaligned and aligned position [Mil93]. The coenergy loop W_{co} defined by (2.5) is exemplary depicted for a constant phase current i_{ph} in fig. 2.4c. In this case, the coenergy loop W_{co} is equal to the maximally available coenergy loop $W_{\mathrm{co,max}}$ between unaligned and aligned position at a given peak phase current $I_{\mathrm{ph,pk}}$. Assuming symmetry of all phases, the machine output torque T_{tot} of the SRG is than calculated by multiplication of the coenergy loop W_{co} of one phase pulse with the number of rotor poles N_{r} and the number of phases N_{ph} (see (2.6)).

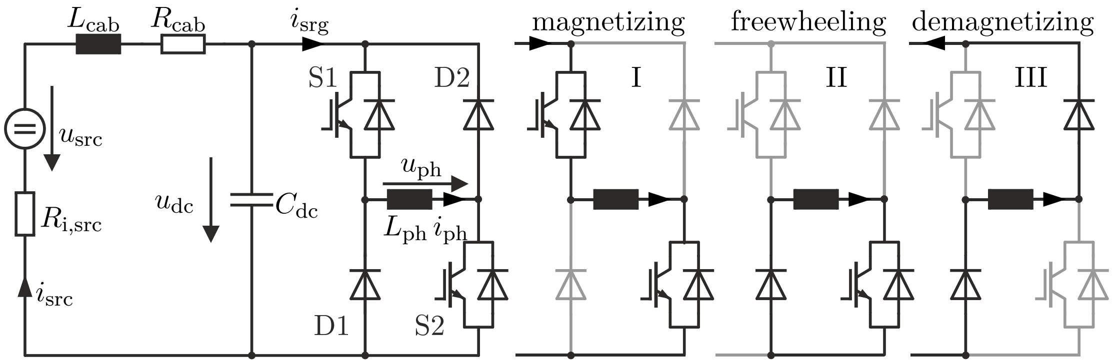

Fig. 2.5: Electric equivalent circuit of a 1-phase SRG and characteristic switching states of an asymmetric-half bridge (AHB).

$$W_{\mathrm{co}} = \oint \Psi_{\mathrm{ph}}(i_{\mathrm{ph}},\theta)\ \mathrm{d}i_{\mathrm{ph}}\ \mathrm{d}\theta \tag{2.5}$$

$$T_{\mathrm{tot}} = N_{\mathrm{ph}} \cdot W_{\mathrm{co}} \cdot \frac{N_{\mathrm{r}}}{2\pi} \tag{2.6}$$

To operate SRGs continuously, a power electronic inverter is required. In [BP98] an overview on possible inverter topologies can be found. Most common is the asymmetric-half bridge (AHB), as shown in fig. 2.5 for a 1-phase SRG. For each phase, an output stage of two switches and two diodes is required. With this topology, the phase current i_{ph} of each phase can be controlled independent from the remaining phases with the three switching states, magnetizing (I), freewheeling (II) and demagnetizing (III), as depicted in fig. 2.6.

During the magnetizing period $\Delta\theta_{\mathrm{mag}}$, (I) defined by (2.7), both switches S1 and S2 are closed and the positive dc-link voltage u_{dc} is applied to the phase. In freewheeling period $\Delta\theta_{\mathrm{fw}}$, (II) defined by (2.8), no external voltage is applied to the phase, as only one of the two available switches is closed. Finally, in demagnetizing (III) both switches are opened, and the negative dc-link voltage u_{dc} is applied to the phase by the two conducting diodes D1 and D2, until the phase current i_{ph} reaches 0 A at the angle θ_{decay}.

$$\Delta\theta_{\mathrm{mag}} = \theta_{\mathrm{fw}} - \theta_{\mathrm{on}} \tag{2.7}$$

$$\Delta\theta_{\mathrm{fw}} = \theta_{\mathrm{off}} - \theta_{\mathrm{fw}} \tag{2.8}$$

An exemplary current profile is depicted in fig. 2.6. The change of current depends on the relation of the applied external voltage during the three switching states and the machine internal voltage drops, defined by (2.9). In (2.9) the first term (a) stands for the ohmic voltage drop caused by the phase resistance $R_{\mathrm{ac,ph}}$ and the phase current i_{ph}. The second term (b) stands for the self-induced voltage drop as well as saturation effects. The last term (c) describes the voltage drop induced by the rotation of the machine and is referred to as back electromotive force (EMF) e.

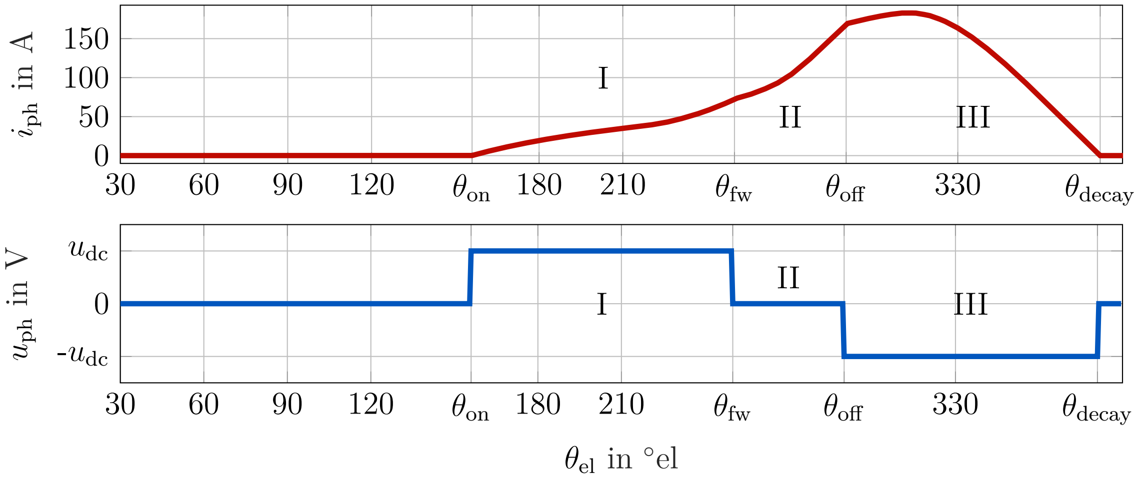

Fig. 2.6: Characteristic control angles, externally applied phase voltage u_{ph} and phase current i_{ph} for one phase during one electric period.

$$\begin{aligned} u_{ph} &= R_{ac,ph} \cdot i_{ph} + \frac{d\Psi_{ph}}{dt} \\ &= \underbrace{R_{ac,ph} \cdot i_{ph}}_{a} + \underbrace{\left(L_{ph}(i_{ph},\theta) + i_{ph} \frac{\partial L_{ph}(i_{ph},\theta)}{\partial i_{ph}} \right) \frac{di_{ph}}{dt}}_{b} + \underbrace{i_{ph} \frac{\partial L_{ph}(i_{ph},\theta)}{\partial \theta} \frac{d\theta}{dt}}_{c} \end{aligned} \tag{2.9}$$

All phase related quantities are influenced by the number of turns per pole $N_{w,pl}$ and the interconnection of individual poles in serial and parallel [Car08; Bra13]. In this thesis, only the parallel connection of all poles of each phase is considered. The phase current i_{ph}, phase flux linkage Ψ_{ph}, phase inductance L_{ph} and total phase resistance $R_{ac,ph}$ can than be calculated by (2.10) - (2.13), respectively.

$$i_{ph} = 2 \cdot n_p \cdot \frac{\Theta_{pl}}{N_{w,pl}} \tag{2.10}$$

$$\Psi_{ph} = \Psi_{pl} = N_{w,pl} \cdot \Phi_{pl} \tag{2.11}$$

$$R_{ac,ph} = {N_{w,pl}}^2 \cdot \frac{R_{ac,pl,1}}{2 \cdot n_p} \tag{2.12}$$

$$L_{ph} = {N_{w,pl}}^2 \cdot \frac{L_{pl,1}}{2 \cdot n_p} \tag{2.13}$$

By changing the number of turns per pole $N_{w,pl}$, the resulting u_{ph} at a constant generator speed n_{SRG} and phase current i_{ph} can be adapted to the available dc-link voltage u_{dc} [Bra13] to achieve a certain current profile at nominal operation point. In hysteresis current control (HCC), i_{ph} can be controlled by the inverter as the relation $u_{dc} \gg u_{ph}$ is valid. Therefore, the system behavior in terms of instantaneous torque or force [Bur+17] can be influenced.

While sacrificing controllability, SRGs are rather operated in single pulse control (SPC) than in HCC to achieve a higher drive efficiency η_{drive}, as discussed in [Bra13] and further analyzed in section 4.1.1. Finally, the continuos conduction mode (CCM) offers the potential to overload SRGs [HHM11], rather than being a steady-state operation mode.

Fig. 2.7 shows exemplary the effect of an increasing number of turns per pole $N_{\mathrm{w,pl}}$ on the pole magneto motive force (MMF) Θ_{pl} (fig. 2.7a) and the resulting coenergy loop W_{co} (fig. 2.7b) of a fixed machine geometry to achieve the same total output torque T_{tot}. The maximum available coenergy loop $W_{\mathrm{co,max}}$ is exemplary depicted by the green dashed line for the SPC in fig. 2.7b. While in HCC the achieved coenergy loop W_{co} is nearly equal to $W_{\mathrm{co,max}}$, in SPC and CCM W_{co} is much smaller than $W_{\mathrm{co,max}}$. The implications on the SRG design process will be discussed in section 3.3.2.

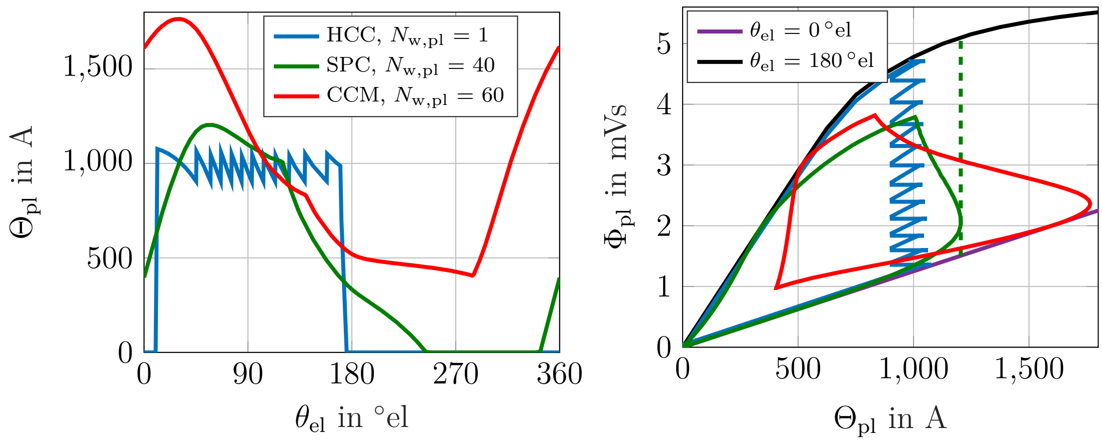

(a) pole MMF Θ_{pl}

(b) coenergy loop W_{co}

Fig. 2.7: Influence of the number of turns on pole MMF Θ_{pl} (left) and coenergy loop W_{co} (right) for a (4,1) SRG at $D_{\mathrm{st}} = 120$ mm.

2.2.1 System Loss Modeling

From the mechanical input power $P_{\mathrm{m,sh}}$ to the electrical power supplied to the source $P_{\mathrm{el,src}}$, a multitude of losses occur in SRG systems. Fig. 2.8 depicts the naming of the input and output power of the different system parts discussed in this thesis and the corresponding losses. Subtracting the machine losses $P_{\mathrm{l,mach}}$ from the mechanical input power $P_{\mathrm{m,sh}}$, the

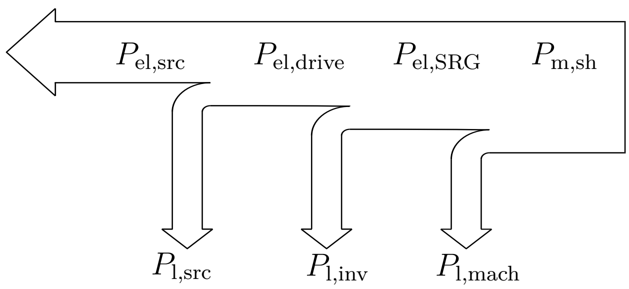

Fig. 2.8: System power flow and corresponding component losses.

	defined relation
gearbox efficiency η_{gear}	$(P_{\text{m,sh}} - P_{\text{l,gear}})/P_{\text{m,sh}}$
generator efficiency η_{mach}	$P_{\text{el,SRG}}/P_{\text{m,sh}}$
inverter efficiency η_{inv}	$P_{\text{el,drive}}/P_{\text{el,SRG}}$
drive efficiency η_{drive}	$P_{\text{el,drive}}/P_{\text{m,sh}}$
system efficiency η_{tot}	$P_{\text{el,src}}/P_{\text{m,sh}}$

Table 2.3: Defined component and system efficiencies.

electric SRG output power $P_{\text{el,SRG}}$ is obtained. From $P_{\text{el,SRG}}$ the inverter losses $P_{\text{l,inv}}$ are subtracted to obtain the drive output power $P_{\text{el,drive}}$. The available charging power $P_{\text{el,src}}$ is finally calculated by subtracting the source losses $P_{\text{l,src}}$ from the drive output power $P_{\text{el,drive}}$. In addition to the losses, the efficiencies listed in table 2.3 are defined.

All losses are summed up to the total system losses $P_{\text{l,tot}}$ as described by (2.14). The sum of inverter losses $P_{\text{l,inv}}$ and machine losses $P_{\text{l,mach}}$ form the drive losses $P_{\text{l,drive}}$. This value is measured on the test bench rather than the complete system losses $P_{\text{l,tot}}$. The machine losses $P_{\text{l,mach}}$ are further separated into total copper losses $P_{\text{l,cu,ac}}$, iron core losses $P_{\text{l,fe}}$ and mechanical losses $P_{\text{l,m}}$ as stated by (2.15). In the following, the underlying formulas for the analytic loss modeling are introduced.

$$\begin{aligned} P_{\text{l,tot}} &= P_{\text{l,drive}} && + P_{\text{l,src}} \\ &= P_{\text{l,mach}} + P_{\text{l,inv}} && + P_{\text{l,src}} \end{aligned} \tag{2.14}$$

$$P_{\text{l,mach}} = P_{\text{l,cu,ac}} + P_{\text{l,fe}} + P_{\text{l,m}} \tag{2.15}$$

Power Source

To reduce the simulation time and the modeling effort, the battery is modeled by an ideal voltage source u_{src} with an internal resistance $R_{\text{i,src}}$ rather than a complex physico-electrochemical model, for example proposed in [Sch17]. The losses in this source can be calculated by (2.16).

$$P_{\text{l,src}} = R_{\text{i,src}} \cdot \frac{1}{T_{\text{el}}} \int_0^{T_{\text{el}}} {i_{\text{src}}}^2 \, \mathrm{d}t \tag{2.16}$$

The source is attached to the inverter by a cable, consisting of R_{cab} and L_{cab} as indicated in fig. 2.5. As R_{cab} is estimated by a factor 100 smaller than $R_{\text{i,src}}$ for reasonable cable lengths in electric vehicles, the related losses are neglected.

Power Electronics

As mentioned before, an AHB with two insulated-gate bipolar transistors (IGBTs) and two diodes per phase is assumed in the power electronic inverter. The losses in the power electronic components consist of conduction losses $P_{\text{l,cond}}$ and switching losses $P_{\text{l,sw}}$. The conduction losses $P_{\text{l,cond}}$ are calculated with the help of the current dependent voltage drop across one device u_{dev}, derived from datasheets, and the device current i_{dev} (2.17). Both values depend on the switching states shown in fig. 2.5 and the phase current i_{ph}.

$$P_{\mathrm{l,cond}} = \sum_{N_{\mathrm{dev}}} \frac{1}{T_{\mathrm{el}}} \int_0^{T_{\mathrm{el}}} u_{\mathrm{dev}}(i_{\mathrm{dev}}) i_{\mathrm{dev}} \,\mathrm{d}t \tag{2.17}$$

The switching losses are calculated by (2.18). $E_{\mathrm{on,dev}}$ and $E_{\mathrm{off,dev}}$ are the current dependent device turn-on and turn-off switching energies, which depend on the instantaneous device current i_{dev} during a certain switching event i. k represents the number of switching events per electric period T_{el}.

$$P_{\mathrm{l,sw}} = \sum_{N_{\mathrm{dev}}} \left[f_{\mathrm{el}} \cdot \left[\sum_{i=1}^{k} \left[E_{\mathrm{on,dev}}(i_{\mathrm{dev},i}) + E_{\mathrm{off,dev}}(i_{\mathrm{dev},i}) \right] \right] \right] \tag{2.18}$$

Copper Losses

The total copper losses $P_{\mathrm{l,cu,ac}}$ (2.19) of an SRG consist of dc copper losses $P_{\mathrm{l,cu,dc}}$ and eddy-current copper losses $P_{\mathrm{l,cu,eddy}}$ caused by skin and proximity effects.

$$P_{\mathrm{l,cu,ac}} = P_{\mathrm{l,cu,dc}} + P_{\mathrm{l,cu,eddy}} \tag{2.19}$$

The dc copper losses $P_{\mathrm{l,cu,dc}}$ can be calculated from the dc phase resistance $R_{\mathrm{dc,ph}}$, the instantaneous phase current i_{ph} and the number of phases N_{ph} by (2.20).

$$P_{\mathrm{l,cu,dc}} = N_{\mathrm{ph}} \cdot R_{\mathrm{dc,ph}} \cdot \frac{1}{T_{\mathrm{el}}} \int_0^{T_{\mathrm{el}}} {i_{\mathrm{ph}}}^2 \,\mathrm{d}t = N_{\mathrm{ph}} \cdot R_{\mathrm{dc,ph}} \cdot {I_{\mathrm{ph,rms}}}^2 \tag{2.20}$$

The ohmic resistance of one phase $R_{\mathrm{dc,ph}}$ can be further separated into the dc-copper resistance of one phase without end-windings $R_{\mathrm{dc,ph,woEw}}$ and an end-winding dc-copper resistance $R_{\mathrm{dc,ph,Ew}}$ (2.21). $R_{\mathrm{dc,ph,woEw}}$ describes the copper in the stator slot parallel to the iron core, while $R_{\mathrm{dc,ph,Ew}}$ describes the copper required to connect the coils at both ends of the machine.

$$R_{\mathrm{dc,ph}} = R_{\mathrm{dc,ph,woEw}} + R_{\mathrm{dc,ph,Ew}} \tag{2.21}$$

For design analysis in section 4.1.1 the two additional ac phase resistance $R_{\mathrm{ac,ph}}$ and eddy-current phase resistance $R_{\mathrm{eddy,ph}}$ are defined by (2.22) and (2.23), respectively.

$$R_{\mathrm{ac,ph}} = \frac{P_{\mathrm{l,cu,ac}}}{N_{\mathrm{ph}} \cdot {I_{\mathrm{ph,rms}}}^2} \tag{2.22}$$

$$R_{\mathrm{eddy,ph}} = \frac{P_{\mathrm{l,cu,eddy}}}{N_{\mathrm{ph}} \cdot {I_{\mathrm{ph,rms}}}^2} \tag{2.23}$$

To analytically estimate the eddy-current copper losses $P_{\mathrm{l,cu,eddy}}$ in non-rotating transformers, [Dow66] developed a method expressed by (2.24), which decomposes i_{ph} in its fundamental components ${}^{k}I$ and applies the well known skin and proximity functions ϕ and ψ, respectively.

$$P_{\mathrm{l,cu,ac}} = R_{\mathrm{dc,ph}} \left[{I_{\mathrm{ph,rms}}}^2 + \sum_{k=1}^{\infty} \left[{}^kI^2 \left(\phi({}^kx) + \frac{n^2-1}{3}\psi({}^kx) \right) \right] \right] \tag{2.24}$$

$${}^kx = \frac{d_{\mathrm{w}}\sqrt{\pi}}{2} \cdot {}^k\beta = \frac{d_{\mathrm{w}}\sqrt{\pi}}{2} \cdot \sqrt{kf_0\pi\sigma\mu} \cdot \sqrt{\frac{w}{w_{slot}}}. \tag{2.25}$$

The method described by (2.24) was applied in [Car08] for a small number of operation points of one SRG, generally underestimating total copper losses $P_{\mathrm{l,cu,ac}}$ compared to a coupled FEA (see section 2.3.2). Further analysis in [Sch15] suggest that simple analytical approaches, such as [Dow66], cannot be applied for SRG with sufficient accuracy. Therefore, the eddy-current copper losses $P_{\mathrm{l,cu,eddy}}$ will be investigated in detail in section 4.1.1 and 5.1.1 by the help of (2.24) and coupled FEA (see section 2.3.2).

Not regarding the calculation method, the eddy-current copper losses $P_{\mathrm{l,cu,eddy}}$ can be described by the frequency dependent eddy-loss ratio p_{eddy} as a function of the total dc-copper losses $P_{\mathrm{l,cu,dc}}$ including the end-windings (2.26). To determine the eddy-current copper losses $P_{\mathrm{l,cu,eddy}}$ it is common to employ a 2-dimensional (2-D) coupled FEA [Car08; Sch15]. For a better comparison with these results, the eddy-current copper losses $P_{\mathrm{l,cu,eddy}}$ can be described as a function of the copper losses without end-windings $P_{\mathrm{l,cu,dc,woEw}}$ by the additional eddy-loss ratio $p_{\mathrm{eddy,woEw}}$ as defined in (2.27).

$$P_{\mathrm{l,cu,eddy}} = p_{\mathrm{eddy}}(f_{\mathrm{el}}) \cdot P_{\mathrm{l,cu,dc}} \tag{2.26}$$

$$P_{\mathrm{l,cu,eddy}} = p_{\mathrm{eddy,woEw}}(f_{\mathrm{el}}) \cdot P_{\mathrm{l,cu,dc,woEw}} \tag{2.27}$$

Iron Core Losses

State of the art for the modeling of iron core losses $P_{\mathrm{l,fe}}$, are empirical or physical models [Kri14; ESH12]. All models have in common, that they fit a certain amount of parameters (k,α,β) on measurement data, e.g. from Epstein frame measurements, retrieved for sinusoidal flux-densities $B_{\mathrm{pt}}(t)$ at different peak flux densities B_{pk} and electric base frequencies f_{el}. The specific iron losses can then be expressed by fitting functions, such as (2.28) - (2.30).

$$p_{\mathrm{SE}} = k \cdot {B_{\mathrm{pk}}}^{\beta} \cdot {f_{\mathrm{el}}}^{\alpha} \tag{2.28}$$

$$p_{\mathrm{Bertotti}} = k_{\mathrm{hyst}} \cdot {B_{\mathrm{pk}}}^{\beta_{\mathrm{hyst}}} \cdot f_{\mathrm{el}} + k_{\mathrm{eddy}} \cdot {B_{\mathrm{pk}}}^2 \cdot {f_{\mathrm{el}}}^2 + k_{\mathrm{excess}} \cdot {B_{\mathrm{pk}}}^{1.5} \cdot {f_{\mathrm{el}}}^{1.5} \tag{2.29}$$

$$p_{\mathrm{IEM5}} = k_1 \cdot {B_{\mathrm{pk}}}^{\beta_1} \cdot f_{\mathrm{el}} + k_2 \cdot {B_{\mathrm{pk}}}^2 \cdot {f_{\mathrm{el}}}^2 + k_3 \cdot {B_{\mathrm{pk}}}^{1.5} \cdot {f_{\mathrm{el}}}^{1.5} + k_4 \cdot {B_{\mathrm{pk}}}^{\beta_4} \cdot {f_{\mathrm{el}}}^2 \tag{2.30}$$

The most basic Steinmetz equation (SE) [Ste92], expressed by (2.28), only employs one term with three fitting parameters. Increasing the number of terms and fitting parameters allows a better fit on the material data for changing peak flux densities B_{pk} and electric base frequencies f_{el}, as investigated in [KBD16b] for SRGs. In this thesis, the SE p_{SE} [Ste92], the Bertotti formula p_{Bertotti} [Ber88] and the IEM5 formula p_{IEM5} [ESH12] are employed to investigate the iron losses. To account for non-sinusoidal flux linkage waveforms, the improved generalized Steinmetz equation (iGSE), proposed by [Ven+02], can be applied to each individual term of p_{Bertotti} and p_{IEM5}, as described in [KBD16b].

To calculate the iron core losses $P_{\mathrm{l,fe}}$ in the complete machine, the iron core is separated into iron core sections N_{pt} with a specific part volume V_{pt}. In the analytical models, a constant magnetic flux density B_{pt} is assumed in these tooth and yoke parts. A specific iron loss density is calculated for each machine part and the iron core losses $P_{\mathrm{l,fe}}$ are then summed up for all iron core sections N_{pt}, as shown exemplary for the SE p_{SE} in (2.31).

$$P_{\mathrm{l,fe}} = \sum_{N_{\mathrm{pt}}} \left[V_{\mathrm{pt}} \cdot p_{\mathrm{SE}}(V_{\mathrm{pt}})\right] \tag{2.31}$$

In the coupled FEA (2.32), a derivate of p_{Bertotti}, is applied to each mesh element at each time step. Afterwards, the iron core losses $P_{\mathrm{l,fe}}$ are retrieved by an integration over the complete iron core volume V_{fe} and one electric period T_{el} (2.33). The results from this equation will be compared to the analytical model with average flux density in section 4.1.2, as calculation time is strongly increased by this approach.

$$p_{\mathrm{FLUX}}(t) = k_{\mathrm{hyst}} \hat{B_{\mathrm{pt}}}^2 f_{\mathrm{el}}^2 + k'_{\mathrm{eddy}} \left(\frac{\mathrm{d}B_{\mathrm{pt}}}{\mathrm{d}t}\right)^2 + k'_{\mathrm{excess}} \left(\frac{\mathrm{d}B_{\mathrm{pt}}}{\mathrm{d}t}\right)^{1.5} \tag{2.32}$$

$$P_{\mathrm{l,fe}} = \int\limits_{V_{\mathrm{fe}}} \int\limits_{0}^{T_{\mathrm{el}}} p_{\mathrm{FLUX}}(t)\ \mathrm{d}t\ \mathrm{d}V \tag{2.33}$$

Mechanical losses

Mechanical losses $P_{\mathrm{l,m}}$ in SRGs consist of windage losses $P_{\mathrm{l,wind}}$ in the air gap, bearing losses $P_{\mathrm{l,bear}}$ and the losses of a potential gearbox $P_{\mathrm{l,gear}}$ as indicated in (2.34).

$$P_{\mathrm{l,m}} = P_{\mathrm{l,wind}} + P_{\mathrm{l,bear}} + P_{\mathrm{l,gear}} \tag{2.34}$$

The double salient structure of SRGs causes air turbulences and high windage losses $P_{\mathrm{l,wind}}$ in the air gap. These losses can be estimated with complex computational fluid dynamics (CFD) calculations. Such calculations were applied to a high-speed turbo charger SRG in [CJS00] for rotor tip radii R_1 from 12.5 to 37.5 mm and air gap lengths d_{g} from 0.1 to 0.3 mm. A good match between the CFD calculations and measurements up to a shaft speed $n_{\mathrm{SRG}} = 50\,\mathrm{krpm}$ was found. However, CFD calculations are very time consuming and, therefore, not suitable for a fast comparison of different machine designs. In [CJS00] an analytical formula is fitted to the CFD results for the investigated range of R_1 and d_{g}. However, in this thesis an air gap length d_{g} between 0.7 and 1.0 mm is considered, not covered by the parameters given in [CJS00]. As the retrieved fitting parameters are non-linear, an extrapolation of the derived analytical formula is not possible.

In [Vra68] an analytical method to calculate the windage losses $P_{\mathrm{l,wind}}$, described by (2.35), is presented. The saliency factor K_{sal} is defined by the rotor pole height $h_{\mathrm{pl,r}}$ and the rotor pole tip radius R_1 as described in (2.36). For a non-salient air gap ($^{h_{\mathrm{pl,r}}}/_{R_1} = 0$), [Vra68] defines $K_{\mathrm{sal}} = 1$. The skin friction coefficient C_{d} has to be determined from approximations, as no analytical description is available [Vra68]. Additionally, the air gap fluid density ρ_{fl}, the rotor pole tip radius R_1, the generator speed n_{SRG} as well as the machine stack length L_{stk} are required to fully define (2.35). A good match between the analytical calculation of windage losses $P_{\mathrm{l,wind}}$ by (2.35) and measurements was found in [KKC14; Kiy+16] for a

60 kW traction machine. The applicability to the machines considered in this thesis will be investigated in section 4.1.3 by measurements.

$$P_{\mathrm{l,wind}} = K_{\mathrm{sal}} \cdot \pi \cdot C_{\mathrm{d}} \cdot \rho_{\mathrm{fl}} \cdot {R_1}^4 \cdot L_{\mathrm{stk}} \cdot \left(\frac{2 \cdot \pi \cdot n_{\mathrm{SRG}}}{60}\right)^3 \tag{2.35}$$

$$K_{\mathrm{sal}} = \begin{cases} 8.5 \cdot \frac{h_{\mathrm{pl,r}}}{R_1} + 2.2 & \text{if } {}^{h_{\mathrm{pl,r}}}/_{R_1} > 0.06 \\ 1 & \text{if } {}^{h_{\mathrm{pl,r}}}/_{R_1} = 0 \end{cases} \tag{2.36}$$

The bearing losses $P_{\mathrm{l,bear}}$ are not of main interest in this thesis, however, they need to be estimated to be able to separate the mechanical losses $P_{\mathrm{l,m}}$ on the test bench. To estimate $P_{\mathrm{l,bear}}$, different calculation methods are common in industry. In [GF07] the bearing drag torque T_{bear} in high-speed bearings ($\nu \cdot n_{\mathrm{SRG}} > 2000$) is given by (2.37). For definition of the relevant bearing parameters it is referred to [GF07]. The speed dependent bearing losses $P_{\mathrm{l,bear}}$ can be assumed to be proportional to ${n_{\mathrm{SRG}}}^{5/3}$ from (2.37).

$$T_{\mathrm{bear}} = 10^{-7} f_0 (\nu \cdot n_{\mathrm{SRG}})^{2/3} d_{\mathrm{m}}^3 + f_1 P_1 d_{\mathrm{m}} \tag{2.37}$$

Estimating gearbox losses $P_{\mathrm{l,gear}}$ is a rather complex task, strongly depending on the tooth shape, the lubrication concept and oil as well as the chosen bearings within the gearbox [NW03]. Within this work, an oil-lubricated one-stage spur gear is applied for the high-speed SRGs. In [NW03] a gearbox efficiency η_{gear} between 98 and 99 % is stated for such gears. A similar value was achieved for a two-speed two-stage oil lubricated spur gear in [AG15]. Hence, for the gearbox a speed independent T_{gear} of 2 % of the nominal generator torque $T_{\mathrm{tot,nom}}$ is assumed for all operation points (2.38). This loss torque accounts for all gear internal losses, including one high-speed bearing as well as all sealings (see fig. 2.3b). The gearbox losses $P_{\mathrm{l,gear}}$ are, therefore, proportional to the generator speed n_{SRG}.

$$T_{\mathrm{gear}} = 0.02 \cdot T_{\mathrm{tot,nom}} \tag{2.38}$$

2.2.2 SRG Prototype examples

Beside as magnet free traction drives [Tak+12; Hof14; WMM15], several applications for SRGs are proposed in research. Since the late 80's SRGs are discussed in aircraft applications as starter-generators for gas turbines [MJ89; Fer+95; RF95; RFR98; Sho+10] with a total input power $P_{\mathrm{m,sh}}$ between 30 and 250 kW. Also the suitability of SRGs as fuel pumps in the range of 90 kW was investigated [Rad92; Rad95]. Since around 2000, gearbox integrated starter-generator [Fah02; SL09] are investigated as well as turbocharger applications [CJS00; MCA12], for hybridization of conventional ICE driven cars.

A wide overview on high-speed SRG research and applications with generator speeds $n_{\mathrm{SRG}} > 20$ krpm can be found in [FBE15]. Machine efficiencies η_{mach} between 89 and 93 % are reached for generating operation at input power ratings $P_{\mathrm{m,sh}} > 20$ kW. However, the listed data shows that most publications are not stating all required information (i.e. iron core material, exact winding design) to evaluate and compare the reached machine efficiencies η_{mach}. Additionally, many publications are only based on simulations or partial load measurements. For the two scenarios described in section 2.1.2 the machines listed in ta-

		low-speed	high-speed
reference		[Lon+03; SL09]	[MJ89; Fer+95]
nominal input power	$P_{\mathrm{m,sh}}$	15 kW	30 kW
operational speed	n_{SRG}	600 − 2500 rpm	27 − 47 krpm
configuration	$N_{\mathrm{s}}/N_{\mathrm{r}}$	18/12	6/4
electric base frequency	f_{el}	120 − 500 Hz	1800 − 3133 Hz
stack length	L_{stk}	85 mm	63.5 mm
total machine length	L_{act}	< 135 mm	113 mm
stator outer diameter	D_{st}	440 mm	159 mm
active material volume	V_{act}	20.5 l	2.2 l
volumetric power density	$\phi_{\mathrm{P,act}}$	0.7 kW/l	13.6 kW/l
volumetric torque density	$\phi_{\mathrm{T,act}}$	7.0 Nm/l	4.7 Nm/l
dc-link voltage	u_{dc}	240 V	270 V
iron core material		(-)	2V49FeCo
iron sheet thickness	$d_{\mathrm{sh,fe}}$	(-)	150 μm
number of turns per pole	$N_{\mathrm{w,pl}}$	64	(-)
wire technology		solid conductors	litz wire
measured machine efficiency	η_{mach}	94.1 %	91 %
	at	1000 rpm, 15 kW	30 krpm, 30 kW

Table 2.4: Reference machines for comparison with prototype machine efficiencies η_{mach} (section 4.1.5) and active material volumes V_{act} (section 4.2.4).

ble 2.4 are chosen as reference. For both machines, simulations and prototype measurements for a speed and power range comparable to the developed low- and high-speed scenario exist.

2.3 Simulation Models

2.3.1 Look-Up Based System Simulation Model

To assess the behavior of the electric drive-train, a system model representing the equivalent circuit shown in fig. 2.5 is employed. The SRG model implements the voltage equation (2.9) as shown in fig. 2.9 with the help of machine characteristic lookup tables (LUTs) (pole torque T_{pl}, MMF Θ_{pl} and radial force $F_{\mathrm{pl,rad}}$) retrieved from static FEAs. The phase voltage u_{ph} input is determined with the help of the current inverter switching state and the machine phase current i_{ph} by the dynamic dc-link. The electrical angle θ_{el} is determined from a constant speed input.

To determine the influence of the control angles, the model is set up at various constant generator speeds n_{SRG}. At each operation point for a range of turn-off angle θ_{off} and free-wheeling period $\Delta\theta_{\mathrm{mag}}$, the corresponding turn-on angle θ_{on} is determined to satisfy the requested total output torque T_{tot}. Mechanical losses $P_{\mathrm{l,m}}$ are neglected, as they cannot be influenced by the control strategy. The dynamic results of one full electric period in steady state are extracted. Beside the ohmic dc copper losses $P_{\mathrm{l,cu,dc}}$ as well as the source losses $P_{\mathrm{l,src}}$, all losses introduced in section 2.2.1 are calculated afterwards in post processing.

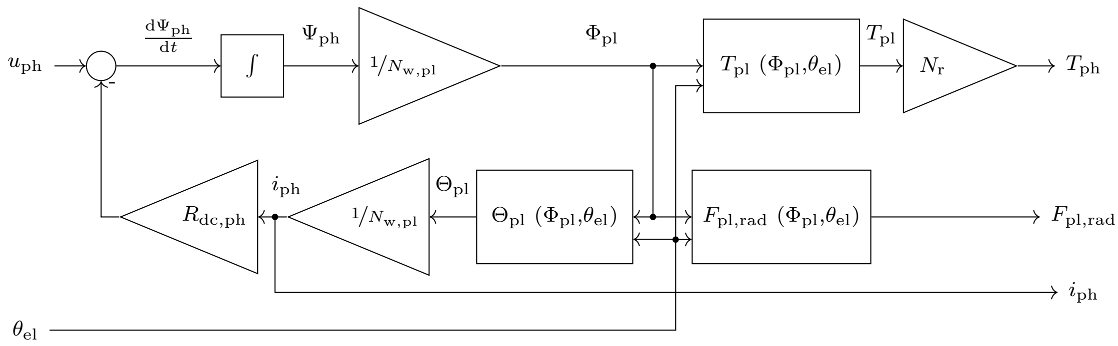

Fig. 2.9: SRG simulation model block diagram based on the pole flux Φ_{pl}.

However, the voltage drops across the power electronic devices, depending on the inverter switching state, are considered for the determination of the phase voltage u_{ph}.

2.3.2 Coupled Finite Element Analysis

To determine the eddy-current copper losses $P_{l,cu,eddy}$ in the machine windings, a 2-D coupled FEA model is built up with the help of the software MATLAB-Simulink and FLUX2D. The complete simulation process is described in detail in [Sch15]. The inputs, machine phase current i_{ph} and electric position θ_{el}, are derived from dynamic drive simulations with the model described in section 2.3.1. As suggested in [Sch15] a step size of 0.5 °el was chosen, as a compromise of accuracy and simulation time. Only selected operation points are simulated with this approach, as each simulation takes about 3 – 6 h on a desktop personal computer (PC) (Intel®Core™ i5-2400, 3.1 GHz, 16 GB RAM, 1 TB HDD, 64-bit operating system), depending on the number of mesh elements.

2.3.3 Thermal Modeling

Thermal modeling approaches for electrical machines are generally numerical, such as CFD and FEA, or analytical, such as lumped parameter thermal network (LPTN). FEA can be very accurate and any machine geometry can be modeled, but rather high model setup and computational time are major drawbacks [Bog+09]. CFD is normally employed to calculate thermal behavior on interfaces, which are in contact with fluids or gases, i.e. air gap, stator-slot, end-winding regions and cooling channels. LPTN are a compromise between accuracy and computational time. A well-parameterized model is needed, to represent the machine parts properly with reduced elements, so that the computational time can be reduced compared to numerical methods [Bog+09; QSD14].

Since the focus of this thesis is to compare different SRG models rather than developing a sophisticated LPTN, the commercial software MotorCAD is employed. This software generates an LPTN upon geometric dimensions as well as material, interface, cooling and accessories parameters. It is based on several scientific publications [SBC05] and constantly updated to new heat transfer research. As described in detail in [Bog+09; BD15] heat transportation occurs in form of conduction, convection and radiation. Since thermal conductivity is a material specific parameter, the relevant values can be gathered from data sheets or literature. Heat flow by convection is more complex than heat conduction. It can be separated into natural convection which occurs only because of a heat gradient, and forced convection when the particle flow is caused by an outer influence, such as the SRG rotor [Bog+09]. It is assumed for this thesis that convection is approximated well enough by MotorCAD. Concluded in [Bra13], radiation is not significant in thermal modeling of liquid cooled SRGs and will therefore not be further considered.

2.3.4 Acoustic Modeling

For the acoustic analysis of the different machines, the modeling process introduced in [Bös14] is applied. To retrieve the vibration response transfer function and to analyze the values of the relevant eigenfrequencies, for each machine structural dynamic FEAs are performed with the software ANSYS. Afterwards, the vibration response is superposed with the spatially and temporally decomposed force excitation of the SRG, retrieved with the help of the dynamic simulation model described in section 2.3.1. That way, the time consuming 3-dimensional (3-D) structural analysis is required only once, while a variation of the control parameters or a speed variable operation can be quickly analyzed with the help of the dynamic system model.

3 Solution Space Based Pre-Design

In certain applications, such as REX, only the available input power $P_{\mathrm{m,sh}}$ is defined at the beginning of the design process. Hence, various SRG configurations, in terms of the number of phases N_{ph} and pole pairs n_{p}, could be suitable as a generator. If a gearbox is employed also different combinations of shaft speed n_{SRG} and nominal machine output torque $T_{\mathrm{tot,nom}}$ increase the number of potential machine designs. Therefore, a quick, but reliable, pre-design evaluation approach is required at the beginning of the design process.

Section 3.1 discusses classic iterative design approaches and their limitations regarding a large number of possible solutions. To overcome these limitations, a new pre-design approach is introduced. Section 3.2 describes the implementation and setup of the solution space for SRGs together with exemplary application independent design findings. The application dependent selection within the solution space and the design choice process are presented in section 3.3. After discussing results for a generic application in section 3.3.5, the SRG prototypes for the two target scenarios from section 2.1.2 are developed. Finally, a chapter conclusion is drawn in section 3.5.

3.1 Design Approach

3.1.1 Classic Design Approaches

Classic iterative design approaches of electrical machines, such as [Mil93] and [HM94], are mainly based on the simplified torque production equation (3.1). This formula links the rotor diameter D_{rot} and the machine stack length L_{stk} with the total machine output torque T_{tot} by the torque constant k_{trq}.

$$T_{\mathrm{tot}} = k_{\mathrm{trq}} \cdot {D_{\mathrm{rot}}}^2 \cdot L_{\mathrm{stk}} \tag{3.1}$$

In many publications, e.g. [KAL88] and [AHR01], equation (3.1) can be found with different focus on electromagnetic aspects or the influence of geometric parameters and mechanical stress. Common to both approaches is the use of different, mostly empirically determined, k_{trq}-factors, which are not directly comprehensible to an inexperienced designer. The approach developed in [Fue+05], has a closer link to the physical working principle of SRGs. The author bases the complete design process on a generalized SRG model with a phase and pole pair number $N_{\mathrm{ph}} = n_{\mathrm{p}} = 1$. From this generalized model, normalized flux linkage curves are derived in order to determine the maximum available coenergy loop $W_{\mathrm{co,max}}$, hence, the name normalized flux linkage method (NFLM). The normalized maximal coenergy loop $W_{\mathrm{co,max}}$ is then scaled by a pole-overlap factor and the stack length L_{stk} to the actual configuration and machine length. A comprehensive design procedure to cover the whole design process of an SRG was derived from this method in [BBD12] and further developed in [Bra13]. The procedure links the design routine to more intuitive design and tuning parameters by applying standard sizing rules for SRGs that have been established and proven validity in the context of SRG design, such as [Law+80], [AHR01] and [Fai+09].

Application specific requirements, e.g. thermal conditions, requested shaft power $P_{\mathrm{m,sh}}$ or nominal speed $n_{\mathrm{SRG,nom}}$, are generally input parameters of iterative design approaches, such as [Bra13; KAL88; AHR01]. This leads to time-consuming calculations of numerous possible geometries and their torque production capability for each pre-design. In this context, all results except for those meeting the design requirements are generally discarded, although they may represent optimal layouts of an application with slightly different specifications.

The calculations are mostly performed with the aid of a reluctance network based simulation software, such as PC-SRD, to speed-up the process. Due to the strongly non-linear magnetic behavior of SRGs, however, the parameters describing the magnetic path, in case of PC-SRD, for example the maximum flux density B_{m} and saturation flux density B_{s} [SPE08], vary considerably for different machine configurations over a wide range of the outer stator diameter D_{st}. Consequently, the solutions obtained need to be verified via time-consuming FEA in order to tune the material parameters as exemplarily shown in fig. 3.1.

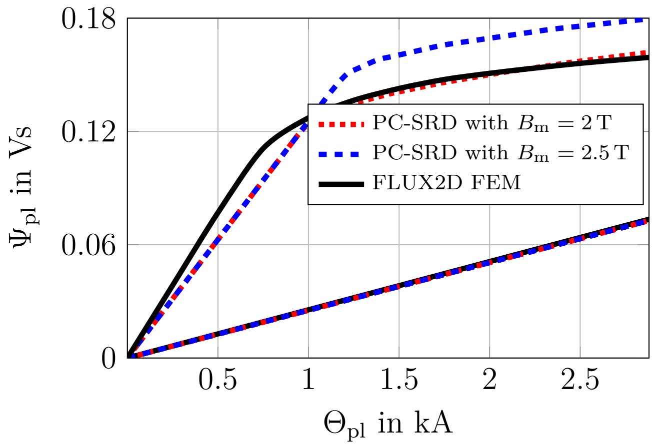

Fig. 3.1: Pole flux linkage Ψ_{pl} vs. pole MMF Θ_{pl} curves calculated with FLUX2D and PC-SRD for the same SRG geometry with $B_{\mathrm{s}} = 1.5\,\mathrm{T}$ and two different B_{m}.

Another aspect is the choice of the iteration parameters as well as the starting and solution points themselves. These parameters influence the quality of the output significantly. For a calculation starting from an unfavorably chosen solution point, only a local minimum might be found. Also, limiting the solution space rigidly, e.g. by a maximum stack length L_{stk}, might cause the underlying algorithm fail to converge, leaving the system designer without a deeper understanding of the range of results.

Both limitations lead to a longer pre-design period than expected, and can inhibit a fast comprehensive drive design. As a machine design is generally a compromise between different technologically conflicting requirements, the designer should furthermore be enabled to quickly evaluate the design potential, e.g. in terms of the active material volume V_{act}, material mass m_{act} or cost, instead of having to tune a set of analytical parameters to obtain a result at all. Therefore, in the first design stage the aim should be to create a reliable comparative overview of different configurations rather than a detailed design. The following section presents a solution to overcome the mentioned disadvantages.

3.1.2 Solution Space Based Pre-Design Approach

To achieve a quick solution overview and to avoid repetitive recalculation of machine characteristics a solution space based pre-design (SSBPD) approach was introduced in [BMD16] and is developed in detail in this thesis. The basic concept is to decouple the solution space calculation from application specific requirements. Based on the assumption that the theoretical torque production capability of the underlying solution space is only defined by geometric parameters of the iron core cross section and by the employed material, two calculation paths are defined as shown in fig. 3.2.

In the first calculation path, the torque characteristics of different SRG configurations defined by the number of phases N_{ph} and pole pairs n_{p} are evaluated. To cover a wider range of designs for each configuration, a geometry variation defined by the stator outer diameter D_{st} and $STPR$ (see table 3.1) is analyzed and stored in a solution database. The exact dataset and its calculation is specified further in the following section 3.2. In the second calculation path, all possible designs are filtered by application dependent parameters, such as the required nominal shaft power $P_{\mathrm{m,sh}}$ and generator speed $n_{\mathrm{SRG,nom}}$, along with thermal and mechanical limitations. These parameters are intuitively and comprehensibly linked to physical boundaries, such as the maximum coil temperature $\vartheta_{\mathrm{coil,max}}$ or the maximum shear stress on the shaft as described in section 3.3.

Instead of optimizing the design in repetitious background computations, the solution space is visualized in a following step, which offers the possibility to adapt the design parameters, and hence obtain a better solution. Based on this information, it is possible to identify the most favorable geometries depending on the application requirements, e.g. a minimal active material volume V_{act}, a specific configuration of the number of phases N_{ph} or pole pairs n_{p}, a fixed stator outer diameter D_{st} or stack length L_{stk}. Afterwards, the selected designs can be fine-tuned regarding the coil temperature, torque ripple or acoustic behavior using more time consuming approaches as presented in [Bra13].

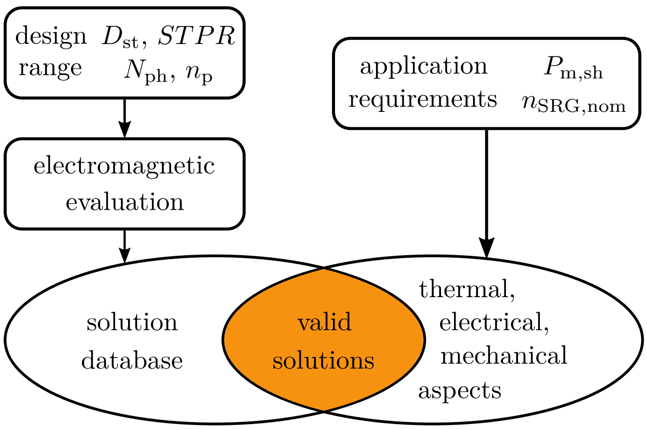

Fig. 3.2: Concept of the solution space based SRG design: decoupling of the solution database and the application specific requirements.

3.2 Solution Database

Setting up a solution database requires an effective way of describing machine cross sections and efficiently storing and addressing a large number of them in an appropriate data structure. For this purpose, the four geometric parameters listed in table 3.1 are utilized. The derivation of the $STPR$, as introduced in [BBD12], is described in appendix A.1.

Quantity	Symbol
stator outer diameter	D_{st}
number of phases	N_{ph}
number of pole pairs	n_{p}
slot-to-pole-pitch-ratio	$STPR$

Table 3.1: Parameters to describe one solution database entry.

The $STPR$ is dimensionless and, combined with standard SRG sizing rules described in section 3.2.1, unambiguously characterizes the stator and rotor outline of the considered SRG configuration by coupling geometric parameters in a single quantity. Therefore, it can be used as a variation parameter to examine the range of possible geometries and magnetic circuits of one specific SRG configuration defined by a certain number of phase N_{ph}, pole pairs n_{p} and a stator outer diameter D_{st}. As the number of phases N_{ph} and the number of pole pairs n_{p} only form reasonable machine configurations for certain combinations, they cannot be varied independently from one another in the solution database. Therefore, the technologically reasonable combinations of N_{ph} and n_{p} form one axis of the 3D database as shown in fig. 3.3.

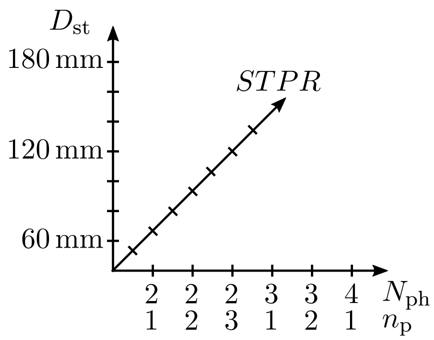

Fig. 3.3: 3-D solution database array. Each design is describe by a design quadruple (N_{ph}, n_{p}, D_{st}, $STPR$) (see section A.2.1).

To achieve the advantages described in the section before, it is necessary to modify the sizing procedure based on the generalized SRG model proposed in [Fue+05] with its empirical tuning parameters. Each database entry is directly described by magnetization curves retrieved from FEA. This offers two main advantages: Firstly, the usage of empirical tuning parameters to describe the magnetic path can be avoided. Secondly, it is no longer necessary to derive the torque capability of the machine configurations from the generalized model by overlap factors as described in [BBD12; Bra13].

The corresponding pole torque characteristic $T_{\text{pl}}\ (\Theta_{\text{pl}})$ is determined by integration of the pole flux linkage $\Psi_{\text{pl}}\ (\Theta_{\text{pl}})$ curves between the aligned and unaligned position (see fig. 2.7b). To cover a machine design range of stator outer diameter $D_{\text{st}} = 60 - 180$ mm and $STPR = 0.59 - 0.77$, nine FEAs were performed for each configuration with a step width of 60 mm for the parameter D_{st}, i.e. three FEAs at different $STPR$ for each of the three outer stator diameter step values $D_{\text{st}} = 60$ mm, 120 mm and 180 mm. Intermediate values for stator outer diameter D_{st}-steps of 5 mm and $STPR$-steps of 0.005, were determined by interpolation of the pole flux linkage Ψ_{pl} characteristic in the D_{st}-$STPR$-plane. For the total number of about 28 000 geometries, the corresponding pole torque curves $T_{\text{pl}}\ (\Theta_{\text{pl}})$ are stored with the pole flux linkage curves $\Psi_{\text{pl}}\ (\Theta_{\text{pl}})$ in the design database. To make the designs electromagnetically comparable and limit the size of the database, the stack lengths are scaled to values so that each geometry features a rotor outer envelope area of 1 m^2.

3.2.1 Database Parametrization

As introduced in the previous section, each database entry is defined by four parameters. In order to describe the detailed stator and rotor cross section defined by a specific database entry, a standard sizing rule is applied to link the four parameters introduced in the previous section to the characteristic geometric quantities shown in fig. 3.4 for a radial flux SRG. The key parameters for this description are the pole arc angles β_{r} and β_{s} for the rotor and stator, respectively. In combination with the machine radii R_{sh}, R_0, R_1, R_2 and R_3, describing the shaft, rotor pole ground, rotor pole tip, stator pole ground and stator outer radius, respectively, the machine is fully described. The air gap length d_{g} is fixed to a value of 0.7 mm for production tolerance reasons.

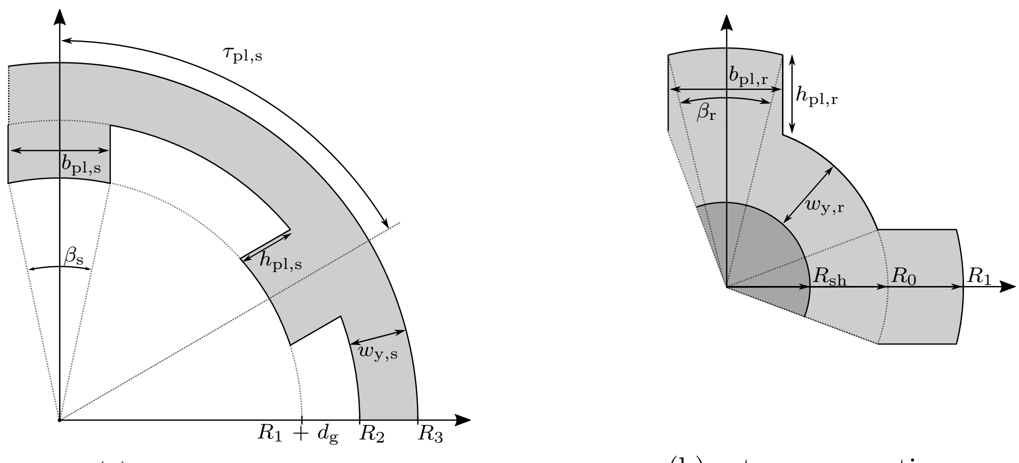

(a) stator cross section (b) rotor cross section

Fig. 3.4: Geometry of considered SRG designs and geometric parameters.

The sizing rule employed in this thesis is based on literature recommendations. A general overview on variations of the main geometric parameters and sizing guidelines can be found in [Mil93; Kri01; Bra13]. As shown in fig. 3.4, the pole lateral sides are considered parallel for stator and rotor. The main parameter stator pole arc angle β_{s} is calculated from the number of stator poles N_{s} and the stator pole width adjustment factor $k_{\text{arc,s}}$ by (3.2).

$$\beta_{\mathrm{s}} = \frac{\tau_{\mathrm{pl,s}}}{2} \cdot k_{\mathrm{arc,s}} = \frac{\pi}{N_{\mathrm{s}}} \cdot k_{\mathrm{arc,s}} \tag{3.2}$$

In [Mil93] it was stated that the stator pole width adjustment factor $k_{\mathrm{arc,s}}$ should not deviate too strongly from a value of one, as this influences the inductance ratio between aligned and unaligned position, hence, the torque capability. In this work the stator pole arc adjustment factor is chosen to $k_{\mathrm{arc,s}} = 0.9$ as a trade-off between machine efficiency and torque production [Bra13]. Commonly, the rotor pole arc angle β_{r} is designed slightly greater than the stator pole arc angle β_{s}, to account for the demagnetization period in the aligned position and to reduce losses in the rotor [Mil93; Kri01]. However, for the pre-design stage only the minimum of both values is important as it defines the effective pole overlap [Bra13]. Therefore, both parameter are set to the same value. The pole width $b_{\mathrm{pl,s}}$ is then directly defined by the trigonometric function (3.3). The rotor pole width $b_{\mathrm{pl,r}}$ is calculated analogously from the rotor pole tip radius R_1 and the rotor pole arc angle β_{r}.

$$b_{\mathrm{pl,s}} = 2 \cdot (R_1 + d_{\mathrm{g}}) \cdot \sin(\frac{\beta_{\mathrm{s}}}{2}) \tag{3.3}$$

Beside the width of the poles, the yoke thicknesses $w_{\mathrm{y,s}}$ and $w_{\mathrm{y,r}}$ of the stator and rotor, respectively, need to be defined. The yoke thickness influences the machine efficiency by material saturation as well as the acoustic behavior [Fie07] and a position sensorless rotor angle acquisition [van12]. A general guideline for the oversizing of the yoke compared to the stator tooth width $b_{\mathrm{pl,s}}$ cannot be given, as this depends on the target application. However, [Mil93] mentions an oversizing of $20 - 40\,\%$ for machines with a number of phases $N_{\mathrm{ph}} > 1$. For a high efficiency, in this work an oversizing value of $50\,\%$ is employed.

Having defined the stator pole arc angle β_{s} and the stator yoke width $w_{\mathrm{y,s}}$, the stator pole height $h_{\mathrm{pl,s}}$ is determined by basic trigonometric relations for fixed values of stator outer radius R_3, rotor pole tip radius R_1 and air gap length d_{g}. For the rotor pole height a value of $h_{\mathrm{pl,r}} = 0.7 \cdot b_{\mathrm{pl,r}}$ is recommended in [Bra13] to minimize stray flux in the unaligned position, as [Rad95] suggests no influence on the unaligned inductance above this value.

Applying all before mentioned design rules for a given stator outer diameter D_{st}, the SRG cross section design range can be simply described by a variation of the $STPR$ as introduced in appendix A.1. A small $STPR$ value indicates SRG cross sections with short and wide stator poles, whereas the stator poles become longer and thinner with increasing $STPR$ as shown in fig. 3.5.

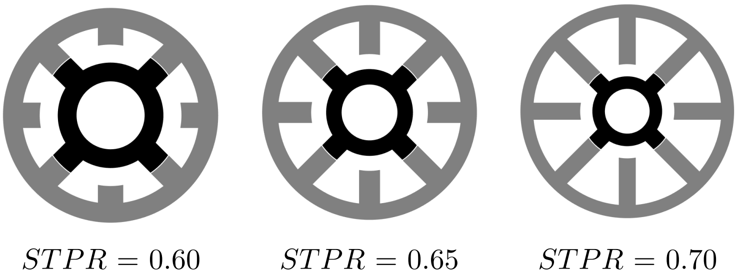

Fig. 3.5: Influence of the $STPR$ on a ($N_{\mathrm{ph}} = 2$, $n_{\mathrm{p}} = 2$) SRG cross section with constant stator outer diameter D_{st}. Taken from [Bur+16].

To fully describe the magnetic behavior, the magnetization characteristic of the material needs to be defined. In the scope of this thesis, a M330-35A material with datasheet parameters is employed. The B-H-curve was quadratically extrapolated up to values of 3 T to cover a wide range of designs. Any effects resulting from 3-D stray flux or the winding design are neglected in the process of building up the solution database.

3.2.2 Database Discussion

As it is necessary to simulate the flux linkage characteristics of each design sample point, i.e. solution database entry, the initial calculation of the design database takes an appreciable computational effort. However, the computations need to be run only once in order to fill the database with the torque output characteristics of the geometries located in the considered design range. Additionally, the database can be gradually improved by adding new configurations or data for an increased diameter range. Organizing the sample geometries in the database in a contiguous structure with continuous quantities allows for an interpolation of the torque characteristic of a specific machine configuration. As a result, the database can be systematically analyzed for the most promising designs for multiple independent sets of performance requirements, e.g. nominal shaft power $P_{\mathrm{m,sh}}$ and generator speed $n_{\mathrm{SRG,nom}}$.

A side effect of the design database preparation is that several general findings about SRG configurations can be derived from the FEA flux linkage characteristics. It was already shown in [Bur+16] that the $STPR$ has a strong impact on the magnetization behavior and hence torque density $\phi_{\mathrm{T,act,pl}}$ of an SRG, as the aligned and unaligned inductances are influenced. In fig. 3.6a, it can be observed that for the saturated pole MMF Θ_{pl} range the pole flux linkage Ψ_{pl} in the aligned position diminishes with an increasing $STPR$. This behavior can be explained with the narrowing and extending stator poles, which cause a higher drop of the pole MMF Θ_{pl} in the stator poles for an increasing $STPR$. For the

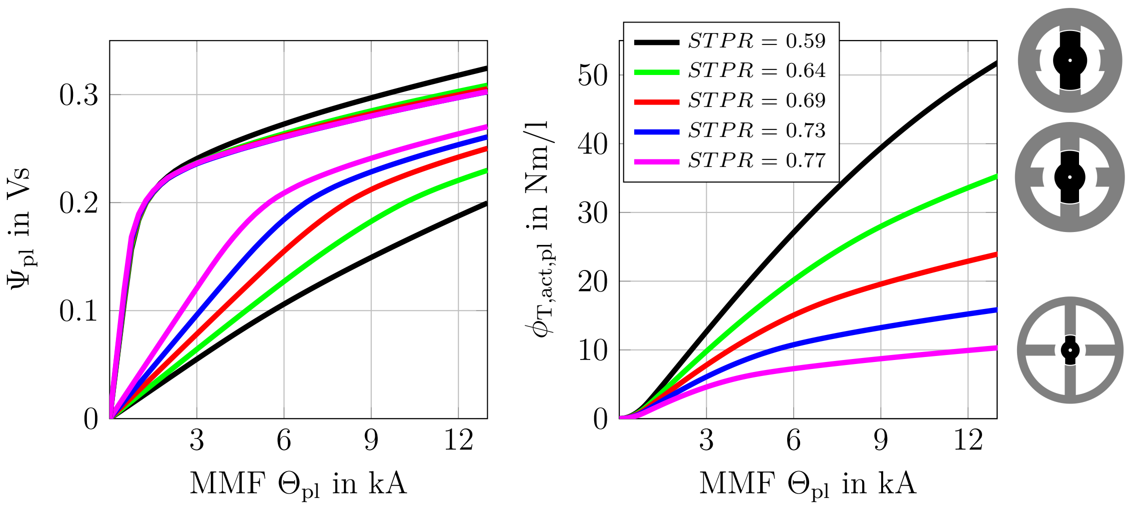

(a) pole flux linkage Ψ_{pl} (b) pole torque density $\phi_{\mathrm{T,act,pl}}$

Fig. 3.6: Influence of $STPR$ on pole flux linkage and pole torque density of a (2,1) SRG. Stator outer diameter $D_{\mathrm{st}} = 120\,\mathrm{mm}$, taken from [Bur+16].

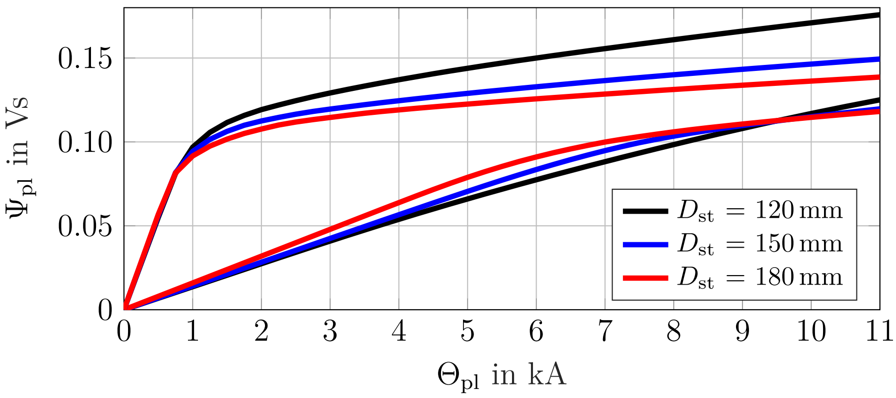

Fig. 3.7: Variation of the stator outer diameter D_{st} of a (2,2) SRG configuration with a constant rotor pole tip radius R_1 and width $b_{pl,r}$.

linear magnetization range, the inductance in the unaligned position increases strongly with an increasing $STPR$, similar to a larger $k_{arc,s}$, as discussed in [Mil93]. The effects on the aligned and unaligned position lead to the torque per volume $\phi_{T,act,pl}$ dependence on $STPR$ depicted in fig. 3.6b.

From the basic torque equation (3.1), it is expected that machines with a constant rotor pole tip radius R_1 and rotor pole width $b_{pl,r}$ yield constant torque, as only the rotor volume is considered. Varying the stator outer diameter D_{st} along with the stator pole ground radius R_2, could be considered a valid approach to increase the slot area $A_{slot,st}$ in case of thermal limitations. Fig. 3.7 shows that the pole flux linkage Ψ_{pl}, and consequently the pole torque T_{pl} is only independent of the stator outer diameter D_{st} as long as the machine is not operated in saturation. Due to the increasing stator pole height $h_{pl,s}$ the length of the saturated iron increases, once the saturation flux density B_s is reached. Hence, for a given rotor only extending the stator teeth to obtain a larger winding area A_w in case of thermal limitations, does not lead to an optimal design. In general, it can be stated that for a given pole MMF Θ_{pl} short-poled geometries achieve a higher torque per working stroke than designs with long and narrow poles.

Another finding concerns the comparison of machines with an equal number of stator poles N_s but a differing number of rotor poles N_r, and consequently a different number of phases N_{ph}. This comparison is shown for four configurations in fig. 3.8. It can be seen that in the unaligned position and at a constant pole MMF Θ_{pl} the pole flux linkage Ψ_{pl} of the 2-phase configurations is lower than the associated higher phase machine. As the pole flux linkage Ψ_{pl} in the aligned position is nearly identical, only influenced by the shorter yoke length in the 2-phase configuration, this leads to an increased pole torque-per-MMF T_{pl}/Θ_{pl} in the 2-phase configurations. A comparison considering the machine output torque, however, is not directly possible, as the electric base frequency f_{el} of the compared machines differs. Hence, beside the T_{pl}/Θ_{pl} value also the remaining frequency dependent eddy-current copper losses $P_{l,cu,eddy}$ and iron losses $P_{l,fe}$ need to be taken into consideration.

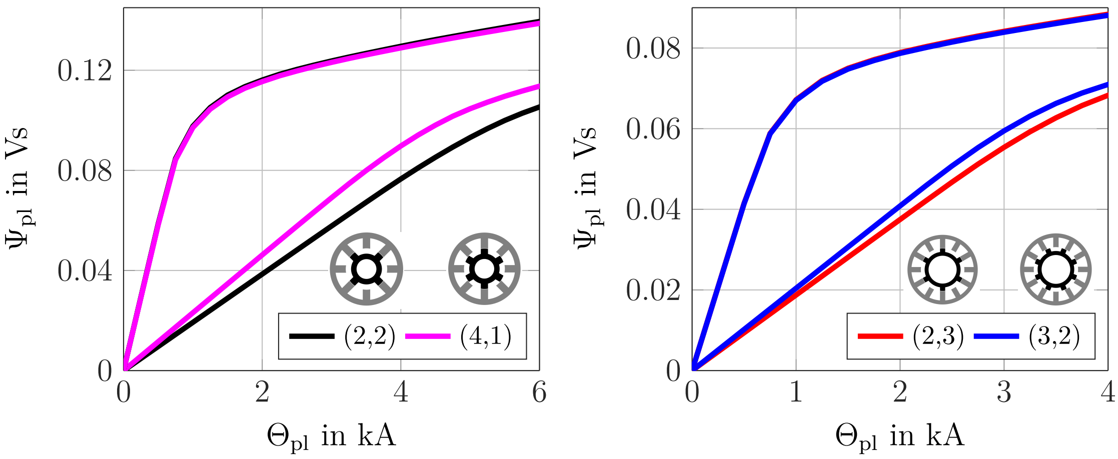

(a) $N_{\mathrm{s}} = 8$, $STPR = 0.64$

(b) $N_{\mathrm{s}} = 12$, $STPR = 0.63$

Fig. 3.8: Comparison of machines with a number of phases $N_{\mathrm{ph}} = 2$ against machines with $N_{\mathrm{ph}} > 2$ and the same number of stator poles N_{s}.

3.3 Application Dependent Design Choice

In the solution database depicted in fig. 3.2, the normalized pole torque capability $T_{\mathrm{pl}}\,(\Theta_{\mathrm{pl}})$ of 28 000 machine geometries together with the corresponding cross sections are available. The next design step is to filter these potential solutions with application dependent requirements and limitations, as shown on the right in fig. 3.2.

The required nominal machine torque $T_{\mathrm{tot,nom}}$ is specified by the nominal shaft power $P_{\mathrm{m,sh}}$ and generator speed $n_{\mathrm{SRG,nom}}$. Mechanical limitations, such as the maximal allowed shear stress on the shaft, directly exclude certain designs with a too small shaft radius R_{sh}.

Having set the required nominal machine output torque $T_{\mathrm{tot,nom}}$, for each configuration quadruple $(N_{\mathrm{ph}}, n_{\mathrm{p}}, D_{\mathrm{st}}, STPR)$ the required stack length L_{stk} could already be determined. However, as shown in fig. 3.6b, increasing the pole MMF Θ_{pl} evidently also increases the volumetric torque density $\phi_{\mathrm{T,act,pl}}$ and consequently reduces the required stack length L_{stk} at a constant stator outer diameter D_{st}. To chose a suitable pole MMF Θ_{pl}, in a first step, the thermally permitted maximal current density $J_{\mathrm{th,max}}$ of each design quadruple needs to be specified. In this work, the heat transfer capability from the windings to the water-cooling jacket is evaluated already at this early design stage by an LPTN for every design quadruple. Setting up the LPTN, as described in section 3.3.1, requires further specification of the winding geometry as well as an analytical loss evaluation. The losses are also influenced by the electric configuration, i.e. the control scheme and consequently the phase current i_{ph}, as described in section 3.3.2.

Having specified the thermally permitted maximal current density $J_{\mathrm{th,max}}$ and consequently the peak pole MMF $\Theta_{\mathrm{pl,pk}}$, one $STPR$ is chosen for each design triple $(N_{\mathrm{ph}}, n_{\mathrm{p}}, D_{\mathrm{st}})$ based on a certain decision criterion. This criterion could be the minimal active material volume V_{act} or an efficiency optimization. Two exemplary criteria are presented in section 3.3.4 together with the corresponding decision process. The decision is repeated for each database entry and visualized over the chosen diameter and configuration range. A generic pre-design discussion is presented in section 3.3.5.

3.3.1 Thermal Design Aspects

The classic approach to compare different machine configurations is to set a fixed current density in the coils from experience or literature. In that case, the power density only depends on the cooling method and the available coil area [HM94; Bra13]. This approach allows a quick comparison, as no calculation of the losses or the specific heat transfer to the cooling medium is required. However, [MRT91] already showed that varying the winding shape results in a changing contact area between the coil and the stator iron, hence, influencing the thermal contact resistances. Therefore, presuming a fixed thermally permitted maximal current density $J_{\mathrm{th,max}}$ for the complete design database might lead to erroneous conclusions about the heat transfer capability of different machine configurations. Especially, the strongly varying pole shapes, exemplarily shown in fig. 3.5, lead to this assumption.

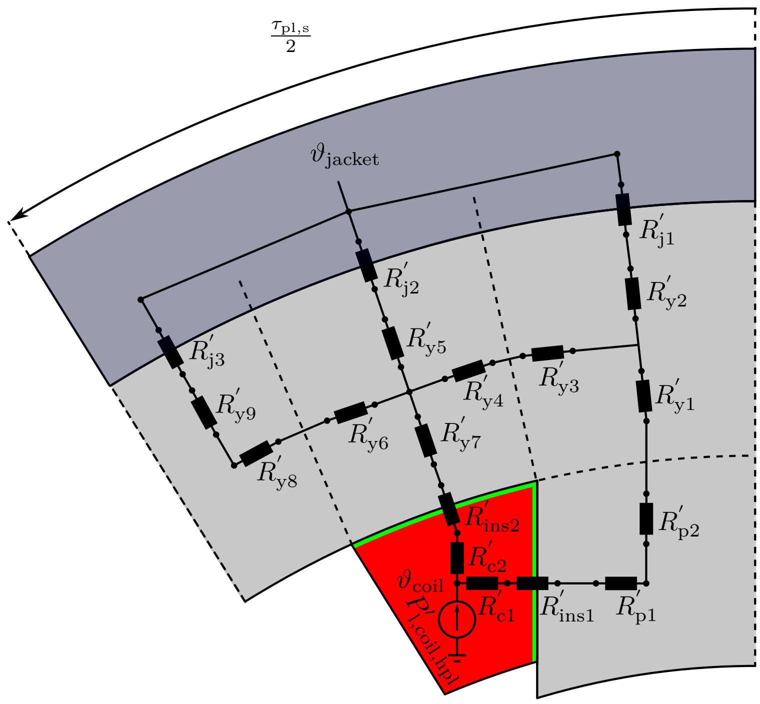

Fig. 3.9: Thermal network of half a stator pole, employed to calculate the thermally permitted maximal current density $J_{\mathrm{th,max}}$. Based on [Bur+16].

To set the comparison on a equal thermal basis, the thermally permitted maximal current density $J_{\mathrm{th,max}}$ for a given maximal coil temperature $\vartheta_{\mathrm{coil,max}}$ is calculated for each database quadruple with the help of the LPTN shown in fig. 3.9. This 2-D LPTN was derived from models described in [MRT91] and [QSD14]. Due to the geometric symmetry in the radial and tangential direction, it is sufficient to set up the LPTN for the half of a stator pole pitch $\tau_{\mathrm{pl,s}}$ including the coils and the stator frame. Thermal steady state conditions are assumed, which cancels out the influence of thermal capacitances. Furthermore, the axial heat flow is neglected. The heat removal from the SRG windings occurs in the form of a forced liquid cooling. This allows considering the machine water jacket temperature $\vartheta_{\mathrm{jacket}}$ to be constant and equal to the coolant temperature.

Introducing an LPTN as shown in fig. 3.9 demands for space resolved heat sources. For simplicity in the pre-design step all heat sources other than the copper losses $P_{\mathrm{l,cu,ac}}$ occurring in the copper coils, i.e. the iron core losses $P_{\mathrm{l,fe}}$ and mechanical losses $P_{\mathrm{l,m}}$, are neglected. This may give the impression of an overly simplified modeling of the heat dissipation all the more as the iron core losses $P_{\mathrm{l,fe}}$ represent a substantial loss part, especially at high generator speeds n_{SRG} and electric base frequencies f_{el}. However, the MotorCAD simulations performed in section 4.2.3 suggest that at a constant electric base frequency f_{el} and generator speed n_{SRG}, neglecting the frequency dependent iron core losses $P_{\mathrm{l,fe}}$ and mechanical losses $P_{\mathrm{l,m}}$, leads to a constant reduction of the coil hot spot temperature $\vartheta_{\mathrm{coil,hs}}$. Therefore, these losses are considered by a reduced maximum coil temperature $\vartheta_{\mathrm{coil,max}}$ in the pre-design stage.

This implementation allows for a valid comparison of machine configurations with an equal electric base frequency f_{el}. As in the final application an increased f_{el} would also imply a reduced machine efficiency η_{mach}, this simplification is acceptable for the aimed purpose of this thesis.

Limiting the 2-D-LPTN to only one heat source in the copper coils and one heat sink in the form of a water-cooling jacket, the given resistive network in fig. 3.9 can be reduced by application of standard network theory rules. The heat source $P'_{\mathrm{l,coil,hpl}}$ causes a temperature rise $\Delta\vartheta_{\mathrm{jacket,coil}}$ in the coils compared to the water-cooling jacket temperature $\vartheta_{\mathrm{jacket}}$ due to the thermal resistance of the half of a stator pole pitch $R'_{\mathrm{th,st,hpl}}$ as described in (3.4).

$$\Delta\vartheta_{\mathrm{jacket,coil}} = \vartheta_{\mathrm{coil}} - \vartheta_{\mathrm{jacket}} = P'_{\mathrm{l,coil,hpl}} \cdot R'_{\mathrm{th,st,hpl}} \tag{3.4}$$

The stack length L_{stk} related coil losses of half a stator pole $P'_{\mathrm{l,coil,hpl}}$ can be expressed by (3.5) with aid of the specific copper resistivity $\varrho_{\mathrm{sp,cu}}$, the copper area A_{cu} on both lateral sides of one stator pole and the effective current density in the copper conductors J_{eff} for a specific torque $T_{\mathrm{tot,nom}}$. The determination of the effective current density J_{eff} is further specified in section 3.3.2.

$$P'_{\mathrm{l,coil,hpl}} = \frac{A_{\mathrm{cu}}}{2} \cdot {J_{\mathrm{eff}}}^2 \cdot \varrho_{\mathrm{sp,cu}} \tag{3.5}$$

Replacing $\vartheta_{\mathrm{coil}}$ by the maximum coil temperature $\vartheta_{\mathrm{coil,max}}$ in (3.4) and inserting (3.5) leads to (3.6). This equation links the geometry dependent copper area A_{cu} and thermal resistance $R'_{\mathrm{th,st,hpl}}$ with a thermally permitted maximal current density $J_{\mathrm{th,max}}$. The latter is the limit for a possible effective current density J_{eff}, and consequently peak pole MMF $\Theta_{\mathrm{pl,pk}}$, of a certain design quadruple in the database.

$$J_{\mathrm{th,max}} = \sqrt{\frac{\vartheta_{\mathrm{coil,max}} - \vartheta_{\mathrm{jacket}}}{1/2 \cdot A_{\mathrm{cu}} \cdot \varrho_{\mathrm{sp,cu}} \cdot R'_{\mathrm{th,st,hpl}}}} \tag{3.6}$$

Winding Design

Due to concentrated windings and the lack of pole shoes, SRG can be produced with preformed coils as well as wound directly on the machine teeth. Preformed coils are preproduced on a dummy, often compressed, and slipped on the teeth afterwards. Both production schemes come in hand with slightly differing geometric boundaries for the coil spacer

d_{csp} and gap spacer d_{gsp} as shown in fig. 3.10 as well as production limitations. These boundaries lead to differing slot fill factors f_{slot}, which describe the ratio between the winding area A_{w} that can be filled by copper, and the available slot area $A_{\text{slot,st}}$. In consequence, different thermal heat transfer characteristics, arising from the varying contact lengths in tangential and radial direction, have to be expected.

The available effective copper area A_{cu} finally depends on the number of turns per pole $N_{\text{w,pl}}$, the wire diameter d_{w} and the wire insulation thickness $d_{\text{ins,w}}$ as well as the slot liner thickness d_{ins}. Assuming that the rectangular winding area A_{w} is filled with wires of a diameter d_{w}, as shown in fig. 3.10a, an effective copper fill factor f_{cu} of approximately 75 % can be achieved. The theoretical maximum for such a winding without insulation is 82.9 %, whereas 90.7 % are attainable neglecting border effects. For wound-in coils, the copper fill factor f_{cu} is below 50 %. Hence, while the winding area A_{w} is larger for wound-in coils (see fig. 3.11a), the advantage is eliminated over a wide range of $STPR$ due to the reduced copper fill factor f_{cu}. Fig. 3.10c shows this comparison for a copper fill factor $f_{\text{cu}} = 50\,\%$ and 75 % for wound-in and preformed coils, respectively. While in preformed coils the copper fill factor f_{cu} can still be slightly increased by compression, for wound-in coils $f_{\text{cu}} = 50\,\%$ is already an optimistic assumption.

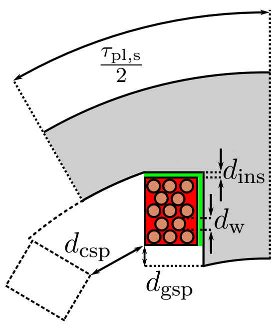

(a) preformed

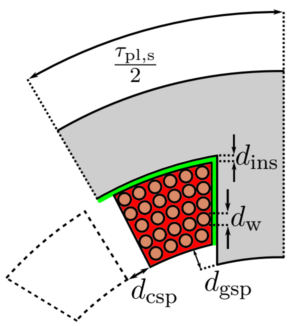

(b) wound-in

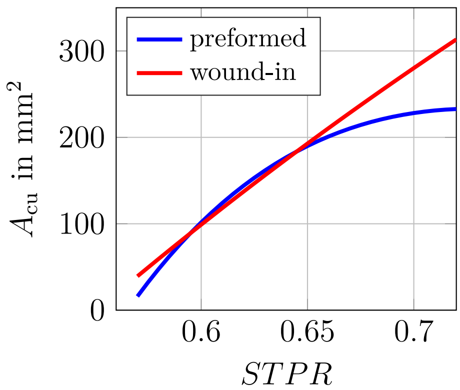

(c) copper area A_{cu} over $STPR$ for (2,2) SRG, $D_{\text{st}} = 120\,\text{mm}$

Fig. 3.10: Geometric implications of winding production schemes considered in this thesis.

Evaluation of Geometric Effects on the Thermal Resistance

For an exemplary evaluation of the thermally permitted maximal current density $J_{\text{th,max}}$ and the thermal resistance $R'_{\text{th,st,hpl}}$ the parametric assumptions listed in table 3.2 were made. This presumes, that the winding area A_{w} is utilized to its maximum and the compound of copper wire and insulation material has a orthotropic thermal conductivity.

Fig. 3.11a shows the effect of the $STPR$ on the slot fill factor f_{slot} for the two winding production schemes discussed in the previous section. For wound-in coils, f_{slot} is monotonically increasing with $STPR$ and decreasing with the number of stator poles N_{s}. For preformed coils, the slot fill factor f_{slot} shows a clear maximum, which shifts to smaller $STPR$ with increasing number of stator poles N_{s}.

paramerter		value
coil spacer and gap spacer	$d_{csp} = d_{gsp}$	0 mm
insulation slot liner thickness	d_{ins}	0.2 mm
copper fill factor	f_{cu}	0.65
heat transfer coefficient stator to jacket	$\alpha_{st,j}$	$1.057 \cdot 10^3\,\mathrm{W/m^2K}$
thermal conductivity stack lamination	λ_{st}	20 W/(mK)
thermal conductivity insulation slot liner	λ_{ins}	0.114 W/(mK)
thermal conductivity insulating resin	λ_{resin}	0.2 W/(mK)
thermal conductivity copper resin compound	λ_{coil}	0.8 W/(mK)
water-cooling jacket temperature	ϑ_{jacket}	60 °C
maximum coil temperature	$\vartheta_{coil,max}$	110 °C

Table 3.2: Parametrization of LPTN for analysis of geometric effects.

Fig. 3.11b shows the influence of the $STPR$ on the different heat paths from the coil to the cooling jacket in the employed LPTN for the green (2,2) configuration in fig. 3.11a. The resistances are added up for the different machine sections to convey a better understanding. These paths are partially in parallel, explaining the fact that they do not add up to the total thermal stator resistance $R'_{th,st}$. From fig. 3.11b it becomes clear that the yoke $R'_{th,y}$ and contact resistance $R'_{th,j}$ have a very small impact on the total thermal stator resistance $R'_{th,st}$. At a low $STPR$, the total thermal stator resistance $R'_{th,st}$ is dominated by the thermal coil resistance $R'_{th,c}$, while at larger $STPR$ this shifts to the pole path due to the increasing length $h_{pl,s}$ and decreasing thickness $b_{pl,s}$ of the stator pole. In sum, it can be stated that the $STPR$ has more effect on preformed coils than on wound-in coils. For this specific configuration $R'_{th,st,hpl}$ varies within a 10 % range over the complete investigated $STPR$ range. Fig. 3.12

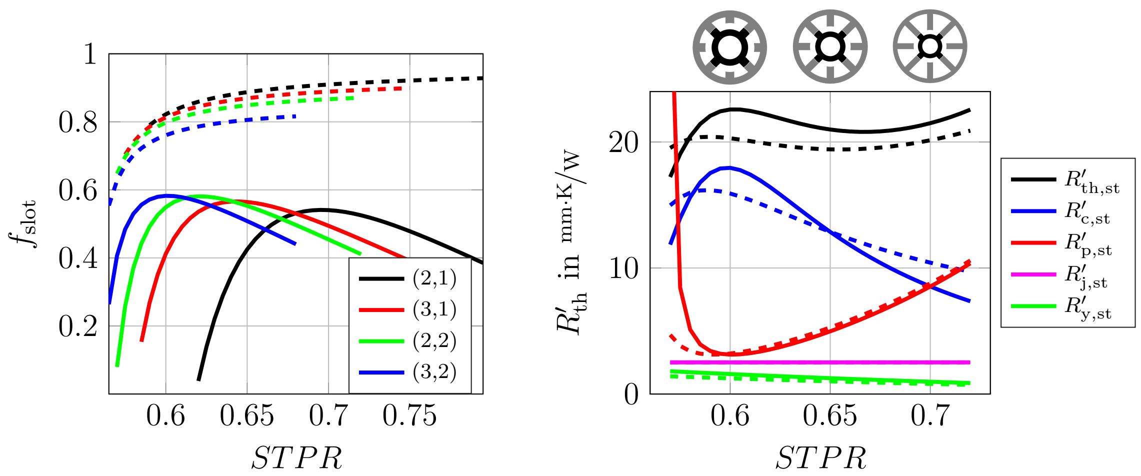

(a) slot fill factor f_{slot} (b) thermal resistances R'_{th} for a (2,2) SRG

Fig. 3.11: Effect of the wound-in (dashed lines) and preformed (solid lines) winding production scheme on the slot fill factor f_{slot} and thermal resistance $R'_{th,st,hpl}$ over $STPR$ at a stator outer diameter $D_{st} = 120$ mm.

depicts the total thermal stator resistance $R'_{\mathrm{th,st}}$ and the resulting thermally permitted maximal current density $J_{\mathrm{th,max}}$ for different machines over a wide stator outer diameter D_{st} range. Fig. 3.12a shows that for various configuration triples (N_{ph},n_{p},D_{st}) the total thermal stator resistance $R'_{\mathrm{th,st}}$ is influenced by the $STPR$ in a different manner. While for the (2,1,90) configuration, $R'_{\mathrm{th,st}}$ increases by 20 % from the minimal to the maximal $STPR$, for the (3,2,90) configuration it decreases by 22 %. Also between configurations of a constant stator outer diameter D_{st}, the total thermal stator resistance $R'_{\mathrm{th,st}}$ varies strongly. Exemplarily, this can be observed for the (3,1,120) and the (2,1,120) configuration, with the latter showing a reduced $R'_{\mathrm{th,st}}$ by 19 % at a $STPR = 0.65$. Combined with the copper area A_{cu} as described in (3.6) and the temperature limits from table 3.2, a decreasing thermally permitted maximal current density $J_{\mathrm{th,max}}$ over the $STPR$ and stator outer diameter D_{st} is obtained (see fig. 3.12b). Therefore, it is not correct from a physical point of view to assume a constant current density over a wide range of $STPR$, outer stator diameters D_{st} and machine configurations of number of phases N_{ph} and pole pairs n_{p}, as it is conventionally done in literature [KAL88; HM94; BBD12].

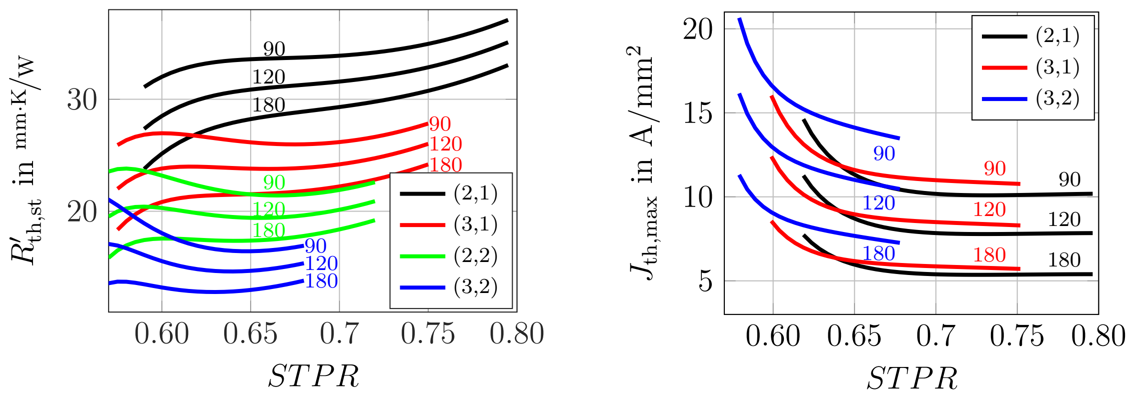

(a) $R'_{\mathrm{th,st}}$

(b) $J_{\mathrm{th,max}}$

Fig. 3.12: Influence of $STPR$ on stator thermal resistance $R'_{\mathrm{th,st}}$ and thermally permitted maximal current density $J_{\mathrm{th,max}}$ for different configurations and stator outer diameters D_{st} with preformed windings. D_{st} indicated next to lines in mm.

3.3.2 Electric Aspects

To achieve an application dependent machine torque $T_{\mathrm{tot,nom}}$, each design in the database requires a certain effective current density J_{eff} ($T_{\mathrm{tot,nom}}$). The effective current density J_{eff} ($T_{\mathrm{tot,nom}}$) needs to be compared to the value resulting from (3.6) in order to filter the database for valid designs with respect to the thermally permitted maximal current density $J_{\mathrm{th,max}}$. The link between the effective current density J_{eff} and the torque characteristic is created by expressing J_{eff} in terms of the peak pole MMF $\Theta_{\mathrm{pl,pk}}$ with (3.7). For idealized rectangular current waveforms, the duty cycle k_{d} is defined by (3.8) only by the geometric quantities number of rotor poles N_{r} and stator poles N_{s} as well as the stator pole width adjustment factor $k_{\mathrm{arc,s}}$. This relation describes the fraction of time during which the peak pole MMF $\Theta_{\mathrm{pl,pk}}$ is applied to the coil during one revolution. The correction factor $k_{\mathrm{d,cor}}$ equals to one in this case. Deviations from the idealized rectangular current profile are discussed below. The copper loss correction factor k_{cu} in (3.7) accounts for the frequency dependent eddy-current copper losses $P_{\mathrm{l,cu,eddy}}$ in relation to the dc copper losses $P_{\mathrm{l,cu,dc}}$ as described by (3.9). Depending on the wire diameter d_{w} and the electric base frequency f_{el}, these eddy-current copper losses $P_{\mathrm{l,cu,eddy}}$ can account for the majority of the total copper losses $P_{\mathrm{l,cu,ac}}$ [Car08; Ral+17] and will be investigated in detail in section 4.1.1 for the nominal operation point as well as for variable speed operation in section 5.1.1.

$$J_{\mathrm{eff}} = \frac{\Theta_{\mathrm{pl,pk}} \cdot k_{\mathrm{d}}}{{}^{1}\!/_{2} \cdot A_{\mathrm{cu}}} \cdot k_{\mathrm{cu}} \tag{3.7}$$

$$k_{\mathrm{d}} = k_{\mathrm{d,cor}} \cdot \sqrt{\frac{N_{\mathrm{r}}}{2 \cdot N_{\mathrm{s}}} \cdot k_{\mathrm{arc,s}}} \tag{3.8}$$

$$k_{\mathrm{cu}} = \sqrt{1 + p_{\mathrm{eddy,woEw}}} \tag{3.9}$$

As mentioned in section 2.2, an SRG can be be operated for drive efficiency η_{drive} reasons in SPC rather than HCC (see fig. 2.7). During the pre-design stage, a current profile deviating from HCC current can be accounted for by the before mentioned duty cycle correction factor $k_{\mathrm{d,cor}}$ and a torque derating factor d_{t}. d_{t} describes the ratio between the effectively used coenergy loop W_{co} and the maximum available coenergy loop $W_{\mathrm{co,max}}$ at a certain peak pole MMF $\Theta_{\mathrm{pl,pk}}$ (3.10). $W_{\mathrm{co,max}}$ is exemplarily depicted by the green dashed line for SPC in fig. 2.7b.

$$d_{\mathrm{t}} = \left. \frac{W_{\mathrm{co}}}{W_{\mathrm{co,max}}} \right|_{\Theta_{\mathrm{pl,pk}}=const} \tag{3.10}$$

The duty cycle k_{d} and torque derating factor d_{t} are depicted in fig. 3.13 for a wide range of

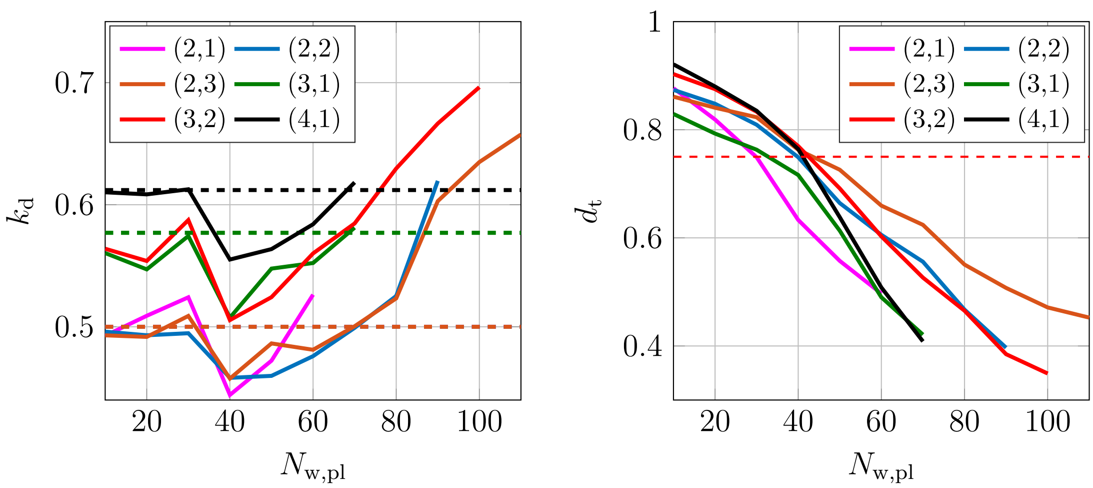

(a) duty cycle factor k_{d} (b) torque derating factor d_{t}

Fig. 3.13: Influence of the number of turns per pole $N_{\mathrm{w,pl}}$ on the duty cycle factor k_{d} and torque derating factor d_{t} for different SRG configurations at $D_{\mathrm{st}} = 150\,\mathrm{mm}$.

number of turns per pole $N_{\mathrm{w,pl}}$ for several machine configurations at a constant stator outer diameter D_{st}. At low numbers of turns per pole $N_{\mathrm{w,pl}}$, the duty cycle k_{d} has approximately the value expressed by (3.8) with a correction factor $k_{\mathrm{d,cor}} = 1$. These values are depicted in fig. 3.13a by dashed lines. At number of turns per pole $N_{\mathrm{w,pl}} = 30 - 40$, where the current takes a single pulse shape, the duty cycle k_{d} drops from $k_{\mathrm{d,cor}} = 1$ to approximately $k_{\mathrm{d,cor}} = 0.9$. From this point on, the duty cycle correction factor $k_{\mathrm{d,cor}}$ rises monotonically for increasing $N_{\mathrm{w,pl}}$. A duty cycle correction factor $k_{\mathrm{d,cor}} = 1$ is reached again at the point where the SRG is operated in CCM.

The torque derating factor d_{t} decreases monotonically with an increasing number of turns per pole $N_{\mathrm{w,pl}}$. For a number of turns per pole $N_{\mathrm{w,pl}} = 30 - 40$, where the current takes a single pulse shape, the negative gradient of the torque derating factor d_{t} increases. Simulations with more number of turns per pole $N_{\mathrm{w,pl}}$-steps showed a torque derating factor $d_{\mathrm{t}} = 0.75$ at the point where single pulse operation starts for all considered configurations. Also configurations with the same number of pole pairs n_{p} show similar values and gradients of the torque derating factor d_{t} at a constant number of turns per pole $N_{\mathrm{w,pl}}$, e.g. configuration (3,2) and (2,2).

For any control scheme at nominal operation point (HCC,SPC,CCM, see fig. 2.7a) a duty cycle correction factor $k_{\mathrm{d,cor}} = 1$ is a valid worst case assumption. This maximizes the effective current density J_{eff} for a certain peak pole MMF $\Theta_{\mathrm{pl,pk}}$. The torque derating factor linearly decreases with an increase in the number of turns $N_{\mathrm{w,pl}}$, as the effectively used coenergy loop W_{co} remains constant, but the maximum available coenergy loop $W_{\mathrm{co,max}}$ increases. Between an idealized rectangular current waveform at a number of turns per pole $N_{\mathrm{w,pl}} = 1$ and the point where SPC is applied, a linear reduction of torque derating factor d_{t} from 1 to 0.75 is advised, based on the simulation results depicted in fig. 3.13b.

3.3.3 Mechanical and Economical Aspects

Mechanical and economical aspects are not of main interest in this thesis. In the scope of the pre-design, two aspects are considered from the mechanical point of view. Firstly, the minimal shaft radius R_{sh} is deduced from the allowed shear stress of the employed shaft material. All designs, which do not meet this requirement are excluded from the comparison. Secondly, the windage losses $P_{\mathrm{l,wind}}$ in the air gap require an increased machine stack length L_{stk} to meet the input power $P_{\mathrm{m,sh}}$ requirement. The windage losses $P_{\mathrm{l,wind}}$ are calculated for each design by the analytical approach proposed in [Vra68]. The economical aspects of a certain machine design are only based on the material costs of the iron core, copper wires and shaft. Production costs and auxiliary devices, such as housing, additional sensors and bearings, are assumed to be constant for all machines of one set of application parameters and, therefore, neglected.

3.3.4 Comparison Criteria

All design quadruples (N_{ph},n_{p},D_{st},$STPR$) stored in the solution database are evaluated under the application specific thermal, electrical, mechanical and economical boundary conditions described in the previous sections. Subsequently, the optimal $STPR$ is found with respect to an application dependent optimization goal for each design triple (N_{ph},n_{p},D_{st}).

Based on the optimization goal and all optimal quadruples found that way, relevant design quantities, such as the stator stack length L_{stk}, the active material volume V_{act} or the material cost, are derived for the entirety of the design triples (N_{ph},n_{p},D_{st}). In a last step, the resulting dataset is used to visualize characteristic machine parameters over the whole investigated design range. To determine the meaning of `optimal` in this context, a comparison criterion needs to be set. Within this work, the two criteria `Maximum Volumetric Torque Density` and `Torque-per-`Θ_{pl} `Peak-Point Derating` were implemented and are explained in detail in the following.

Maximum Volumetric Torque Density

It can be shown that the volumetric torque density $\phi_{\mathrm{T,act,pl}}$ of the active material can be directly derived from the normalized torque characteristic if the winding overhangs are neglected [BBD12]. For any SRG design, the $\phi_{\mathrm{T,act,pl}}$ ($\Theta_{\mathrm{pl,pk}}$) curve strictly rises with the applied peak pole MMF $\Theta_{\mathrm{pl,pk}}$ as exemplarily shown in fig. 3.6b. To find the $STPR$ with the maximum volumetric torque density $\phi_{\mathrm{T,act,pl}}$ for a certain design triple (N_{ph},n_{p},D_{st}), it is thus necessary to determine the maximal permitted thermal current $J_{\mathrm{th,max}}$ for each $STPR$.

Fig. 3.14 exemplarily illustrates how the optimal $STPR$ in terms of the volumetric torque density $\phi_{\mathrm{T,act,pl}}$ of one design triple (N_{ph},n_{p},D_{st}) is found. In the left part of fig. 3.14, the thermally permitted maximal current density $J_{\mathrm{th,max}}$ for all $STPR$ of a (3,2,120 mm) configuration is depicted. The curve is determined with the help of the LPTN as described in section 3.3.1. In the right part, the corresponding $\phi_{\mathrm{T,act,pl}}$ curves are depicted over the effective current density J_{eff} for four exemplary $STPR$. These curves are determined from the $\phi_{\mathrm{T,act,pl}}$ (Θ_{pl}) curves stored in the database, by substitution of Θ_{pl} with the help of (3.7) as described in section 3.3.2.

Combining the left and the right part of fig. 3.14, as shown by the dashed lines for the four exemplary $STPR$, the maximal torque density $\phi_{\mathrm{T,act,pl}}$ of each $STPR$ is found. In the given example of a (3,2,120 mm) configuration, the $STPR = 0.63$ features the highest torque per active volume $\phi_{\mathrm{T,act,pl}}$. On the first view, this seems to be in contradiction to

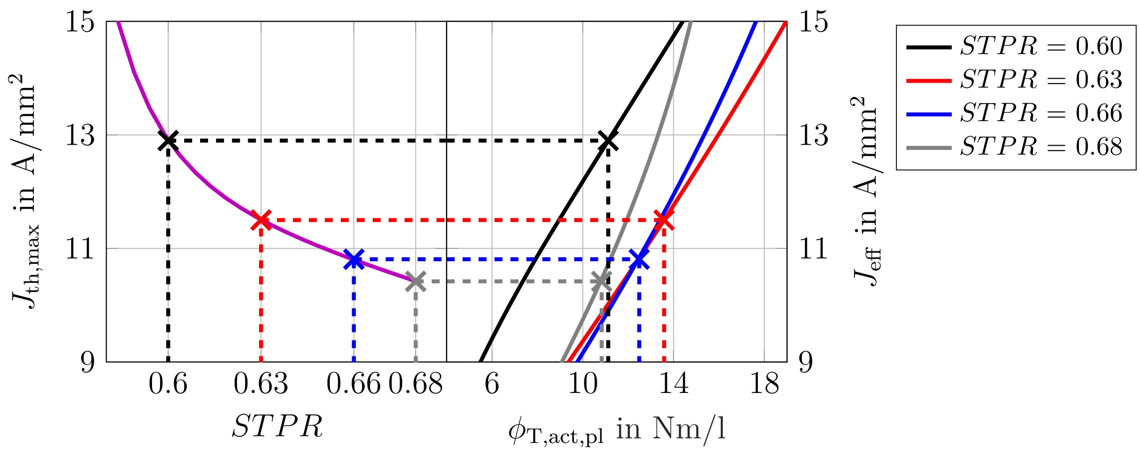

Fig. 3.14: Determination of optimal $STPR$ for `Maximum Volumetric Torque Density`. SRG configuration (3,2,120 mm), $\vartheta_{\mathrm{jacket}} = 60\,°\mathrm{C}$, $\vartheta_{\mathrm{coil,max}} = 110\,°\mathrm{C}$.

the finding in section 3.2.2, stating that the lowest $STPR$ show the highest torque densities $\phi_{\mathrm{T,act,pl}}$. The reason can be seen in fig. 3.10c. As the available copper area A_{cu} decreases with decreasing $STPR$, the effective current density J_{eff} increases for a constant pole MMF Θ_{pl}. The example outlines the importance to consider both thermal and electric aspects in the pre-design process. The same procedure is repeated for each design triple (N_{ph},n_{p},D_{st}) in the solution database.

Torque-per-MMF Peak-Point Derating

One approach to efficiently operate electric machines is to operate them in the point of maximum torque per current. Applied to SRG, the pole torque curves T_{pl} (Θ_{pl}) stored in the solution database are divided by the corresponding pole MMF Θ_{pl}. In the next step, the Θ_{pl} is substituted by J_{eff} with the help of (3.7) as described in section 3.3.2. Due to the saturation of the iron core, the resulting curves, exemplarily depicted for four $STPR$ of a (2,1,120 mm) configuration in fig. 3.15, show a characteristic maximum. Analyses conducted in [BBD12] showed that the peak pole MMF $\Theta_{\mathrm{pl,pk}}$ values for an operation with the maximum machine efficiency η_{mach} corresponded to pole torque-per-MMF $^{T_{\mathrm{pl}}}/_{\Theta_{\mathrm{pl}}}$-ratios located slightly below the characteristic maximum of the pole torque-per-MMF $^{T_{\mathrm{pl}}}/_{\Theta_{\mathrm{pl}}}$-curve. The derating can be expressed by a torque-per-MMF derating factor d_{derate} as described in (3.11) and ranges between 3 % and 10 %. As the volumetric torque density $\phi_{\mathrm{T,act,pl}}$ increases monotonically with the effective current density J_{eff}, the derated peak-point in the $^{T_{\mathrm{pl}}}/_{\Theta_{\mathrm{pl}}}$-curve is a compromise between efficiency and maximum torque density.

$$\mathrm{design}\left(^{T_{\mathrm{pl}}}/_{\Theta_{\mathrm{pl}}}\right) = d_{\mathrm{derate}} \cdot \max\left(^{T_{\mathrm{pl}}}/_{\Theta_{\mathrm{pl}}}\right) \tag{3.11}$$

With the help of fig. 3.15 the effective current density values for the design ($^{T_{\mathrm{pl}}}/_{\Theta_{\mathrm{pl}}}$)-points are determined. Those geometries with an effective current density J_{eff} exceeding the thermally permitted maximal current density $J_{\mathrm{th,max}}$ (see (3.6)) are excluded from the further evaluation. The remaining thermally valid geometries are compared with each other

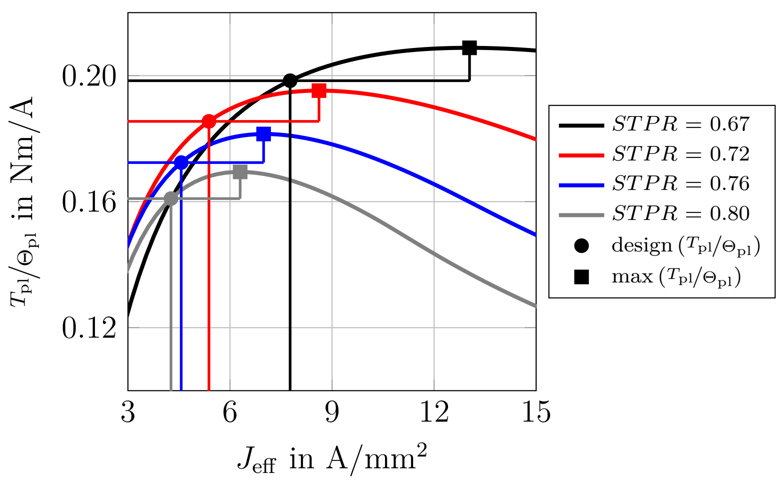

Fig. 3.15: $^{T_{\mathrm{pl}}}/_{\Theta_{\mathrm{pl}}}$ derating with $d_{\mathrm{derate}} = 0.95$.
SRG configuration (2,1,120 mm), $\vartheta_{\mathrm{jacket}} = 60\,°\mathrm{C}$, $\vartheta_{\mathrm{coil,max}} = 110\,°\mathrm{C}$.

to find the $STPR$ providing the maximum design ($^{T_{\mathrm{pl}}}/_{\Theta_{\mathrm{pl}}}$) of the pole torque-per-MMF ratio $^{T_{\mathrm{pl}}}/_{\Theta_{\mathrm{pl}}}$. In the given example, the geometry with $STPR = 0.67$ yields the highest value for the $^{T_{\mathrm{pl}}}/_{\Theta_{\mathrm{pl}}}$ peak-point derating. The resulting effective current density J_{eff} is then used to determine the volumetric torque density $\phi_{\mathrm{T,act,pl}}$, and consequently the required stack length L_{stk}. This procedure is analogously applied to the other configuration triples (N_{ph},n_{p},D_{st}) in the solution database.

3.3.5 General Pre-Design Result Discussion

To visualize the effect of SSBPD, the outlined approach was applied to the solution space from section 3.2 for an application with the specifications listed in table 3.3. The complete solution space of approximately 28 000 geometries, with the stator outer diameter D_{st} range and configurations as depicted in fig. 3.3, was considered. The LPTN was parametrized as described in table 3.2. Additionally, from the discussion of the electric aspects in section 3.3.2, a torque derating factor $d_{\mathrm{t}} = 0.75$ for SPC is assumed. Frequency dependent copper losses $P_{\mathrm{l,cu,eddy}}$ are taken into account with a copper loss correction factor $k_{\mathrm{cu}} = 1.5$, iron core losses $P_{\mathrm{l,fe}}$ are considered by the reduced maximal coil temperature $\vartheta_{\mathrm{coil,max}}$ as discussed in section 3.3.1. The frequency dependent losses are assumed constant for all configurations, which can be considered as an advantage for configurations with higher number of pole pairs n_{p}, hence electric base frequency f_{el}. The comparison is performed for the two optimization criteria, `Maximum Volumetric Torque Density` and `Torque-per-`Θ_{pl} `Peak-Point Derating`. For the latter a torque-per-MMF derating factor $d_{\mathrm{derate}} = 0.95$ is assumed.

	Symbol	Value
output power	$P_{\mathrm{m,sh}}$	20 kW
nominal speed	n_{sh}	25 000 rpm
torque derating factor	d_{t}	0.75
copper loss correction	k_{cu}	1.5
torque-per-MMF derating factor	d_{derate}	0.95

Table 3.3: Application specifications for the exemplary pre-design discussion.

In fig. 3.16, the resulting active material volumes V_{act} and weights m_{act} for an optimization criterion `Maximum Volumetric Torque Density` over a wide range of the stator outer diameter D_{st} are depicted. Both parameters, V_{act} and m_{act}, show a similar behavior over the investigated stator outer diameter D_{st} range. At lower stator outer diameters D_{st}, configurations with fewer stator poles show a lower active material volume V_{act} and weight m_{act}. Comparing 2-phase configurations, for a stator outer diameter $D_{\mathrm{st}} > 105\,\mathrm{mm}$, the (2,3) configuration shows a lower active material volume V_{act} than the (2,2) configuration. In terms of the active material weight m_{act}, the (2,3) configuration shows values similar to the (2,2) configuration for a stator outer diameter $D_{\mathrm{st}} > 110\,\mathrm{mm}$. The (2,1) configuration, with again fewer stator poles, would only show a reduced volume and weight compared to the (2,2) configuration for stator outer diameters $D_{\mathrm{st}} < 60\,\mathrm{mm}$, which is outside the investigated diameter range of the solution database. A similar behavior can be observed for the 3-phase

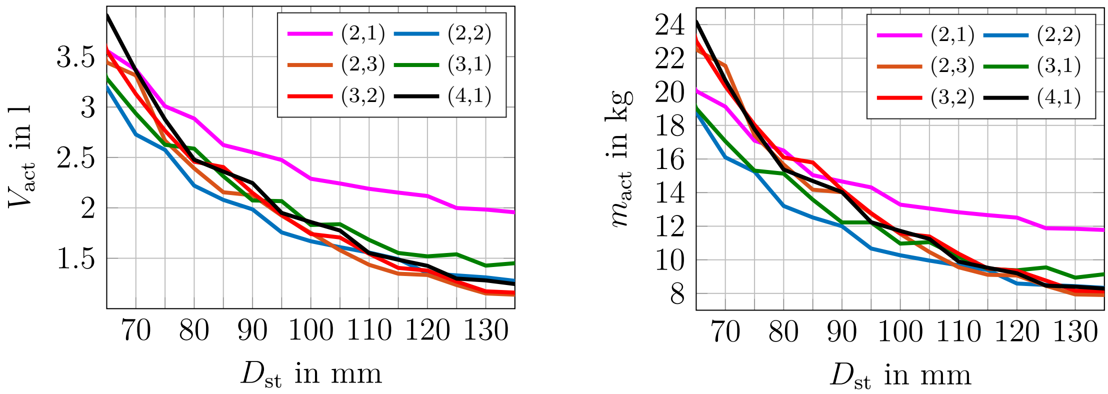

(a) volume of the active material

(b) mass of the active material

Fig. 3.16: Comparison of the active material volume V_{act} and mass m_{act}. application specifications: table 3.3; optimization criterion: `Maximum Volumetric Torque Density`

configurations (3,1) and (3,2). The (3,2) configuration shows a lower active material volume V_{act} for stator outer diameters $D_{st} > 90\,\text{mm}$, while a lower active material weight m_{act} can be observed for $D_{st} > 115\,\text{mm}$.

The frequency dependent copper $P_{l,cu,eddy}$ and iron losses $P_{l,fe}$ are assumed to be constant as mentioned before. This can be considered a valid assumption for machines with similar number of rotor poles N_r, hence constant electric base frequency f_{el} (see (2.4)), e.g. for the (2,2) and (3,1) configurations. Investigating fig. 3.16 again, it can be seen, that at any stator outer diameter D_{st} the (2,2) configuration shows a lower active material volume V_{act} and weight m_{act} compared to the (3,1) configuration. The same relation can be observed for the (2,3) and the (4,1) configuration. In terms of the volumetric torque density $\phi_{T,act}$ and power density $\phi_{P,act}$, generally higher values can be found in 2-phase machines at a constant electric base frequency f_{el}.

To analyze the effect of the LPTN in more detail, fig. 3.17a depicts the resulting thermally permitted maximal current density $J_{th,max}$ for the results from fig. 3.16 in the range of a stator outer diameter $D_{st} = 120 - 140\,\text{mm}$. The thermally permitted maximal current density $J_{th,max}$ increases with the number of stator poles N_s defined by (2.1). Configurations of the same number of stator poles N_s, i.e. (2,2) and (4,1), show a comparable thermally permitted maximal current density $J_{th,max}$ as only the stator cross section defines this value.

Finally, fig. 3.17 compares the results from fig. 3.16a with results for a constant thermally permitted maximal current density $J_{th,max}$ in a range of the stator outer diameter $D_{st} = 120 - 140\,\text{mm}$. $J_{th,max}$ was chosen to a value of $11\,\text{A/mm}^2$, stated in literature [Car08; Bra13] as reasonable for water jacket cooled machines. Obviously, the LPTN limits the thermally permitted maximal current density $J_{th,max}$ to much lower values. Generally, this results in higher active material volumes V_{act}.

More important for the pre-design comparison approach are two other findings. Firstly, the relative reduction of the active material volume V_{act} over the stator outer diameter D_{st} is lower in fig. 3.17b compared to fig. 3.17c. This behavior is directly linked to the diminishing thermally permitted maximal current density $J_{th,max}$ over the stator outer di-

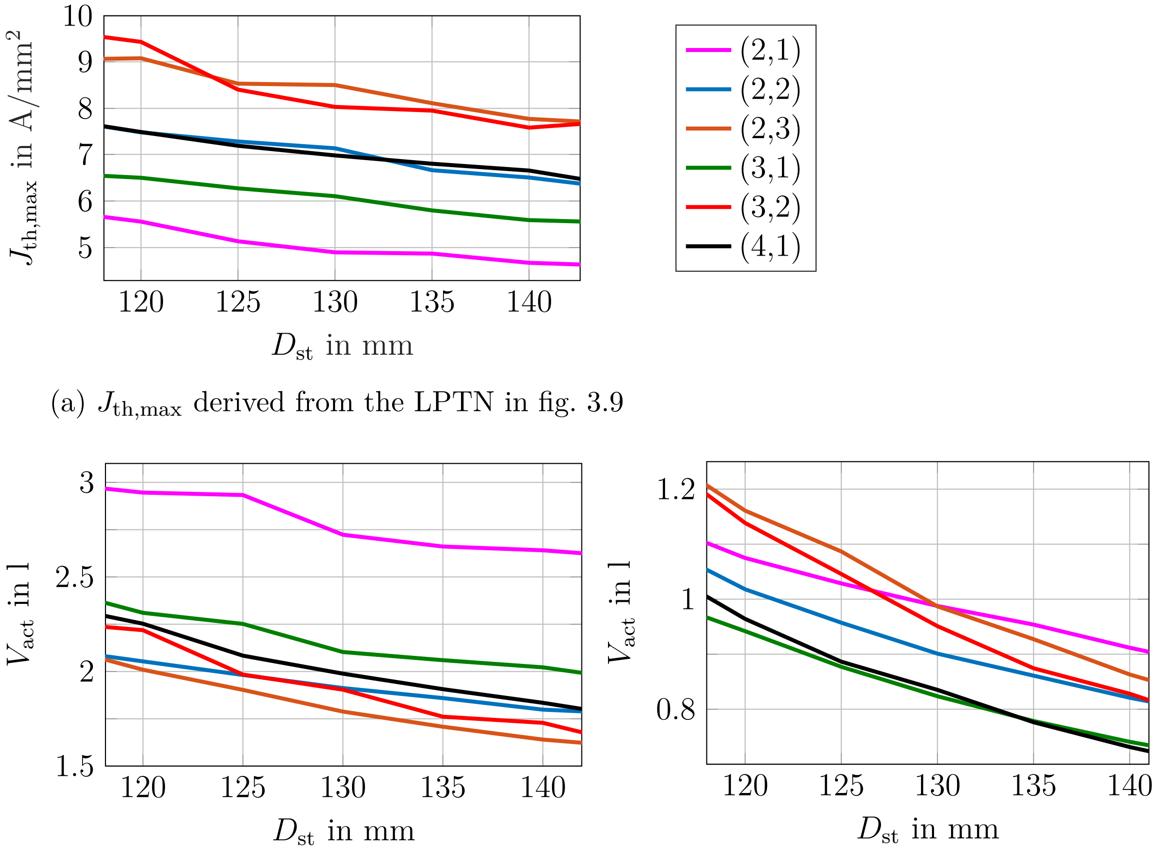

(a) $J_{\mathrm{th,max}}$ derived from the LPTN in fig. 3.9

(b) $J_{\mathrm{th,max}}$ from fig. 3.17a

(c) $J_{\mathrm{th,max}} = 11\,\mathrm{A/mm^2}$

Fig. 3.17: Comparison of the active material volume V_{act} for a $J_{\mathrm{th,max}}$ derived from an LPTN (left) and a constant value for $J_{\mathrm{th,max}}$ (right).
application specifications: table 3.3; optimization criterion: `Maximum Volumetric Torque Density`

ameter D_{st} shown in fig. 3.17a in contrast to a fixed value. Therefore, increasing the stator outer diameter D_{st} becomes less advantageous in terms of a relative reduction of the active material volume V_{act} than expected when presuming a constant value for the thermally permitted maximal current density $J_{\mathrm{th,max}}$. Secondly, for a given stator outer diameter D_{st} the thermal modeling affects the ranking order when sorting the configurations according to the corresponding active material volumes V_{act}. When $J_{\mathrm{th,max}}$ is derived from the LPTN, the (2,2) configuration, for example, shows a lower active material volume V_{act} at a stator outer diameter $D_{\mathrm{st}} = 140\,\mathrm{mm}$ than the (3,1) configuration. This is inversed for a fixed thermally permitted maximal current density $J_{\mathrm{th,max}} = 11\,\mathrm{A/mm^2}$ as can be seen from fig. 3.17c. Again, the reason can be found in fig. 3.17a. At a constant stator outer diameter D_{st} the thermally permitted maximal current density $J_{\mathrm{th,max}}$ for the (3,1) configuration is approximately $1\,\mathrm{A/mm^2}$ lower than for the (2,2) configuration.

It can be summarized, that considering a geometry dependent LPTN has a significant effect on the thermally permitted maximal current density $J_{\mathrm{th,max}}$ as already discussed in section 3.3.1. Compared to a constant $J_{\mathrm{th,max}}$, the resulting variable $J_{\mathrm{th,max}}$ leads to strongly

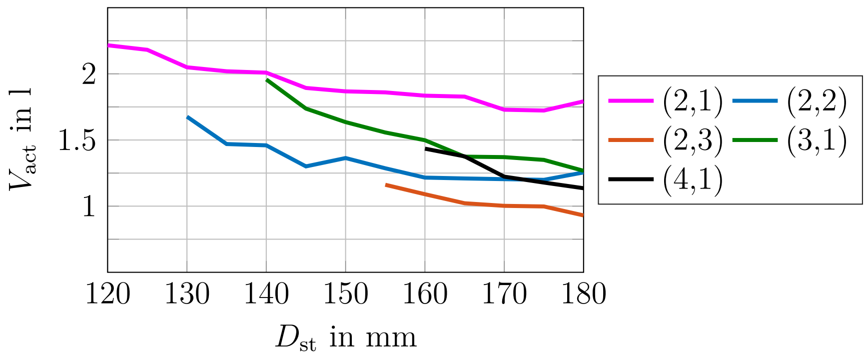

Fig. 3.18: Volume of the active material V_{act} for different machine configurations for `Torque-per-`Θ_{pl} `Peak-Point Derating` and $d_{derate} = 0.95$.

differing results in terms of a minimal active material volume V_{act}. Especially, when many machine configurations are compared over a wide range of stator outer diameter D_{st}, a constant thermally permitted maximal current density $J_{th,max}$ could mislead a designer in an early pre-design stage with respect to the achievable torque density $\phi_{T,act,pl}$ as well as the most advantageous machine configuration.

Finally, fig. 3.18 depicts results for the set of parameters from table 3.3 for a `Torque-per-`Θ_{pl} `Peak-Point Derating` with $d_{derate} = 0.95$. The thermally permitted maximal current density $J_{th,max}$ is derived again with the help of the LPTN. No solutions are found for small stator outer diameters D_{st} for certain configurations. For these configurations the effective current density J_{eff} is larger than the thermally permitted maximal current density $J_{th,max}$ at the design ($^{T_{pl}}/_{\Theta_{pl}}$) point. As discussed in section 3.3.4, the `Torque-per-`Θ_{pl} `Peak-Point Derating` optimization criterion is a compromise between efficiency and torque density $\phi_{T,act,pl}$. The penalty in terms of the active material volume V_{act} can be determined by exemplarily comparing fig. 3.18 with fig. 3.17b. For a stator outer diameter $D_{st} = 130\,\text{mm}$ the (2,2) configuration features an active material volume V_{act} increased by 30 % compared to the corresponding design with a `Maximum Volumetric Torque Density`.

3.4 Prototype Machines

To verify and support the theoretical analysis, three different generators were designed, built and evaluated in the course of this thesis for the two scenarios introduced in section 2.1.2. Preliminary considerations with the analytical tool PC-SRD as well as selected coupled FEA are performed to narrow down the design range (configuration, nominal generator speed $n_{SRG,nom}$) in a first step. One of the three generators was designed using an iterative optimization process, as described in [BBD12; Bra13], for the low speed scenario (see section 2.1.2.1). The other two generators were developed with the help of the SSBPD approach, described in the previous sections of this chapter, for the high-speed scenario (see section 2.1.2.2). The designed prototypes are afterwards employed to validate the SSBPD approach and to asses the potential of the SRG technology for REX in chapter 4. The prototypes considered in the further analysis are renamed as indicated in section A.2.1, as in the detailed analysis the number of turns per pole $N_{w,pl}$ is an important design parameter.

3.4.1 Low-Speed Scenario Generator

An iterative design approach as presented in [BBD12] is most suitable for the low-speed scenario, as the envelope volume and nominal speed $n_{\mathrm{SRG,nom}}$ of the generator are defined in advance (see table 2.1). However, due to the time consuming iterative approach the choice of configurations has to be limited by preliminary considerations.

The fixed design parameters (stator outer diameter D_{st}, stack length L_{stk}, nominal generator speed $n_{\mathrm{SRG,nom}}$) suggest the use of a fixed thermally permitted maximal current density $J_{\mathrm{th,max}}$ for this design. However, the general discussion in section 3.3.5 showed much lower possible thermally permitted maximal current density $J_{\mathrm{th,max}}$ based on the LPTN, than the $12\,\mathrm{A/mm^2}$ proposed in literature [Car08; Bra13]. Therefore, the machines are designed to meet the required stack length L_{stk} with the lowest possible effective current density J_{eff}.

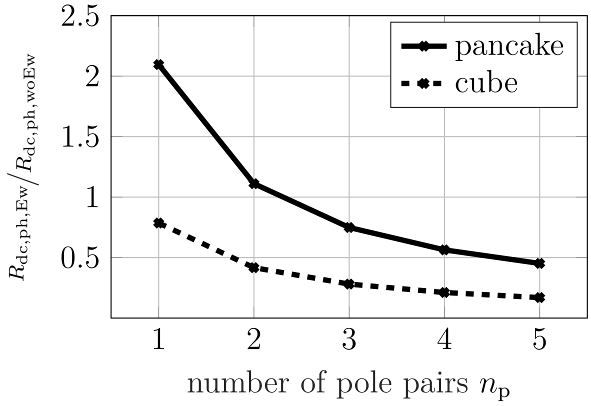

Fig. 3.19: End-winding dc-resistance $R_{\mathrm{dc,ph,Ew}}$ in relation to the $R_{\mathrm{dc,ph,woEw}}$.
pancake: $D_{\mathrm{st}}/L_{\mathrm{stk}} = 3.5$, cube: $D_{\mathrm{st}}/L_{\mathrm{stk}} = 1.75$

The design boundaries in table 2.1 require a short stack length L_{stk} compared to the stator outer diameter D_{st}. This fact leads to the following general design considerations.

Machines with a large stator outer diameter D_{st} and a short stack length L_{stk}, sometimes referred to as pancake design, suffer from the end-winding size. The end-windings are the winding overhangs at both machine ends, which may form a large part of the whole axial length of the machine, compared to the stack length L_{stk} of the iron core in such pancake designs. This results in high copper losses $P_{\mathrm{l,cu,dc,Ew}}$ (see (2.20)), which do not contribute to the electromagnetic energy conversion. Fig. 3.19 shows the ratio of $R_{\mathrm{dc,ph,Ew}}$ to $R_{\mathrm{dc,ph,woEw}}$ for a pancake ($D_{\mathrm{st}}/L_{\mathrm{stk}} = 3.5$) and a cube ($D_{\mathrm{st}}/L_{\mathrm{stk}} = 1.75$) shaped 2-phase machine over the number of pole pairs n_{p}. The ratio between the additional $R_{\mathrm{dc,ph,Ew}}$ and the stack length related $R_{\mathrm{dc,ph,woEw}}$ diminishes with the number of pole pairs n_{p}. For the designs investigated in fig. 3.19 it is more than twice as high for the pancake shaped compared to the cube shaped machine. Apart from the findings in fig. 3.19, which illustrates the influence on the dc copper losses $P_{\mathrm{l,cu,dc}}$, the number of pole pairs n_{p} also defines the electric base frequency f_{el} (see (2.2) and (2.4)), which is linked to the frequency dependent eddy current copper losses $P_{\mathrm{l,cu,eddy}}$ and iron core losses $P_{\mathrm{l,fe}}$. The machine efficiency η_{mach} will be influenced in a negative way by an increased number of pole pairs n_{p} if the gained positive effect of a lower end-winding resistance $R_{\mathrm{dc,ph,Ew}}$ and active material volume V_{act} (see fig. 3.16) is compensated by the increased frequency dependent losses.

		(2,2)	(2,3)
prototype name		LS2ph2p68N	LS2ph3p60N
phase rms current	$I_{\mathrm{ph,rms}}$	100 A	118 A
current density	J_{eff}	11.2 A/mm^2	9.8 A/mm^2
active material weight	m_{act}	14.6 kg	14.5 kg
generator efficiency	η_{mach}	94.4 %	93.8 %

Table 3.4: Analytical design results for an iterative machine design for the low-speed scenario retrieved with the algorithm proposed in [BBD12; Bra13].

To overcome the negative effects of the increased electric base frequency f_{el} at higher number of pole pairs n_{p} the designer can make use of the following influencing factors. The type of iron material has an impact on the iron core losses $P_{\mathrm{l,fe}}$. It will be discussed in detail in section 4.1.2, how higher-grade materials allow higher electric base frequencies f_{el} without a significant reduction of machine efficiency η_{mach}. Another key factor is the dc-link voltage u_{dc}, as it defines the possible number of turns per pole $N_{\mathrm{w,pl}}$ and, consequently, the exploitable winding area A_{w} without strong increase in eddy-current copper losses $P_{\mathrm{l,cu,eddy}}$, as will be discussed in detail in section 4.1.1.

After the preliminary considerations in this section and section 2.1.2.1, the iterative design process from [BBD12; Bra13] was used to derive a (2,2) and a (2,3) machine design that fulfill the design specifications from table 2.1 with the lowest possible effective current density J_{eff}. The resulting reference parameters of these two machine designs are shown in table 3.4. The primary design parameters active material weight m_{act} and machine efficiency η_{mach} for both designs only differ slightly. The (2,2) machine has a smaller root mean square (RMS) current $I_{\mathrm{ph,rms}} = 100\,\mathrm{A}$ compared to the (2,3) design with 118 A. However, the resulting current density $J_{\mathrm{eff}} = 11.2\,\mathrm{A/mm^2}$ is greater than of the (2,3) design (9.8 A/mm^2).

As the shown reference parameters cannot be used for a clear decision, the acoustic behavior is considered in this case. Due to the increased electric base frequency f_{el}, the (2,3) machine offers a lower harmonic density compared to the (2,2) machine, hence, a beneficial acoustic behavior is expected for the (2,3) configuration based on literature [Fie07]. This expectation will be discussed in section 4.3, with the help of surface velocity v_{surf} simulations at the nominal operation point. All machine parameters of the final (2,3,220) and (2,2,220) configuration can be found in table A.2 and table A.6, respectively.

3.4.2 High-Speed Scenario Generator

The SSBPD introduced in this chapter is most suitable for the high-speed scenario, as the machine envelope volume as well as the nominal generator speed $n_{\mathrm{SRG,nom}}$ can be freely chosen. However, an increased nominal generator speed $n_{\mathrm{SRG,nom}}$ and electric base frequency f_{el} (see (2.4)) affects the machine efficiency η_{mach}. As long as these effects are not precisely modeled in the SSBPD, the nominal generator speed $n_{\mathrm{SRG,nom}}$ and configurations need to be narrowed down by preliminary considerations comparable to the low-speed scenario.

The effect on the generator efficiency η_{mach} and the machine active parts volume V_{act} are shown in fig. 3.20 for a (2,2) machine configuration retrieved from PC-SRD. Each design,

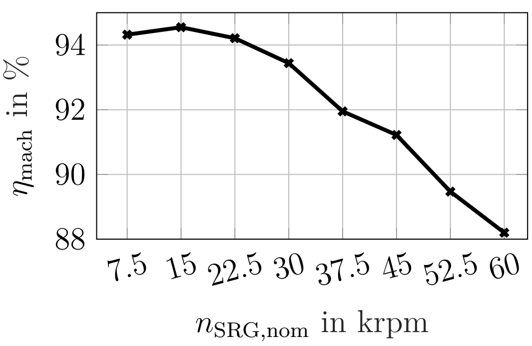

(a) generator efficiency

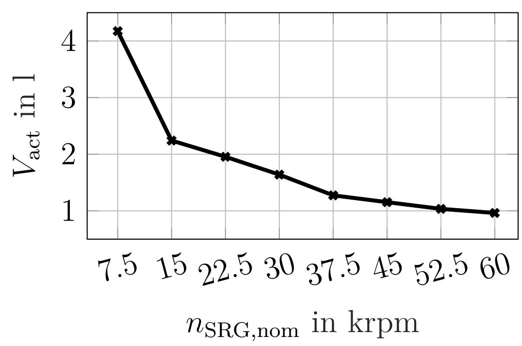

(b) active material volume

Fig. 3.20: Effect of the nominal generator speed $n_{\mathrm{SRG,nom}}$ on the machine efficiency η_{mach} and active material volume V_{act} of a (2,2) machine configuration. $P_{\mathrm{m,sh}} = 20\,\mathrm{kW}$, design process: [BBD12], simulation software: PC-SRD

at a certain nominal generator speed $n_{\mathrm{SRG,nom}}$, was chosen with the help of the design process proposed in [BBD12] and a constant maximal permitted thermal current density $J_{\mathrm{th,max}} = 12\,\mathrm{A/mm^2}$. It is important to keep in mind that PC-SRD completely neglects frequency dependent eddy-current copper losses $P_{\mathrm{l,cu,eddy}}$ in the stator coils. In this case, a nominal speed $n_{\mathrm{SRG,nom}}$ up to 37.5 krpm offers an active material volume V_{act} reduction by a factor four, limiting the efficiency reduction to about 2 pp.

A more detailed look at the speed range from 20 to 30 krpm for three configurations is taken in fig. 3.21. The (3,1) and (3,2) configuration are added to the discussion due to their reduced torque ripple (see section 2.1.2.2). Each design for a certain nominal generator speed $n_{\mathrm{SRG,nom}}$ was again chosen with the help of PC-SRD and the design process proposed in [BBD12] and a constant maximal permitted thermal current density $J_{\mathrm{th,max}} = 12\,\mathrm{A/mm^2}$.

Neglecting eddy-current copper losses $P_{\mathrm{l,cu,eddy}}$ and employing a M330-35A iron core material, the (3,2) configuration shows a lower machine efficiency η_{mach} by 4 – 5 pp compared to the (2,2) and (3,1) configuration, which is due to the doubled electric base frequency f_{el}. As a constant maximal permitted thermal current density $J_{\mathrm{th,max}}$ was assumed, the (3,2) configuration results in the lowest active material weight m_{act}, as expected from section 3.3.5. However, at $n_{\mathrm{SRG,nom}} = 30\,\mathrm{krpm}$ the (3,1) configuration shows a comparable active material weight m_{act}. The (2,2) configuration shows an active material weight m_{act} approximately 0.75 kg higher than the (3,1) configuration over the complete speed range. This ranking order based on the active weight is expected to be reversed, if the thermal behavior of the stator is included in the design process by the LPTN (see fig. 3.17).

A coupled FEA, as described in section 2.3.2, is used to analyze the frequency dependent losses of the (2,2) configuration from fig. 3.21 at $n_{\mathrm{SRG,nom}} = 20\,\mathrm{krpm}$ and 25 krpm in more detail. The results for the machine losses $P_{\mathrm{l,mach}}$ of the FEA are listed in table 3.5. To achieve a comparable machine efficiency η_{mach} in the FEA an improved iron material NO20 was used. The resulting machine efficiency η_{mach} of the machine with $n_{\mathrm{SRG,nom}} = 20\,\mathrm{krpm}$ is slightly higher than that of the machine with $n_{\mathrm{SRG,nom}} = 25\,\mathrm{krpm}$. The results from table 3.5 suggest that with the improved iron material NO20, the machine efficiency η_{mach} is only slightly influenced by the machine speed $n_{\mathrm{SRG,nom}}$ up to 25 krpm. This is in accordance with the analytical results from fig. 3.21.

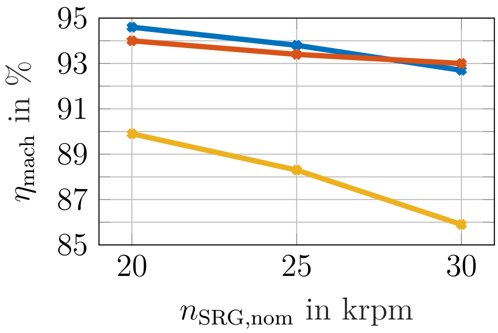

(a) η_{mach}

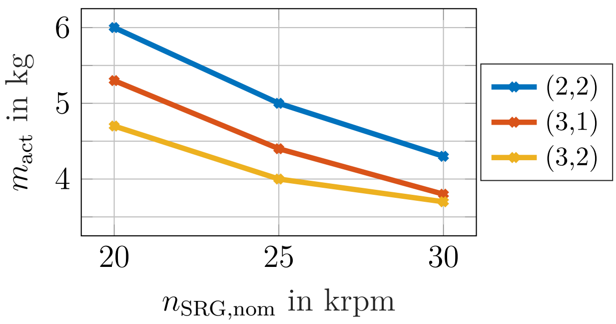

(b) m_{act}

Fig. 3.21: Effect of the nominal generator speed $n_{\mathrm{SRG,nom}}$ on the machine efficiency η_{mach} and active material weight m_{act} in the speed range $n_{\mathrm{SRG,nom}} = 20 - 30\,\mathrm{krpm}$. simulation software: PC-SRD, iron core material: M330-35A

$n_{\mathrm{SRG,nom}}$	J_{eff}	$P_{\mathrm{l,fe}}$	$P_{\mathrm{l,cu,eddy}}$	$P_{\mathrm{l,cu,dc}}$	$P_{\mathrm{l,wind}}$	$P_{\mathrm{l,mach}}$	η_{mach}
20 krpm	14 A/mm^2	510 W	200 W	610 W	140 W	1460 W	93.7 %
25 krpm	13.9 A/mm^2	540 W	250 W	510 W	220 W	1520 W	93.4 %

Table 3.5: Comparison of coupled FEA results for (2,2) machines at different nominal speeds $n_{\mathrm{SRG,nom}}$. $\vartheta_{\mathrm{coil}} = 100\,°\mathrm{C}$, iron material: NO20, $P_{\mathrm{l,bear}} = P_{\mathrm{l,gear}}$ 0 W.

From the preliminary considerations regarding the machine efficiency η_{mach}, the final prototype choice for a validation of the design process is limited to the (3,1) and (2,2) configuration. Beside the discussion on efficiency and weight, which suggests a nominal machine speed $n_{\mathrm{SRG,nom}}$ up to 37.5 krpm, mechanical limitations have to be taken into consideration. To be able to build the prototypes with standard catalog ball bearings and machine sealings, the maximal nominal generator speed $n_{\mathrm{SRG,nom}}$ was limited to 25 krpm. This pragmatic choice was based on the experience of the prototype manufacturers.

The final prototype choice is made with the SSBPD process described in section 3.2 and 3.3. The application dependent parameters for the high-speed scenario are listed in table 3.6. The major deviation from previous sections are the gap spacer d_{gsp} and coil spacer d_{csp} (see fig. 3.10). These two parameters strongly influence the eddy-current copper losses $P_{\mathrm{l,cu,eddy}}$ and are initially chosen based on the author's experience. Their influence will be discussed with the help of coupled FEA in section 4.1.1. The copper loss correction factor k_{cu} and maximum coil temperature $\vartheta_{\mathrm{coil,max}}$ represent the frequency dependent eddy-current copper losses $P_{\mathrm{l,cu,eddy}}$ and iron core losses $P_{\mathrm{l,fe}}$ in the analytical pre-design, respectively. These correction factors need to be chosen from experience, as no electric base frequency f_{el} dependent loss model is implemented in the design process (see section 3.3). To show their effect on the machine designs, the SSBPD is carried out for three different values of k_{cu} and $\vartheta_{\mathrm{coil,max}}$ in the parameter range stated in table 3.6. A value of $k_{\mathrm{cu}} = 1$ for the copper loss correction factor and a maximum coil temperature $\vartheta_{\mathrm{coil,max}} = 180\,°\mathrm{C}$ mean that no frequency dependent losses are considered in the determination of the maximal permitted thermal current density $J_{\mathrm{th,max}}$. The value of $\vartheta_{\mathrm{coil,max}}$ for no iron core losses $P_{\mathrm{l,fe}}$ depends on the chosen insulation class of the copper wires, class H in the course of this thesis.

Quantity		Value
nominal speed	$n_{\mathrm{SRG,nom}}$	25 000 rpm
maximal coil temperature	$\vartheta_{\mathrm{coil,max}}$	130 – 170 °C
torque derating factor	d_{t}	0.75
copper loss correction	k_{cu}	1 – 2
gap spacer	d_{gsp}	5 mm
coil spacer	d_{csp}	2 mm
copper fill factor	f_{cu}	0.75
copper wire price	c_{Cu}	10 €/kg
electric steel price	c_{NO30}	1 €/kg
shaft material price	c_{steel}	1.8 €/kg
optimization criterion	`Maximum Volumetric Torque Density`	

Table 3.6: Design specifications for the SSBPD for the high-speed scenario. Additional thermal parameters as specified in table 3.2.

In fig. 3.22, the results from the SSBPD are depicted for a variation of the parameters k_{cu} and $\vartheta_{\mathrm{coil,max}}$. While one parameter is varied, the other parameter is kept constant. The active material volume V_{act}, does not show any optimum in the considered stator outer diameter D_{st} range and decreases with an increased D_{st} as expected from fig. 3.16a. The active material weight m_{act} seems to converge and even forms a minimum at larger stator outer diameter D_{st}. For the parameter set ($k_{\mathrm{cu}} = 1$, $\vartheta_{\mathrm{coil,max}} = 150\,°\mathrm{C}$), for example, a minimum in the stator outer diameter range $D_{\mathrm{st}} = 140 - 160\,\mathrm{mm}$ is found. Generally, the (2,2) configuration shows lower values for both the active material volume V_{act} and weight m_{act} over the complete considered outer stator diameter D_{st} range.

As the two considered parameters do not show clear minima, a stator outer diameter D_{st} choice for the prototypes is not possible. Therefore, the material costs are additionally taken into consideration. For all combinations of the copper loss correction factor k_{cu} and maximum coil temperature $\vartheta_{\mathrm{coil,max}}$ a minimum can be found in the stator outer diameter range of $D_{\mathrm{st}} = 120 - 160\,\mathrm{mm}$. This behavior can be explained with the copper mass of the end-windings, which grows in relation to the copper mass in the stator slots when further increasing the stator outer diameter. This effect over-compensates the expected reduction of the active material at larger diameter values, as copper is considered more expensive than the iron core material (see table 3.6). From this analysis, a stator outer diameter $D_{\mathrm{st}} = 140\,\mathrm{mm}$ is chosen for the prototype machines, as it is in the middle of the cost optimal diameter range.

Fixing the stator outer diameter D_{st} and $STPR$, the machine geometry is completely defined as described in section 3.2. The exact design, however, still depends on the choice of the copper loss correction factor k_{cu} and maximal coil temperature $\vartheta_{\mathrm{coil,max}}$. Therefore, fig. 3.23 depicts the resulting stack length L_{stk}, the thermally permitted maximal current density $J_{\mathrm{th,max}}$ and the $STPR$ for the machine designs from fig. 3.22b in the cost optimal stator outer diameter D_{st} range with a copper loss factor $k_{\mathrm{cu}} = 1.5$. The latter was chosen as a reasonable value from the author's experience as mentioned before for an electric base frequency $f_{\mathrm{el}} = 1.67\,\mathrm{kHz}$. As the (2,2) configuration shows a lower active material volume

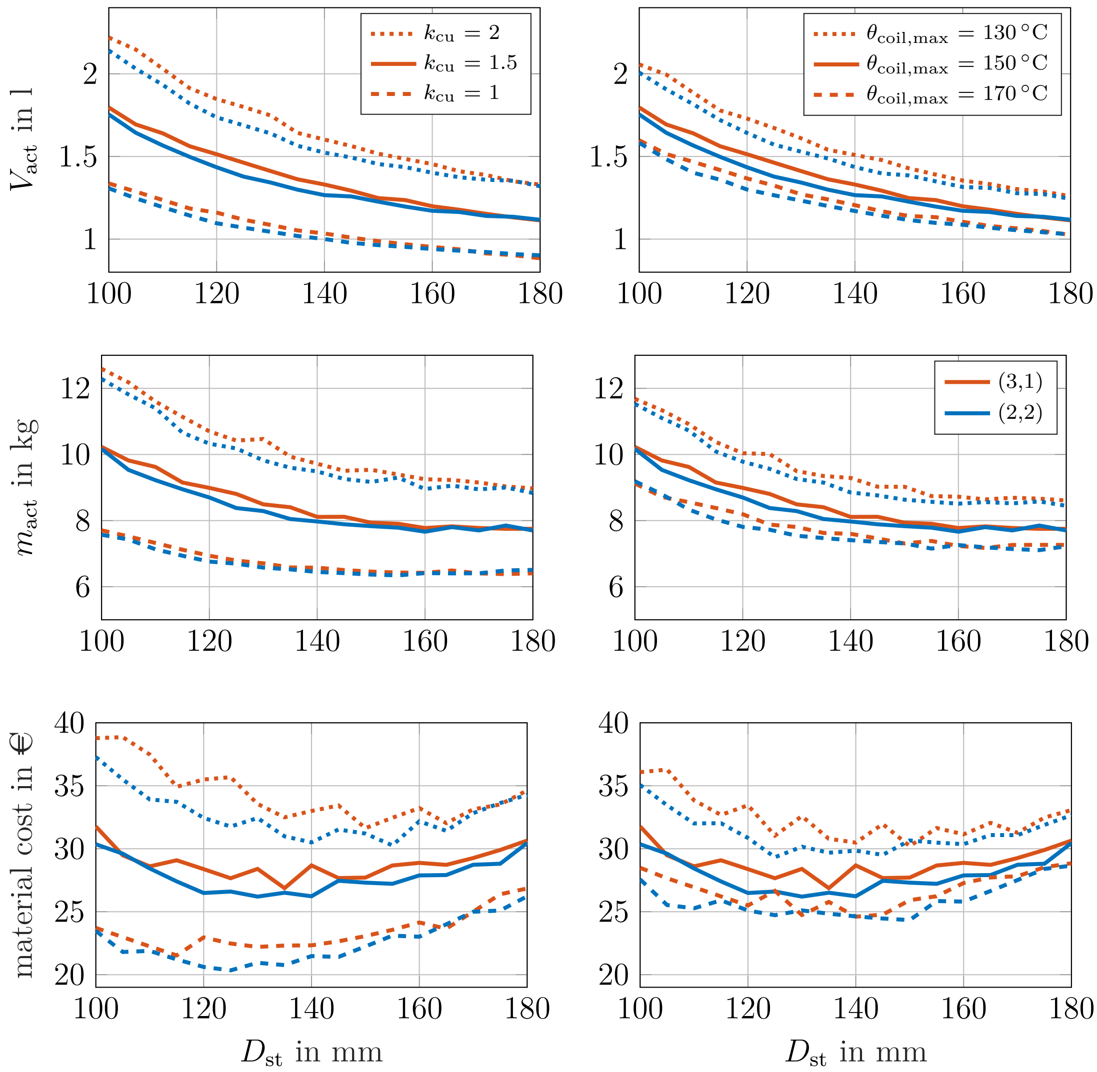

(a) variation of the copper loss correction factor k_{cu}, $\vartheta_{coil,max} = 150\,°C$

(b) variation of the maximum coil temperature $\vartheta_{coil,max}$, $k_{cu} = 1.5$

Fig. 3.22: Influence of the copper loss correction factor k_{cu} and the maximum coil temperature $\vartheta_{coil,max}$ on various machine parameters of a (2,2) configuration (blue) and (3,1) configuration (red) over the stator outer diameter D_{st}. high-speed scenario specifications: table 3.6

V_{act} than the (3,1) configuration in fig. 3.22, the required stack length L_{stk} depicted in fig. 3.23a is obviously also smaller at a constant stator outer diameter D_{st}. The resulting thermally permitted maximal current density $J_{th,max}$ from the LPTN of all designs depicted in fig. 3.23b are below the $J_{th,max} = 12\,A/mm^2$ mentioned for water jacket cooled machines in literature [Car08; Bra13]. Finally, the *STPR* does not show a strong dependence on the maximal coil temperature $\vartheta_{coil,max}$. The discontinuities arise from the discrete *STPR* stored in the database structure. When matching the effective current density J_{eff} to the thermally permitted maximal current density $J_{th,max}$ no interpolation is performed.

For validation, two machines with a stack length $L_{stk} = 80\,mm$ are finally chosen. This

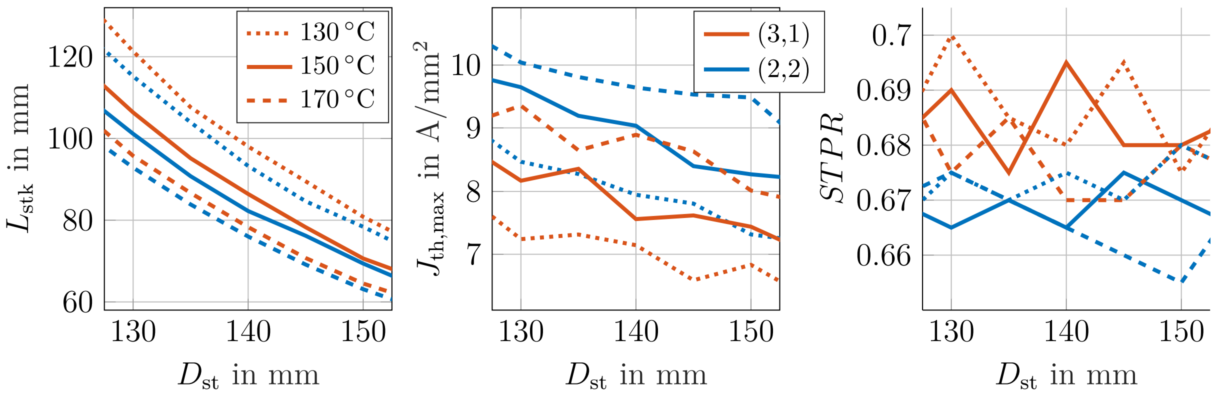

(a) L_{stk} over D_{st} (b) $J_{\mathrm{th,max}}$ over D_{st} (c) $STPR$ over D_{st}

Fig. 3.23: Generator stack length L_{stk}, thermally permitted maximal current density $J_{\mathrm{th,max}}$ and $STPR$ of a (2,2) configuration (blue) and (3,1) configuration (red) in the range of the minimal material cost from fig. 3.22. copper loss correction factor $k_{\mathrm{cu}} = 1.5$, maximum coil temperature $\vartheta_{\mathrm{coil,max}}$ = variable

L_{stk} is located between the results of $\vartheta_{\mathrm{coil,max}} = 150 - 170\,°\mathrm{C}$. Preliminary simulations with MotorCAD proved this to be a reasonable range. A more detailed analysis based on measurements and simulations will be performed in 4.2.3. The constant stack length L_{stk} is chosen for production simplicity, to employ the same housing for both machines. In the prototypes, therefore, a higher coil temperature $\vartheta_{\mathrm{coil,max}}$ is to be expected in the (3,1) configuration compared to the (2,2) configuration. The $STPR$ for both machines was chosen at the lower end of the found results, as both coil parameters gap spacer d_{gsp} and coils spacer d_{csp} were assumed as worst case limits in the pre-design. The complete geometric parameters of the built (2,2,140,0.655) and (3,1,140,0.67) machine can be found in table A.2.

3.5 Chapter Conclusion

In this chapter, a solution space based pre-design (SSBPD) for SRGs is introduced, which decouples the geometry dependent electromagnetic torque capability from application specific requirements. A wide range of configurations and geometries are calculated using FEA and stored in a solution database. This database is computed once for the complete design range, e.g. outer diameter, air gap length, material. The process does not require any magnetic tuning parameters in the pre-design stage. After this step, the thermally permitted maximal current densities $J_{\mathrm{th,max}}$ are calculated for each geometry separately with the help of a geometry dependent LPTN. For this evaluation, beside the geometry only intuitive and comprehensible application specific parameters, such as the shaft power $P_{\mathrm{m,sh}}$, the maximal coil temperature $\vartheta_{\mathrm{coil,max}}$ or the copper fill factor f_{cu}, are required. In a final step, from all thermally valid designs the most suitable designs in terms of a given optimization criteria, such as minimal active material volume, are chosen. These designs are depicted to the designer over a wide range of stator outer diameter D_{st} and configurations.

With the proposed SSBPD approach a fast overview over a specific solution space and potential machine designs is obtained. The evaluation of the solution space of approximately

28 000 machine designs, takes only 15 s on a standard laptop (Intel®Core™ i7-5600U, 8 GB RAM, 256 GB SSD hard drive). One single FEA to evaluate the aligned and unaligned flux linkage characteristic with the software FLUX2D takes about 14 min of calculation time, without any export and model setup considered. Based on the fast overview, the most promising designs can be further analyzed with more time consuming simulations, such as detailed FEA for the losses or structural analysis for the acoustic evaluation.

From the result discussion in section 3.3.5, the following conclusions are drawn. Firstly, a geometry dependent calculation of the thermally permitted maximal current density $J_{\mathrm{th,max}}$ instead of a constant value, strongly influences the comparison of different SRG configurations in terms of the achievable torque density $\phi_{\mathrm{T,act}}$ and finally the active material volume V_{act}, as shown in fig. 3.17. Therefore, comparing different machine configurations with a constant $J_{\mathrm{th,max}}$ is leading to erroneous assumptions in pre-design and should be avoided.

Secondly, in fig. 3.16 it can be seen that for a given stator outer diameter D_{st}, one configuration of maximal torque density $\phi_{\mathrm{T,act}}$ with a specific number of stator poles N_{s} exists. Hence, the effect of an increasing number of pole pairs n_{p} and, consequently, the electric base frequency f_{el} on $\phi_{\mathrm{T,act}}$ strongly depends on the stator outer diameter D_{st}. A generalization, that a higher electric base frequency f_{el} leads to a larger torque density $\phi_{\mathrm{T,act}}$ is, therefore, not possible.

Finally, in fig. 3.16 it can be seen that for a given stator outer diameter D_{st}, the investigated 2-phase configurations show a higher torque density $\phi_{\mathrm{T,act}}$ than the configurations with a higher number of phases N_{ph} with the same number of rotor poles N_{r}. If torque ripple is not a criterion for the configuration choice, 2-phase configurations, therefore, should not be excluded from the design choice.

4 Generator Design and Discussion

This chapter addresses the different areas of SRG design in detail, based on the prototypes chosen in section 3.4 and listed in table A.2 - A.6. With the help of simulations and measurements at the nominal operation point, the assumptions made in chapter 3, e.g. in terms of reachable active material torque density $\phi_{\mathrm{T,act}}$ in fig. 3.22, are verified and generalized for other SRG if possible. The analysis of the SRG comprises the machine efficiency (section 4.1), the torque and power density (section 4.2), as well as the acoustic behavior (section 4.3). After discussing additional design aspects (section 4.4), the chapter is wrapped up in a conclusion (section 4.5). As mentioned in chapter 1, while only SRGs are mentioned in the discussion, the general findings can be transferred to switched reluctance machines as well.

4.1 Machine Efficiency

To estimate the machine efficiency η_{mach} as defined in table 2.3 and to identify the influence of the underlying design parameters, the machine losses $P_{\mathrm{l,mach}}$ have to be calculated and analyzed. As defined by (2.15), the machine losses $P_{\mathrm{l,mach}}$ consist of the total copper losses $P_{\mathrm{l,cu,ac}}$, the iron core losses $P_{\mathrm{l,fe}}$ and the mechanical losses $P_{\mathrm{l,m}}$.

A crucial influencing factor of the total copper losses $P_{\mathrm{l,cu,ac}}$ and iron core losses $P_{\mathrm{l,fe}}$ is the winding design of the machine. This comprises the selection of the number of turns per pole $N_{\mathrm{w,pl}}$ as well as the individual sizing and placement of the windings in the stator slot. As introduced in section 2.2 by equations (2.9) - (2.13) and depicted in fig. 2.7, the number of turns per pole $N_{\mathrm{w,pl}}$ influences the phase voltage u_{ph} of the SRG and, consequently, the phase current i_{ph} and pole flux Φ_{pl}. These quantities directly influence the total copper losses $P_{\mathrm{l,cu,ac}}$ (see (2.20)) and iron core losses $P_{\mathrm{l,fe}}$ (see (2.28)), as introduced in section 2.2.1. The individual winding diameter d_{w} and placement influences not only the phase resistance $R_{\mathrm{dc,ph}}$, but also the amount of pole flux Φ_{pl} penetrating individual coils and hence the eddy-current copper losses $P_{\mathrm{l,cu,eddy}}$ caused by proximity and skin effect (see (2.24)). The iron core losses $P_{\mathrm{l,fe}}$ can additionally be influenced by the choice of iron sheet material. Finally, the mechanical losses $P_{\mathrm{l,m}}$ are influenced by the generator speed n_{SRG}, the bearing size as well as air turbulences in the machine air gap.

The SRG designs listed in table A.2 as well as their permutations listed in table A.3 are employed to analyze the machine losses $P_{\mathrm{l,mach}}$. The investigation includes the influence of the winding design (section 4.1.1), the iron core material and different loss calculation methods (section 4.1.2) as well as mechanical variations (section 4.1.3). In each section, loss improvements are proposed. After validating the simulation results with measurements in section 4.1.4 all proposed improvements are summarized in section 4.1.5 and the complete effect on the machine efficiency η_{mach} is discussed.

4.1.1 Winding Design

As discussed in detail for two different traction SRG in [Car08] and [Ral+17], the frequency dependent eddy-current copper losses $P_{\mathrm{l,cu,eddy}}$ in an SRG can be significantly larger than the dc copper losses $P_{\mathrm{l,cu,dc}}$ and form the largest part of the total copper losses $P_{\mathrm{l,cu,ac}}$ (see (2.19)). The strong impact of the winding design on the total copper losses $P_{\mathrm{l,cu,ac}}$ was already shown in [Car08] and is transferred to the investigated SRG in this section.

Firstly, the choice of number of turns per pole $N_{\mathrm{w,pl}}$ is analyzed, as it defines the dynamic electromagnetic behavior of the SRG (see fig. 2.7) and, consequently, the losses. Secondly, having chosen a certain $N_{\mathrm{w,pl}}$, assuming coils made of one discrete wire, the wire diameter d_{w} and the individual placement of each wire are parameters to further influence the total copper losses $P_{\mathrm{l,cu,ac}}$. The influence of the dc-link voltage u_{dc} on the total copper losses is analyzed next, as it offers another degree of freedom in the winding design. After analyzing the effect of an increased coil temperature $\vartheta_{\mathrm{coil}}$ on the total copper losses $P_{\mathrm{l,cu,ac}}$, analytical approaches to determine eddy-current copper losses $P_{\mathrm{l,cu,eddy}}$ are benchmarked against the coupled FEAs performed in this section. The section concludes with a brief discussion of further reduction potential by the application of litz-wires.

To determine the effect of the winding design on the total copper losses $P_{\mathrm{l,cu,ac}}$, as described in section 2.2.1 and according to literature [Car08; Sch15], coupled FEA simulations are required for each winding configuration. In the coupled FEA as well as in the design process proposed in chapter 3, the phase resistance $R_{\mathrm{dc,ph,est}}$ is estimated by adding half circles to each straight wire at both ends of the machine. This method neglects the additional copper needed to connect all coils of one phase at the machine terminals as well as extra distances to the stator core added for insulation reasons. The resulting additional resistance can be expressed by a resistance correction factor $k_{\mathrm{R,dc}}$ as defined in (4.1).

$$R_{\mathrm{dc,ph}} = R_{\mathrm{dc,ph,est}} \cdot (1 + k_{\mathrm{R,dc}}) \tag{4.1}$$

The phase resistance $R_{\mathrm{dc,ph}}$ is determined by measuring the voltage at the phase terminals at $\vartheta_{\mathrm{coil}} = 20\,^{\circ}\mathrm{C}$, while different constant current levels are impressed for a short period. The phase resistance $R_{\mathrm{dc,ph}}$ ($\vartheta_{\mathrm{coil}}$) at different coil temperatures $\vartheta_{\mathrm{coil}}$ is then calculated by the thermal coefficient $\alpha_{\mathrm{cu,20}}$ of copper and (4.2).

$$R_{\mathrm{dc,ph}}(\vartheta_{\mathrm{coil}}) = R_{\mathrm{dc,ph}}(20\,^{\circ}\mathrm{C}) \cdot (1 + \alpha_{\mathrm{cu,20}} \cdot (\vartheta_{\mathrm{coil}} - 20\,^{\circ}\mathrm{C})) \tag{4.2}$$

To show the difference between measured phase resistance $R_{\mathrm{dc,ph}}$ and estimated phase resistance $R_{\mathrm{dc,ph,est}}$, both values are shown in table 4.1 for four different prototype machines. The measurement results show an almost identical correction factor $k_{\mathrm{R,dc}}$ of 7.4 % for the first three machines (HS3ph1p49N, HS2ph2p45N, LS2ph3p60N), while the fourth machine HS3ph3p25N shows a slightly larger correction factor of 8.7 %. Due to the similar dc-link voltage (see table A.2 and A.6) the insulation requirements and, consequently resistance correction factors $k_{\mathrm{R,dc}}$, are nearly constant for all machines. Therefore, a constant $k_{\mathrm{R,dc}}$ for all the winding permutations mentioned in table A.3 is assumed reasonable. A similar value should be taken into account for efficiency predictions of new designs of a comparable dc-link voltage u_{dc}.

For an existing machine configuration, the number of turns per pole $N_{\mathrm{w,pl}}$ is defined by

	$R_{dc,ph,est}$	$R_{dc,ph}$	$k_{R,dc}$
HS3ph1p49N	56.0 mΩ	60.1 mΩ	0.074
HS2ph2p45N	32.9 mΩ	35.4 mΩ	0.074
LS2ph3p60N	26.2 mΩ	28.1 mΩ	0.073
HS3ph3p25N [Ral+17]	17.5 mΩ	19.0 mΩ	0.087

Table 4.1: Estimated phase resistance $R_{dc,ph,est}$ and extrapolated $R_{dc,ph}$ at $\vartheta_{coil} = 170\,°C$, $R_{dc,ph}$ extrapolated with (4.2) from measurements at $\vartheta_{coil} = 20\,°C$. For machine naming convention, see appendix A.2.1.

the available dc-link voltage u_{dc} and the desired phase current i_{ph} profile (comp. fig. 2.7) at nominal generator speed $n_{SRG,nom}$. The number of turns per pole $N_{w,pl}$ can be used to improve the machine efficiency η_{mach} by a SPC, as analytically shown in [Bra13]. This method is only possible if the instantaneous torque and force profile play a secondary role.

To validate the analytical assumption, several coupled FEA were performed for the HS2ph2p45N machine (see table A.2) and its permutations HS2ph2p27N - HS2ph2p57N (see table A.3). For each permutation with changed $N_{w,pl}$, the iron cross section is kept constant. Also a constant copper cross section A_{cu} is obtained by adjusting the wire diameter d_w for two different number of turns per pole $N_{w,pl,1}$ and $N_{w,pl,2}$ with relation (4.3). For the coupled FEA the maximal available phase current $I_{ph,pk}$ is limited to 300 A by the power electronics and the dc-link voltage u_{dc} is kept constant at 400 V.

$$A_{cu} = \pi \cdot \frac{d_{w,1}^2}{4} \cdot N_{w,pl,1} = \pi \cdot \frac{d_{w,2}^2}{4} \cdot N_{w,pl,2} \quad \Leftrightarrow \quad d_{w,1} = d_{w,2} \cdot \sqrt{\frac{N_{w,pl,2}}{N_{w,pl,1}}} \tag{4.3}$$

Fig. 4.1 depicts the total copper losses $P_{l,cu,ac}$ (see (2.19)) and iron core losses $P_{l,fe}$ (see (2.31)) over the number of turns per pole $N_{w,pl}$. The design with $N_{w,pl} = 27$ represents the

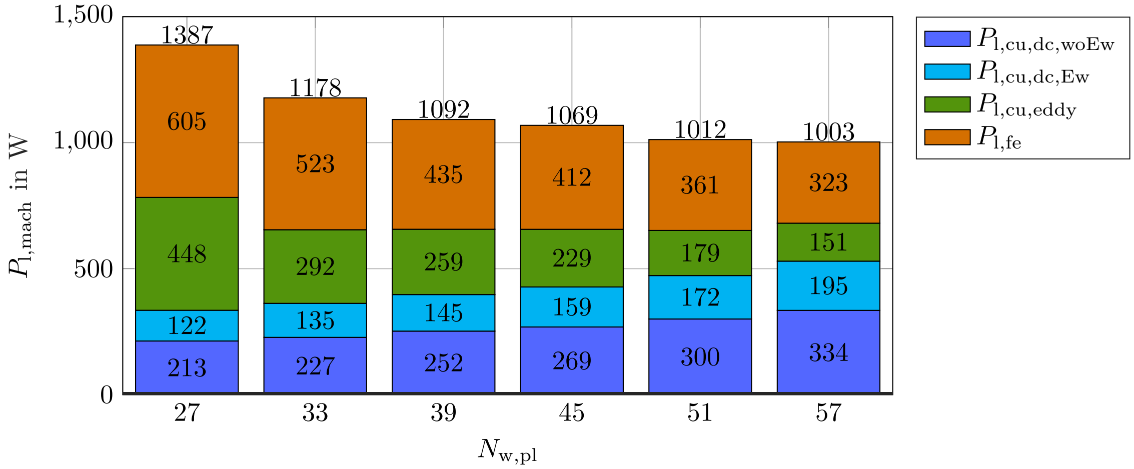

Fig. 4.1: Influence of number of turns $N_{w,pl}$ on total copper losses $P_{l,cu,ac}$ (see (2.19)) and iron core losses $P_{l,fe}$ (see (2.31)) for constant copper area A_{cu}. Permutations of HS2ph2p45N at operation point NOP_S (see table A.10).

limit between HCC and SPC (see fig. 2.7a). An increased $N_{\mathrm{w,pl}}$ leads to increasing dc-copper losses $P_{\mathrm{l,cu,dc}}$, the sum of $P_{\mathrm{l,cu,dc,Ew}}$ and $P_{\mathrm{l,cu,dc,woEw}}$. This can be explained by the larger $I_{\mathrm{ph,rms}}$ required to reach a constant torque as the torque derating factor d_{t} decreases with an increased number of turns per pole $N_{\mathrm{w,pl}}$ (see fig. 2.7a and section 3.3.2). The eddy-current losses $P_{\mathrm{l,cu,eddy}}$ decrease with increasing number of turns per pole $N_{\mathrm{w,pl}}$. This correlation can be explained as follows. With increasing numbers of turns per pole $N_{\mathrm{w,pl}}$ the phase inductance L_{ph} increases and results in lower phase current gradients (see fig. 2.7a). In addition, the individual wire diameter d_{w} decreases with increased $N_{\mathrm{w,pl}}$ (see (4.3)). Both effects subsequently reduce the eddy currents in the individual wires and, therefore, $P_{\mathrm{l,cu,eddy}}$. The total copper losses $P_{\mathrm{l,cu,ac}}$, the sum of $P_{\mathrm{l,cu,dc,woEw}}$, $P_{\mathrm{l,cu,dc,Ew}}$ and $P_{\mathrm{l,cu,eddy}}$ (see (2.20) and (2.19)), merely changes in the range of $N_{\mathrm{w,pl}} = 33 - 51$.

The nearly constant total copper losses $P_{\mathrm{l,cu,ac}}$ in the range of number of turns per pole $N_{\mathrm{w,pl}} = 33 - 51$ for the HS2ph2p45N machine, offers the potential to reduce the iron core losses $P_{\mathrm{l,fe}}$. Similar to the findings in [Bra13], the results depicted in fig. 4.1, retrieved with the help of p_{Bertotti}, show a reduction of iron core losses $P_{\mathrm{l,fe}}$ for an increased number of turns per pole $N_{\mathrm{w,pl}}$. This is important for the power density discussion in section 4.2.4, as an increase in $N_{\mathrm{w,pl}}$ decreases the torque density $\phi_{\mathrm{T,tot}}$ due to a decreased torque derating factor d_{t} (see fig. 3.13b). At the same time the thermal behavior is positively influenced by the decreased sum of total copper losses $P_{\mathrm{l,cu,ac}}$ and iron core losses $P_{\mathrm{l,fe}}$. For the permutations of the HS2ph2p45N machine, between $N_{\mathrm{w,pl}} = 45 - 51$ lowest total copper losses $P_{\mathrm{l,cu,ac}}$ are obtained. Considering additionally the iron core losses $P_{\mathrm{l,fe}}$, the range of lowest losses is shifted to $N_{\mathrm{w,pl}} = 51 - 57$. For prototype validation, $N_{\mathrm{w,pl}} = 45$ was finally chosen.

To reduce the dc copper losses $P_{\mathrm{l,cu,dc}}$ (sum of $P_{\mathrm{l,cu,dc,woEw}}$ and $P_{\mathrm{l,cu,dc,Ew}}$) the copper area A_{cu} and, consequently, the wire diameter d_{w} should be maximized. However, analytical investigations in [Dow66; Car08], suggest a negative effect of an increased copper wire diameter d_{w}. To verify the effect on the total copper losses $P_{\mathrm{l,cu,ac}}$, several coupled FEA were performed for the HS2ph2p45N machine (see table A.2) and its permutations HS2ph2p45N1 - HS2ph2p45N4 (see table A.3). A fixed iron core cross section and a constant wire insulation thickness $d_{\mathrm{ins,w}} = 0.05\,\mathrm{mm}$ is considered for all machine permutations.

While the HS2ph2p45N, HS2ph2p45N1 and HS2ph2p45N2 machines can be produced with preformed wires, the HS2ph2p45N3 machine can only be produced with wound-in coils (see fig. 3.10). The HS2ph2p45N4 machine with a copper wire diameter $d_{\mathrm{w}} = 2.2\,\mathrm{mm}$ obtains the maximum available copper area A_{cu} by increasing the wire diameter d_{w} until the complete slot is filled (see table A.3). This machine represents the case of minimally achievable dc-copper losses $P_{\mathrm{l,cu,dc}}$, neglecting any frequency dependent eddy-current copper losses $P_{\mathrm{l,cu,eddy}}$ and without questioning the feasibility of the winding design for production.

In fig. 4.2a, the eddy-current copper losses $P_{\mathrm{l,cu,eddy}}$ are depicted over the electrical angle θ_{el} for the five machine permutations. It is clearly seen, that an increase in copper wire diameter d_{w} strongly increases the instantaneous $P_{\mathrm{l,cu,eddy}}$. Fig. 4.2b depicts the total copper losses $P_{\mathrm{l,cu,ac}}$, separated in the individual losses $P_{\mathrm{l,cu,dc,Ew}}$, $P_{\mathrm{l,cu,dc,woEw}}$ and $P_{\mathrm{l,cu,eddy}}$ (2.19). As already expected from analyzing fig. 4.2a, the eddy-current copper losses $P_{\mathrm{l,cu,eddy}}$ increase strongly with the wire diameter d_{w}. In contrast the dc-copper losses $P_{\mathrm{l,cu,dc}}$ (sum of $P_{\mathrm{l,cu,dc,Ew}}$ and $P_{\mathrm{l,cu,dc,woEw}}$) decrease with an increased wire diameter d_{w}, as the dc phase resistance $R_{\mathrm{dc,ph}}$ decreases (2.20). Up to a wire diameter $d_{\mathrm{w}} = 1.7\,\mathrm{mm}$ the increase in eddy-current copper losses $P_{\mathrm{l,cu,eddy}}$ is compensated by the decrease in dc copper losses $P_{\mathrm{l,cu,dc}}$.

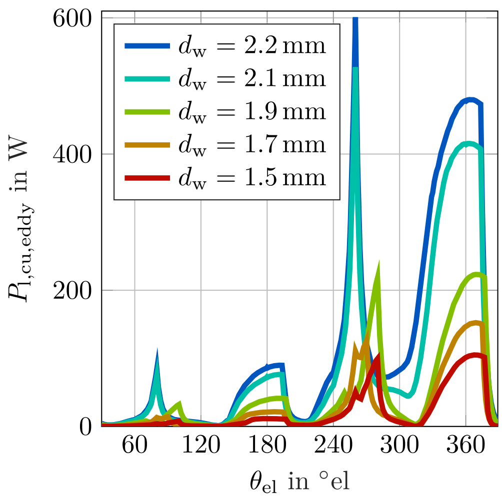

(a) $P_{l,cu,eddy}$ over electrical angle θ_{el}

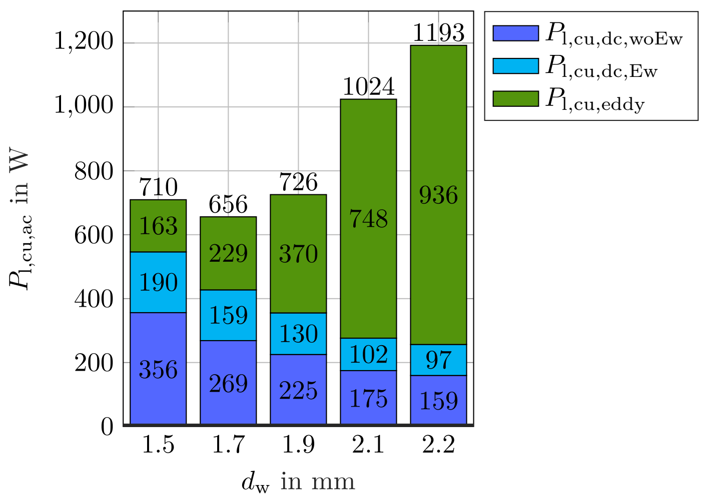

(b) $P_{l,cu,ac}$ separated in individual losses

Fig. 4.2: Calculated total copper losses $P_{l,cu,ac}$ for variation of wire diameter d_w and $N_{w,pl} = 45$. Permutation HS2ph2p45N1 - HS2ph2p45N4 (see table A.3) of HS2ph2p45N (see table A.2) at operation point NOP_S (see table A.10).

Above a wire diameter $d_w = 1.7\,\mathrm{mm}$ the total copper losses $P_{l,cu,ac}$ increase strongly. The HS2ph2p45N4 machine with $d_w = 2.2\,\mathrm{mm}$ has the lowest dc-copper losses $P_{l,cu,dc}$, however, exhibits total copper losses $P_{l,cu,ac}$ increased by 182 % compared to $d_w = 1.7\,\mathrm{mm}$. Therefore, it can be concluded that it is not beneficial in terms of machine efficiency η_{mach} to use the largest possible wire diameter d_w in SRG of input power $P_{l,m} = 20\,\mathrm{kW}$ range at electric base frequency $f_{el} = 1.6\,\mathrm{kHz}$. For the HS2ph2p45N machine a wire diameter $d_w = 1.7\,\mathrm{mm}$ was chosen.

Table 4.2 lists the eddy-loss ratio $p_{eddy,woEw}$ and ac phase resistance $R_{ac,ph}$ for permutations of the HS2ph2p45N and HS3ph1p49N machine (see table A.2) at constant number of turns per pole $N_{w,pl}$. The prototype configuration HS3ph1p49N with a wire diameter

	d_w	d_{gsp}	$b_{pl,s}$	$p_{eddy,woEw}$	$R_{ac,ph}$
HS2ph2p45N1	1.5 mm	6.7 mm	13.2 mm	0.46	57 mΩ
HS2ph2p45N	1.7 mm	5.1 mm		0.85	55.4 mΩ
HS2ph2p45N2	1.9 mm	3.5 mm		1.6	58.5 mΩ
HS2ph2p45N4	2.2 mm	0.0 mm		5.9	82.5 mΩ
HS3ph1p49N1	1.85 mm	5.1 mm	15.1 mm	0.81	102 mΩ
HS3ph1p49N	2.0 mm	4.0 mm		1.1	99 mΩ
LS2ph3p60N	1.7 mm	4.4 mm	16 mm	0.4	33.8 mΩ

Table 4.2: Influence of copper wire diameter d_w and gap spacer d_{gsp} on eddy-loss ratio $p_{eddy,woEw}$ (2.27) and ac phase resistance $R_{ac,ph}$ (2.22) at constant number of turns per pole $N_{w,pl}$. Machine configurations from table A.2 and A.3 at operation point NOP_S (see table A.10).

$d_w = 2$ mm has the maximal copper area A_{cu} for preformed coils (see fig. 3.10a) for this 3-phase machine configuration. The HS3ph1p49N1 machine has a comparable gap spacer d_{gsp} as the HS2ph2p45N machine. This comparison is important, as such a winding design arises from a fixed value of d_{gsp} in the pre-design stage as done in section 3.4.2.

The simulation results listed in table 4.2 lead to several conclusions. Firstly, a fixed gap spacer d_{gsp} (see fig. 3.10) leads to comparable values for the eddy-loss ratio $p_{eddy,woEw}$ for the HS2ph2p45N and the HS3ph1p49N machine at constant electric base frequency f_{el}. Therefore, it is valid to fix k_{cu} in (3.9) in the pre-design to obtain a fair comparison of different machine configurations at constant electric base frequency f_{el}. Secondly, the gap spacer d_{gsp} and wire diameter d_w of minimal ac phase resistance $R_{ac,ph}$, and consequently total copper losses $P_{l,cu,ac}$ (see (2.22)) are not constant for different machines. Therefore, a further optimization for each design with the help of coupled FEA is advised. For the machines considered in this thesis, minimal ac phase resistances $R_{ac,ph}$ were found in the range of $d_{gsp} = 25 - 40\,\%$ of the stator pole width $b_{pl,s}$, which can be taken as a general starting point for further investigations.

Beside the wire diameter d_w, the explicit placing of the wires in the slot influences the eddy-current copper losses $P_{l,cu,eddy}$, as the amount of flux Φ_{pl} passing through the individual wires changes (see [Car08; Sch15]). Fig. 4.3 depicts the total copper losses $P_{l,cu,ac}$ for three different number of turns per pole $N_{w,pl}$ and two different wire arrangements each. Each wire arrangement is defined by a certain number of wire columns and individual wires in each column. As exemplary shown in fig. 4.3, the HS2ph2p27N has four columns with up to seven wires per column, while the HS2ph2p27N1 has five columns with up to six wires per column. This increases the gap spacer d_{gsp} by about 150 % from 2.3 mm to 5.8 mm. At the same time, the end-windings of the machine and the total machine length L_{act} are increased by about 4 mm or 4 %. The rearrangement reduces the eddy-current copper losses $P_{l,cu,eddy}$ by 35 %, while the end-winding dc copper losses $P_{l,cu,dc,Ew}$ are increased by 9 %. Fig. 4.3, emphasizes the importance that a reasonable d_{gsp} is chosen. While for the HS2ph2p45N machine the total copper losses $P_{l,cu,ac}$ do not change significantly, for the HS2ph2p27N and

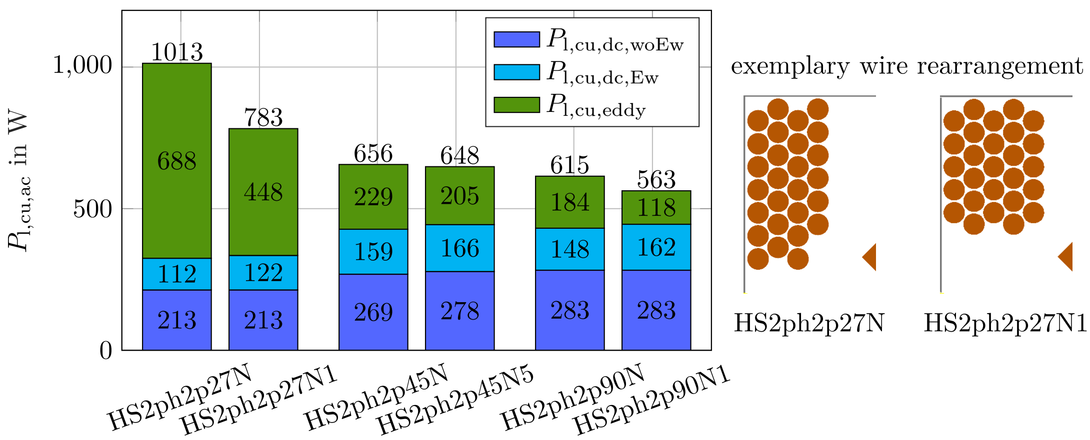

Fig. 4.3: Influence of an alternative wire arrangement on total copper losses $P_{l,cu,ac}$ for three different number of turns per pole $N_{w,pl}$. Machine configurations listed in table A.2 and A.3 at operation point NOP_S (see table A.10).

HS2ph2p90N a reduction of total copper losses $P_{\mathrm{l,cu,ac}}$ by 23 % and 9 % is possible.

The previous discussions show the strong influence of the number of turns per pole $N_{\mathrm{w,pl}}$, the wire diameter d_{w} and the wire placement on the total copper losses $P_{\mathrm{l,cu,ac}}$ and, consequently, machine efficiency η_{mach}. As shown by (2.9) - (2.13) the chosen number of turns per pole $N_{\mathrm{w,pl}}$ influences the resulting phase voltage u_{ph}. For an energy efficient SPC the phase voltage u_{ph} has to be matched to the available dc-link voltage u_{dc} by an appropriate choice of number of turns $N_{\mathrm{w,pl}}$. Therefore, the available dc-link voltage u_{dc} influences the total copper losses $P_{\mathrm{l,cu,ac}}$. This is investigated with the help of permutations of the HS2ph2p45N machine (see table A.2) for various combinations of dc-link voltage u_{dc} and number of turns $N_{\mathrm{w,pl}}$. From the HS2ph2p45N machine with $u_{\mathrm{dc}} = 400\,\mathrm{V}$ and number of turns $N_{\mathrm{w,pl}} = 45$, the dc-link voltage u_{dc} of the HS2ph2p18N and HS2ph2p90N1 machines (see table A.3) is calculated by (4.4) to 160 V and 800 V, respectively. As the available copper cross section A_{cu} is constant for all machines, the wire diameter d_{w} is inversely proportional to $N_{\mathrm{w,pl}}$ as described in (4.3). Operating the HS2ph2p45N machine with constant number of turns per pole $N_{\mathrm{w,pl}} = 45$ at an increased dc-link voltage $u_{\mathrm{dc}} = 800\,\mathrm{V}$ is depicted for reference in fig. 4.4a. This combination of $N_{\mathrm{w,pl}}$ and u_{dc} results in a HCC phase current i_{ph} as depicted in fig. 4.4b.

$$u_{\mathrm{dc},2} = u_{\mathrm{dc},1} \cdot \frac{N_{\mathrm{w,pl},2}}{N_{\mathrm{w,pl},1}} \tag{4.4}$$

Fig. 4.4a depicts the total copper losses $P_{\mathrm{l,cu,ac}}$ for the HS2ph2p45N, HS2ph2p18N and HS2ph2p90N1 machines. The total copper losses $P_{\mathrm{l,cu,ac}}$ decrease with an increase in dc-link voltage u_{dc}. This is caused by the decrease in eddy-current copper losses $P_{\mathrm{l,cu,eddy}}$, due to the decrease in wire diameter d_{w} (see fig. 4.2b). Increasing the dc-link voltage u_{dc} by 250 % from 160 V to 400 V, the eddy-current copper losses $P_{\mathrm{l,cu,eddy}}$ are reduced by 268 W or 54 %. The ideal reduction of 60 % is not reached, as the wires cannot be placed exactly at the same positions in the slot (see coil design in table A.2 and A.3). A further increase in dc-link voltage u_{dc} by another 200 % decreases the eddy-current copper losses $P_{\mathrm{l,cu,eddy}}$ by 111 W or 48 %. This ratio is close to the ideal 50 %.

The simultaneous change in dc-link voltage u_{dc} and number of turns $N_{\mathrm{w,pl}}$ at constant generator speed n_{SRG} and input power $P_{\mathrm{m,sh}}$ results in the phase currents i_{ph} depicted in fig. 4.4b. The resulting peak phase current $I_{\mathrm{ph,pk}}$ and rms-phase current $I_{\mathrm{ph,rms}}$ are listed in table 4.3 together with the individual parts of the ac phase resistances $R_{\mathrm{ac,ph}}$. $I_{\mathrm{ph,pk}}$ and $I_{\mathrm{ph,rms}}$ are inversely proportional to the dc-link voltage u_{dc} when the number of turns per pole $N_{\mathrm{w,pl}}$ is changed according to (4.4). Again, the ideal reduction in peak phase current $I_{\mathrm{ph,pk}}$ as well as rms-phase current $I_{\mathrm{ph,rms}}$ is not reached. Increasing, for example, the dc-link voltage u_{dc} by 250 % from 160 V to 400 V, $I_{\mathrm{ph,pk}}$ and $I_{\mathrm{ph,rms}}$ are only decreased by 59.5 % and 59 %, respectively. As at the same time the dc phase resistance $R_{\mathrm{dc,ph}}$ is increased by a factor 6.35 instead of the ideal 6.25 ($= 2.50^2$) the dc copper losses $P_{\mathrm{l,cu,dc}}$ are increased by 33 W or 8.4 %. Therefore, the reduction in total copper losses $P_{\mathrm{l,cu,ac}}$ by an increased dc-link voltage u_{dc} is lower than expected from the reduction in eddy-current copper losses $P_{\mathrm{l,cu,eddy}}$.

Fig. 4.4c depicts the eddy-loss ratio $p_{\mathrm{eddy,woEw}}$ (see (2.27)) calculated from the losses in fig. 4.4a for the permutations of the HS2ph2p45N machine over the inverse dc-link voltage

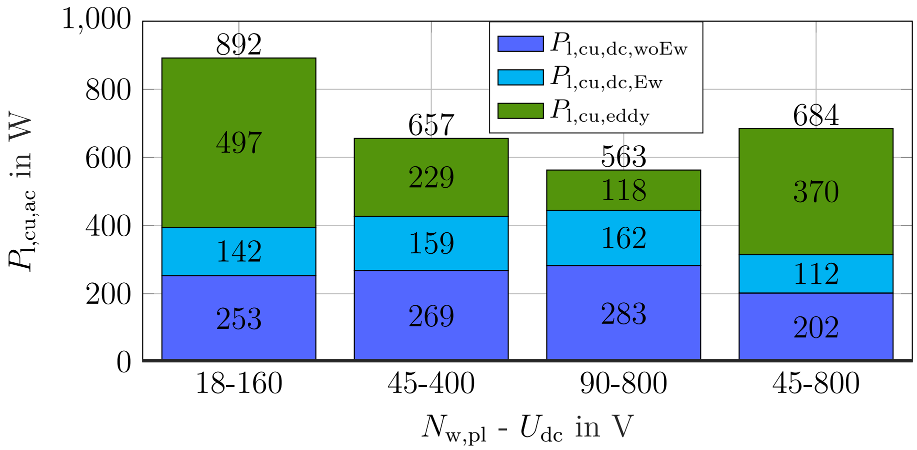

(a) total machine losses $P_{\mathrm{l,cu,ac}}$

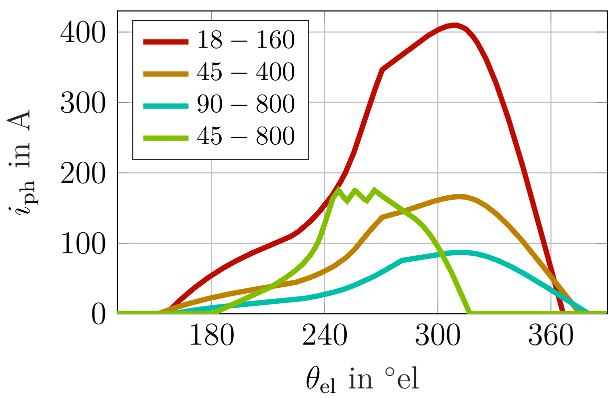

(b) phase current i_{ph}

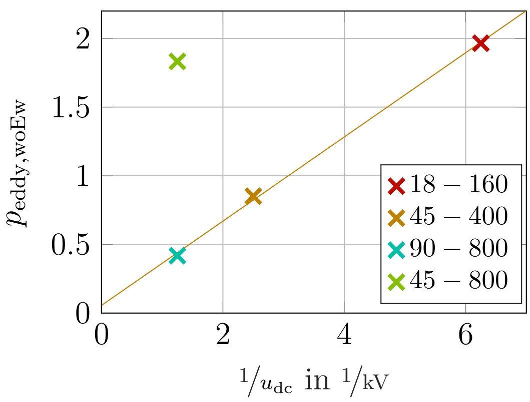

(c) eddy-loss ratio $p_{\mathrm{eddy,woEw}}$

Fig. 4.4: Calculated total copper losses $P_{\mathrm{l,cu,ac}}$, phase current i_{ph} and eddy-loss ratio $p_{\mathrm{eddy,woEw}}$ for various combinations of number of turns per pole $N_{\mathrm{w,pl}}$ and dc-link voltage u_{dc}. Permutations of HS2ph2p45N (see table A.2 and A.3) at operation point NOP_{S} (see table A.10).

$1/u_{\mathrm{dc}}$. The results of the three machines HS2ph2p18N, HS2ph2p45N and HS2ph2p90N1, for which the dc-link voltage u_{dc} was simultaneously increased with the number of turns $N_{\mathrm{w,pl}}$, can be described by (4.5), despite the previously discussed deviations from the ideal behavior. This linear interpolation of eddy-loss ratio $p_{\mathrm{eddy,woEw}}$ over $1/u_{\mathrm{dc}}$ is important for the pre-design approach discussed in chapter 3. By such a relation, the dc-link voltage u_{dc} dependence of the copper loss correction factor k_{cu} introduced in (3.9) can be described. However, for a generalization further investigations with different machines are required. In addition, the reduction potential in machines with a lower electric base frequency f_{el} is reduced, due to the inherently lower $p_{\mathrm{eddy,woEw}}$ (compare HS2ph2p45N with LS2ph3p60N machine in table 4.2).

$$p_{\mathrm{eddy,woEw}}(u_{\mathrm{dc}}) = 0.056 + \frac{0.307\,\mathrm{kV}}{u_{\mathrm{dc}}} \tag{4.5}$$

machine	$N_{\mathrm{w,pl}}$ - u_{dc}	$I_{\mathrm{ph,pk}}$	$I_{\mathrm{ph,rms}}$	$R_{\mathrm{dc,ph}}$	$R_{\mathrm{eddy,ph}}$	$R_{\mathrm{ac,ph}}$
HS2ph2p18N	18 - 160	409 A	188 A	5.6 mΩ	7.0 mΩ	12.6 mΩ
HS2ph2p45N	45 - 400	166 A	77 A	36.1 mΩ	19.3 mΩ	55.4 mΩ
HS2ph2p90N1	90 - 800	87 A	40 A	139.1 mΩ	36.9 mΩ	175.9 mΩ
HS2ph2p45N	45 - 800	175 A	66 A	36.1 mΩ	42.5 mΩ	78.5 mΩ

Table 4.3: Calculated peak phase current $I_{\mathrm{ph,pk}}$, rms phase current $I_{\mathrm{ph,rms}}$ and resulting phase resistances for permutations of HS2ph2p45N (see table A.2 and A.3) at operation point NOP_{S} (see table A.10) depicted in fig. 4.4.

The linear relation between dc-link voltage u_{dc} and eddy-current copper losses $P_{\mathrm{l,cu,eddy}}$ as well as eddy-loss ratio $p_{\mathrm{eddy,woEw}}$ is only valid if the control scheme, in this case SPC, is kept constant. At a constant number of turns $N_{\mathrm{w,pl}}$ and increased dc-link voltage u_{dc} from 400 V to 800 V, the machine operation changes to HCC ($45 - 400$ to $45 - 800$ in fig. 4.4b). This change in control is caused by the constant phase voltage u_{ph} (see (2.9)). The higher current gradients (see fig. 4.4b) at constant wire diameter d_{w} compared to the operation with SPC at $u_{\mathrm{dc}} = 400\,\mathrm{V}$ cause an increase in eddy-current copper losses $P_{\mathrm{l,cu,eddy}}$ by 141 W or 62 %. This increase is not compensated by the decrease in dc copper losses $P_{\mathrm{l,cu,dc}}$ caused by the higher torque derating factor (see fig. 3.13b) and consequently lower $I_{\mathrm{ph,rms}}$ (see $45 - 400$ and $45 - 800$ in table 4.3) in HCC. In consequence, the eddy-loss ratio $p_{\mathrm{eddy,woEw}}$ is strongly increased at constant number of turns per pole $N_{\mathrm{w,pl}}$ (see fig. 4.4c)

This section clearly demonstrates that not only the number of turns per pole $N_{\mathrm{w,pl}}$ and the individual wire diameter d_{w} but also the dc-link voltage u_{dc} has to be carefully chosen in an SRG. An increase in dc-link voltage u_{dc} positively influences the machine efficiency η_{mach} in machines with a high electric base frequency f_{el} and consequently eddy-loss ratio $p_{\mathrm{eddy,woEw}}$. Such machines cannot be rewired for lower dc-link voltages u_{dc} without a decrease in machine efficiency η_{mach}. From a system perspective, an active input current filter for the SRG as discussed in [KBD16a] might be necessary. If a dc-dc converter is employed, an increase in dc-link voltage u_{dc} should be considered. In that case, the additional filter losses might be compensated by the reduction of eddy-current copper losses $P_{\mathrm{l,cu,eddy}}$, as shown in fig. 4.4a.

Temperature Dependency of Copper Losses

Equation (4.2) shows the direct influence of the coil temperature $\vartheta_{\mathrm{coil}}$ on the total copper losses $P_{\mathrm{l,cu,ac}}$. The dc copper losses $P_{\mathrm{l,cu,dc}}$ increase linear with the increasing dc copper resistance $R_{\mathrm{dc,ph}}$ (see (2.20)) if the coil temperature $\vartheta_{\mathrm{coil}}$ increases. However, it is expected that the eddy-current copper losses $P_{\mathrm{l,cu,eddy}}$ decrease as an increased dc copper resistance $R_{\mathrm{dc,ph}}$ reduces the induction of eddy currents.

Fig. 4.5 shows simulated total copper losses $P_{\mathrm{l,cu,ac}}$ of the HS2ph2p45N machine (see table A.2) at variable coil temperature $\vartheta_{\mathrm{coil}}$. An increase of coil temperature by 50 °C from 120 °C to 170 °C increases the dc copper losses $P_{\mathrm{l,cu,dc}}$ by 62 W or 16 %, while the eddy-current copper losses $P_{\mathrm{l,cu,eddy}}$ decrease by 32 W or 11 %. For larger temperature ranges, in [Sch15] a non-linear temperature dependency of the total copper losses $P_{\mathrm{l,cu,ac}}$ is described.

However, in the investigated small temperature range of the HS2ph2p45N machine the resistances $R_{\mathrm{eddy,ph}}$ and $R_{\mathrm{dc,ph}}$ are linearly depending on the coil temperature $\vartheta_{\mathrm{coil}}$. In the HS2ph2p45N machine, the resulting temperature dependence of the ac copper resistance is reduced by approximately 50 %, due to the large share of eddy-current phase resistance $R_{\mathrm{eddy,ph}}$ in the ac phase resistance $R_{\mathrm{ac,ph}}$.

The exact temperature dependence of a certain machine changes with the share of eddy-current phase resistance $R_{\mathrm{eddy,ph}}$ in the ac phase resistance $R_{\mathrm{ac,ph}}$. Also, in reality the temperature distribution in the coil is not uniform. Thus, an exact prediction of the behavior prior to tests on a test bench is only possible with a rather fine FEA simulation, which couples copper losses $P_{\mathrm{l,cu,ac}}$ with a space resolved temperature distribution in the coils. From the investigation on the temperature behavior in the HS2ph2p45N machine and the total copper losses $P_{\mathrm{l,cu,ac}}$ in table 4.2 it is, however, sensible to assume a lower temperature dependence of total copper losses $P_{\mathrm{l,cu,ac}}$ in both high-speed machines (HS3ph1p49N and HS2ph2p45N) compared to the low-speed machine LS2ph3p60N. In the HS2ph2p45N and HS3ph1p49N machine the increased dc copper losses $P_{\mathrm{l,cu,dc}}$ are stronger compensated by lower eddy-current copper losses $P_{\mathrm{l,cu,eddy}}$ than in the LS2ph3p60N machine with a low overall eddy-loss ratio $p_{\mathrm{eddy,woEw}}$.

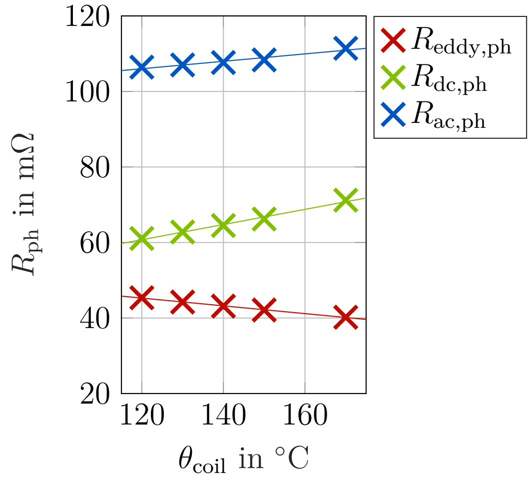

(a) phase resistances R_{ph}

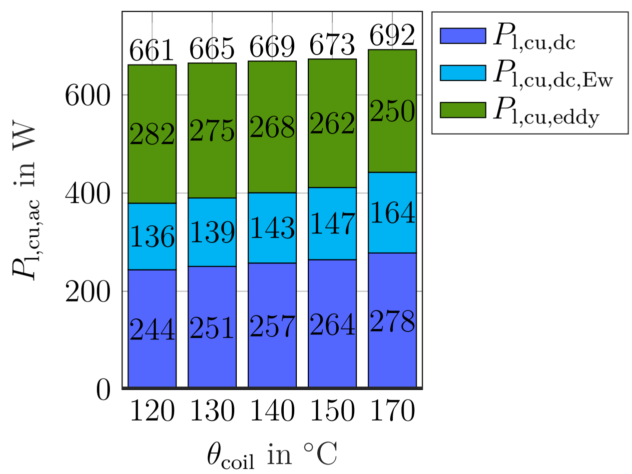

(b) total copper losses $P_{\mathrm{l,cu,ac}}$

Fig. 4.5: Phases resistances R_{ph} with interpolation curves and total copper losses $P_{\mathrm{l,cu,ac}}$ for variation of coil temperature $\vartheta_{\mathrm{coil}}$. HS2ph2p45N (see table A.2) at operation point NOP_{S} (see table A.10).

Analytical Prediction of Eddy-Current Copper Losses

A large number of coupled FEA was performed in this thesis, to analyze the effect of winding design on the prototype SRGs. This offers the potential, to assess the quality of analytical prediction methods described by (2.24) in section 2.2.1.

Fig. 4.6a depicts the eddy-loss ratio $p_{\mathrm{eddy,woEw}}$ for the variation of number of turns $N_{\mathrm{w,pl}}$ in the HS2ph2p45N machine (see table A.2 and A.3). The analytic approach described by (2.24) [Dow66] models the tendencies similar to the coupled FEA. However, the analytical

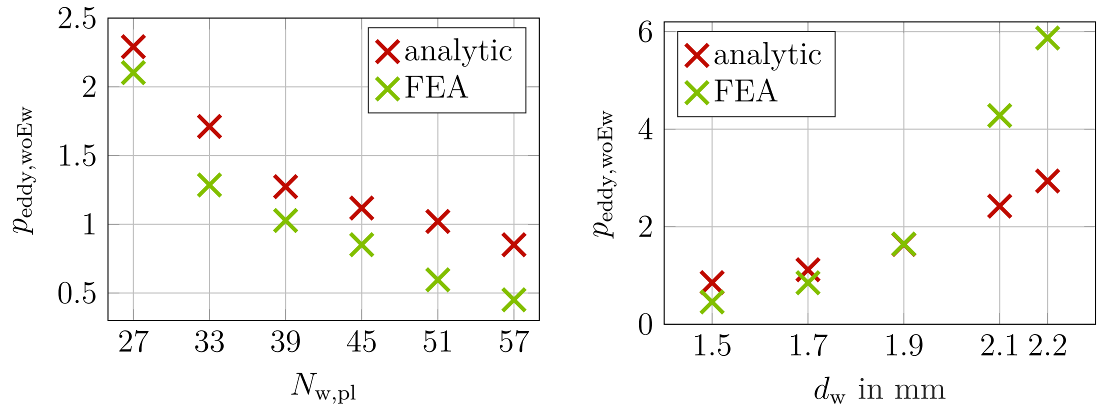

(a) variation of number of turns per pole $N_{\text{w,pl}}$ at wire diameter $d_{\text{w}} = 1.7\,\text{mm}$

(b) variation of wire diameter d_{w} at number of turns per pole $N_{\text{w,pl}} = 45$

Fig. 4.6: Comparison of analytical (see (2.24)) predicted eddy-loss ratio $p_{\text{eddy,woEw}}$ with coupled FEA results. Permutations of HS2ph2p45N (see table A.2 and A.3) at operation point NOP_{S} (see table A.10).

approach obtains an eddy-loss ratio $p_{\text{eddy,woEw}}$ increased by 9.5 % at $N_{\text{w,pl}} = 27$ and 88.9 % at $N_{\text{w,pl}} = 57$ compared to the coupled FEA. This is in contrast with known literature (e.g. [Car08; Sch15]), which expects an underestimation by the analytical approach due to the main pole flux Φ_{pl} passing through the wires.

Fig. 4.6b depicts the obtained eddy-loss ratio $p_{\text{eddy,woEw}}$ for a variation of wire diameter d_{w} in the HS2ph2p45N machine (see table A.2 and A.3). At wire diameters $d_{\text{w}} < 1.9\,\text{mm}$ and resulting large gap spacer d_{gsp}, the eddy-loss ratio $p_{\text{eddy,woEw}}$ is overestimated by up to 90 % at $d_{\text{w}} = 1.5\,\text{mm}$. At wire diameters $d_{\text{w}} > 1.9\,\text{mm}$ and resulting small gap spacers d_{gsp} the eddy-loss ratio $p_{\text{eddy,woEw}}$ is underestimated by up to 50 % at $d_{\text{w}} = 2.2\,\text{mm}$ for the analyzed HS2ph2p45N machine. This leads to the following assumptions. Compared to the coupled FEA, the self-induced proximity and skin effect, due to multiple wire layers in each coil and electric base frequency f_{el}, is overestimated. This effect predominates at large gap spacer d_{gsp}. The effect of the pole flux Φ_{pl} passing through the wires cannot be modeled at all by the analytical approach. This effect predominates at small gap spacer d_{gsp}.

Further analysis of analytical prediction methods will be discussed for different electric base frequencies f_{el} and machine configurations in section 5.1.1.

Further Reduction Potential

Beside the variations discussed for solid conductors, the losses can also be reduced by the use of stranded coils [Car08] or litz wires [RJ10]. Some investigations propose uninsulated, stranded wire as low-cost alternative to litz wire [TS03; TS04]. However, all these measures decrease the copper fill factor f_{cu} and increase the production costs. Especially in the case of stranded wires, the placement and twisting of the individual strands have to be considered very carefully. Otherwise, circulating currents between the individual strands might occur due to the strong gradients of the magnetic field in the stator slot [Car08].

In [Car08] one traction machine design was built and measured with three different coil designs. Employing coils with 13 parallel and twisted strands, the eddy-current copper losses $P_{\mathrm{l,cu,eddy}}$ were reduced by around 80 %, compared to solid conductors with an eight times larger copper cross section of the individual wires. For profiled and compacted litz wire, the expected copper fill factor f_{cu} from the wire arrangement (comp. section 3.3.1) has to be reduced to 75 − 80 % of a single wire technology. In case of the HS2ph2p45N machine, $d_{\mathrm{w}} = 1.9\,\mathrm{mm}$ is the maximum wire diameter for preformed coils. Reducing the copper fill factor f_{cu} to 80 % leads to an equivalent dc-resistance of a single wire with a wire diameter $d_{\mathrm{w}} = 1.7\,\mathrm{mm}$. Assuming a reduction of eddy-current copper losses $P_{\mathrm{l,cu,eddy}}$ by 75 %, the total copper losses $P_{\mathrm{l,cu,ac}}$ could be reduced to 485 W or by 26 % compared to the HS2ph2p45N prototype. This value stands in contrast to the additional production cost and the reduced thermal conductivity in the slot.

4.1.2 Iron Core Material and Losses

In this section, the influence of the iron core material and the calculation methods introduced in section 2.2.1 on the iron losses $P_{\mathrm{l,fe}}$ are analyzed. For the prototype machines, two different types of iron core material are used. The LS2ph3p60N machine was built with NO30, while both high-speed machines HS2ph2p45N and HS3ph1p49N were built with NO20. The iron core losses $P_{\mathrm{l,fe}}$ are mainly reduced by the different steel sheet thickness $d_{\mathrm{sh,fe}}$ of 300 μm (NO30) and 200 μm (NO20), respectively. Additionally, an NO10 material with steel sheet thickness $d_{\mathrm{sh,fe}} = 100\,\mu\mathrm{m}$ is investigated to quantify the loss reduction potential of further improved iron core material.

Fig. 4.7 depicts the datasheet values for dc magnetization curve (fig. 4.7a) and specific core losses p_{fe} (fig. 4.7b) of the employed materials in the relevant frequency range. While the magnetization curve of the investigated materials is nearly identical, the specific core losses are directly proportional to the reduced steel sheet thickness $d_{\mathrm{sh,fe}}$. Especially for the high-speed HS2ph2p45N and HS3ph1p49N machines, with an electric base frequency

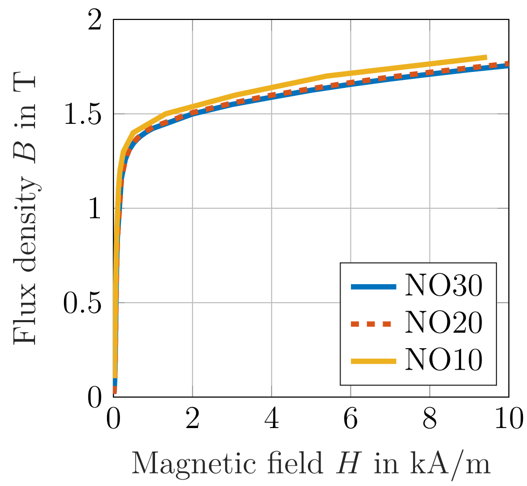

(a) dc magnetization curves

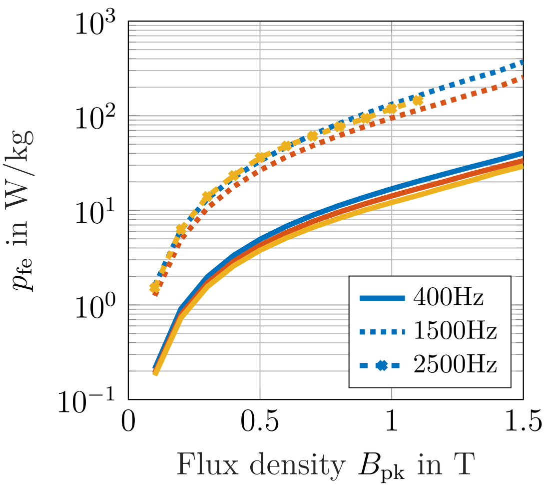

(b) specific core losses p_{fe}

Fig. 4.7: Datasheet values of magnetization curves and iron loss density of NO10 (yellow), NO20 (red) and NO30 (blue) iron core material.

$f_{\mathrm{el}} > 1.5\,\mathrm{kHz}$, a significant advantage of the NO20 material is expected compared to the NO30 material. For NO10 no datasheet values of the specific core losses at 1.5 kHz were available. However, the specific losses of this material at 2.5 kHz are comparable to the data of NO20 and NO30 at 1.5 kHz (see fig. 4.7b). Therefore, this material is especially interesting for the HS2ph2p45N and HS3ph1p49N machines.

The specific core losses p_{fe} are generally obtained by measurements on an Epstein frame at 20 °C ambient temperature. [Kri14] has investigated the effect of an increased core temperature on the iron core losses $P_{\mathrm{l,fe}}$, as it influences the hysteresis loop as well as the sheet resistance and, consequently, the eddy currents in the material. An increase of 75 °C resulted in a decrease of the specific core losses p_{fe} of around 25 % at 1.3 T [Kri14]. At the same time, the increased core temperature decreased the saturation flux density B_{s} of the material. As an SRG is operated in saturation, it can be assumed, that the negative effect of a reduced saturation flux density B_{s} compensates in part the advantage of an increased core temperature. In addition, the temperature distribution in the core is non-uniform. As will be seen in table 4.15 the maximal core temperature in the stator tooth of the HS2ph2p45N machine is about 45 °C higher than the temperature in the stator yoke. As both effects cannot be quantified exactly, the datasheet values are employed for all further investigations.

In table 4.4, the iron core losses $P_{\mathrm{l,fe}}$ of the three prototypes investigated in this thesis are listed, retrieved with the four fitting functions (2.28) - (2.30) and (2.32). Comparing the three approaches with averaged flux densities B_{pt} (p_{SE}, p_{Bertotti} and p_{IEM5}), the following relations are found. For the two high-speed HS2ph2p45N and HS3ph1p49N machines, the p_{Bertotti} losses are slightly higher than the p_{SE} and the p_{IEM5} losses. For the low-speed LS2ph3p60N machine, this relation is inversed. However, for both speeds the deviations between the different models are in the range of only 5 – 10 %.

	p_{SE}	p_{Bertotti}	p_{IEM5}	p_{FLUX}
HS2ph2p45N	376 W	412 W	386 W	480 W
HS3ph1p49N	413 W	439 W	416 W	459 W
LS2ph3p60N	249 W	234 W	243 W	266 W

Table 4.4: Influence of the calculation method on iron core losses $P_{\mathrm{l,fe}}$ for the three prototypes (see table A.2) at operation point NOP_{S} (see table A.10). iron core material: NO20

Calculating the iron losses $P_{\mathrm{l,fe}}$ for each individual mesh element with p_{FLUX} results in highest iron core losses $P_{\mathrm{l,fe}}$ for all three investigated prototypes, which was already found for the HS2ph2p51N machine (see table A.2) in [BMD16]. The increase compared to the models with averaged flux density B_{pt} (see (2.31)) is for all three prototypes in the range of 5 – 15 %. In [KBD16b] a space resolved approach applies p_{IEM5} separately to the flux density of each mesh element of the HS2ph2p45N machine[(i)]. With the `FE Model` in [KBD16b] the calculated iron core losses $P_{\mathrm{l,fe}}$ are almost 10 % lower compared to the application of p_{IEM5} to averaged flux densities B_{pt}.

[(i)]This approach is referred to as `FE model` in [KBD16b]

The discussion shows that the calculation of iron core losses $P_{\mathrm{l,fe}}$ is sensitive to the calculation method as well as the assumed flux distribution. However, the deviations between the different calculation methods are below 10 %. For the comparison of various control parameters, only the methods with averaged flux density B_{pt} are suitable, as the calculation takes only several seconds, while the required coupled FEA takes 3 – 6 h per operation point.

In table 4.5 the iron core losses $P_{\mathrm{l,fe}}$, calculated with average flux densities B_{pt} and p_{Bertotti} for the three prototype machines at operation point NOP_{M} (see table A.11), are listed for different iron core materials. For the LS2ph3p60N machine, an efficiency benefit of only 0.34 pp can be reached by the use of NO20 material instead of NO30. In the HS2ph2p45N and the HS3ph1p49N machines, approximately 30 % of iron core losses $P_{\mathrm{l,fe}}$ can be eliminated with the NO20 material instead of NO30 (see table A.15). For the HS2ph2p45N and the HS3ph1p49N machines, the particular efficiency benefit is 0.72 pp and 0.89 pp, respectively. Further improving the iron core material to NO10 offers a similar improvement potential. Changing the material from NO30 to NO10, the efficiency of the LS2ph3p60N machine can be improved by 0.61 pp. In the HS2ph2p45N and HS3ph1p49N machines with 1.56 pp and 1.79 pp, respectively, the efficiency benefit is about 2 - 3 times higher than for the LS2ph3p60N machine. While for the LS2ph3p60N machine about 40 % of the iron core losses $P_{\mathrm{l,fe}}$ can be saved with the NO10 material compared to NO30, for the HS2ph2p45N and HS3ph1p49N machines the loss reduction is about 60 % (see table A.15). The resulting efficiency benefit leads to higher material costs but also influences the thermal behavior of the machine. Both aspects will be discussed in section 4.2 and 4.4.

material change	LS2ph3p60N	HS2ph2p45N	HS3ph1p49N
NO30 → NO20	69 W / 0.34 pp	143 W / 0.72 pp	178 W / 0.89 pp
NO20 → NO10	53 W / 0.27 pp	167 W / 0.84 pp	179 W / 0.90 pp
NO30 → NO10	122 W / 0.61 pp	310 W / 1.56 pp	357 W / 1.79 pp

Table 4.5: Calculated reduction of the iron core losses $P_{\mathrm{l,fe}}$ and the efficiency benefit in pp by a change of iron core material for the built prototype machines (see table A.2). $P_{\mathrm{l,fe}}$ calculated with averaged flux densities B_{pt} and p_{Bertotti} at operation point NOP_{S} (see table A.10). Absolute results listed in table A.15.

4.1.3 Mechanical Losses

For comparison of the two speed scenarios, the mechanical losses $P_{\mathrm{l,m}}$, as defined in (2.34), have to be analyzed. To validate the analytical models for the windage losses $P_{\mathrm{l,wind}}$ from [Vra68], different measurements were performed to separate the mechanical losses $P_{\mathrm{l,m}}$ into windage losses $P_{\mathrm{l,wind}}$, bearing losses $P_{\mathrm{l,bear}}$ and gearbox losses $P_{\mathrm{l,gear}}$.

To measure the complete mechanical losses $P_{\mathrm{l,m}}$ the device under test is externally driven by a load machine and the mechanical drag torque T_{m} of the complete system is measured by a torque meter. This `direct measurement` allows the measurement of the mechanical losses $P_{\mathrm{l,m}}$ under stable thermal conditions, as the generator speed n_{SRG} can be kept constant until all mechanical parts reached a constant temperature. At the same time, the `direct measurement` is prone to measurement uncertainties of the torque meter, especially if a torque meter with the nominal torque of the machine is applied. Due to the chosen bearing

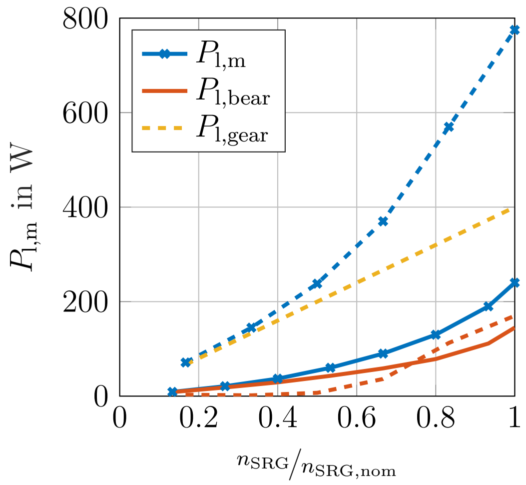

(a) mechanical losses $P_{\mathrm{l,m}}$ (crosses) for LS2ph3p60N machine (solid line) and HS3ph1p49N (dashed line).

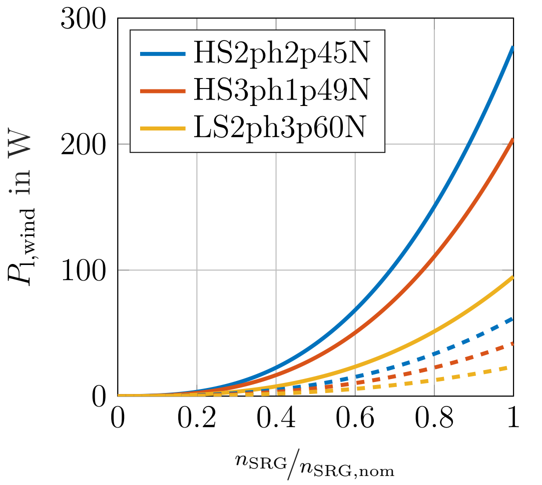

(b) calculated windage losses $P_{\mathrm{l,wind}}$ from [Vra68], salient (solid lines) and non-salient (dashed lines)

Fig. 4.8: Measured mechanical losses $P_{\mathrm{l,m}}$ retrieved for the HS3ph1p49N and LS2ph3p60N machine (see table A.2) by `direct measurement`. $P_{\mathrm{l,bear}}$ is determined with the help of calculated windage losses $P_{\mathrm{l,wind}}$ ((2.35), fig. 4.8b) and estimated $P_{\mathrm{l,gear}}$ (see section 2.2.1).

concept of the high-speed machines (see fig. 2.3b), only the complete $P_{\mathrm{l,m}}$, including the gearbox losses $P_{\mathrm{l,gear}}$, can be determined. As these losses are estimated from literature (see section 2.2.1), the determination of windage losses $P_{\mathrm{l,wind}}$ is difficult by the `direct measurement`.

Fig. 4.8a depicts the results from the `direct measurement` of the HS3ph1p49N and the LS2ph3p60N machine (see table A.2) over the normalized machine speed $n_{\mathrm{SRG}}/n_{\mathrm{SRG,nom}}$. Due to the lower nominal generator speed $n_{\mathrm{SRG,nom}}$ of the LS2ph3p60N machine, the total mechanical losses $P_{\mathrm{l,m}} = 240\,\mathrm{W}$ are by $535\,\mathrm{W}$ or $70\,\%$ lower compared to the $775\,\mathrm{W}$ of the HS3ph1p49N machine at $n_{\mathrm{SRG,nom}}$. At this speed, the gearbox losses $P_{\mathrm{l,gear}}$ account for $400\,\mathrm{W}$ or over $50\,\%$ of the total mechanical losses $P_{\mathrm{l,m}}$ in the HS3ph1p49N machine.

The windage losses $P_{\mathrm{l,wind}}$ determined by (2.35) [Vra68] are depicted for all three prototype machines (see table A.2) in fig. 4.8b for a salient and non-salient air gap. As no gearbox is present in the LS2ph3p60N machine, the bearing losses $P_{\mathrm{l,bear}}$ can be directly calculated by subtracting the calculated windage losses $P_{\mathrm{l,wind}}$ from the measured mechanical losses $P_{\mathrm{l,m}}$. For the HS3ph1p49N machine the additional gearbox losses $P_{\mathrm{l,gear}}$ need to be subtracted from the total mechanical losses $P_{\mathrm{l,m}}$. At $n_{\mathrm{SRG,nom}}$, the bearing losses $P_{\mathrm{l,bear}}$ of the two grease lubricated low-speed bearings in the LS2ph3p60N machine account for $140\,\mathrm{W}$, while the single grease lubricated high-speed bearing in the HS3ph1p49N machine accounts for $168\,\mathrm{W}$. The speed dependence of the bearing losses $P_{\mathrm{l,bear}}$ in the HS3ph1p49N machine also shows that the approximation of gearbox losses $P_{\mathrm{l,gear}}$ is prone to errors, as the losses increase linear from $60 - 100\,\%$ of the nominal generator speed $n_{\mathrm{SRG,nom}}$.

An alternative approach to determine mechanical losses $P_{\mathrm{l,m}}$ is the `indirect measurement`, for which the generator speed $n_{\mathrm{SRG}}(t)$ during a deceleration test is recorded.

Therefore, the rotor is accelerated to maximum speed by an external motor, which is then disconnected. During deceleration, the radial surface acceleration is measured by a piezo-sensor. A Fourier transformation is applied to the signal and the mechanical base frequency f_{m} is detected. From the mechanical base frequency $f_{\mathrm{m}}(t)$ the angular frequency $\omega_{\mathrm{SRG}}(t)$ is derived by (4.6) and a fitting function is applied. From the derivative of the fitted polynomial $\dot{\omega}_{\mathrm{SRG}}(t)$, the mechanical drag torque $T_{\mathrm{m}}(t)$ can be obtained by (4.7). The inertias of the different rotor structures J_{rot} are estimated from computer aided design (CAD) models. To finally obtain $P_{\mathrm{drag}}(\omega_{\mathrm{SRG}})$, the time t is substituted by the fitted polynomial $\omega_{\mathrm{SRG}}(t)$.

$$\omega_{\mathrm{SRG}}(t) = 2\pi f_{\mathrm{m}}(t) \tag{4.6}$$

$$T_{\mathrm{m}}(t) = J_{\mathrm{rot}} \cdot \dot{\omega}_{\mathrm{SRG}}(t) \tag{4.7}$$

$$P_{\mathrm{l,m}}(t) = 2\pi \cdot T_{\mathrm{m}}(t) \cdot n \tag{4.8}$$

Errors in the `indirect measurement` arise from measurement uncertainties of the determined $\omega_{\mathrm{SRG}}(t)$ and the applied curve fitting. In addition, the thermal conditions in the bearings during deceleration cannot be directly controlled. Finally, the rotor inertia determined from CAD models might deviate from the built up rotor prototypes.

In this thesis, the `indirect measurement` is performed on a mechanical dummy with the housing and stator core cross section of the HS2ph2p45N machine (see table A.2) and different rotor structures, named and depicted in fig. 4.9 together with an exemplary assembled mechanical dummy in fig. 4.9a. It is called a mechanical dummy, as only the mechanical structure needs to be equal to the prototype machine. The employed rotors do not need to be magnetically active, e.g. a full rotor or a bare shaft can be easily constructed out of massive steel. The bearing concept is identical to the low-speed scenario depicted in fig. 2.3a. Both bearings are identical to the employed grease-lubricated grooved ball bearing (B4 in fig. 2.3b) of the high-speed prototypes.

To investigate the effect of closed rotor and stator slots, measurements were performed with the combinations of stators and rotors listed in table 4.6. The non-salient stator is

(a) assembled mech. dummy (I) (II) (III)

Fig. 4.9: Mechanical dummy of HS2ph2p45N machine and utilized bare shaft (I), salient (II) and non-salient (III) rotor to separate mechanical losses $P_{\mathrm{l,m}}$.

variation	rotor structure	stator structure
V0	bare shaft (I)	salient, no windings
V1	salient (II)	non-salient
V2	non-salient (III)	salient, with windings
V3	non-salient (III)	salient, no windings
V4	salient (II)	salient, no windings

Table 4.6: Investigated rotor and stator variations of the mechanical dummy.

manufactured by filling the stator slot with a silicon resin, obtaining a smooth cylinder with an inner radius of the sum of rotor pole tip radius R_1 and air gap length d_g. To determine the mechanical losses $P_{l,m}$, a 4^{th}-order polynomial is applied in case of rotor (II) and (III) (see fig. 4.9), exemplary shown in fig. 4.10a. For the bare shaft (I), a quadratic fitting function achieved the best results. In fig. 4.10a, it can be seen that the fitting at low-speeds gets erroneous, due to the relatively low frequency resolution. Therefore, the loss results at speeds below 25 % of the nominal speed $n_{SRG,nom}$ have to be analyzed with caution.

Several measurements with the bare shaft (I) in configuration V0 (see table 4.6) were performed. Fig. 4.10b shows the resulting mechanical losses $P_{l,m}$ over normalized generator speed ${}^{n_{SRG}}/_{n_{SRG,nom}}$ for several test runs. Between Run 4 and Run 1 the mechanical losses $P_{l,m}$ differ by 76 W or 20 % at nominal speed $n_{SRG,nom}$. All runs were performed with the same bearings, which were new at the first run. As Run 1 shows the highest mechanical losses $P_{l,m}$, the differences are assumed to be partly due to changing grease distribution. In addition, the thermal state of the bearings might have changed between individual runs. As the windage losses $P_{l,wind}$ can be neglected for configuration V0, fig. 4.10b depicts the bearing losses $P_{l,bear}$. For further loss separation purpose, the bearing losses $P_{l,bear}$ are approximated

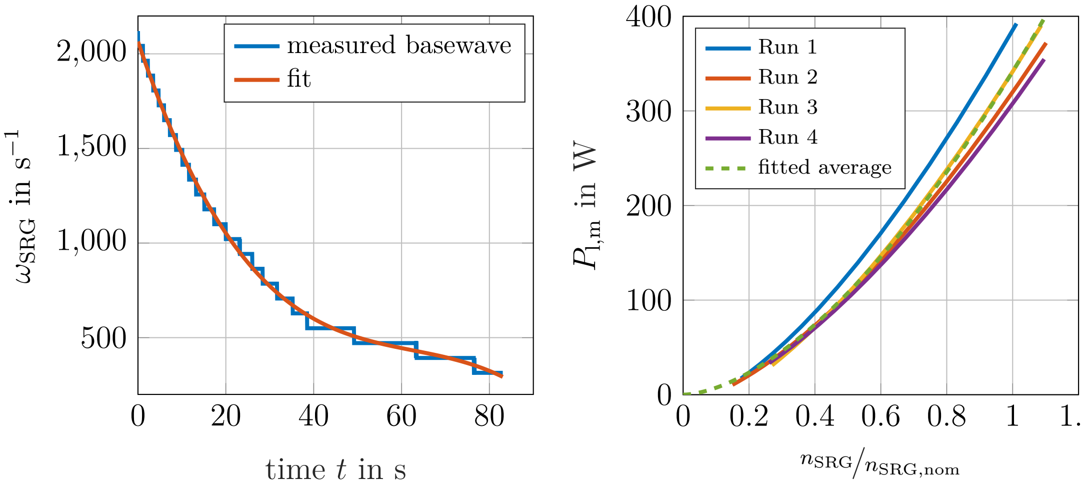

(a) exemplary deceleration run of configuration V3 (see table 4.6)

(b) calculated mechanical losses $P_{l,m}$ (4.8) for configuration V0 (see table 4.6)

Fig. 4.10: Deceleration run with curve-fit of `indirect measurement` and calculated mechanical losses $P_{l,m}$.

with (4.9), which is an average of the performed runs shown in fig. 4.10b. With (4.9) the bearing losses $P_{\mathrm{l,bear}}$ of one high-speed grease lubricated grooved ball bearing are calculated to 174 W at $n_{\mathrm{SRG}} = 25$ krpm. From the separation of the direct measurement (see fig. 4.8a) for the HS3ph1p49N machine the bearing losses $P_{\mathrm{l,bear}}$ were estimated to 170 W for the same bearing.

$$P_{\mathrm{l,bear}} = -1.6299 \cdot 10^{-5} \cdot {n_{\mathrm{SRG}}}^{5/3}; \tag{4.9}$$

Fig. 4.11a depicts the resulting mechanical losses $P_{\mathrm{l,m}}$ from `indirect measurement` for configurations V1-V4 (see table 4.6) as well as the estimated $P_{\mathrm{l,bear}}$ from (4.9). Configuration V4, with salient rotor and stator exhibits the highest mechanical losses $P_{\mathrm{l,m}}$. Closing the rotor or stator slots in V1 - V3 has exactly the same effect on the mechanical losses $P_{\mathrm{l,m}}$. Both measures lead to a reduction of the mechanical losses $P_{\mathrm{l,m}}$ by around 135 W or 25 % at $n_{\mathrm{SRG}} = 23.5$ krpm. Adding the coils to the stator (V2 compared to V3) has no effect on the mechanical losses $P_{\mathrm{l,m}}$.

Comparing the mechanical losses $P_{\mathrm{l,m}}$ of the different configurations in fig. 4.11a with the estimated bearing losses $P_{\mathrm{l,bear}}$ makes the before mentioned measurement errors of the indirect method obvious. At $n_{\mathrm{SRG}} < 0.4 \cdot n_{\mathrm{SRG,nom}}$, the estimated bearing losses $P_{\mathrm{l,bear}}$ are higher than the measured mechanical losses $P_{\mathrm{l,m}}$. This results in calculated windage losses $P_{\mathrm{l,wind}} < 0$ ($P_{\mathrm{l,m}}$ - $P_{\mathrm{l,bear}}$) as shown in fig. 4.11b. It is believed that this behavior arises from the fitting uncertainty shown in fig. 4.10a as well as the changing thermal state of the bearings during the various runs. While the run-down of the bare shaft (V0) take less than 5 s, the run-down of the salient and non-salient rotors (V1-4) takes up to 120 s, due to the

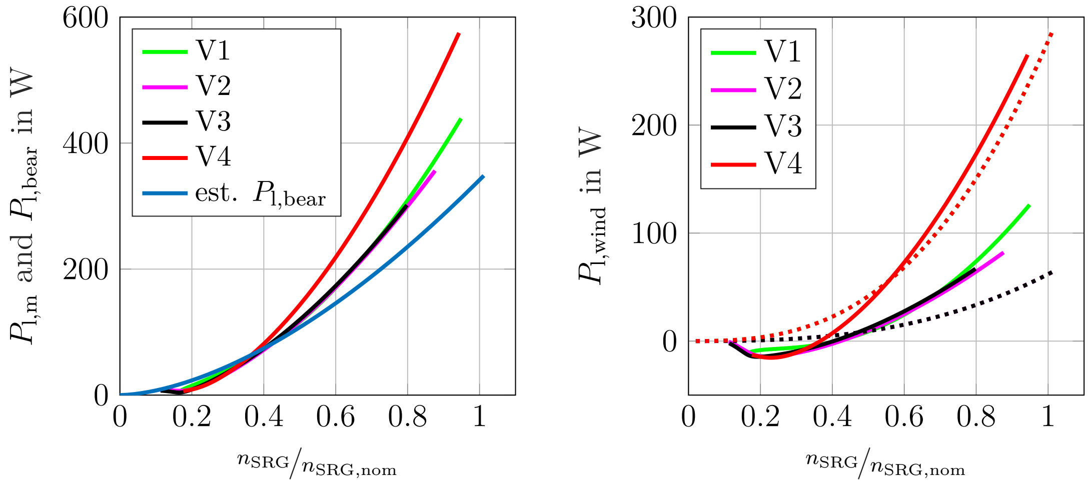

(a) measured mechanical losses $P_{\mathrm{l,m}}$ of `indirect measurement` and estimated $P_{\mathrm{l,bear}}$ (4.9)

(b) calculated windage losses $P_{\mathrm{l,wind}}$ from indirect measurement ($P_{\mathrm{l,m}}$ - $P_{\mathrm{l,bear}}$)

Fig. 4.11: Measured mechanical losses $P_{\mathrm{l,m}}$ and determined windage losses $P_{\mathrm{l,wind}}$ from `indirect measurement`. Configurations defined in table 4.6. Dashed lines in fig. 4.11b indicate the calculated $P_{\mathrm{l,wind}}$ by [Vra68] for salient (red) and non-salient (black) air gap for reference.

larger inertia J_{rot}. During this time the bearings can heat up, reducing the grease viscosity and consequently the bearing losses $P_{\mathrm{l,bear}}$.

To assess the prediction quality of [Vra68], in fig. 4.11b the resulting windage losses $P_{\mathrm{l,wind}}$ estimated with (2.35) for a salient and non-salient rotor structure are depicted, in addition. At high-speeds ($n_{\mathrm{SRG}} > 60\,\%\, n_{\mathrm{SRG,nom}}$) the turbulent windage losses $P_{\mathrm{l,wind}}$ for a salient rotor and stator (V4) are estimated higher than predicted with (2.35) (red dashed line compared to V4). The analytical model promises a reduction of windage losses $P_{\mathrm{l,wind}}$ by nearly 4.5 (black dashed line compared to red dashed line). In reality for all configurations with one non-salient part (V1-3) only a reduction by a factor two is achieved. Adding windings on the stator (V2 compared to V3) offers only an advantage of below 10 W at $n_{\mathrm{SRG,nom}}$, barely noticeable in fig. 4.11b. This difference is assumed to be below the measurement uncertainty of the performed deceleration tests. From the results it can be concluded, that for the employed salient rotor and stator structures of the HS2ph2p45N machine, [Vra68] proves to be a viable analytical prediction for windage losses $P_{\mathrm{l,wind}}$. The reduction potential by a non-salient rotor or stator, however, is overestimated. Based on the results in fig. 4.11 it was found, that only the rotor or only the stator needs to be non-salient. Therefore, keeping the mechanical difficulties and the resulting costs of a non-salient SRG rotor in mind, it can be deduced that closing the stator slots for these kind of high-speed machines is the favorable option.

Table 4.7 lists the mechanical losses $P_{\mathrm{l,m}}$ of the three prototype LS2ph3p60N, HS2ph2p45N and HS3ph1p49N machines (see table A.2) at nominal machine speed $n_{\mathrm{SRG,nom}}$ and a water-jacket inlet temperature $\vartheta_{\mathrm{inlet}} = 25\,°\mathrm{C}$. The gearbox losses $P_{\mathrm{l,gear}}$ and bearing losses $P_{\mathrm{l,bear}}$ for the HS2ph2p45N and HS3ph1p49N machine are calculated with the help of section 2.38 and (4.9), respectively. For the LS2ph3p60N machine the bearing losses $P_{\mathrm{l,bear}}$ are deduced from the measured mechanical losses $P_{\mathrm{l,m}}$ by subtracting the calculated windage losses $P_{\mathrm{l,wind}}$. The salient windage losses $P_{\mathrm{l,wind}}$ are calculated for all machines with (2.35) [Vra68], as the previous investigations suggest a good match of this analytical prediction. The non-

	LS2ph3p60N		HS2ph2p45N		HS3ph1p49N	
	sal.	non-sal.	sal.	non-sal.	sal.	non-sal.
n_{SRG}	7500 rpm		24 705 rpm			
$P_{\mathrm{l,gear}}$	-		400 W			
$P_{\mathrm{l,bear}}$	145 W		171 W			
$P_{\mathrm{l,wind}}$	95 W	48 W	273 W	137 W	204 W	102 W
calculated $P_{\mathrm{l,m}}$	(-)	193 W	844 W	707 W	772 W	673 W
measured $P_{\mathrm{l,m}}$	240 W	(-)	(-)	(-)	775 W	(-)

Table 4.7: Summary of calculated mechanical losses $P_{\mathrm{l,m}}$ at nominal machine speed $n_{\mathrm{SRG,nom}}$ and water-jacket inlet temperature $\vartheta_{\mathrm{inlet}} = 25\,°\mathrm{C}$. Estimated gearbox losses $P_{\mathrm{l,gear}}$ from section 2.38. Calculated bearing losses $P_{\mathrm{l,bear}}$ from (4.9) for HS2ph2p45N and HS3ph1p49N and ($P_{\mathrm{l,m}}$-$P_{\mathrm{l,wind}}$) for LS2ph3p60N. Salient windage losses $P_{\mathrm{l,wind}}$ from [Vra68], non-salient estimated to 50 % salient $P_{\mathrm{l,wind}}$. Measured $P_{\mathrm{l,m}}$ from `direct measurement`.

	HS2ph2p45N	HS2ph2p45NX	
ϑ_{inlet}	25 °C	25 °C	60 °C
$P_{\text{l,m}}$	844 W	738 W	529 W

Table 4.8: Effect of mechanical redesign and water-jacket inlet temperature ϑ_{inlet} on mechanical losses $P_{\text{l,m}}$ of HS2ph2p45N and HS2ph2p45NX machine (see section A.2.1.1) retrieved from `direct measurements`.

salient windage losses $P_{\text{l,wind}}$ are estimated to 50 % of the corresponding salient $P_{\text{l,wind}}$, as the reduction potential by a non-salient rotor or stator is overestimated by [Vra68].

To estimate the temperature influence on the mechanical losses $P_{\text{l,m}}$ a `direct measurement` of the HS2ph2p45NX machine (see section A.2.1.1) at variable water-jacket inlet temperature ϑ_{inlet} between 25 – 60 °C is performed. The housing temperature close to the bearings is directly proportional to ϑ_{inlet} at no-load conditions. Table 4.8 lists the results for two different inlet temperatures ϑ_{inlet}. By increasing the inlet temperature ϑ_{inlet} from 25 °C to 60 °C the losses are reduced by over 200 W or 1 pp at nominal input power $P_{\text{m,sh}} = 20\,\text{kW}$.

With the help of the HS2ph2p45NX machine (see section A.2.1.1), the improvement potential of mechanical redesigns can be identified. At inlet temperature $\vartheta_{\text{inlet}} = 25\,°\text{C}$ the mechanical losses $P_{\text{l,m}}$ of the HS2ph2p45NX are by 110 W lower than the mechanical losses $P_{\text{l,m}}$ determined for the HS2ph2p45N (see table 4.8). The reduction arises mainly from the exchanged sealing. Further loss improvement potential arises from a complete removal of the sealing and the replacement of the grease-lubricated bearings (B4 see fig. 2.3b) by oil-lubricated bearings.

4.1.4 Measurement Validation at Nominal Operation Point

Fig. 4.12 depicts the total machine losses $P_{\text{l,mach}}$ (see (2.15)) of the three built prototypes (see table A.2) for simulation and measurement at nominal operation point NOP_{M} (see table A.11). The simulation results were retrieved with the help of the dynamic simulation model described in section 2.3. For the calculation of the total copper losses $P_{\text{l,cu,ac}}$ an average coil temperature $\vartheta_{\text{coil}} = 170\,°\text{C}$ and the eddy-loss ratios $p_{\text{eddy,woEw}}$ from table 4.2 were assumed. The iron core losses $P_{\text{l,fe}}$ were calculated with the help of p_{Bertotti} and datasheet loss parameters without temperature adaptation. The mechanical losses $P_{\text{l,m}}$ are calculated at 25 °C, including the gearbox with its estimated efficiency of 98 % as discussed in section 4.1.3. As stated in section 2.3.1, the eddy-current copper losses $P_{\text{l,cu,eddy}}$, the iron core losses $P_{\text{l,fe}}$ and the mechanical losses $P_{\text{l,m}}$ are calculated in post-processing. Therefore, setting the same input power $P_{\text{m,sh}}$ in simulation than on the test bench leads to an increased electrical generator power $P_{\text{el,SRG}}$ and, consequently, an overestimation of the dc copper losses $P_{\text{l,cu,dc}}$. As the mentioned frequency dependent losses are larger in the HS2ph2p45N and HS3ph1p49N machine, the mismatch is larger here.

The measurements were performed with a water-jacket inlet temperature ϑ_{inlet} and ambient temperature ϑ_{amb} of 25 °C resulting in hot spot coil temperatures $\vartheta_{\text{coil,hs}}$ in the range of 140 – 155 °C as stated in section A.4.3. The measurements of the high-speed machines

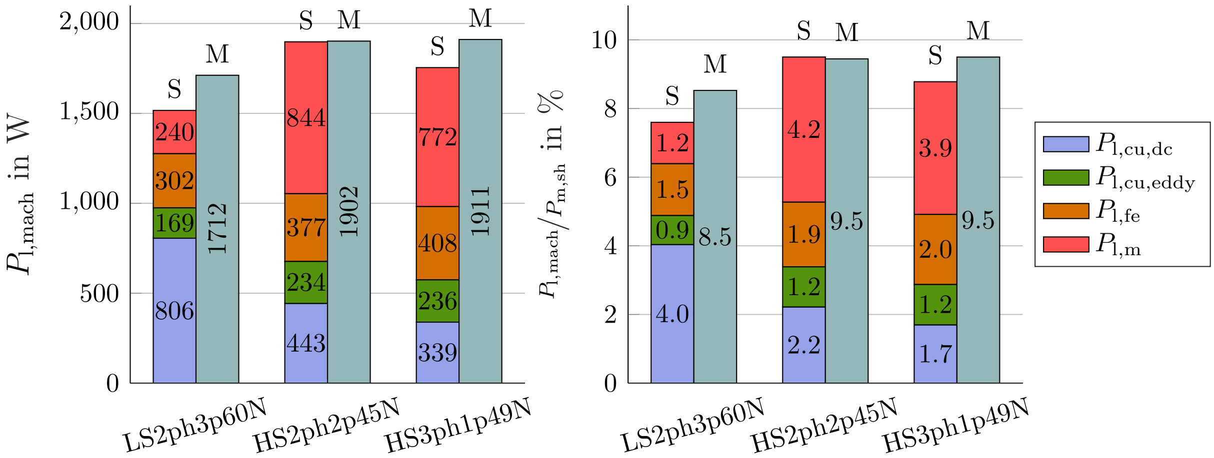

(a) absolute losses

(b) losses relative to $P_{\mathrm{m,sh}}$

Fig. 4.12: Comparison of simulated (S) and measured (M) machine losses $P_{\mathrm{l,m}}$ for the prototypes listed in table A.2. operation point: NOP_{M} (see table A.11)

include the gearbox as it cannot be detached from the SRG. The measurement uncertainty of the test bench is determined in section A.4.1 table A.9 to be up to 2.2 %. Between simulation and measurement there was also a minor input power $P_{\mathrm{m,sh}}$ mismatch, as the control angles can only be set with an accuracy of 0.35 °el on the test bench. This shifts slightly the relative numbers in fig. 4.12b compared to simulation. The exact input power $P_{\mathrm{m,sh}}$ for measurement and simulation is listed in section A.4.3.

Despite the fact that the simulation was performed with an increased coil temperature $\vartheta_{\mathrm{coil}}$ compared to the resulting hot spot coil temperature $\vartheta_{\mathrm{coil,hs}}$, the losses are underestimated compared to measurement in the HS3ph1p49N and LS2ph3p60N machine by 0.7 pp. This deviation is in the range of 10 % of the total machine losses $P_{\mathrm{l,mach}}$. Deviations between coupled FEA and measurements in a similar range were found in [Ral+17] for the HS3ph3p25N machine (see table A.6). Multiple reasons for the deviations are possible. First, the temperature distribution in the coils is non-uniform in measurements, compared to simulations. Second, mutual coupling is completely neglected in the simulations. In [Kle18] the effect of mutual coupling on the HS2ph2p45N machine is investigated with the help of coupled FEA using the phase voltage u_{ph} or the phase current i_{ph} as a model input. Thirdly, eddy-current copper losses $P_{\mathrm{l,cu,eddy}}$ in the end-windings are completely neglected. Finally, the assumption of load independent mechanical losses $P_{\mathrm{l,m}}$ might be erroneous. The exact reasons for the deviations cannot be found with measurements on a complete prototype, but have to be analyzed in further investigations of the individual losses. However, the accuracy based on simulation models without further parametrization of a prototype is in the range of the measurement accuracy on the test bench (see section A.4.1). Therefore, the results can be employed to analyze the individual parts of the machine losses $P_{\mathrm{l,mach}}$ as well as comparing the different machines in terms of reachable machine efficiency η_{mach}.

Taking a closer look at the simulated machine losses $P_{\mathrm{l,mach}}$ in fig. 4.12a, it can be seen that comparing the low-speed LS2ph3p60N machine to the high-speed HS2ph2p45N and HS3ph1p49N machines, losses are shifted from frequency independent dc copper losses

$P_{\mathrm{l,cu,dc}}$ to frequency dependent mechanical losses $P_{\mathrm{l,m}}$, iron core losses $P_{\mathrm{l,fe}}$ and eddy-current copper losses $P_{\mathrm{l,cu,eddy}}$. While dc copper losses $P_{\mathrm{l,cu,dc}}$ are reduced by around 50 %, the mechanical losses $P_{\mathrm{l,m}}$ are increased by over 300 %.

From fig. 4.12b it can be derived that in measurement, all three machines reach a machine efficiency $\eta_{\mathrm{mach}} > 90\,\%$. The LS2ph3p60N machine shows a machine efficiency η_{mach} by 1 pp higher than both high-speed machines HS2ph2p45N and HS3ph1p49N considering the gearbox. Without the gearbox, the HS2ph2p45N and HS3ph1p49N machines have a 1 pp higher machine efficiency η_{mach} than the LS2ph3p60N machine. For evaluation of the mechanical redesign, also a measurement of the HS2ph2p45NX machine was performed. The reached machine efficiency of 91.1 % signifies a machine loss $P_{\mathrm{l,mach}}$ reduction by 120 W. This is in accordance with the found reduction of the mechanical losses $P_{\mathrm{l,m}}$ in table 4.8.

4.1.5 Efficiency Conclusion at Nominal Operation Point

In table 4.9 the reached machine losses and efficiencies are listed and compared to the improved values, if all of the following changes are undertaken for the built designs. As discussed at the end of section 4.1.1 a relative reduction of $P_{\mathrm{l,cu,eddy}}$ of 75 % is assumed by employing adequate litz wire. By changing the iron core material to NO10, the individual loss reduction according to table 4.5 is taken into account for the iron core losses $P_{\mathrm{l,fe}}$. The mechanical losses $P_{\mathrm{l,m}}$ calculated for a non-salient stator are considered as listed in table 4.7. For both high-speed HS3ph1p49N and HS2ph2p45N machines, the mechanical improvements performed in the HS2ph2p45NX machine are assumed. Therefore, the mechanical losses $P_{\mathrm{l,m}}$ listed in table 4.7 are further reduced by 110 W (see table 4.8).

The built prototypes reach a machine efficiency η_{mach} of 90 – 92 %. The LS2ph3p60N prototype shows a higher machine efficiency η_{mach} by 1 – 2 pp compared to the HS2ph2p45N and HS3ph1p49N machines. All machines with the described improvements are in the range of a total machine efficiency η_{mach} of 93 – 94 %. Considering, that simulated machine

	LS2ph3p60N		HS2ph2p45N		HS3ph1p49N	
loss basis	reached P & I1	improved I2	reached P & I1	improved I2	reached P & I1	improved I2
$P_{\mathrm{l,cu,ac}}$	975 W	849 W	677 W	502 W	575 W	398 W
$P_{\mathrm{l,fe}}$	302 W	188 W	377 W	209 W	408 W	232 W
$P_{\mathrm{l,m}}$	240 W	192 W	844 W	598 W	772 W	563 W
$P_{\mathrm{l,mach}}$	1517 W	1229 W	1898 W	1309 W	1755 W	1193 W
η_{mach} sim	92.4 %	93.9 %	90.5 %	93.5 %	91.2 %	94.0 %
η_{mach} meas	91.5 %	(93.0 %)	90.5 %	(93.5 %)	90.5 %	(93.3 %)
loss reduction	1.5 pp/20 %		3 pp/32 %		2.8 pp/32 %	

Table 4.9: Summary of improved and reached machine losses $P_{\mathrm{l,mach}}$ efficiency η_{mach} for all built machines (see table A.2) at operation point NOP_{M} (see table A.11). Basis are the simulated losses from fig. 4.12 and the improvements discussed in the previous sections. Loss basis for power density (see section 4.2.4) and cost (see section 4.4.1) discussion.

efficiency η_{mach} of the HS2ph2p45N machine was matched best with the measurement results all machines reach comparable efficiency with the performed improvements. As all improvements aim at reducing the frequency dependent losses, the improvement effect is only 1.5 pp for the low speed LS2ph3p60N machine, while 3 pp and 2.8 pp are reached in the high-speed HS2ph2p45N and HS3ph1p49N machines, respectively. In total, the losses of the LS2ph3p60N machine can be reduced by 20 %, while in the HS2ph2p45N and HS3ph1p49N machines a reduction of 32 % is possible. Influence of control and operation point on the machine efficiency will be further investigated in chapter 5.

Comparing the reached efficiencies with literature values listed in table 2.4 shows that the achieved values are competitive. In case of the LS2ph3p60N machine, a machine efficiency by 2.7 pp lower than the reference machine from [SL09] is achieved. However, at the operation point of measurement the reference machine has an electric base frequency $f_{\text{el}} = 200\,\text{Hz}$ or 27 % of the LS2ph3p60N machine. This low electric base frequency f_{el} offers the potential to use a larger share of the available slot area $A_{\text{slot,st}}$ for the windings as the resulting eddy-current copper losses $P_{\text{l,cu,eddy}}$ are reduced (see fig. 5.6). The HS2ph2p45N and HS3ph1p49N machines including the gearbox losses $P_{\text{l,gear}}$ reach a reduced machine efficiency η_{mach} by 0.5 pp, compared to the reference machine from [Fer+95]. In this case, however, the improved values from table 4.9 should be considered, as the reference machine employs iron core material of a sheet thickness $d_{\text{sh,fe}} = 150\,\mu\text{m}$ and litz wire in the stator. In addition, a stator slot oil cooling is employed and the stator slots are filled with a thermal conductive resin, to reduce the windage losses $P_{\text{l,wind}}$. Comparing these values, the HS2ph2p45N and HS3ph1p49N machine show an increased machine efficiency η_{mach} including the gearbox by 2.5 pp and 2.3 pp, respectively. Subtracting the remaining gearbox losses of 1.4 pp after the mechanical improvements, the increase is even by 3.9 pp and 3.7 pp, respectively.

4.2 Thermal Behavior and Power Density

Torque density $\phi_{\text{T,tot}}$ and power density $\phi_{\text{P,tot}}$ are limited by material properties (see (3.1)) and thermal boundaries. In this thesis, a 2-D-LPTN of reduced complexity was developed in section 3.3.1 for a fast comparison of a large number of machine designs. In this section, the results of this simplified model with only one heat source and only radial heat flow (see fig. 3.9) are compared to static and dynamic measurements as well as simulations of a more complex MotorCAD-LPTN (see fig. 4.13). To assess the prototypes on the test bench, they were employed with thermo sensors. The measured temperatures are fitted to the MotorCAD-LPTN, which is then employed to study the effects of loss and design variations for the built prototypes. The section ends with a conclusion on the reachable power and torque density.

4.2.1 Static Thermal Validation

Static measurements are performed, to validate the stack length related thermal resistance of half a stator pole $R'_{\text{th,st,hpl}}$ developed in section 3.3.1. A constant phase current i_{ph} is applied to the machine phases wired in series of each machine and the resulting phase voltage u_{ph} is measured. The applied phase current i_{ph} is adjusted to the machine resistances, to generate similar dc copper losses $P_{\mathrm{l,cu,dc}}$ in the range of 470 – 500 W as listed in table 4.10. The temperature rise between coils and water-cooling jacket $\Delta\vartheta_{\mathrm{jacket,coil}}$ can be calculated by (3.4). In this equation, stack length related ac copper losses $P'_{\mathrm{l,coil,hpl}}$ have to be substituted for validation by two different dc copper losses. Firstly, the stack length related dc copper losses of half a stator pole $P'_{\mathrm{l,cu,dc,hpl}}$, which consider the complete dc copper losses $P_{\mathrm{l,cu,dc}}$ including the dc end-winding copper losses $P_{\mathrm{l,cu,dc,Ew}}$ to be dissipated by the stator core. Secondly, the stack length related dc copper losses of half a stator pole without end-windings $P'_{\mathrm{l,cu,dc,woEw,hpl}}$, which consider only the dc copper losses without end-windings $P_{\mathrm{l,cu,dc,woEw}}$ to be dissipated through the stator core. This behavior is assumed by the 2-D-LPTN (see fig. 3.9) introduced for pre-design in section 3.3.1. In table 4.10 measured and predicted temperature rise between coils and water-cooling jacket $\Delta\vartheta_{\mathrm{jacket,coil}}$ are listed for the three prototypes in table A.2. The measured temperature rise between coils and water-cooling jacket $\Delta\vartheta_{\mathrm{jacket,coil}}$ is for all three salient machines higher than the predicted $\Delta\vartheta_{\mathrm{jacket,coil}}$ considering only the stack length related dc copper losses of half a stator pole without end-windings $P'_{\mathrm{l,cu,dc,woEw,hpl}}$. The error is lowest in the HS2ph2p45N machine and highest in LS2ph3p60N machine. As can be seen for the three considered salient machines in table 4.10, the error between prediction and measurement correlates with increasing dc copper losses in the end-windings $P_{\mathrm{l,cu,dc,Ew}}$ in relation to dc copper losses without end-windings $P_{\mathrm{l,cu,dc,woEw}}$. This indicates that the dc copper losses in the end-windings $P_{\mathrm{l,cu,dc,Ew}}$ are partially dissipated by the stator core, hence, leading to an increased $\vartheta_{\mathrm{coil,hs}}$ in reality compared to prediction. Another source of error is the fact that the stack length related thermal resistance of half a stator pole $R'_{\mathrm{th,st,hpl}}$ is calculated based on the average distance of the wires to the stator core rather than for individual wires. In combination, the temperature rise $\Delta\vartheta_{\mathrm{jacket,coil}}$ predicted

stator slots	LS2ph3p60N salient	HS2ph2p45N non-salient	HS2ph2p45N salient	HS3ph1p49N salient
		static measurement		
i_{ph} in A	100	88	88	56
measured u_{ph} in V	4.91	5.37	5.56	8.33
$P_{\mathrm{l,cu,dc}}$ in W	491	472	489	467
$P'_{\mathrm{l,cu,dc,hpl}}$ in W/mm	0.34	0.37	0.38	0.36
$P'_{\mathrm{l,cu,dc,woEw,hpl}}$ in W/mm	0.18	0.23	0.24	0.29
$\vartheta_{\mathrm{inlet}}$ °C		30		
$\vartheta_{\mathrm{coil,hs}}$ in °C	150.2	100.8	126.2	144.7
$\Delta\vartheta_{\mathrm{jacket,coil}}$ in °C	120.2	70.8	96.2	114.7
		predicted $\Delta\vartheta_{\mathrm{jacket,coil}}$		
$R'_{\mathrm{th,st,hpl}}$ in mm·K/W	319	333.0		314.4
$P_{\mathrm{l,cu,dc,Ew}}/P_{\mathrm{l,cu,dc,woEw}}$	0.87	0.6		0.69
$\Delta\vartheta_{\mathrm{jacket,coil}}$ ($P'_{\mathrm{l,cu,dc,hpl}}$) in °C	108.8	122.8	127.3	114.6
$\Delta\vartheta_{\mathrm{jacket,coil}}$ ($P'_{\mathrm{l,cu,dc,woEw,hpl}}$) in °C	58.2	77.2	80.0	90.7

Table 4.10: Predicted and measured temperature rise between coils and water-cooling jacket $\Delta\vartheta_{\mathrm{jacket,coil}}$. Predicted thermal resistances by (3.4) with parametrization of table 3.2 from section 3.3.1.

with the simplified 2-D-LPTN (see fig. 3.9) introduced for pre-design in section 3.3.1 is underestimated for machines with a short stack length compared to the end-winding length. This has to be considered in addition to the eddy-current copper losses $P_{\mathrm{l,cu,eddy}}$ with the help of the copper loss correction factor k_{cu} (3.9) introduced in section 3.3.2.

The non-salient HS2ph2p45N machine has to be investigated separately. In this machine, the thermal contact of the coils to the stator core is improved by a potting. Different materials to improve the thermal contact of the windings to the stator are investigated in [Nat+14]. In the non-salient HS2ph2p45N machine, a silicon resin Elan-tron® SK 6220 with a low thermal conductivity of 0.32 W/(m · K) was employed in the stator slot and around the end-windings. The hot spot coil temperature $\vartheta_{\mathrm{coil,hs}}$ is reduced in this particular machine by 26 °C compared to the salient HS2ph2p45N machine. This is believed to be partially caused by a reduced stack length related thermal resistance of half a stator pole $R'_{\mathrm{th,st,hpl}}$ but especially, by an improved thermal contact of the end-windings to the stator core compared to the salient HS2ph2p45N machine.

4.2.2 MotorCAD Simulation Model

Additionally to the simplified LPTN developed for the SSBPD in section 3.3.1, a MotorCAD-LPTN model with a more complex machine description is employed in this thesis for validation. In the MotorCAD model, all individual machine losses $P_{\mathrm{l,mach}}$ are considered as heat sources in the machine coils, iron core as well as the air gap and machine bearings, respectively. Also the MotorCAD model comprises a representation of the winding overhangs, hence, an axial heat flow in addition to the radial heat flow in the stator core. Purpose of this more complex model is a representation of the windings' hot spot temperatures, so that the machines become thermally comparable. Based on this model, design and loss alterations can be performed to assess the potential of the efficiency improvements discussed in section 4.1.

Model Setup

All three MotorCAD models are setup with geometry information from production 3-D-CAD models (model data listed in table A.2). As the MotorCAD geometry editor is limited, for the geometries depicted in table A.2 the following simplifications had to be made. The straight stator slot is replaced with an arc of stator pole ground radius R_2, the rotor step in case of the LS2ph3p60N and HS2ph2p45N machines is omitted and a constant average air gap length $(d_{\mathrm{g}} + d_{\mathrm{g,step}})/2$ is setup. The water jacket cooling is modeled by a spiral channel in case of the LS2ph3p60N machine and axial channels in case of the HS2ph2p45N and HS3ph1p49N machines. The effective cooling channel surface area is matched with the original surface area from the 3-D-CAD models. A $50/50$ ethylene-glycol water mixture is employed as coolant fluid. For initial validation of the model, the water-jacket inlet temperature $\vartheta_{\mathrm{inlet}}$ is set to 25 °C and the cooling fluid flow rate Q_{flow} is set to 12 l/min, to match the measurements (see fig. 4.15). In [Bra13] it was shown for a high-speed machine that the cooling fluid flow rate Q_{flow} has, above a minimal value, no significant influence on machine temperatures. Remaining material parametrization is done with the help of the MotorCAD material database. The employed parameters are listed in table A.8.

There are several interfaces in an SRG, which influence the heat path from its source to the heat sink, i.e. the housing water jacket. As described in [Bra13] the resulting thermal resistance at two interfaces is usually not negligible, unless two metals are soldered or welded together. Contacts that have a severe influence on the machine's temperatures are, as concluded in [Bra13], winding to stator and stator to housing. Since the contact between windings and stator is implicitly determined in MotorCAD via the impregnation and slot liner parametrization, the influence is investigated further, later on. For the stator to housing interface, MotorCAD only offers a rough matching by three options, for which `good` was chosen.

The injection of power, i.e. losses, is based on the results discussed in section 4.1. The total copper losses $P_{\mathrm{l,cu,ac}}$ are evenly distributed in the coils and the iron core losses $P_{\mathrm{l,fe}}$ are separated by the location of occurrence, i.e. stator poles, stator yoke, rotor poles and rotor yoke (see table A.15). The mechanical losses $P_{\mathrm{l,m}}$ are separated into windage losses $P_{\mathrm{l,wind}}$ in the air gap and bearing losses $P_{\mathrm{l,bear}}$ at the front and rear of the machine.

The employed model is the default MotorCAD-LPTN without any customization in structure, as shown in 4.13. The default LPTN features one slice in axial direction. Setting up the model of the HS3ph1p49N machine with nine slices resulted in a temperature decrease of the hot spot of below 2 %. Therefore, the 1-slice model is used for further investigation as a worst-case prediction.

Finally, it has to be mentioned, that the gearbox is neglected in all simulations. It is assumed, that all gearbox related losses are dissipated by its own water-cooling jacket. The influence of a fixed shaft temperature ϑ_{sh} on the temperatures in the stator core and coils will be discussed by a parameter variation in section 4.2.3. While the temperatures in the gearbox bearings are monitored, a fitting is omitted due to the simplified modeling.

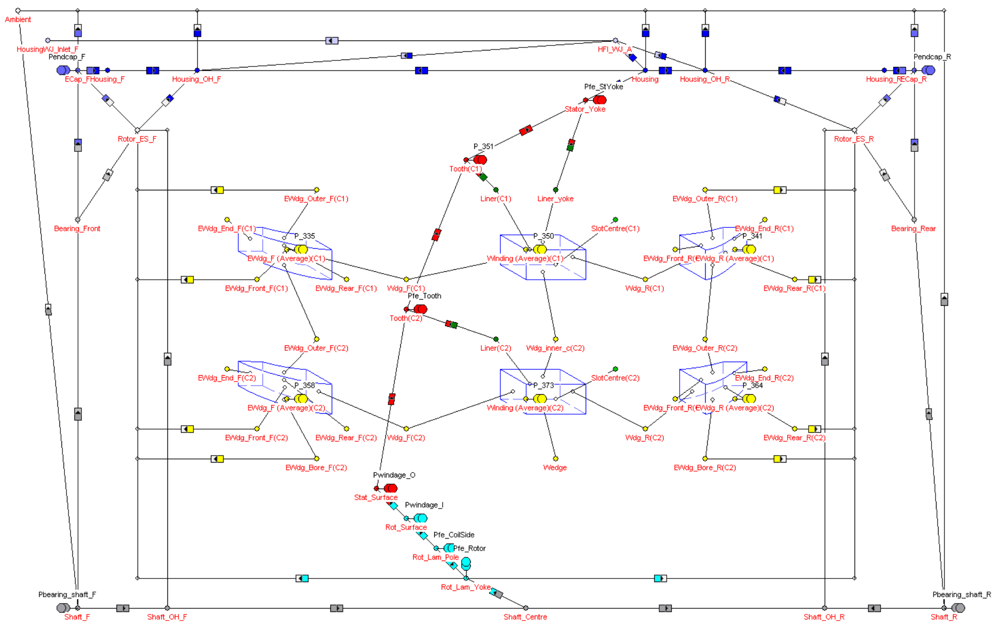

Fig. 4.13: Employed default MotorCAD-LPTN.

Temperature Sensor Assignment

All prototypes are equipped with several thermal sensors as depicted in fig. 4.14, to identify temperature critical positions. To perform loss and model variations in section 4.2.3 and to assess the reachable power density, the available temperature sensors are matched to nodes of the 1-slice MotorCAD-LPTN shown in fig. 4.13. As the available temperature sensors are not exactly in the geometric position of the MotorCAD nodes, a preliminary discussion of the temperature distribution in the machine is required for this matching. Therefore, fig. 4.15 depicts relevant measured temperatures for all three prototypes at the nominal operation point NOP_{M} (see table A.11) with a water-jacket inlet temperature $\vartheta_{\mathrm{inlet}} = 25\,°\mathrm{C}$. At the vertical red line, the electric generator power $P_{\mathrm{el,SRG}}$ is shut down and the SRG is slowed down to standstill, hence, air ventilation ceases.

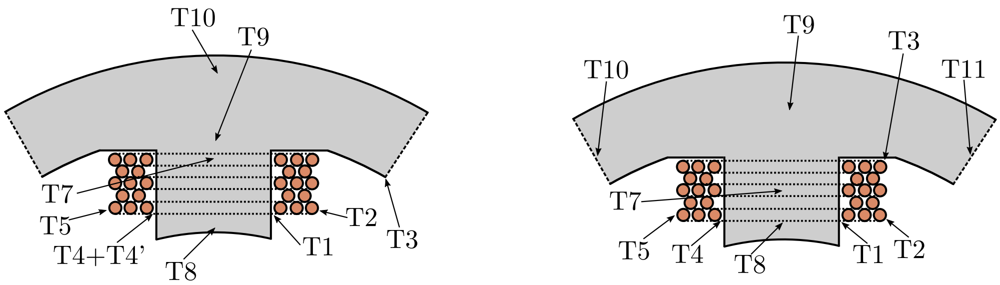

(a) LS2ph3p60N

(b) HS2ph2p45N, HS3ph1p49N

Fig. 4.14: Positioning of temperature sensors for thermal validation. Sensors T1-T5 + T4' axially centered, T7 attached to the end-windings. Remaining sensors attached at one axial end on stator/coils.

The highest temperatures in the prototypes are found in fig. 4.15 at the edge of the coils with the longest distance to the stator core, measured at sensor T2 and T5 (see fig. 4.14) on both sides of a stator tooth. This is in accordance with simulative findings based on thermal FEA with distributed total copper losses $P_{\mathrm{l,cu,ac}}$ performed in [Sch15] for the HS3ph3p25N machine listed in table A.6. In the HS2ph2p45N and LS2ph3p60N machine, a temperature difference is observed between the temperatures measured at sensor T2 and T5 in fig. 4.15a and fig. 4.15b before the generator power $P_{\mathrm{el,SRG}}$ is shut down at the vertical red line and the machines are run down to standstill. The temperature difference can be caused either by unsymmetrical eddy-current copper losses $P_{\mathrm{l,cu,eddy}}$ [Sch15] or even more likely by turbulent airflows that are different on the "ingoing" and "outgoing" side of the stator pole. The measurements support the hypothesis of different airflows on the two sides of the stator pole. This can be seen in fig. 4.15. Shortly after the electrical power $P_{\mathrm{el,SRG}}$ is shut down and the machines have run down to standstill (LS2ph3p60N approximately 50 s after the vertical red line; HS2ph2p45N approximately 100 s after the vertical red line) the temperature measured with sensor T5 rises in both machines to the same value as measured with sensor T2. While in the HS2ph2p45N machine sensor T2 shows no ventilation effect, in the LS2ph3p60N machine the temperature measured at this sensor rises about 3 °C when standstill is reached. In the HS3ph1p49N machine, temperatures measured at sensor T2 and T5 only show a much smaller difference without the characteristic increase in temperature after run down to standstill approximately 150 s after the vertical red line.

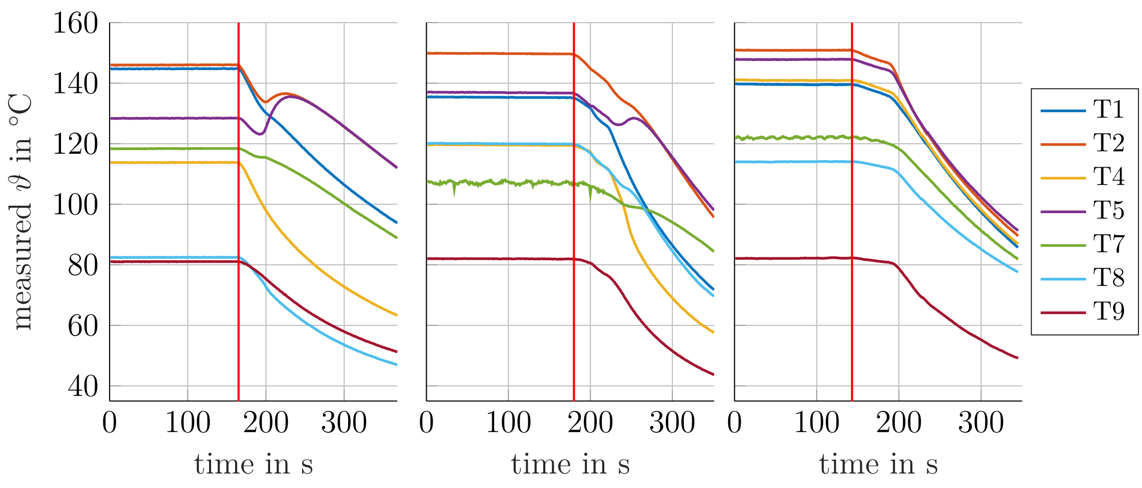

(a) LS2ph3p60N (b) HS2ph2p45N (c) HS3ph1p49N

Fig. 4.15: Measured steady state temperatures (see fig. 4.14) at operation point NOP_{M} (see table A.11). At vertical red line electric generator power $P_{\mathrm{el,SRG}}$ is shut down and the SRGs are slowed down to standstill.

For the HS2ph2p45N and HS3ph1p49N machines, the same sensor assignment is implemented. From the previous discussion, sensor T2, which does not show any ventilation effect in both machines, is assigned to the corresponding MotorCAD hot spot node `Slot Center C2`. Sensor T5 is assigned to the node `Wedge` close to the air gap, expecting a certain error in the HS2ph2p45N machine due to the ventilation offset. Temperature sensor T1 is matched with `Wdg Average C2`, while sensor T4 cannot be adequately matched, since the basic MotorCAD-LPTN does not offer inhomogeneous loss distribution in windings. Therefore, the different temperatures measured at sensor T1 and T4 observed in fig. 4.15b and 4.15c cannot be modeled. T3 is most closely matched by the node `Liner-Yoke`. Temperature sensor T7 is matched to the node `Ewdg Rear R C2`, where EWdg stands for end-winding and R is for rear as defined by MotorCAD. Sensor T8 is mounted on the end-winding facing the stator tooth represented by the node `EWdg Bore R`. Sensor T9 is represented by the node `Endspace R`, although sensor T9 is mounted on the stator core and `Endspace R` is located in the gap between end-windings, housing and stator. With the help of `Endspace R` the temperatures at the stator on one end can be roughly estimated in the simulation model. As `Endspace R` is connected via thermal resistances with bearing, housing, end-windings it will probably show a higher temperature than sensor T9, being directly attached to the stator core. Remaining temperatures sensors T10 and T11 on the stator yoke cannot be matched to suitable MotorCAD nodes.

For the LS2ph3p60N machine, the temperature sensor assignment is slightly differing from the high-speed machines. The assignment of sensor T2 to `Slot Center C2` is not possible, due to the discussed ventilation offset observed in fig. 4.15a. Sensors T1 and T5 are matched similar to the high-speed machines to `Wdg Average C2` and `Wedge`, respectively. Temperature sensor T7 is matched to the the MotorCAD node `EWdg Front F C1` on the end-windings, where F stands for front, due to the sensor placement on the other side compared to the high-speed machines. In the LS2ph3p60N machine, temperature sensor T8 is attached

LS2ph3p60N			HS2ph2p45N, HS3ph1p49N		
Sensor	MotorCAD node	fit	Sensor	MotorCAD node	fit
T1	Wdg Average C2	x	T1	Wdg Average C2	x
T2	Wedge	x	T2	Slot Center C2	x
			T5	Wedge	x
T7	Ewdg Front F C1	x	T7	EWdg Rear R C2	x
T8	Stator Surface		T8	EWdg Bore R	x
T9	EndSpace F		T9	Endspace R	
T4'	Tooth C2		T3	Liner-Yoke	

Table 4.11: Assignment of temperature sensors to MotorCAD nodes for validation and coil temperatures (x) employed for impregnation goodness ζ_{winding} fitting.

on the stator tooth close to the air gap facing the end-windings and matched to node `Stator surface`, which represents in the model the surface of the stator tooth facing the air gap. Sensor T9 is matched to `EndSpace F` for same reasons as in the high-speed machines.

All matched temperature sensors and MotorCAD nodes are listed in table 4.11. As the matching of the hot spot temperature in the coil is of highest importance, only the coil temperatures marked in table 4.11 are employed for the impregnation goodness ζ_{winding} fitting, described in the following.

Parameter Determination

In MotorCAD, the winding connection to the stator is influenced by the material choice of the impregnation and the slot liner as well as the corresponding correction factors impregnation goodness ζ_{winding} and ζ_{liner}. With these correction factors, it is possible to account in the simulation models for manufacturing uncertainties due to the winding placement or enclosed air pockets. In publications, the thermal conductivity of winding impregnation differs strongly: a range of $0.15 - 0.31\,{}^{W}/_{m\cdot K}$ is given in [Liu+16], but also $0.2 - 2\,{}^{W}/_{m\cdot K}$ is stated in [GWG16]. Higher values can be achieved by adding Al_2O_3 or AlN micro powder to epoxy, as done in [Liu+16]. Considering slot liners, $0.1 - 5\,{}^{W}/_{m\cdot K}$ has been assumed in [GWG16]. For common slot liner material, such as `Nomex410` or `ThermaVolt AR`, thermal conductivities of $0.103 - 0.175\,{}^{W}/_{m\cdot K}$ and $0.1 - 0.23\,{}^{W}/_{m\cdot K}$ are stated in data sheets, respectively.

In the MotorCAD model, epoxy with a thermal conductivity of $0.22\,{}^{W}/_{m\cdot K}$, a slot liner thickness of 0.22 mm and impregnation goodness $\zeta_{\text{liner}} = 1.75$ are fixed, while the temperature fitting is performed by a varying impregnation goodness ζ_{winding}. A fit could also be achieved by setting the thermal conductivity higher and reducing the impregnation goodness ζ_{winding} or altering the slot line thickness and impregnation goodness ζ_{liner}. The specific parameters have different effects on the coil internal temperature distribution, however, as these temperatures cannot be measured, the result at the surface of the coil is the same. The effect of a changing impregnation goodness ζ_{winding} on the deviation between the matched temperature sensors and nodes (see table 4.11) is evaluated by the root-mean-square-error $RMSE$ as defined in (4.10). In (4.10) $\hat{\vartheta}_{\text{i}}$ are measured and ϑ_{i} are simulated temperatures at a water-jacket inlet temperature $\vartheta_{\text{inlet}} = 25\,°\text{C}$. Sensor measuring characteristics as well as installation conditions and sensor wires influence the temperatures measured on a test bench [SC03; Qi+16]. As the exact error of each sensor cannot be quantified in the prototypes, the model is directly fit to the measured temperatures discussed previously.

$$RMSE = \sqrt{\frac{\sum(\vartheta_\mathrm{i} - \hat{\vartheta}_\mathrm{i})^2}{n}} \tag{4.10}$$

In fig. 4.16, the resulting root-mean-square-error $RMSE$ for the three prototypes is depicted together with the relative deviation of simulated temperatures ϑ_i to measured temperatures $\hat{\vartheta}_\mathrm{i}$ over the variated impregnation goodness ζ_winding from 0.75 – 2.5. The $RMSE$ shows a minimum for all three machines in this parameter range, marked with red circles in fig. 4.16a. At impregnation goodnesses ζ_winding below this value, the fitted coil temperatures

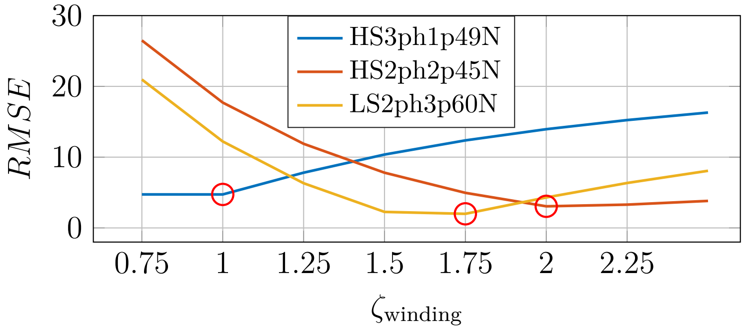

(a) $RMSE$ over impregnation goodness ζ_winding
red circles indicate chosen ζ_winding for the three machines.

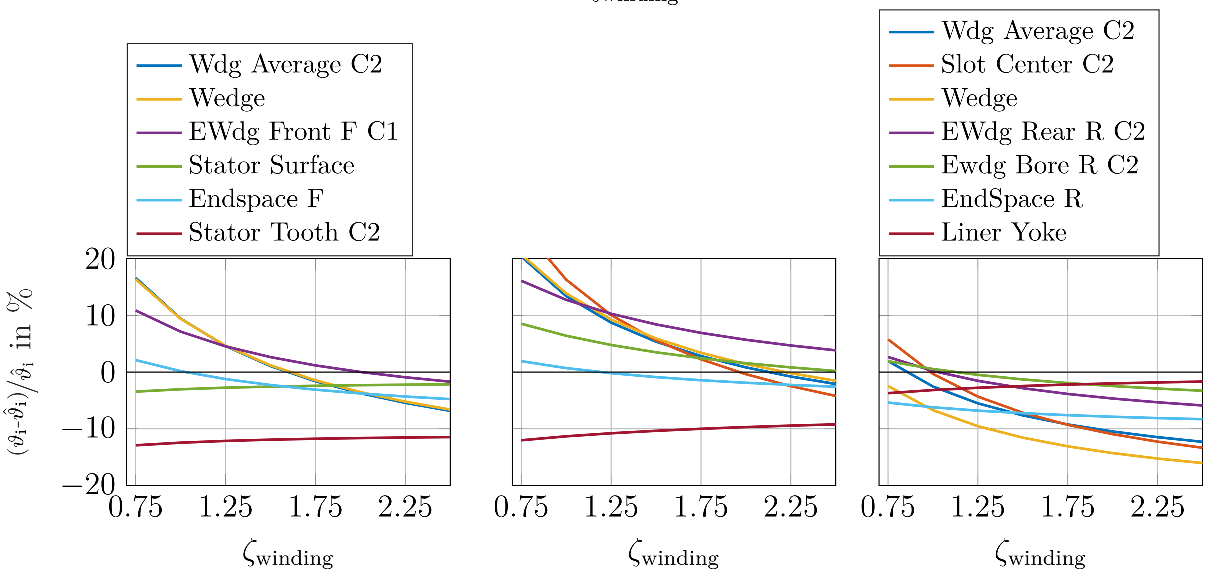

(b) LS2ph3p60N (c) HS2ph2p45N (d) HS3ph1p49N

Fig. 4.16: Root-mean-square-error $RMSE$ and temperature deviation over impregnation goodness ζ_winding for sensor assignment listed in table 4.11. MotorCAD parametrization: section A.3.1; water-jacket inlet temperature $\vartheta_\mathrm{inlet} = 25\,°\mathrm{C}$

(see table 4.11) are overestimated, above they are underestimated. As can be observed in fig. 4.16b - 4.16d, the winding temperatures are influenced stronger than the stator temperatures by a change of the impregnation goodness ζ_{winding}. Therefore, it is valid to minimize the root-mean-square-error $RMSE$ only for the matched coil temperatures listed in table 4.11. For further investigations, the impregnation goodness ζ_{winding} indicated with red circles in fig. 4.16a are employed.

Model Validation at Nominal Thermal Conditions

Measurement and simulation results at the operation point NOP_{M} (see table A.11) for the LS2ph3p60N, HS2ph2p45N and HS3ph1p49N machines (see table A.2) are listed in table 4.12 and table 4.13. With the final parameter set derived in the previous sections and listed in table A.8, the thermal simulation is additionally performed at the nominal thermal condition of a water-jacket inlet temperature $\vartheta_{\text{inlet}} = 60\,°\text{C}$ to evaluate the hot spot temperatures in the target application. The losses are not adjusted with the increased temperatures, somehow expecting lower temperatures than in measurement. In addition to measurements with a water-jacket inlet temperature $\vartheta_{\text{inlet}} = 25\,°\text{C}$, a measurement of the HS2ph2p45NX machine at NOP_{M} (see table A.11) and of the LS2ph3p60N machine at an increased input power $P_{\text{m,sh}} = 22\,\text{kW}$ at nominal generator speed $n_{\text{SRG,nom}}$ and an inlet temperature $\vartheta_{\text{inlet}} = 60\,°\text{C}$ are available for validation of the extrapolation.

In the LS2ph3p60N machine, the measured end-winding temperature at sensor T7 is about 23 °C below the maximal measured temperature at sensor T2 (see table 4.12). This temperature difference could be caused by the eddy-current copper losses $P_{\text{l,cu,eddy}}$, which are expected to occur mainly in the slot (see section 2.2.1) as well as by the better ventilation of the end-winding [Jun+12] compared to the stator slot. The hot spot temperature estimated

		Temperatures in °C					
	$P_{\text{m,sh}}$	NOP_{M} (see table A.11)				22 kW	
	ϑ_{inlet}	25 °C		60 °C	$\Delta\vartheta_{\text{inlet}}$	60 °C	
sensor	MotorCAD node	meas	sim	sim	sim	meas	sim
T1	`Wdg Average C2`	144.8	142.4	171.4	29	179.7	182.1
T2	`Wedge`	146.0	143.9	172.8	28.9	183.3	184.7
T3	*	52.6	*	*	*	79.5	*
T4	*	113.9	*	*	*	151.0	*
T4’	`Tooth C2`	88.7	78.2	107.2	29	119.5	111.4
T5	*	128.5	*	*	*	165.5	*
*	`Slot Center C2`	*	163.4	192.3	28.9	*	205.2
T7	`Ewdg Front F C1`	120.7	121.0	149.9	28.9	154.5	158.5
T8	`Stator Surface`	82.5	80.5	109.4	28.9	111.2	113.6
T9	`Endspace F`	81.1	78.5	107.1	28.6	119.1	111.1
T10	*	50.9	*	*	*	80.9	*

Table 4.12: Comparison of measured and simulated temperatures of LS2ph3p60N machine. MotorCAD parametrization: section A.3.1; $\Delta\vartheta_{\text{inlet}}$: Temperature increase between $\vartheta_{\text{inlet}} = 25\,°\text{C}$ and $60\,°\text{C}$; *: sensor/node not available

in simulation by the MotorCAD node `Slot Center C2` is again about 20 °C higher. This difference is close to the 15 °C ventilation offset observed in fig. 4.15a. Therefore, in the LS2ph3p60N machine the hot spot is expected to be located close to the coil surface facing the air gap.

The influence of the thermal interface formed by the slot liner between the coils and the stator tooth can be investigated with the help of sensor T4 and T4' in the LS2ph3p60N machine. These sensors are placed close to each other axially centered at the interface between coil and stator tooth. T4' is placed directly on the iron core, while T4 is placed on the coil just separated from T4' by the slot liner (see fig. 4.14). In table 4.12 it can be observed that the slot liner interface is responsible for a temperature drop of around 25 °C in this spot. Another qualitative discussion can be performed regarding the stator temperatures measured at sensor T3 and T8 - T10 in the LS2ph3p60N machine. The stator tooth shows a uniform temperature as can be deduced from temperatures measured with sensor T8 at the air gap and T9 above the windings (see fig. 4.14). The yoke temperatures measured with sensor T3 in the axial center and T10 at the end of the stator are both close to 50 °C. All temperatures measured on the stator are below 90 °C, hence, uncritical in terms of power density estimation of the machine.

In both high-speed HS2ph2p45N and HS3ph1p49N machines, the measured end-winding temperature at sensor T7 is about 30 °C below the maximal measured temperature at sensor T2 (see table 4.13). Reasons are the same as for the LS2ph3p60N machine. Due to the fit of `Slot Center C2` to sensor T2, the measured temperature matches closely the simulation. All stator temperatures measured with sensors T9 - T11 on the stator yoke are similar in both high-speed HS2ph2p45N and HS3ph1p49N machines. This indicates that the thicker yoke in the HS3ph1p49N machine is compensated by the lower total copper losses $P_{\mathrm{l,cu,ac}}$ (see fig. 4.12a) compared to the HS2ph2p45N machine. Close to the stator tooth, sensor T9 shows with approximately 82 °C the highest stator yoke temperature, similar to the temperature found in the LS2ph3p60N machine at the comparable sensor T9.

Increasing the water-jacket inlet temperature $\vartheta_{\mathrm{inlet}}$ by 35 °C from 25 °C to 60 °C in the simulation of the LS2ph3p60N machine, results in increased temperatures by 29 °C (see table 4.12). For the HS3ph1p49N and HS2ph2p45N machines, increased temperatures by 33 °C are found in table 4.13. This suggests the possibility to extrapolate temperatures from measurements obtained at lower water-jacket inlet temperature $\vartheta_{\mathrm{inlet}}$.

With the help of measurements at an increased input power $P_{\mathrm{m,sh}} = 22\,\mathrm{kW}$ the result of a constant offset is validated. The measurements listed in table 4.12 show increased winding temperatures by $35 - 40$ °C compared to the measurement at an inlet temperature $\vartheta_{\mathrm{inlet}} = 25$ °C. The stator temperatures are only increased by 30 °C (see table 4.12). The simulation shows a constant offset of winding temperatures around 40 °C and of stator temperatures around 33 °C, without taking in consideration the increase of $P_{\mathrm{l,mach}}$ due to the increased winding temperature. The fitted temperatures in the simulation, especially the critical coil temperatures `Wedge` and `Wdg Average C2`, closely match the corresponding sensor temperatures. At node `Wedge` the simulation overestimates the temperature by 1.3 °C compared to measurement, while the highest deviations are found for nodes `Tooth C2` and `Endspace F`, at which the temperature in simulation is underestimated by approximately 9 °C.

For the HS2ph2p45N and HS2ph2p45NX machines, the measurement results are not

	ϑ_{inlet}	Temperatures in °C 25 °C		60 °C	$\Delta\vartheta_{\text{inlet}}$
sensor	MotorCAD node	meas	sim	sim	sim
T1	`Wdg Average C2`	139.5	135.9	168.9	33.0
T2	`Slot Center C2`	150.9	150.4	183.4	33.0
T3	`Liner Yoke`	90.1	87.3	120.4	33.1
T4	*	140.9	*	*	*
T5	`Wedge`	147.9	138.0	171.0	33.0
T7	`Ewdg Rear R C2`	121.8	122.1	155.1	33.0
T8	`Ewdg Bore R`	114.1	114.8	147.7	33.0
T9	`Endspace R`	82.3	77.2	110.1	33.0
T10	*	55.8	*	*	*
T11	*	61.9	*	*	*

(a) HS3ph1p49N (see table A.2) at operation point NOP_{M} (see table A.11);

		Temperatures in °C HS2ph2p45N				HS2ph2p45NX		
	ϑ_{inlet}	25 °C		60 °C	$\Delta\vartheta_{\text{inlet}}$	25 °C	60 °C	$\Delta\vartheta_{\text{inlet}}$
sensor	MotorCAD node	meas	sim	sim	sim	meas	meas	meas
T1	`Wdg Average C2`	135.3	136.4	169.2	32.9	111.4	141.1	29.7
T2	`Slot Center C2`	149.7	149.1	181.9	32.8	145.8	176.4	30.6
T3	`Liner Yoke`	98.2	88.6	121.6	33	101.4	130.8	29.4
T4	*	119.5	*	*	*	122.7	151.7	29.0
T5	`Wedge`	136.7	138.7	171.5	32.8	142.9	174.4	31.4
T7	`Ewdg Rear R C2`	118.1	124.9	157.7	32.8	113.7	142.2	28.4
T8	`Ewdg Bore R`	119.9	121.8	154.6	32.8	98.3	129.1	30.7
T9	`Endspace R`	81.9	80.4	113.1	32.8	57.3	89.1	31.8
T10	*	55.8	*	*	*	52.9	84.1	31.2
T11	*	64.0	*	*	*	*	*	*

(b) HS2ph2p45N and HS2ph2p45NX (see section A.2.1.1) at operation point NOP_{M} (see table A.11);

Table 4.13: Comparison of measured and simulated temperatures of high-speed machines. MotorCAD parametrization: section A.3.1; $\Delta\vartheta_{\text{inlet}}$: Temperature increase between $\vartheta_{\text{inlet}} = 25\,°\text{C}$ and 60 °C; *: sensor/node not available

directly comparable, as two different hand-built prototypes had to be employed for the tests, hence, sensor installation is not identical. This effect can be clearly seen at sensor T1, which shows a decrease in temperature of 24 °C between the two measurements at a water-jacket inlet temperature $\vartheta_{\text{inlet}} = 25\,°\text{C}$ (see table 4.13b). In addition, sensors T8 and T9 show much lower temperatures in the HS2ph2p45NX machine, indicating that in the HS2ph2p45N machine these sensors are attached more closely to the winding and stator. A positive deviation can be found for sensor T5, for which the measured temperatures range in the HS2ph2p45NX very close to temperatures measured at sensor T2, hence, the hot spot.

For this particular sensor it is believed, that it was positioned within the direct airflow in the HS2ph2p45N machine, while being covered by material in the HS2ph2p45NX machine. For the hot spot sensor T2, a reduction of 4 °C is reported in table 4.13b, indicating a less good attachment to the coil. Increasing the water-jacket inlet temperature $\vartheta_{\mathrm{inlet}}$ in the HS2ph2p45NX machine shows that all temperatures are increased by about 30 − 31 °C, again below the offset expected from the increase of $\vartheta_{\mathrm{inlet}}$. Considering the 4 °C offset for temperatures measured with sensor T2, the simulation fits quite precisely the increased water-jacket inlet temperature $\vartheta_{\mathrm{inlet}}$.

The measurement validations show that the simulation model fitted on measurements at a water-jacket inlet temperature $\vartheta_{\mathrm{inlet}} = 25\,°\mathrm{C}$ can be employed to extrapolate hot spot temperatures to higher inlet temperatures $\vartheta_{\mathrm{inlet}}$. For all three machines, the hot spot is found on the coil surface close to the air gap in the axial center of the stator rather than in the end-winding. Both hot spot temperatures in the high-speed machines HS2ph2p45N and HS3ph1p49N are very close to the 180 °C hot spot temperature target of a class H wire insulation (see table 4.13). The LS2ph3p60N hot spot temperature, however, is with 192.3 °C by 7 % over the 180 °C target.

4.2.3 Machine Model and Loss Variations

In this section, variations of the machine model as well as the loss-input to the model are discussed. This comprises a variation of the gearbox cooling as well as an increase in machine stack length L_{stk}. In terms of loss variation, in a first step the improvements regarding eddy-current copper losses $P_{\mathrm{l,cu,eddy}}$ (see section 4.1.1), iron core losses $P_{\mathrm{l,fe}}$ (see section 4.1.2) and windage losses $P_{\mathrm{l,wind}}$ (see section 4.1.3) are discussed separately. In a second step, the combined improvements discussed in section 4.1.5 are employed. Basis for all variations are the machine models listed in table A.2 with the MotorCAD parametrization listed in appendix A.3.1.

As the MotorCAD nodes listed in table 4.14 stand for characteristic average and hot spot temperatures in the active parts of the SRG (i.e. stator, rotor and coils), specific variables are assigned to them for a more intuitive discussion.

MotorCAD node	variable name	MotorCAD node	variable name
`Stator Back Iron`	$\vartheta_{\mathrm{st,bi}}$	`Rotor Back Iron`	$\vartheta_{\mathrm{rt,bi}}$
`Stator Surface`	$\vartheta_{\mathrm{st,hs}}$	`Rotor Surface`	$\vartheta_{\mathrm{rt,hs}}$
`Winding Average`	$\vartheta_{\mathrm{coil}}$	`Shaft Active`	$\vartheta_{\mathrm{sh,act}}$
`Slot Center C2`	$\vartheta_{\mathrm{coil,hs}}$		

Table 4.14: Assigned variables to characteristic machine temperatures.

Increase of Machine Stack Length

In the previous section it was found that all built prototypes show a hot spot temperature $\vartheta_{\mathrm{coil,hs}}$ (`Slot Center C2` in table 4.12 - 4.13) above the 180 °C target for a class H coil insulation at a water-jacket inlet temperature $\vartheta_{\mathrm{inlet}} = 60\,°\mathrm{C}$. While the hot spot coil temperatures

$\vartheta_{\mathrm{coil,hs}}$ of the HS2ph2p45N and HS3ph1p49N machines almost reach the target with 181.9 °C and 183.4 °C, respectively, the $\vartheta_{\mathrm{coil,hs}}$ of the LS2ph3p60N machine reaches 192.3 °C.

To be able to compare the machines at similar thermal conditions, their outer dimensions need to be adapted. This can be done by reemploying the complete design tool-chain to obtain a new machine cross section, hence, change copper area A_{cu} and stack length related stator thermal resistance $R'_{\mathrm{th,st}}$. Another solution is a simple increase of the active stack length L_{stk} of existing prototypes (see table A.2). Both measures are prone to errors, as they do not only influence the thermal but also the electromagnetic behavior and ultimately the losses. For the increase of stack length L_{stk}, considering constant losses is rather a worst-case estimation, as this measure reduces the phase rms-current $I_{\mathrm{ph,rms}}$ and the pole flux linkage Ψ_{pl} and consequently the total copper losses $P_{\mathrm{l,cu,ac}}$ (see (2.19)) and iron core losses $P_{\mathrm{l,fe}}$ (see (2.31)).

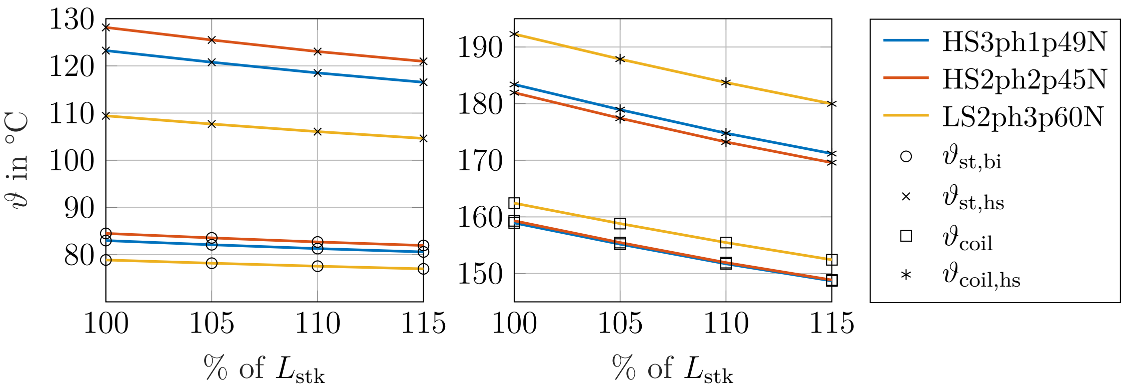

Fig. 4.17: Influence of stack length L_{stk} on stator and coil temperatures. Increase relative to prototype parameters listed in table A.2; Operation point NOP_{M} (see table A.11); MotorCAD parametrization: appendix A.3.1; water-jacket inlet temperature $\vartheta_{\mathrm{inlet}} = 60\,°\mathrm{C}$

In fig. 4.17, the effect of an increased L_{stk} on the relevant machine temperatures is depicted. The housing and coil length was increased by the same increase in stack length L_{stk}, keeping end-winding overhand and additional housing components constant. As the hot spot is located in the axial center of the machine, the reduction of hot spot coil temperature $\vartheta_{\mathrm{coil,hs}}$ is not exactly linear proportional to the relative increase of stack length L_{stk}. However, this effect should be compensate by the expected reduction of electromagnetic losses due to the stack length increase. To reach the target hot spot coil temperature $\vartheta_{\mathrm{coil,hs}} = 180\,°\mathrm{C}$ in simulation, the HS2ph2p45N, HS3ph1p49N and LS2ph3p60N machine stack length L_{stk} needs to be increased by 2 %, 4 % and 15 %, respectively.

Gearbox Cooling Influence

For the impregnation goodness ζ_{winding} fitting, the end-shaft temperature ϑ_{sh} was not predefined. The influence of a gearbox oil cooling in high-speed machines can be modeled by fixing ϑ_{sh} to a range of temperatures. In fig. 4.18, the effect on the characteristic stator, rotor and coil temperatures as well as the shaft center temperature $\vartheta_{\mathrm{sh,act}}$ of the HS2ph2p45N machine is depicted. Not defining the end-shaft temperature ϑ_{sh} leads to a node temperature

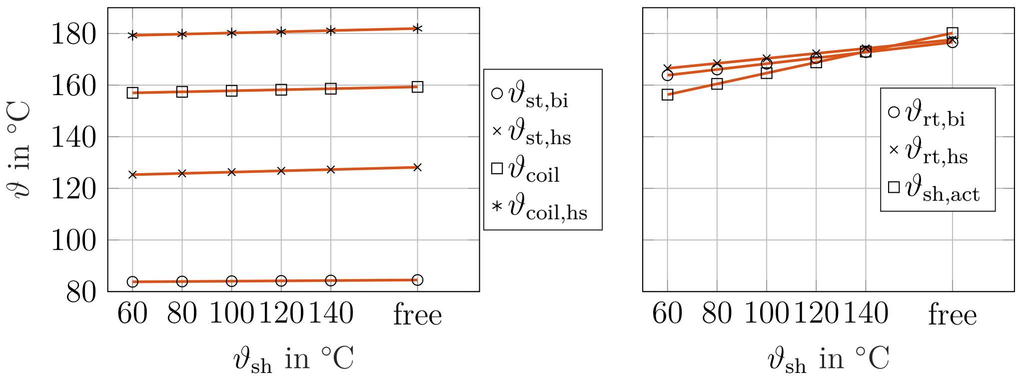

Fig. 4.18: Influence of an end-shaft temperature ϑ_{sh} variation on stator, rotor and coil temperatures in the HS2ph2p45N machine. Model data: table A.2; Operation point NOP_{M} (see table A.11); MotorCAD parametrization: appendix A.3.1; water-jacket inlet temperature $\vartheta_{\mathrm{inlet}} = 60\,°\mathrm{C}$

of approximately 175 °C in this machines. It can be seen, that a free end-shaft temperature ϑ_{sh} is resulting in the highest temperatures, hence a worst-case estimation. Reducing the front shaft temperature ϑ_{sh} has most impact on rotor and shaft temperatures, while for coil and stator temperatures only a reduction by less than 3 °C is observed (e.g. from 182 °C at $\vartheta_{\mathrm{sh}} = \mathrm{free}$ to 179.3 °C at $\vartheta_{\mathrm{sh}} = 60\,°\mathrm{C}$ for coil hot spot temperature $\vartheta_{\mathrm{coil,hs}}$). This improvement ranges close to the deviation of measured to simulated hot spot coil temperature $\vartheta_{\mathrm{coil,hs}}$ in the HS2ph2p45N machine (see table 4.13b).

The reduction of the rotor temperatures is below 15 °C (e.g. from 177.6 °C at $\vartheta_{\mathrm{sh}} = \mathrm{free}$ to 166.5 °C at $\vartheta_{\mathrm{sh}} = 60\,°\mathrm{C}$ for rotor hot spot temperature $\vartheta_{\mathrm{rt,hs}}$). Therefore, if rotor temperatures are of critical interest for the power density, the shaft cooling has to be considered. However, the simulated and measured temperatures allow the assumption that neglecting any loss input and cooling of the gearbox is valid for coil hot spot prediction in the high-speed machines.

Variation of Iron Core Losses

To investigate the influence of the iron core material on the thermal behavior of the machines, the simulated loss values listed in table A.15 were input to the MotorCAD models. In addition, the achievable temperatures with no iron core losses are simulated, to validate the approach of a single thermal heat source for coil temperature estimation developed in section 3.3.1. The material parametrization listed in section A.3.1 was not adjusted to the changed iron core materials.

In fig. 4.19, the resulting characteristic stator and coil temperatures are depicted. The reduced iron core losses $P_{\mathrm{l,fe}}$ between NO30 and NO10 lead to reduced hot spot coil temperatures by 3 °C, 8.5 °C and 10 °C in the LS2ph3p60N, HS2ph2p45N and HS3ph1p49N machines, respectively. Similar temperature reductions are found for the stator hot spot temperatures. Hence, employing a lower loss iron core material, such as NO10, is primarily interesting for an improvement of the machine efficiency η_{mach}, rather than the potential increase in power density $\phi_{\mathrm{P,tot}}$.

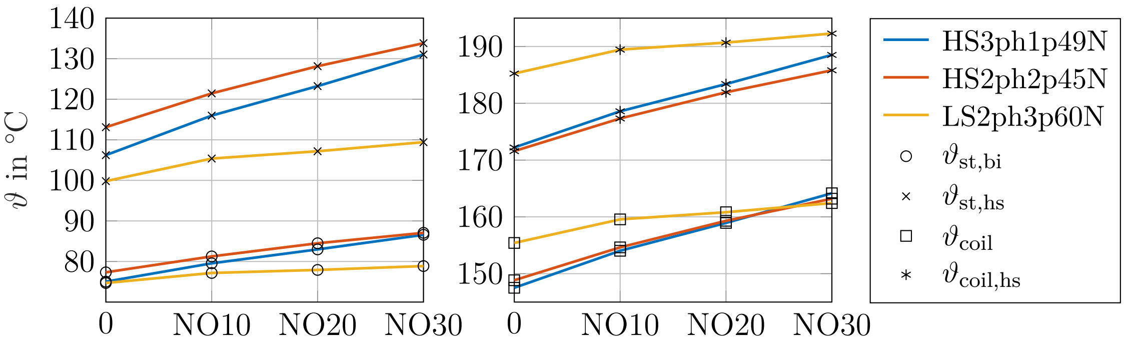

Fig. 4.19: Influence of iron core loss $P_{\mathrm{l,fe}}$ variation on stator and coil temperatures. Model data: table A.2; Operation point NOP_{M} (see table A.11) with iron core loses $P_{\mathrm{l,fe}}$ listed in table A.15 (0 signifies $P_{\mathrm{l,fe}} = 0\,\mathrm{W}$); MotorCAD parametrization: appendix A.3.1 (no adaptation to changed iron core material); water-jacket inlet temperature $\vartheta_{\mathrm{inlet}} = 60\,°\mathrm{C}$

The machine prototypes are built with NO20 in case of the high-speed HS2ph2p45N and HS3ph1p49N machine and NO30 in case of the LS2ph3p60N machine. Setting the iron core losses $P_{\mathrm{l,fe}} = 0\,\mathrm{W}$ results in a reduction in hot spot coil temperature $\vartheta_{\mathrm{coil,hs}}$ by 7 °C, 10.4 °C and 11.2 °C in the LS2ph3p60N, HS2ph2p45N and HS3ph1p49N machines, respectively (see fig. 4.19). This indicates, that for the HS2ph2p45N and HS3ph1p49N machines of comparable electric base frequency f_{el}, a constant temperature offset can account for the iron core losses $P_{\mathrm{l,fe}}$ in the pre-design (see section 3.3.1). However, the chosen offset around 20 °C in section 3.4 for the high-speed machines is higher than the 10 °C found with the help of the detailed analysis in this section. This accounts rather for the difference between average coil temperature $\vartheta_{\mathrm{coil}}$ and hot spot coil temperature $\vartheta_{\mathrm{coil,hs}}$, which is in the range of 25 °C.

Variation of Eddy-Current Copper Losses

Based on the prototype machine losses $P_{\mathrm{l,mach}}$ depicted in fig. 4.12a at the operation point NOP_{M} (see table A.11), reduced eddy-current copper losses $P_{\mathrm{l,cu,eddy}}$ in 25 % steps were input to the MotorCAD models. The lower thermal conductivity of litz wire, due to the added insulation between individual strands, as well as the changed loss distribution in the coil, due to the location of eddy-current copper losses $P_{\mathrm{l,cu,eddy}}$ close to the air gap, are neglected.

In fig. 4.20, the resulting characteristic stator and coil temperatures are depicted. Employing litz-wire technology, a reduction of the eddy-current copper losses $P_{\mathrm{l,cu,eddy}}$ by 75 % was deduced realistic in section 4.1. This reduction leads to reduced hot spot coil temperatures by 15.7 °C, 25.1 °C and 30.8 °C in the LS2ph3p60N, HS2ph2p45N and HS3ph1p49N machines, respectively. The reduction potential is evidently higher in the two high-speed machines, due to the increased share of eddy-current copper losses $P_{\mathrm{l,cu,eddy}}$ on the total copper losses $P_{\mathrm{l,cu,ac}}$ (see fig. 4.12b).

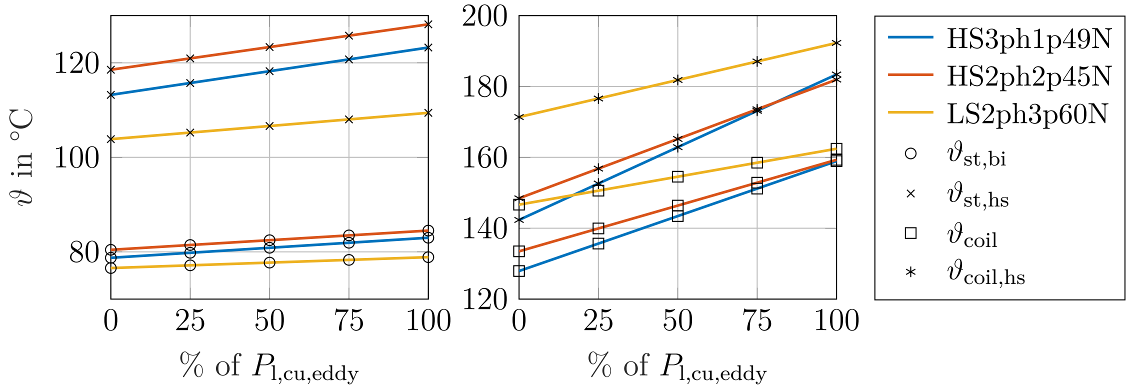

Fig. 4.20: Influence of eddy-current copper losses $P_{l,cu,eddy}$ variation on stator and coil temperatures. Model data: table A.2; Operation point NOP_M (see table A.11). Loss variation relative to prototype $P_{l,cu,eddy}$ depicted in fig. 4.12a; MotorCAD parametrization: appendix A.3.1 (no adaptation of coil thermal conductivity); water-jacket inlet temperature $\vartheta_{inlet} = 60\,°C$

Variation of Windage Losses

Based on the prototype machine losses $P_{l,mach}$ depicted in fig. 4.12a at the operation point NOP_M (see table A.11) and the mechanical losses $P_{l,m}$ listed in table 4.7, reduced windage losses $P_{l,wind}$ in 10 % steps were input to the MotorCAD models. The effect of reduced airflow and turbulence in the stator slots by a closure as well as the improved thermal conductivity of the stator slot by the employed silicon resin are neglected.

In fig. 4.21, the resulting characteristic stator and coil temperatures are depicted. Employing a stator slot closure, a reduction of the windage losses $P_{l,wind}$ by 50 % was found realistic in section 4.1.3. This reduction leads to reduced hot spot coil temperatures by 1.5 °C, 5.6 °C and 4.3 °C in the LS2ph3p60N, HS2ph2p45N and HS3ph1p49N machines,

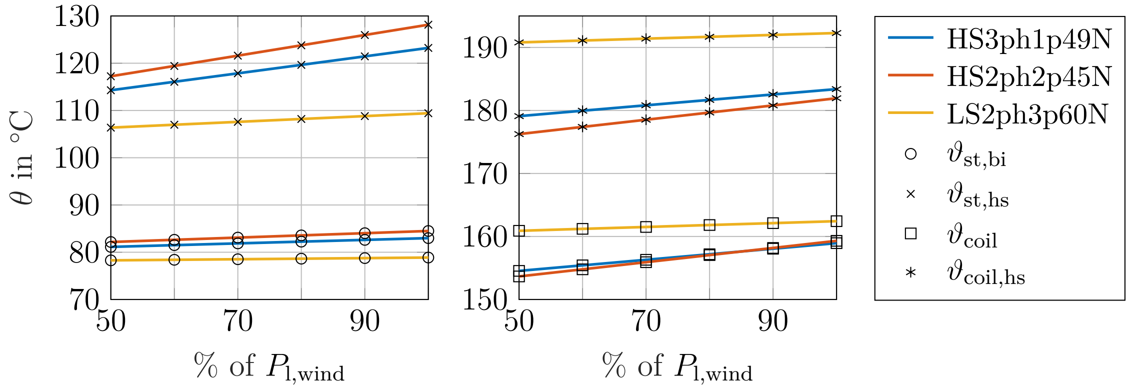

Fig. 4.21: Influence of windage loss $P_{l,wind}$ variation on stator and coil temperatures. Model data: table A.2; Operation point NOP_M (see table A.11). Loss variation relative to prototype $P_{l,wind}$ listed in table 4.7; MotorCAD parametrization: appendix A.3.1 (no adaptation of coil thermal conductivity and air flow in air gap); water-jacket inlet temperature $\vartheta_{inlet} = 60\,°C$

respectively. The effect on hot spot stator temperatures is approximately by a factor two higher (3 °C, 11 °C and 8.9 °C in the LS2ph3p60N, HS2ph2p45N and HS3ph1p49N machines, respectively). The reduction of $P_{\mathrm{l,wind}}$ by stator slot closure has the lowest impact on the investigated temperatures off all considered loss reductions. Again the reduction potential is higher in the high-speed machines, due to the increased windage losses $P_{\mathrm{l,wind}}$ (see table 4.7).

Combining the found reduction potential (see fig. 4.21) with the measured temperature reduction by 25.4 °C in the static characterization for the HS2ph2p45N machine (see table 4.10), a reduction of hot spot coil temperature $\vartheta_{\mathrm{coil,hs}}$ by 30 °C in the high-speed machines is realistic.

Combined Loss Improvements

Finally, the thermal effects shown in fig. 4.19 - fig. 4.21 are combined. Namely these are, reduced windage losses $P_{\mathrm{l,wind}}$ by 50 %, iron core losses $P_{\mathrm{l,fe}}$ calculated with NO10 iron core material and reduced eddy-current copper losses $P_{\mathrm{l,cu,eddy}}$ by 75 %. Beside the loss input, no changes in the machine cross sections and stack length L_{stk} listed in table A.2 as well as material parameters are performed.

Table 4.15 lists the temperatures in machines with the combined loss reductions (I2) compared to the prototype machines (P) LS2ph3p60N, HS2ph2p45N and HS3ph1p49N (see table A.2). The combined loss reductions lead to reduced hot spot coil temperatures by 20 °C, 35.4 °C and 39.9 °C in the LS2ph3p60N, HS2ph2p45N and HS3ph1p49N machines, respectively. The reduction in the stator is lower than in the coils (e.g. reduction of the stator hot spot temperature $\vartheta_{\mathrm{st,hs}}$ in the HS2ph2p45N machine by 24.8 °C). The rotor temperatures profit especially from the reduced iron core losses $P_{\mathrm{l,fe}}$ in the high-speed machines (e.g. reduction of the rotor hot spot temperature $\vartheta_{\mathrm{rt,hs}}$ in the HS2ph2p45N machine by 43.7 °C).

	Temperatures in °C					
	LS2ph3p60N		HS2ph2p45N		HS3ph1p49N	
	P	I2	P	I2	P	I2
$\vartheta_{\mathrm{st,bi}}$	78.9	74.9	84.5	75.9	83.0	74.5
$\vartheta_{\mathrm{st,hs}}$	109.4	98.2	128.2	103.3	123.2	99.5
$\vartheta_{\mathrm{coil,hs}}$	192.3	172.3	181.9	146.5	183.4	143.5
$\vartheta_{\mathrm{coil}}$	162.4	146.2	159.3	129.6	158.9	126.4
$\vartheta_{\mathrm{rt,bi}}$	128.4	111.8	176.6	134.5	182.6	137.4
$\vartheta_{\mathrm{rt,hs}}$	129.3	111.9	177.6	133.9	179.3	134.3
$\vartheta_{\mathrm{sh,act}}$	129.7	114.3	180.2	142.2	185.3	144.6

Table 4.15: Influence of combined loss improvements on stator, rotor and coil temperatures. P: Prototype machines listed in table A.2. I2: iron core losses with NO10 (table A.15), 25 % $P_{\mathrm{l,cu,eddy}}$ (fig. 4.12a), 50 % $P_{\mathrm{l,wind}}$ (table 4.7). Operation point NOP_{M} (see table A.11); MotorCAD parametrization: appendix A.3.1 (no adaptation of material data); water-jacket inlet temperature $\vartheta_{\mathrm{inlet}} = 60$ °C

4.2.4 Power Density Estimation

To compare the initially built prototypes LS2ph3p60N, HS2ph2p45N and HS3ph1p49N (see table A.2) at equal thermal conditions, two model variations were performed with the help of MotorCAD. For the first variation the obtained losses of the prototypes LS2ph3p60N, HS2ph2p45N and HS3ph1p49N ("reached" in table 4.9) are kept constant and the stack length L_{stk} is increased to obtain a coil hot spot temperature $\vartheta_{\mathrm{coil,hs}}$ of 180 °C. For the second variation the reduced losses ("improved" in table 4.9) are applied to the MotorCAD model and the stack length L_{stk} is reduced to obtain again a coil hot spot temperature of 180 °C. The active parts length L_{act} and total machine length L_{tot} are changed in both cases by the same absolute value as the stack length L_{stk}. The resulting machine lengths are listed in table A.4. The machine cross sections described in table A.2 are kept constant for all variations and the influence of the changed stack length L_{stk} on dynamic phase voltage u_{ph} (see (2.9)) and, consequently, coil design and coenergy loop W_{co} are neglected.

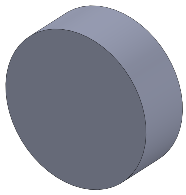

(a) LS2ph3p60N

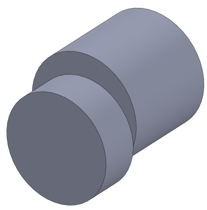

(b) HS2ph2p45N, HS3ph1p49N

Fig. 4.22: Bodies for calculation of machine and gearbox volumes V_{SRG} and V_{gear}.

Based on nominal input power $P_{\mathrm{m,sh}}$ and machine torque $T_{\mathrm{tot,nom}}$, the volumetric and gravimetric power density $\phi_{\mathrm{P,tot}}$ and $\xi_{\mathrm{P,tot}}$ as well as the volumetric and gravimetric torque densities $\phi_{\mathrm{T,tot}}$ and $\xi_{\mathrm{T,tot}}$ are calculated. The volumes of the machines are simplified with cylindrical bodies as shown in fig. 4.22. The weights are calculated with the help of 3-D-CAD models, neglecting small parts, such as screws and bearings as well as the cooling fluids. To evaluate the prediction accuracy, the weights of the built prototypes LS2ph3p60N, HS2ph2p45N and HS3ph1p49N are measured and compared to the calculated values. Beside the volumetric and gravimetric power density $\phi_{\mathrm{P,tot}}$ and $\xi_{\mathrm{P,tot}}$ of the complete machines, the corresponding values of the active parts, stator, rotor and coils, are calculated. All retrieved values are listed in table 4.16.

To reach a coil hot spot temperature $\vartheta_{\mathrm{coil,hs}} = 180$ °C the stack length L_{stk} needs to be prolonged by 9 mm or 15 % in the LS2ph3p60NI1 machine compared to the LS2ph3p60N machine (see fig. 4.17). This leads to an increased m_{act} and m_{SRG} by 1.6 kg and 2.3 kg or 13 % and 11 %, respectively (see table 4.16). Consequently, the power and torque densities are reduced in the LS2ph3p60NI1 machine compared to the built LS2ph3p60N prototype. Regarding the active parts, power densities $\xi_{\mathrm{P,act}}$ of 1.4 kW/kg and $\phi_{\mathrm{P,act}}$ of 5.3 kW/l are realistic for this scenario. The torque related values $\xi_{\mathrm{T,act}}$ and $\phi_{\mathrm{T,act}}$ are comparable with 1.8 Nm/kg and 6.8 Nm/l, respectively. Regarding the complete machine, the gravimetric values are reduced by a factor two, while the volumetric values are reduced by a factor three. In total a gravimetric power density $\xi_{\mathrm{P,tot}}$ of 0.7 kW/kg and volumetric power density of 1.8 kW/l of the complete machine are realistic. The efficiency improvements in this scenario offer a potential reduction of the stack length L_{stk} by 15 mm or 22 % in the LS2ph3p60NI2

	LS2ph3p60N			HS2ph2p45N			HS3ph1p49N		
	P	I1	I2	P	I1	I2	P	I1	I2
L_{stk} in mm	60.0	69.0	54.0	80.0	81.6	50.0	80.0	83.2	46.0
m_{act} in kg	12.2	13.8	11.2	8.0	8.1	5.3	8.0	8.3	5.0
m_{gear} in kg		-			4.4			4.4	
pred. m_{SRG} in kg	26.1	28.4	24.6	16.6	16.9	12.6	16.7	17.1	12.1
meas. m_{SRG} in kg	28.9	-		18.3	-		17.5	-	
V_{act} in l	3.4	3.8	3.2	1.7	1.7	1.3	1.8	1.9	1.3
V_{gear} in l		-			2.8			2.8	
V_{SRG} in l	10.6	11.2	10.1	7.6	7.7	6.5	7.6	7.7	6.4
	active parts								
$\xi_{\mathrm{P,act}}$ in kW/kg	1.6	1.4	1.8	2.5	2.5	3.8	2.5	2.4	4.0
$\phi_{\mathrm{P,act}}$ in kW/l	5.8	5.3	6.3	11.6	11.4	15.8	11.0	10.7	15.5
$\xi_{\mathrm{T,act}}$ in Nm/kg	2.1	1.8	2.3	1.0	1.0	1.5	1.0	0.9	1.5
$\phi_{\mathrm{T,act}}$ in Nm/l	7.4	6.8	8.0	4.5	4.4	6.1	4.3	4.1	6.0
	complete machine								
$\xi_{\mathrm{P,tot}}$ in kW/kg	0.8	0.7	0.8	1.2	1.2	1.6	1.2	1.2	1.7
$\phi_{\mathrm{P,tot}}$ in kW/l	1.9	1.8	2.0	2.6	2.6	3.1	2.6	2.6	3.2
$\xi_{\mathrm{T,tot}}$ in Nm/kg	1.0	0.9	1.0	1.9	1.9	2.5	1.9	1.9	2.6
$\phi_{\mathrm{T,tot}}$ in Nm/l	2.4	2.3	2.5	4.2	4.1	4.9	4.2	4.1	5.0

Table 4.16: Masses, volumes, gravimetric and volumetric power and torque densities of built prototypes (P) (see table A.2). I1: HS2ph2p45NI1, HS3ph1p49NI1 and LS2ph3p60NI1 machines with increased stack length L_{stk} to reach $\vartheta_{\mathrm{coil,hs}} = 180\,°\mathrm{C}$ (see table A.4). I2: HS2ph2p45NI2, HS3ph1p49NI2 and LS2ph3p60NI2 with combined loss reductions (see section 4.2.3) and decreased stack length L_{stk} to reach $\vartheta_{\mathrm{coil,hs}} = 180\,°\mathrm{C}$ (see table A.4).

machine compared to the LS2ph3p60NI1 machine. This leads to an increase of total gravimetric power density $\xi_{\mathrm{P,tot}}$ by 0.1 kW/kg and volumetric power density $\phi_{\mathrm{P,tot}}$ by 0.2 kW/l compared to the realistic values of the LS2ph3p60NI1 machine.

Both high-speed machines HS2ph2p45N and HS3ph1p49N were already close to the hot spot coil temperature $\vartheta_{\mathrm{coil,hs}} = 180\,°\mathrm{C}$, hence, to reach the target, the stack length L_{stk} needs only to be increased by 1.6 mm and 3.2 mm or 2 % and 4 % in the HS2ph2p45NI1 and HS3ph1p49NI1 machines, respectively (see fig. 4.17). The increase in material weights has only a small effect on the realistic gravimetric and volumetric power and torque densities (see table 4.16). Regarding the active parts, a power density $\xi_{\mathrm{P,act}}$ of 2.4 kW/kg and $\phi_{\mathrm{P,act}}$ of 10.7 kW/l is realistic for the HS3ph1p49NI1 machine. The torque related values $\xi_{\mathrm{T,act}}$ and $\phi_{\mathrm{T,act}}$ are much lower with 0.9 Nm/kg and 4.1 Nm/l in the HS3ph1p49NI1 machine, respectively. The values of the HS2ph2p45NI1 machine are only by 0.1 kW/kg and 0.7 kW/l or 0.1 Nm/kg and 0.1 Nm/l higher than for the HS3ph1p49NI1 machine. Regarding the total machines, a gravimetric power density of 1.2 kW/kg and a volumetric power density of 2.6 kW/l is reached in both high-speed HS2ph2p45NI1 and HS3ph1p49NI1 machines. Torque related values of 1.9 Nm/kg and 4.1 Nm/l are reached in the HS2ph2p45NI1 and HS3ph1p49NI1 machines. The total volumetric torque density $\phi_{\mathrm{T,tot}}$ is comparable to the active parts volumetric torque density $\phi_{\mathrm{T,act}}$, as the gearbox only adds 2.8 l to the complete machine volume but increases the output torque by over a factor 4. The efficiency improvements in this high-speed scenario offer a potential reduction of the stack length L_{stk} by 37.2 mm or 45 % in the HS3ph1p49NI2 machine compared to the HS3ph1p49NI1 machine. The reduced stack length L_{stk} leads to an increase of total gravimetric power density $\xi_{\mathrm{P,tot}}$ by 0.5 kW/kg and volumetric power density by 0.6 kW/l. For the HS2ph2p45NI2 compared to HS2ph2p45NI1 machine the reduction potential is lower with 31.6 mm or 39 %. The increase of total gravimetric power density $\xi_{\mathrm{P,tot}}$ by 0.4 kW/kg and volumetric power density by 0.5 kW/l is consequently also lower.

Comparing the two scenarios, the effect of an increased nominal generator speed $n_{\mathrm{SRG,nom}}$ on the realistic power and torque densities (I1 in table 4.16) can be analyzed. Comparing the active parts, the high-speed machine HS2ph2p45NI1 offers an increase in gravimetric and volumetric active material power density $\xi_{\mathrm{P,act}}$ and $\phi_{\mathrm{P,act}}$ by 1.1 kW/kg and 6.1 kW/l or 79 % and 115 % compared to the LS2ph3p60NI1 machine, respectively. The gravimetric and volumetric torque density $\xi_{\mathrm{T,act}}$ and $\phi_{\mathrm{T,act}}$ is in the HS2ph2p45NI1 machine reduced by 0.8 Nm/kg and 2.4 Nm/l or 44 % and 35 % compared to the LS2ph3p60NI1 machine, respectively. This is caused by the reduced total torque T_{tot} of the high-speed machines by a factor 3.3 due to the gearbox. The relative values explain, why the increase of $n_{\mathrm{SRG,nom}}$ by a factor close to three between the low-speed and the high-speed scenario only offers a power density increase of below a factor two. The thermal behavior of the high-speed machines are limiting a further increase, while electromagnetically smaller machines could be achieved. Considering the complete machine, the high-speed HS2ph2p45NI1 machine offers an increase in gravimetric and volumetric power density $\xi_{\mathrm{P,tot}}$ and $\phi_{\mathrm{P,tot}}$ by 0.5 kW/kg and 0.8 kW/l or 71 % and 44 % compared to the LS2ph3p60NI1 machine. On the gravimetric power density $\xi_{\mathrm{P,tot}}$ the gearbox only has a minor effect, as for the LS2ph3p60NI1 machine a heavy shaft of nearly the same weight is required.

As the efficiency improvement offers a larger potential to decrease the stack length L_{stk} in the high-speed HS2ph2p45NI2 and HS3ph1p49NI2 machines compared to the low speed LS2ph3p60NI2 machine, the differences in reachable power and torque densities between the two scenarios are consequently bigger than considering the HS2ph2p45NI1 and LS2ph3p60NI1 machine. In table 4.16 the highest total values are found for the HS3ph1p49NI2 machine. In terms of gravimetric and volumetric power density $\xi_{\mathrm{P,tot}}$ and $\phi_{\mathrm{P,tot}}$ an increase by 0.9 kW/kg and 1.2 kW/l or 113 % and 60 % compared to the LS2ph3p60NI1 machine is obtained, respectively. Higher increases are found for the gravimetric and volumetric torque density $\xi_{\mathrm{T,tot}}$ and $\phi_{\mathrm{T,tot}}$ by 1.6 Nm/kg and 2.5 Nm/l or 160 % and 100 %

For the machines listed in table 2.4, only volumetric reference values were found in the corresponding literature. The volumetric active material torque density $\phi_{\mathrm{T,act}} = 7\,\mathrm{Nm/l}$ is only by 0.2 Nm/l higher than the LS2ph3p60NI1 machine. Due to its low nominal generator speed $n_{\mathrm{SRG,nom}} = 1000\,\mathrm{rpm}$, the machine from [SL09] reaches a volumetric active material power density $\phi_{\mathrm{P,act}} = 0.7\,\mathrm{kW/l}$, by a factor 7.6 below the LS2ph3p60NI1 machine listed in table 4.16. The high-speed machine from [MJ89; Fer+95] has a nominal generator speed

$n_{\mathrm{SRG,nom}} = 27$ krpm and reaches with 13.6 kW/l a volumetric active material power density $\phi_{\mathrm{P,act}}$ by 2.2 kW/l above the HS2ph2p45NI1 machine and by the same value below the HS2ph2p45NI2 machine. Also the volumetric active material torque density $\phi_{\mathrm{T,act}}$ ranges with 4.7 Nm/l between this two machines.

4.2.5 Thermal and Power Density Conclusion

Static characterization in table 4.10 shows that the simplified estimation of the hot spot coil temperature in the center of the windings introduced in section 3.3.1 is prone to errors. Especially, the introduction of losses from the end-winding and the offset between average and hot spot temperature have to be modeled correctly. For machines with the same electric base frequency f_{el}, it was found valid to model the iron losses $P_{\mathrm{l,fe}}$ by a constant temperature offset in pre-design (see fig. 4.19).

In section 4.2.2 it was shown that coil temperatures at various water-jacket inlet temperature $\vartheta_{\mathrm{inlet}}$ can be estimated by constant offsets with the help of a thermal model fitted to measurements at a water-jacket inlet temperature $\vartheta_{\mathrm{inlet}} = 25\,°\mathrm{C}$. Extrapolating MotorCAD simulations to $\vartheta_{\mathrm{inlet}} = 60\,°\mathrm{C}$ with constant machine losses $P_{\mathrm{l,mach}}$ showed good accordance with measurements (see table 4.12 and table 4.13b). Employing the thermal model for loss variation showed that reducing the eddy-current copper losses $P_{\mathrm{l,cu,eddy}}$ has the largest thermal influence on the critical hot spot coil temperatures $\vartheta_{\mathrm{coil,hs}}$. Reducing the iron core losses $P_{\mathrm{l,fe}}$ as well as the windage losses $P_{\mathrm{l,wind}}$ is rather interesting for efficiency η_{mach} improvements than a reduction of hot spot coil temperature $\vartheta_{\mathrm{coil,hs}}$.

To reach a comparable coil hot spot temperature $\vartheta_{\mathrm{coil,hs}} = 180\,°\mathrm{C}$, the active material stack length L_{stk} of the LS2ph3p60N, HS2ph2p45N and HS3ph1p49N prototypes needs to be increased by 15 %, 2 % and 4 %, respectively. Due to the thermal behavior of the high-speed machines HS2ph2p45NI1 and HS3ph1p49NI1, the power density potential of the increased nominal generator speed $n_{\mathrm{SRG,nom}}$ by 230 % compared to the LS2ph3p60N machine, is not fully exploitable. Only an increase of around 79 % in gravimetric active material power density $\xi_{\mathrm{P,act}}$ is achieved, with a final value of 1.2 kW/kg. The gravimetric active material torque density $\xi_{\mathrm{T,act}}$ is at the same time reduced by 44 %. Improved cooling and machine efficiency η_{mach}, therefore, offers still a significant power-density potential, as electromagnetically the machines are not at their limits.

Employing NO10 iron core material, litz wire and a stator slot closing, the frequency dependent machine losses $P_{\mathrm{l,fe}}$, $P_{\mathrm{l,cu,eddy}}$ and $P_{\mathrm{l,wind}}$ can be reduced as listed in table 4.9. The resulting reduced hot spot coil temperature $\vartheta_{\mathrm{coil,hs}}$ (see table 4.15) offer the potential to reduce the active material stack length L_{stk} by 15 %, 39 % and 45 % in the LS2ph3p60NI2, HS2ph2p45NI2 and HS3ph1p49NI2 machines compared to the LS2ph3p60NI1, HS2ph2p45NI1 and HS3ph1p49NI1 machines, respectively (see section 4.2.4). This leads to achievable gravimetric total power densities $\xi_{\mathrm{P,tot}}$ of 0.8 kW/kg, 1.6 kW/kg and 1.7 kW/kg in the LS2ph3p60NI2, HS2ph2p45NI2 and HS3ph1p49NI2 machine, respectively (see table 4.16).

4.3 Acoustic Analysis

Due to the presence of an ICE in a REX application, the acoustic behavior of the electric machine is of lower importance than in a pure electric vehicle. However, the pulsed operation principle in combination with the salient rotor and stator structure and the small air gap length d_g of SRG produces high radial forces $F_\mathrm{pl,rad}$, which cause strong vibrations. Therefore, reviewing the acoustic behavior of SRG during the design process as recommended in [Bös14], offers an additional decision aspect between different machine configurations. A wide overview on the influence of structural changes on SRG can be found in [Fie07; Kas11; Bös14]. Some general points are summarized in the following.

The choice of number of pole pairs n_p and number of phases N_ph defines the fundamental electric frequency f_el (see (2.4)), the harmonic density (harmonics/Hz) as well as the relevant eigenmodes (see fig. 4.23). In all cylindrical machines, the mode_0 mode shape is present. The lowest effective none-zero $\mathrm{mode}_{n_\mathrm{m}}$ of a certain configuration is defined by (4.11), hence, increases with number of pole pairs n_p.

$$n_\mathrm{m} = \frac{N_\mathrm{s}}{N_\mathrm{ph}} = \frac{2 \cdot n_\mathrm{p} \cdot N_\mathrm{ph}}{N_\mathrm{ph}} = 2 \cdot n_\mathrm{p} \tag{4.11}$$

The stator outer diameter D_st, the stack length L_stk and the yoke thickness $w_\mathrm{y,s}$ define the explicit values of the eigenfrequencies f_eig. Lowering D_st and increasing L_stk shifts the eigenfrequencies f_eig to higher values [Fie07]. The same effect can be also achieved by an increased stator yoke thickness $w_\mathrm{y,s}$. The explicit value of none-zero eigenfrequencies (e.g f_M2, f_M4, f_M6) increases with mode order n_m [Fie07]. Increasing the number of pole pairs n_p is stated to have a positive effect in [Fie07] as long as the lowest effective non-zero eigenfrequency is below the value of the mode_0 eigenfrequency f_M0. The increased $\mathrm{mode}_{n_\mathrm{m}}$ compensates the lowered eigenfrequencies f_eig as the yoke thickness $w_\mathrm{y,s}$ decreases. Especially the mode_2 is advised to be avoided generally in literature [Fie07; Hof14]. Shifting the eigenfrequencies f_eig by structural adaptations or a change of configuration influences the machine efficiency η_mach [Hof14]) as well as the volumetric power density $\phi_\mathrm{P,tot}$.

Beside the consideration of the transfer function and the location of the eigenfrequencies f_eig, psychoacoustic parameters, e. g. loudness and sharpness, should be considered. A lower electric base frequency f_el increases the number of harmonics in the audible range and, therefore, reduces the sharpness of the noise [Fie07]. At the same time it is more difficult to find low-noise operating points in the operation range of the the generator [Bös14].

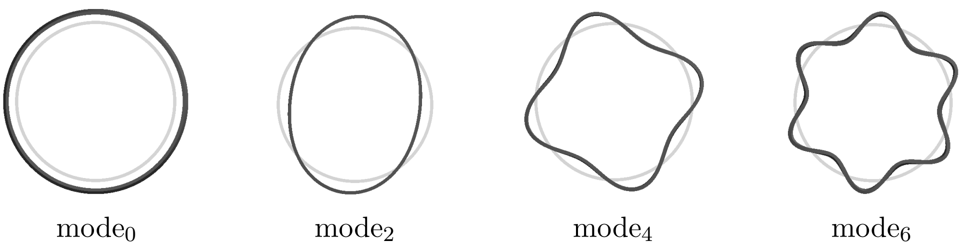

Fig. 4.23: Free vibration mode orders $\mathrm{mode}_{n_\mathrm{m}}$ (see (4.11)) of cylindrical objects relevant for the machines considered in this thesis.

For the two scenarios, differing considerations arise from this general discussion. As for the low-speed scenario the outline of the generator is fixed, the relative position of the harmonics to mode$_0$ eigenfrequency f_{M0} is relevant, as well as the influence of the harmonic density on the choice of operation points. To assess the effect of a changing number of pole pairs n_{p}, the LS2ph2p68N (2,2) configuration listed in table 3.4 is considered in the simulative discussion together with the LS2ph3p60N machine. For the high-speed scenario, from a machine efficiency η_{mach} perspective only a (2,2) and a (3,1) configuration are reasonable (see section 3.4.2). The HS2ph2p45N (2,2) configuration is expected to have higher radial force $F_{\mathrm{pl,rad}}$ amplitudes as the torque is produced by only two phases. The HS3ph1p49N (3,1) configuration excites the critical low-frequency mode$_2$ eigenfrequency f_{M2}. A comparison of the two scenarios is only performed in a qualitative way, as the housings differ strongly. Still, the influence of the changing harmonic density by the increased nominal generator speed $n_{\mathrm{SRG,nom}}$ in the high-speed scenario compared to the low-speed scenario can be discussed.

4.3.1 Force Excitation and Harmonic Content

In the SRGs considered in this thesis the peak radial pole forces $F_{\mathrm{pl,rad}}$ at pole MMF $\Theta_{\mathrm{pl}} = 4500\,\mathrm{A}$ are between a factor 3.6, in case of the HS2ph2p45N machine, and a factor 6, in case of the LS2ph2p68N machine, higher than the tangential forces. This is in line with findings in [Kas11]. Therefore, to assess the acoustic behavior in simulation, only the pole radial force $F_{\mathrm{pl,rad}}$, retrieved from FEA, are considered in this thesis. Any asymmetries, such as eccentricities or production tolerances, are also neglected in the following analysis.

Fig. 4.24 depicts the pole radial force $F_{\mathrm{pl,rad}}$ for one electric period of the LS2ph2p68N, LS2ph3p60N, HS2ph2p45N and HS3ph1p49N machines considered in this thesis. In fig. 4.24a, it can be seen that at constant pole MMF $\Theta_{\mathrm{pl}} = 4500\,\mathrm{A}$ at an electric angle $\theta_{\mathrm{el}} = 220\,°\mathrm{el}$, the pole radial force $F_{\mathrm{pl,rad}}$ decreases by 580 N or 25 % when changing the number of pole pairs n_{p} from two to three. By changing n_{p} from one to two, a reduction of 306 N or 17 % can be observed between the points of maximal pole radial force $F_{\mathrm{pl,rad}}$ of the

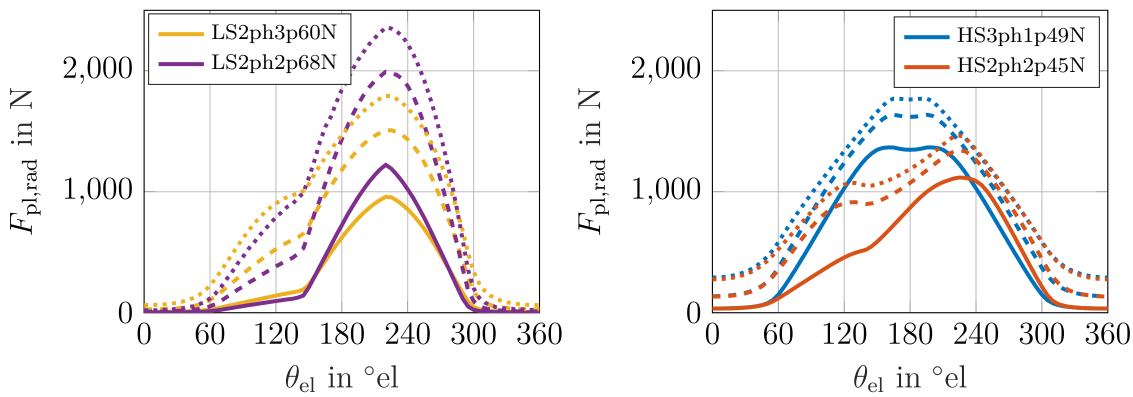

(a) low-speed machines (b) high-speed machines

Fig. 4.24: Pole radial force $F_{\mathrm{pl,rad}}$ over electrical angle θ_{el} at various constant pole MMF Θ_{pl} for machines listed in table A.2 and table A.6. solid lines: $\Theta_{\mathrm{pl}} = 1500\,\mathrm{A}$, dashed lines: 3000 A, dotted lines: 4500 A.

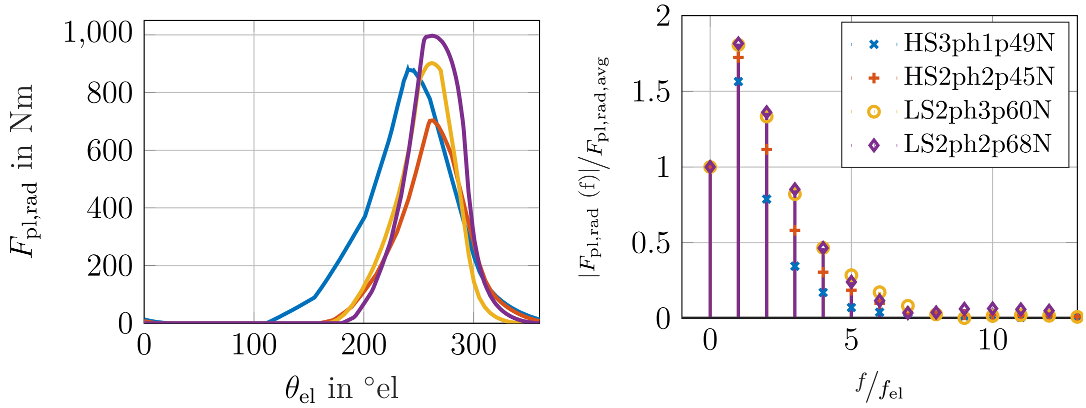

(a) dynamic radial force at one pole (b) radial force harmonic content

Fig. 4.25: Dynamic pole radial force $F_{\mathrm{pl,rad}}$ and harmonic content of low- and high-speed machines (see table A.2 and A.6) at operation point NOP_{M} (see table A.11).

HS2ph2p45N and HS3ph1p49N machine (see fig. 4.24b), even when switching from number of phases $N_{\mathrm{ph}} = 3$ to $N_{\mathrm{ph}} = 2$. The asymmetries in the 2-phase LS2ph2p68N, LS2ph3p60N and HS2ph2p45N machines arise from the rotor step described later in section 4.4.2.

Analyzing the static characteristics (see fig. 4.24) does not give directly information about the pole radial force $F_{\mathrm{pl,rad}}$ applied to the stator poles during machine operation. Fig. 4.25a depicts the dynamic force of the LS2ph2p68N, LS2ph3p60N, HS2ph2p45N and HS3ph1p49N machines at the operation point NOP_{M} (see table A.11) over one electric period. The peak values of the pole radial force $F_{\mathrm{pl,rad}}$ of all machines are in the range of 700 – 1000 Nm. The LS2ph2p68N machine has the highest absolute pole radial force $F_{\mathrm{pl,rad}}$, the HS2ph2p45N machine the lowest. The LS2ph3p60N and HS3ph1p49N machine show a similar magnitude of pole radial force $F_{\mathrm{pl,rad}}$, while the nominal torque $T_{\mathrm{tot,nom}}$ is reduced by a factor of four between these two machines (see table A.2). The harmonic content in fig. 4.25b shows that the excitation of the pole force harmonics decreases with their order. Relevant amplitudes can be found up to $6 \cdot f_{\mathrm{el}}$ in the LS2ph2p68N, LS2ph3p60N, HS2ph2p45N and HS3ph1p49N machines. The two low-speed LS2ph2p68N and LS2ph3p60N machines show the highest excitation amplitudes of equal magnitude, while the HS3ph1p49N machine shows the lowest amplitude.

Analyzing the dynamic pole radial forces $F_{\mathrm{pl,rad}}$ and its harmonic content is only the first step in the acoustic analysis. Only in combination with the structural analysis, the location of certain pole force $F_{\mathrm{pl,rad}}$ harmonics in relation to their corresponding eigenfrequencies f_{eig} at a certain operation point can be analyzed.

4.3.2 Structural Analysis

Detailed 3-D manufacturing CAD models were taken as basis for the structural analysis to determine the location of relevant eigenfrequencies f_{eig}. From these models, all moving parts, as well as small features, such as small holes, chamfers and rounds, were removed. These simplifications reduced in case of the LS2ph3p60N machine the required number of mesh elements from 147 000 to 72 000 by approximately a factor two. The maximal element size was set for all machines to 0.01 m. A sensitivity analysis for the mesh size in the LS2ph3p60N machine with half the element size showed a shift in the eigenfrequencies f_{eig} below 1 %, while prolonging the simulation time from 10 min to 3 h by a factor 18 on a high-performance computing cluster (Intel Xeon X7550, 2.0 GHz, 256 GB RAM, 64-Bit operating system). For parametrization of the structural model, guidelines from [Kas11] were applied. Especially, the weight of the windings is considered in the stator, as it was confirmed in parameter variations to have the largest impact on eigenfrequencies, if neglected.

(a) LS2ph3p60N and LS2ph2p68N (b) HS2ph2p45N and HS3ph1p49N

Fig. 4.26: Meshed structural models of machine housings.

The resulting eigenfrequencies f_{eig} of significant modes from the harmonic response analysis are listed in table 4.17 for various machine surfaces. The relevant mode shapes are mode$_0$ for all machines, mode$_2$ for the HS3ph1p49N machine, mode$_4$ for HS2ph2p45N and LS2ph2p68N machine and mode$_6$ for LS2ph3p60N machine. The surface of the machine's housing, which is basically represented by a cylindrical shell, is named `Main`. The surface of the side facing the ICE is named `Front`, and the opposite end plate is named `Back`. From table 4.17 it can be observed that the eigenfrequency f_{eig} of the various surfaces for a given mode$_{n_{\mathrm{m}}}$ only differs in the range of 1 %.

The general implications drawn from literature ([Fie07; Kas11]) are supported by these results. The HS2ph2p45N and HS3ph1p49N machines with lower outer stator diameter D_{st} and larger stack length L_{stk} compared to the LS2ph3p60N and LS2ph2p68N machines show a higher mode$_0$ eigenfrequency f_{M0} (see table 4.17). As the HS2ph2p45N and HS3ph1p49N machine have a constant stator outer diameter D_{st} and stack length L_{stk} the mode$_0$ eigenfrequency f_{M0} is with approximately 8.5 kHz also similar, only slightly shifted by the differing stator yoke thickness $w_{\mathrm{y,s}}$. The eigenfrequencies f_{M2}, f_{M4} and f_{M6} of the non-zero modes mode$_{n_{\mathrm{m}}}$ increase with increasing mode order n_{m}.

Beside these general implications, more explicit conclusions can be drawn from the location of the eigenfrequencies listed in table 4.17. In the LS2ph2p68N machine, the mode$_4$ and mode$_0$ eigenfrequency f_{M4} and f_{M0} are very close to each other. Avoiding the eigenfrequencies by shifting the operational speed as suggested in [Bös14] might be impossible as the electric base frequency f_{el} of 500 Hz at nominal generator speed $n_{\mathrm{SRG,nom}}$ leads to a high harmonic density. The LS2ph3p60N machine shows a difference of about 1700 Hz between mode$_0$ and mode$_6$ eigenfrequencies. For the low-speed scenario this machine is, therefore, preferable.

For the HS3ph1p49N machine, the mode$_2$ eigenfrequency f_{M2} is located around 3.6 kHz in the well audible range. This low value signifies that around 13 500 rpm the 4$^{\mathrm{th}}$ harmonic

	Surface		
	`Main`	`Back`	`Front`
f_{M0}	8509	8425	8554
f_{M2}	3609	3619	3619

(a) HS3ph1p49N

	Surface		
	`Main`	`Back`	`Front`
f_{M0}	8550	8433	8610
f_{M4}	12910	13100	12890

(b) HS2ph2p45N

	Surface		
	`Main`	`Back`	`Front`
f_{M0}	6331	6300	6366
f_{M4}	5813	5881	5835

(c) LS2ph2p68N

	Surface		
	`Main`	`Back`	`Front`
f_{M0}	5685	5696	5701
f_{M6}	7361	7366	7379

(d) LS2ph3p60N

Table 4.17: Eigenfrequencies f_{eig} of relevant mode orders n_{m} for machine surfaces calculated with ANSYS. Machine data listed in table A.2 and A.6. Considered housing depicted in fig. 4.26.

of the electric base frequency f_{el} will excite f_{M2} within the operation range of the SRG. Due to the high amplitude of such a low harmonic, as depicted in fig. 4.25b, strong vibrations have to be expected. In the HS2ph2p45N machine the mode$_4$ eigenfrequency f_{M4} ranges around 13 kHz and is, therefore, only excited by harmonics of an order greater than seven. As the excitation of mode$_0$ eigenfrequency f_{M0} is expected to be similar in both machines, due to the similar frequency value as well as the equal electric base frequency f_{el} in both machines, the HS2ph2p45N machine is preferable for the high-speed scenario.

4.3.3 Acoustic Analysis at Nominal Operation Point

To support the general discussion in section 4.3.1 - 4.3.2, the average surface velocities v_{surf} depicted fig. 4.27 for simulations and measurements are analyzed at the stationary operation point NOP_{M} (see table A.11). For this analysis efficiency optimal control angles (θ_{on},θ_{fw},θ_{off}) as listed in table A.12 - A.14 are employed.

Fig. 4.27a depicts the simulated average radial surface velocity v_{surf} of the three surfaces listed in table 4.17 for the LS2ph2p68N, LS2ph3p60N, HS2ph2p45N and HS3ph1p49N machines. For frequencies up to 6 kHz the odd harmonics, which excite a mode$_4$, show a higher amplitude than the even harmonics, which excite a mode$_0$, in the LS2ph2p68N machine. At 5.5 kHz and 6 kHz the 11^{th} and 12^{th} harmonic show the highest absolute amplitudes of all harmonics in this machine with 54.6 dB and 50.8 dB, respectively. Both harmonics are close to their corresponding eigenfrequencies f_{M4} and f_{M0} (see table 4.17c). In the LS2ph3p60N machine even harmonics, which excite a mode$_0$, show a higher amplitude than the odd harmonics, which excite a mode$_6$. The 8^{th} harmonic at 6 kHz shows with 51.4 dB the highest amplitude in this machine as it is close to the corresponding mode$_0$ eigenfrequency f_{M0}. The mode$_6$ eigenfrequency f_{M6} is most closely excited by the 9^{th} harmonic, which shows with 40.3 dB a amplitude by 11.1 dB below the 8^{th} harmonic. Due to the lower electric frequency f_{el} the LS2ph2p68N shows clearly a higher harmonic density than the LS2ph3p60N machine.

As expected from the discussion in section 4.3.2, in the HS3ph1p49N machine the 2nd harmonic at 3.3 kHz, which excites a mode$_2$, shows the highest amplitude with 42 dB due to its proximity of the mode$_2$ eigenfrequency f_{M2} around 3.6 kHz (see table 4.17a). Excitation of the mode$_0$ eigenfrequency f_{M0} at about 8.5 kHz is irrelevant for this specific machine and operation point, as the exciting 6th harmonic is sufficiently far away at 9.9 kHz. In the HS2ph2p45NX machine, the two relevant mode$_0$ and mode$_4$ eigenfrequencies f_{M0} and f_{M4} (see table 4.17b) are not excited by corresponding even and odd harmonics, respectively. The highest amplitudes can be found for the 2nd and 4th harmonics, which excite a mode$_0$,

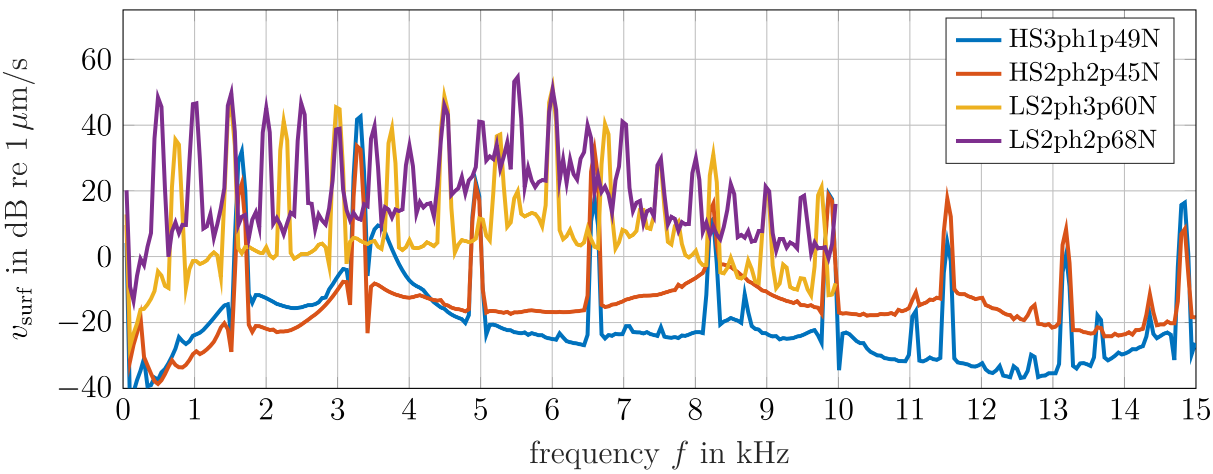

(a) simulated v_{surf} on surface `Main`, `Front` and `Back` (see section 4.3.2).

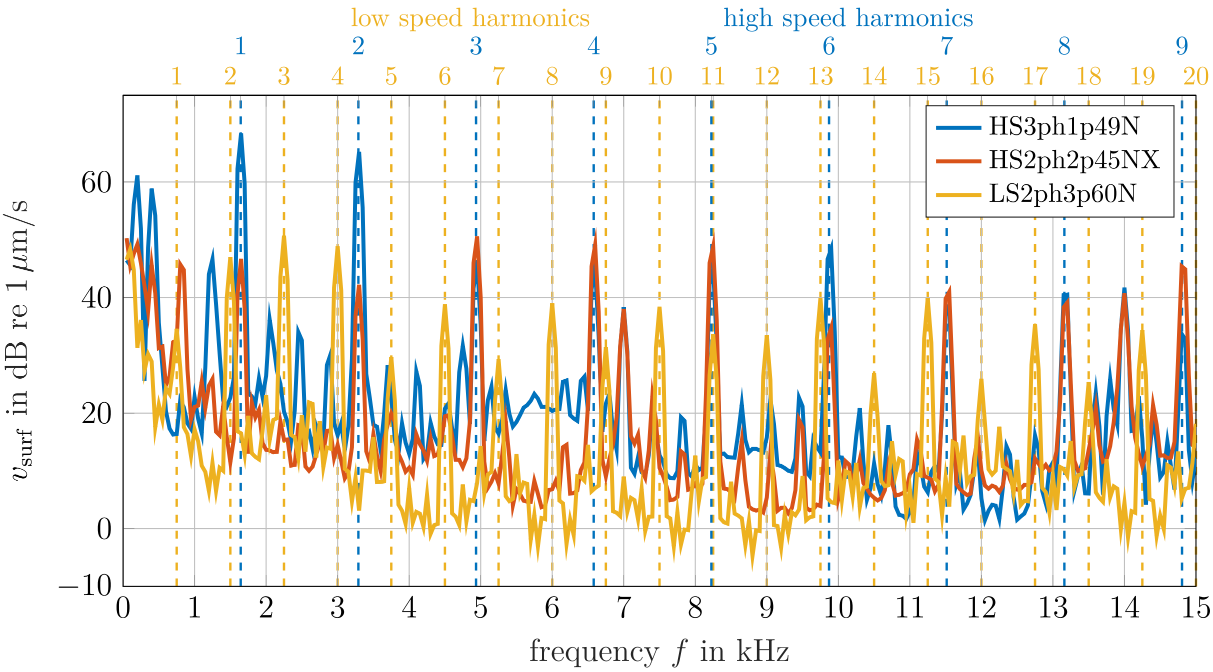

(b) measured v_{surf} on `Main` surface. Sensor positions specified in section A.4.1

Fig. 4.27: Comparison of simulated and measured average radial surface velocity v_{surf} at operation point NOP_{M} (see table A.11).

with approximately 33 dB. While the 1st and 2nd harmonic show higher amplitudes in the HS3ph1p49N machine compared to the HS2ph2p45N machine, the 4th and 7th harmonics show a higher amplitude in the HS2ph2p45N machine.

In fig. 4.27b, the average measured surface velocity on the `Main` surface is depicted for the three built prototypes LS2ph3p60N, HS2ph2p45NX and HS3ph1p49N. In accordance with the simulation results even harmonics, which excite a mode_0, show a higher amplitude than the odd harmonics, which excite a mode_6, in the measurements of the LS2ph3p60N machine. In contrast to simulation, the 2nd, 3rd and 4th harmonic show with about 51 dB a higher amplitude than the 8th with 39 dB. Also the amplitude of harmonics above 7 kHz are increased compared to simulation. In the measurement of the HS3ph1p49N machine, the 1st and 2nd harmonics show with 68.4 dB and 65.2 dB, respectively, similar amplitudes. As the 2nd harmonic is farther away than the 4th harmonic from the corresponding mode_2 eigenfrequency f_{M2} (see table 4.17a), the mode_2 vibration form can be expected to be problematic throughout the complete operation range. In the measurement of the HS2ph2p45NX machine, the 3rd, 4th and 5th harmonics show with 50.6 dB, 49.1 dB and 48.9 dB, respectively, similar amplitudes. These values suggest that mode_0 and mode_4 excitation is comparable in reality, in contrast to the simulation results. For both high-speed machines, the measurements are underestimated by around 20 dB. Reasons for this error could be found in a wrong quantitative force excitation as well as a too high damping ratio or stator stiffness in the structural model. Another reason might be the limited number of measurement points, while in simulation an average over the complete outer surface was evaluated.

In simulation, the excitation of the structure by mechanical effects caused by the rotational speed n_{SRG} and n_{ICE} is completely neglected. This fact, leads to a generally increased surface velocity amplitude, especially below 1 kHz, when comparing fig. 4.27a with fig. 4.27b. In the high-speed machines, additional distinctive peaks can be perceived in the mechanical noise compared to the LS2ph3p60N machine (see fig. 4.27b), due to the double excitation of high- and low-speed shaft. Furthermore, in the high-speed machines the tooth engagement frequency f_{trans} in the gearbox as defined in (4.12) is present.

$$f_{\mathrm{trans}} = N_{\mathrm{teeth,pinion}} \cdot \frac{n_{\mathrm{SRG}}}{60} \tag{4.12}$$

Due to the 17 pinion teeth on the SRG shaft, this excitation can be found at $f_{\mathrm{trans}} = 7\,\mathrm{kHz}$ in fig. 4.27b. Both HS3ph1p49N and HS2ph2p45N show an identical amplitude, suggesting that the increased torque ripple of the HS2ph2p45N machine has no negative impact on the vibrations caused by the gearbox. The amplitude of the mechanical excitation in fig. 4.27b is at least 10 dB below the electromagnetic excitation by the harmonics of the electric base frequency f_{el}.

4.3.4 Conclusion on Acoustics at Nominal Operation Point

Some preliminary conclusions about the acoustic behavior of the considered LS2ph2p68N LS2ph3p60N, HS2ph2p45N and HS3ph1p49N machines can be drawn from the analysis of the force excitation (see section 4.3.1), the location of the eigenfrequencies f_{eig} (see section 4.3.2) and the behavior at the operation point NOP_{M} (see table A.11) (see section 4.3.3). Further analysis regarding dynamic operation and the coupling with an ICE will be conducted in section 5.3.

The HS2ph2p45N machines offers a reduced peak pole radial force $F_{\mathrm{pl,rad}}$ by 30 % compared to the LS2ph2p68N machine and 20 % compared to the HS3ph1p49N and LS2ph3p60N machines (see fig. 4.25a). Due to the increased electric base frequency f_{el}, the harmonic content is lower in the HS2ph2p45N and HS3ph1p49N machine compared to the low-speed LS2ph3p60N and LS2ph2p68N machines. The amplitude of the harmonics is lowest in the HS3ph1p49N machine (see fig. 4.25b), due to its 3-phase configuration. From this force analysis, it can be concluded that the high-speed HS2ph2p45N and HS3ph1p49N machines are advantageous over the low-speed LS2ph3p60N and LS2ph2p68N machines.

The high-speed HS2ph2p45N and HS3ph1p49N machines show higher mode$_0$ eigenfrequencies f_{M0} compared to the low-speed LS2ph3p60N and LS2ph2p68N machines (see table 4.17). Higher eigenfrequencies are favorable according to [Fie07], therefore, both high-speed machines are advantageous considering mode$_0$ vibrations. Considering the non-zero modes, the HS3ph1p49N machines shows a critical mode$_2$ eigenfrequency f_{M2} at 3.6 kHz, while the mode$_4$ eigenfrequency f_{M4} of the LS2ph2p68N machine is with 5.9 kHz close to the mode$_0$ eigenfrequency f_{M0} at 6.3 kHz. The HS2ph2p45N and LS2ph3p60N machines are uncritical with their relevant non-zero eigenfrequencies f_{M4} and f_{M6} around 13 kHz and 7.4 kHz, respectively. While the HS2ph2p45N machine is most advantageous from the structural analysis, the LS2ph3p60N machine is preferable for the low-speed scenario.

Simulation results at the operation point NOP_{M} (see table A.11) confirmed, that the high harmonic density and the proximity of the f_{M4} and f_{M0} eigenfrequencies in the LS2ph2p68N machine leads to high average surface velocity v_{surf} amplitudes around 6 kHz (see fig. 4.27a). The lower harmonic density of the LS2ph3p60N machine in combination with the higher f_{M6} eigenfrequency leads to less strong excited harmonics in the audible range. This dynamic analysis supports the findings of the structural analysis for the low-speed scenario. Comparing the simulation results of both high-speed HS2ph2p45N and HS3ph1p49N machine, no clear conclusion can be drawn, as to which machine is more favorable.

In the measurement, the HS3ph1p49N machine shows a high amplitude of the 1$^{\mathrm{st}}$ and 2$^{\mathrm{nd}}$ harmonic. The maximal amplitude is by 18 dB and 20 dB higher than in the LS2ph3p60N and HS2ph2p45N machine, respectively. While the HS2ph2p45N is clearly preferable for the high-speed scenario, the comparison of the two scenarios is ambivalent. Up to 5 kHz the LS2ph3p60N machine shows higher harmonic amplitudes than the HS2ph2p45N machine, above 5 kHz the HS2ph2p45N harmonics are higher. The preferred machine might depend, therefore, on the fact, which frequency range is more critical in the complete system. At the same time, the HS2ph2p45N shows a harmonic density by a factor two lower than the LS2ph3p60N machine. This can be advantageous to avoid eigenfrequencies f_{eig} of additional components in the complete system, such as the ICE housing or other mechanical parts.

4.4 Additional Aspects

4.4.1 Material Costs

To compare the different solutions from an economic point of view, the material costs are evaluated. Only the iron core material in the employed grade, the copper wires, the housing as well as the shaft and gearbox are included in this comparison. For the gearbox, an aluminum housing and steel gearwheels are assumed. Any additional components, such as screws, o-rings, sealing and bearings, as well as variations in the production steps, are neglected. The resulting material weights of the considered machines in this section are listed in table A.5. For the different employed materials, the specific costs listed in table 4.18 are considered. The prices are derived from commodity exchange prices in 2018 and commercial offers available. As prices are volatile, it is not possible to offer a general comparison. However, with the material weights listed in table A.5 a recalculation with different prices is easily possible.

c_{Al}	c_{Cu}	c_{litz}	c_{steel}	c_{NO10}	c_{NO20}	c_{NO30}
2 €/kg	10 €/kg	20 €/kg	1.8 €/kg	4 €/kg	2 €/kg	1 €/kg

Table 4.18: Considered specific material prices for machine comparison in fig. 4.28.

As shown in fig. 4.28 the copper wires account for the largest cost share for all machines. However, for the LS2ph3p60N machine, not the iron core material, but the housing follows second. This is due to the heavy endcaps and thick shaft required by the pancake shaped design. The increase in stack length L_{stk} in the HS2ph2p45NI1, HS3ph1p49NI1 and LS2ph3p60NI1 by 2 %, 4 % and 15 % compared to the LS2ph3p60N,

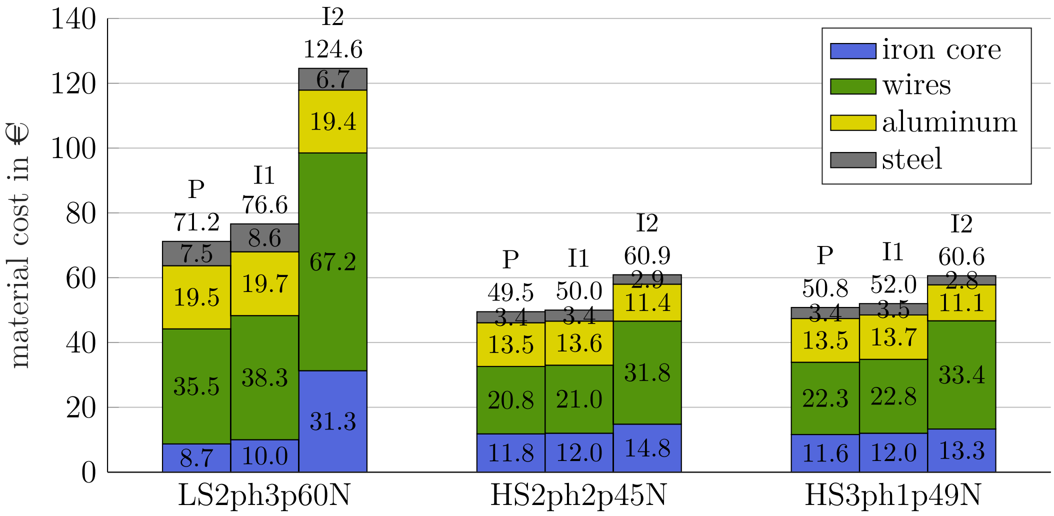

Fig. 4.28: Overview on the material cost of machine permutations(see table A.4 - A.5). P: built prototypes; I1: thermally equal machines with increased stack length L_{stk}; I2: machines with iron core material NO10 and litz wire (see section 4.2.3) and decreased stack length L_{stk}.

HS2ph2p45N and HS3ph1p49N machine, respectively, has nearly no effect in the high-speed machines HS2ph2p45NI1 and HS3ph1p49NI1, only increasing the total costs by 8 % in the LS2ph3p60N machine. Comparing the thermally equal machines, the HS2ph2p45NI1 machine offers the lowest material costs, by 2 € and 26.6 € lower than the HS3ph1p49NI1 and LS2ph3p60NI1 machine, respectively.

The reduction of the stack length L_{stk} in the improved LS2ph3p60NI2, HS2ph2p45NI2 and HS3ph1p49NI2 machine with NO10 iron core material and litz wire (see section 4.2.4) compensates in partial the increased material costs compared to the LS2ph3p60NI1, HS2ph2p45NI1 and HS3ph1p49NI1 machines. While the LS2ph3p60NI2 machine shows a cost increase by 48 €, for the HS2ph2p45NI2 and HS3ph1p49NI2 high-speed machines the total cost are only increased by 10.9 € and 8.6 €, respectively. The efficiency benefit in the HS2ph2p45NI2 and HS3ph1p49NI2 machines of approximately 3 pp only requires a cost increase of approximately 20 %, while the LS2ph3p60NI2 machine efficiency benefit of 1.5 pp requires a 50 % material cost increase.

Comparing the two speed scenarios, about 35 % of the material cost can be saved by increasing $n_{\mathrm{SRG,nom}}$ from 7.5 krpm in the LS2ph3p60NI1 machine to 25 krpm in the HS2ph2p45NI1 machine. This cost saving effect arises from to the reduced required copper and smaller housing. The increased cost of NO20 iron core material compared to NO30 is nearly compensated in the HS2ph2p45NI1 machine compared to the LS2ph3p60NI1 machine by the reduced amount of material required. For the improved machines, the cost reduction is with 51 % between the HS3ph1p49NI2 and the LS2ph3p60NI2 machine larger than for the I1 machines. Up to a specific cost of 30 €/kg for c_{litz}, the high-speed HS3ph1p49NI2 machines has a lower total material cost than the LS2ph3p60NI1 machine at a better efficiency by about 2 pp.

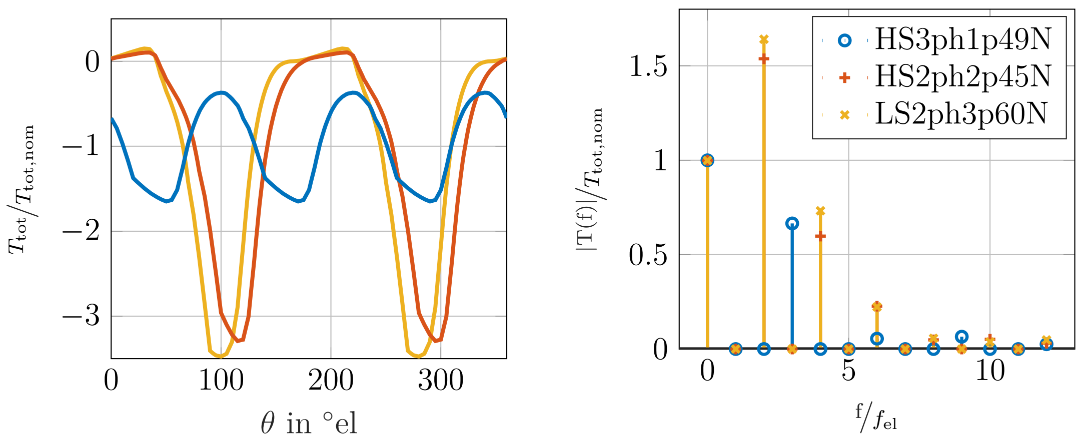

(a) dynamic torque ripple

(b) torque harmonic content

Fig. 4.29: Torque harmonic content of low- and high-speed machines (see table A.2 and table A.6) at operation point NOP_{M} (see table A.11).

4.4.2 Torque Profile

As mentioned in section 4.1.1, operating the machine in SPC improves the machine efficiency but limits the torque controllability. Fig. 4.29 depicts the dynamic output torque T_{tot} and the harmonic content of the three prototype machines. The torque ripple always appears at N_{ph} multiples of f_{el}. The total harmonic distortion (THD) (see table 4.19) of both the HS2ph2p45N and the LS2ph3p60N are very similar, while the THD of the HS3ph1p49N machine is by a factor three lower. The relation of peak torque $T_{tot,pk}$ to $T_{tot,nom}$ of the HS3ph1p49N machine is by a factor two lower compared to the 2-phase machines. Both values define the required strength of shafts and gearboxes. However, as long as the generators are combined with classical ICE, from a system perspective no negative influence is expected. On the one hand, the torque ripple of a 4-stroke ICE is expected to be higher than these values, on the other hand, the base frequency of the ripple at nominal speed is at $2 \cdot f_{el}$, hence 1.5 kHz for the low-speed machine. Compared to 62.5 Hz of a four stroke single-cylinder ICE [MST12; And+17] as employed in [Ind+16] this high-frequency oscillations are expected to be barely noticeable.

	LS2ph3p60N	HS2ph2p45N	HS3ph1p49N
THD	293 %	267 %	87 %
$T_{tot,pk}/T_{tot,nom}$	3.5	3.3	1.65

Table 4.19: Dynamic torque behavior at 20 kW.

Starting Torque

To avoid an external starter as secondary component, the generator needs to be able to start the combustion engine at any mechanical position. 3-phase machines offer this inherently due to the phase overlap. For the 2-phase machines, a starting adaptation, in terms of an unsymmetrical rotor as shown in table A.2 for the HS2ph2p45N and LS2ph3p60N machine, is required. Fig. 4.30 shows the effect of such an asymmetric rotor pole on T_{tot} of the

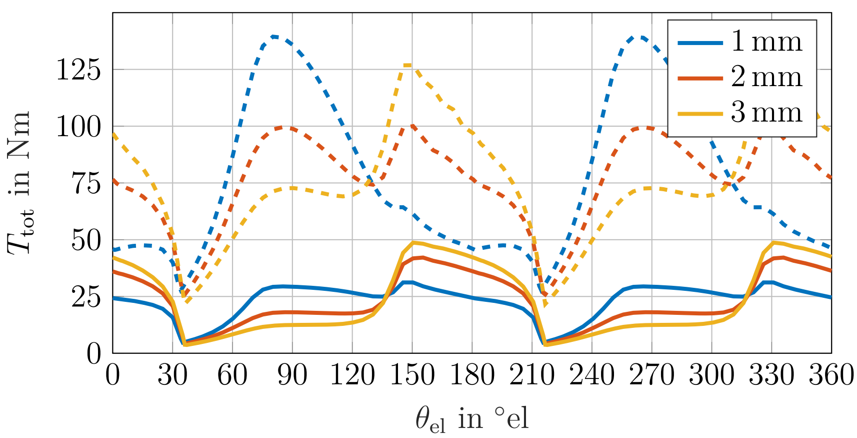

Fig. 4.30: Influence of $d_{g,step}$ on static positive torque of LS2ph3p60N machine. i_{ph} = 200 A (solid lines) and 500 A (dashed lines)

LS2ph3p60N machine at two constant currents. The total rotor pole angle is two times β_r (see fig. 3.4b) in this case. To achieve a rather constant T_{tot} over a wide range, d_{gsp} needs to be chosen between 1- and 2-times d_g. The former applies if the unsaturated torque is sufficient, while the latter is a better choice in the saturated region. The dip around 30 °el can be reduced by a wider step, however, this introduces a dip around 120 °el. From experience, increasing the total rotor pole angle by an additional 4 – 8 °el is a good compromise between the two torque dips.

4.5 Chapter Conclusion

In this chapter, the three prototypes listed in table A.2 were analyzed in detail at the nominal operation point in terms of machine efficiency, thermal behavior and power density, acoustic behavior as well as material cost and torque profile.

For the low-speed LS2ph3p60N prototype, a machine efficiency η_{mach} of 91.5 % was measured. This value is 1 pp higher than the measured η_{mach} of the high-speed HS2ph2p45N and HS3ph1p49N machines including a gearbox (see section 4.1.5). The measured efficiency difference between the low- and high-speed machines is reduced to 0.4 pp with small mechanical changes, as measurements of the HS2ph2p45NX machine (see section A.2.1.1) achieved a machine efficiency of 91.1 %. Therefore, it can be concluded that an increase of the nominal generator speed $n_{SRG,nom}$ from 7.5 to 25 krpm can be performed without a significant reduction in machine efficiency of the resulting design.

Furthermore, the potential impact of litz wire and high performance NO10 iron core material was analyzed by extensive FEAs. In combination with a stator slot closure, for all machines mentioned above, machine efficiencies $\eta_{mach} >= 93\,\%$ are predicted in simulation (see section 4.1.5). As these efficiency improvements reduce the frequency dependent losses, namely eddy-current copper losses $P_{l,cu,eddy}$, iron core losses $P_{l,fe}$ and mechanical losses $P_{l,m}$, the highest efficiency is reached for the high-speed HS2ph2p45NI2 machine with 93.5 %, including the gearbox. Without a gearbox, a machine efficiency η_{mach} around 95 % is predicted.

From the conducted analysis the following design advise for SRG with high electric base frequency f_{el} is derived in terms of eddy-current copper losses $P_{l,cu,eddy}$. As the dc-link voltage u_{dc} influences the possible number of turns per pole $N_{w,pl}$ and the effective copper diameter d_w, consequently, the eddy-current copper losses $P_{l,cu,eddy}$ are affected (see fig. 4.4a). Thus, a variation of the dc-link voltage u_{dc} directly influences the reachable machine efficiency η_{mach}. Therefore, high electric frequencies f_{el} are not advised for low-voltage applications (e.g. 48 V) of 20 kW-SRG.

The conducted analysis and measurements have confirmed gravimetric total power densities $\xi_{P,tot}$ of 0.7 kW/kg and 1.2 kW/kg for the low-speed (LS2ph3p60N) and the high-speed (HS2ph2p45N, HS3ph1p49N) machines, respectively (see table 4.16; derived for a coil hot spot temperature $\vartheta_{coil,hs} = 180\,°C$). The increase of the nominal speed $n_{SRG,nom}$ from 7.5 to 25 krpm only leads to an increase in power density by about 72 %. This means, the active material torque density $\phi_{T,act}$ of the high-speed machines is lower than that of the low-speed machine. Therefore, it can be concluded that the high-speed machines are limited in their power density by the thermal boundaries, rather than the electromagnetic torque capability. Employing the above mentioned efficiency improvements (litz wire, NO10, stator slot closure) an increase of the total power density $\xi_{\mathrm{P,tot}}$ to 0.8 kW/kg and 1.7 kW/kg in the low-speed and the high-speed machines is predicted, respectively (see table 4.16).

For the thermal prediction in pre-design stage it was found that iron core losses $P_{\mathrm{l,fe}}$ have a minor influence on the hot spot coil temperature $\vartheta_{\mathrm{coil,hs}}$ (see fig. 4.19), while a correct approximation of the eddy-current copper losses $P_{\mathrm{l,cu,eddy}}$ is more important for all considered machines (see fig. 4.20). Static measurements showed, that for a accurate prediction of the hot spot coil temperature $\vartheta_{\mathrm{coil,hs}}$ the influence of the end-winding copper losses $P_{\mathrm{l,cu,dc,Ew}}$ has to be further analyzed (see section 4.2.1). Finally, the knowledge that the hot spot in SRGs is located rather on the air gap facing coil surface has to be incorporate in the reduced LPTN, employed in pre-design (see section 3.3.1).

Simulations showed reduced peak pole radial force $F_{\mathrm{pl,rad}}$, lower amplitudes of the force harmonics and higher mode$_0$ eigenfrequencies f_{M0} for the high-speed machines compared to the low-speed machines (see section 4.3.1 and table 4.17). However, the HS3ph1p49N machine has a critical mode$_2$ eigenfrequency f_{M2} at 3.6 kHz. Therefore, the 2-phase HS2ph2p45N machine is most advantageous considering the structural analysis. These findings are supported by dynamic measurements, in which the 3-phase HS3ph1p49N machine shows a high amplitude of the 1$^{\mathrm{st}}$ and 2$^{\mathrm{nd}}$ harmonic. The maximal amplitude of an individual harmonic is up to 20 dB higher than in the LS2ph3p60N and HS2ph2p45N machine. Based on the results, at a given electric base frequency f_{el}, a 2-phase machine with a higher pole pair number n_{p} is preferred regarding acoustic behavior.

In terms of material costs, it was found that the copper wires account for the largest cost share for all machines, followed by the iron core material in the high-speed machines and the housing in the low-speed machine (see fig. 4.28). About 35 % of the material cost can be saved by increasing $n_{\mathrm{SRG,nom}}$ from 7.5 to 25 krpm. The reduced stack length L_{stk} in the analyzed machines with the efficiency improvements (litz wire, NO10, stator slot closure; see section 4.2.4) compensates partially the increased material costs.

Finally, the resulting torque profile of the machine designs were compared in simulation. Results show that torque ripple is increased by approximately a factor two in the 2-phase machines compared to the 3-phase machine (see table 4.19). However, no negative effect of this increased torque ripple was observed in the acoustic measurements at nominal operation speed (see section 4.3.3). In a REX it is, therefore, only considered a minor disadvantage of the 2-phase configurations.

5 Control and Power Variation

In this chapter the influence of varying control parameters on the SRG operation at nominal and partial load are investigated. Firstly, a fast empirical-analytical method to predict eddy-current copper losses $P_{\mathrm{l,cu,eddy}}$ over a wide generator speed range is introduced with the help of coupled FEA analysis. Secondly, the effect of the control parameters on machine efficiency η_{mach} at full and partial load is investigated in simulation and measurement. Thirdly, acoustic behavior at variable power is analyzed, including a discussion of acoustic improvement potential by means of control. Finally, the chapter summarizes system aspects, regarding the power electronic components and the power source, and closes with a conclusion.

5.1 Control Strategy

At full load, SRG are often operated in single pulse control (SPC) to obtain a high machine efficiency η_{mach} (see fig. 4.1). From pre-tuned control angles (i.e. θ_{on}, θ_{off}), a closed loop control of θ_{on} is derived for example in [ST04]. By the choice of control parameters, the machine efficiency η_{mach} [KM06] or acoustic behavior can be influenced [Kle+14].

In recent publications [KMV13; NB13; KD15; KD17] the positive effect on machine efficiency η_{mach} of an additional freewheeling period $\Delta\theta_{\mathrm{fw}}$, also called zero-voltage-loop (ZVL), is discussed for 3-phase SRG. [KMV13] derives a control strategy with constant turn-off angle θ_{off} and a ZVL from classic approaches without ZVL, such as [ST04]. [NB13] investigates the effect of a freewheeling period $\Delta\theta_{\mathrm{fw}}$ on the iron core losses $P_{\mathrm{l,fe}}$ in a 250 kW high-speed SRG in motoring mode. Finally, in [KD15; KD17] the investigation focused on machine efficiency η_{mach} improvements at partial load for an automotive traction drive. The presented publications have in common, that they leave out an analysis of frequency dependent eddy-current copper losses $P_{\mathrm{l,cu,eddy}}$ in the coils.

In the machines discussed in this thesis, the eddy-current copper losses $P_{\mathrm{l,cu,eddy}}$ account for a relevant share of the total copper losses $P_{\mathrm{l,cu,ac}}$ (e.g. 40 % in the HS3ph1p49N machine, see fig. 4.12a). Therefore, the impact of a freewheeling period $\Delta\theta_{\mathrm{fw}}$ on these losses is of interest, to identify machine efficiency η_{mach} improvement potential.

5.1.1 Analysis of Eddy-Current Copper Losses

Design influences on eddy-current copper losses $P_{\mathrm{l,cu,eddy}}$ were discussed in section 4.1.1. To analyze the effect of SRG control parameters on eddy-current copper losses $P_{\mathrm{l,cu,eddy}}$ a wide range of turn-off angles θ_{off} and freewheeling periods $\Delta\theta_{\mathrm{fw}}$ as well as operational speeds is analyzed with the help of coupled FEA, described in section 2.3 and [Sch15]. As calculation of eddy-current copper losses $P_{\mathrm{l,cu,eddy}}$ by the coupled FEA is very time consuming, the retrieved results are used for a generalization for fast drive simulations.

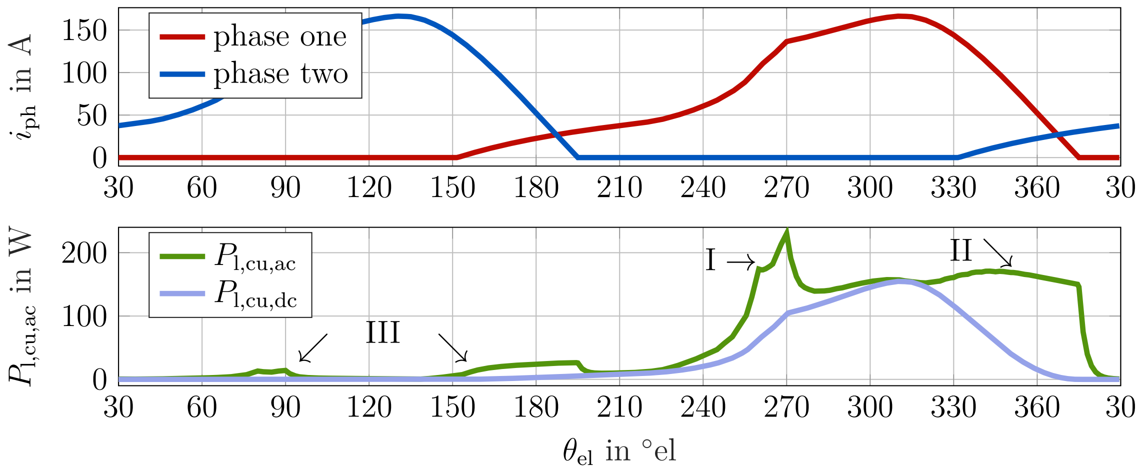

Fig. 5.1: Exemplary current i_{ph} and total copper loss $P_{l,cu,ac}$ waveforms. HS2ph2p45N machine (see table A.2) at operation point NOP_S (see table A.10).

Fig. 5.1 depicts an exemplary phase current i_{ph} and the resulting total copper losses $P_{l,cu,ac}$ in comparison to the dc copper losses $P_{l,cu,dc}$. It can be seen that the total copper losses $P_{l,cu,ac}$ deviate from the dc copper losses $P_{l,cu,dc}$ mainly in three areas. The high eddy-current copper losses $P_{l,cu,eddy}$ are caused by the high gradients in i_{ph} during magnetization (I) and demagnetization (II). The deviation around (III) is caused by the corresponding peaks (I) and (II) in the second machine phase.

To analyze the effect of turn-off angle θ_{off} and freewheeling period $\Delta\theta_{fw}$ on the eddy-current copper losses $P_{l,cu,eddy}$, one parameter is kept constant, while the second parameter is variated. For each combination ($\Delta\theta_{fw}$ - θ_{off}), the corresponding turn-on angle θ_{on} is then searched to deliver the requested nominal total output torque $T_{tot,nom}$ of the specific operation point.

Influence of Turn-Off Angle

The influence of turn-off angle θ_{off} on eddy-current copper losses $P_{l,cu,eddy}$ is analyzed with the help of the HS3ph1p49N machine at the operation point NOP_S (see table A.10). For several turn-off angle θ_{off}, the corresponding freewheeling period $\Delta\theta_{fw}$ of lowest machine losses is found. Then the turn-off angle θ_{off} is increased and decreased by 10 °el. The resulting total copper losses $P_{l,cu,ac}$ of four sets are shown in fig. 5.2a.

For all sets, increasing turn-off angle θ_{off} increases the eddy-current copper losses $P_{l,cu,eddy}$. The strongest effect can be found around turn-off angle $\theta_{off} = 270$ °el and 290 °el, where eddy-current copper losses $P_{l,cu,eddy}$ are increased by 70 W or 26 %. At the turn-off angle θ_{off} set around 230 °el, eddy-current copper losses $P_{l,cu,eddy}$ increase even while the dc copper losses $P_{l,cu,dc}$ decrease, due to a reduced phase RMS current $I_{ph,rms}$. The reason for the increase in eddy-current copper losses $P_{l,cu,eddy}$ can be deduced from the losses over electrical angle θ_{el} depicted in fig. 5.2b. An increased peak around turn-off angle θ_{off} can be found, caused by the main flux running for a longer period through the winding. Therefore, the turn-off angle θ_{off} of minimal total copper losses $P_{l,cu,ac}$, including the eddy-current copper losses $P_{l,cu,eddy}$, is slightly lower compared to the θ_{off} of minimal dc copper losses $P_{l,cu,dc}$.

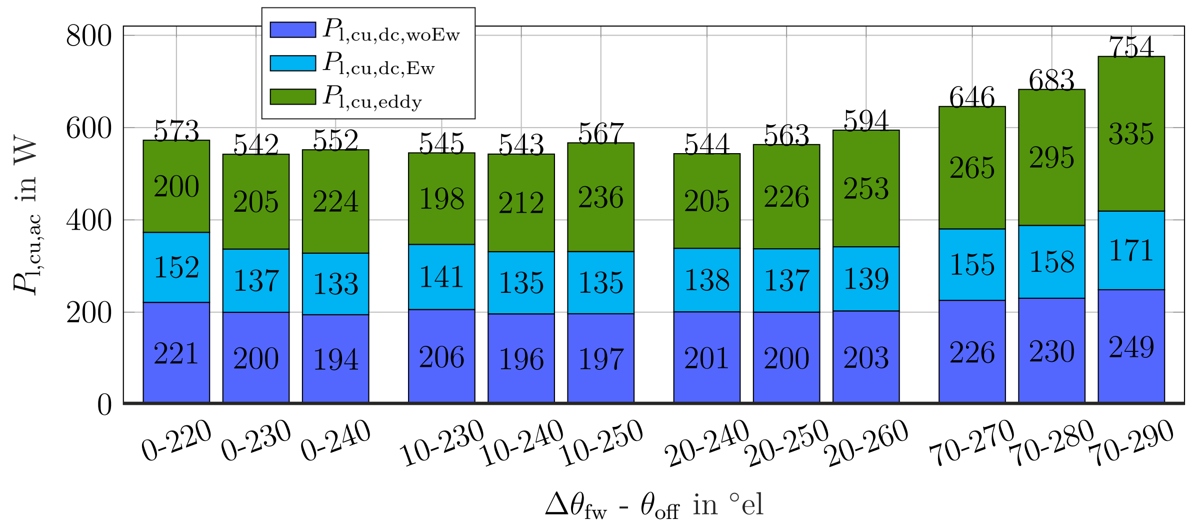

(a) separation of copper losses $P_{\mathrm{l,cu,ac}}$

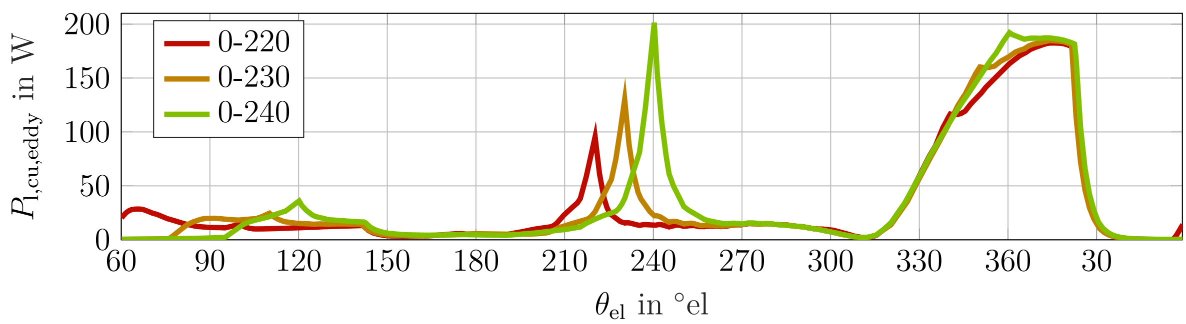

(b) eddy-current copper losses $P_{\mathrm{l,cu,eddy}}$ over electrical angle θ_{el} in one phase for selected control combinations ($\Delta\theta_{\mathrm{fw}}$ - θ_{off}) from fig. 5.2a

Fig. 5.2: Separation of copper losses $P_{\mathrm{l,cu,ac}}$ for variation of turn-off angle θ_{off} with constant freewheeling period $\Delta\theta_{\mathrm{fw}}$ for each set of three θ_{off}. θ_{on} adapted to fulfill torque requirement. Coupled FEA of HS3ph1p49N machine (see table A.2) at operation point NOP_{S} (see table A.10).

Influence of Freewheeling Period

Fig. 5.3 depicts eddy-current copper losses $P_{\mathrm{l,cu,eddy}}$ over the electrical angle θ_{el} for a freewheeling period $\Delta\theta_{\mathrm{fw}} = 0 - 20\,°\mathrm{el}$ at turn-off angle $\theta_{\mathrm{off}} = 240\,°\mathrm{el}$. Introducing a freewheeling period $\Delta\theta_{\mathrm{fw}}$ of 10 °el, the eddy-current copper losses $P_{\mathrm{l,cu,eddy}}$ peak shown in fig. 5.3 around turn-off angle θ_{off} is reduced from 201 W to 91 W by 55 % compared to $\Delta\theta_{\mathrm{fw}} = 0\,°\mathrm{el}$. This can be explained by a reduced change in pole flux linkage Ψ_{pl}, due to the zero voltage at the phase terminals during freewheeling period $\Delta\theta_{\mathrm{fw}}$. The remaining loss waveform is only minimally affected, resulting in reduced eddy-current copper losses $P_{\mathrm{l,cu,eddy}}$ by 12 W and total copper losses $P_{\mathrm{l,cu,ac}}$ by 9 W for a $\Delta\theta_{\mathrm{fw}} = 10\,°\mathrm{el}$ compared to 0 °el at $\theta_{\mathrm{off}} = 240\,°\mathrm{el}$ depicted in fig. 5.2a.

At a larger turn-off angle $\theta_{\mathrm{off}} = 270\,°\mathrm{el}$ also a reduction of eddy-current copper losses $P_{\mathrm{l,cu,eddy}}$ can be seen in fig. 5.4 when a freewheeling period is introduced. At this turn-off angle θ_{off}, the eddy-current copper losses $P_{\mathrm{l,cu,eddy}}$ can be reduced by 103 W or 28 % with a

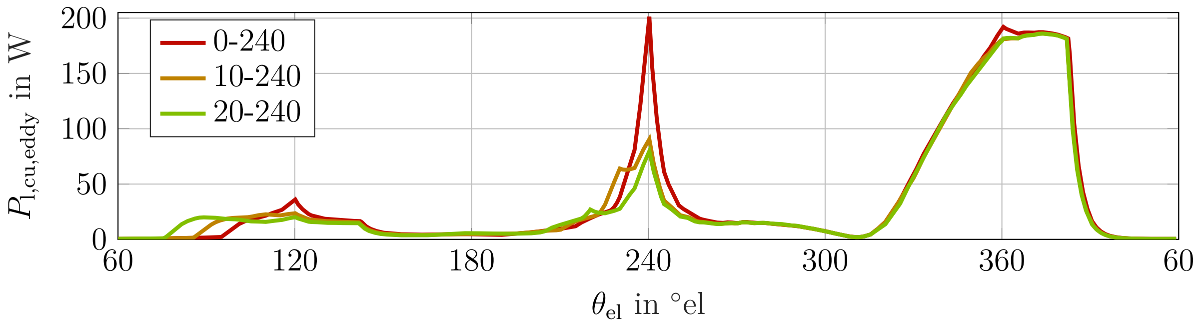

Fig. 5.3: Eddy-current copper losses $P_{\mathrm{l,cu,eddy}}$ over electrical angle θ_{el} for variation of freewheeling period $\Delta\theta_{\mathrm{fw}}$ at $\theta_{\mathrm{off}} = 240\,°\mathrm{el}$. Corresponding losses depicted in fig. 5.2a. Coupled FEA of HS3ph1p49N (see table A.2) machine at operation point NOP_{S} (see table A.10).

freewheeling period $\Delta\theta_{\mathrm{fw}} = 60\,°\mathrm{el}$ compared to $0\,°\mathrm{el}$. A freewheeling period $\Delta\theta_{\mathrm{fw}} > 60\,°\mathrm{el}$, leads to an increase in eddy-current copper losses $P_{\mathrm{l,cu,eddy}}$ along with dc copper losses $P_{\mathrm{l,cu,dc}}$. This can be linked to a non-linear increasing phase RMS current $I_{\mathrm{ph,rms}}$, as the turn-on angle θ_{on} needs to be strongly reduced to still reach the requested generator output torque $T_{\mathrm{tot,nom}}$.

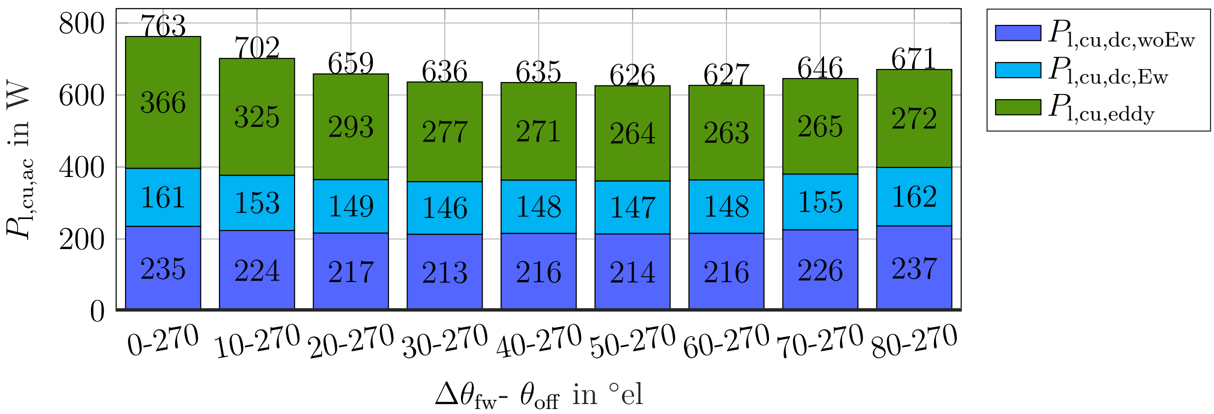

Fig. 5.4: Separation of copper losses $P_{\mathrm{l,cu,ac}}$ for variation of freewheeling period $\Delta\theta_{\mathrm{fw}}$ at $\theta_{\mathrm{off}} = 270\,°\mathrm{el}$. θ_{on} selected to fulfill torque requirement $T_{\mathrm{tot,nom}}$. Coupled FEA of HS3ph1p49N (see table A.2) machine at operation point NOP_{S} (see table A.10).

Analysis at Variable Speed

Fig. 5.5 depicts machine losses $P_{\mathrm{l,mach}}$ for varying turn-off angle θ_{off} and the freewheeling period $\Delta\theta_{\mathrm{fw}}$ for lowest total system losses $P_{\mathrm{l,tot}}$ at two different operational speeds with constant generator output torque T_{tot}. It can be seen that the loss optimal freewheeling period $\Delta\theta_{\mathrm{fw}}$ and turn-off angle θ_{off} are smaller at high speed compared to low speed, which is caused by the reduced back EMF e at lower speed. By applying an increasing freewheeling period $\Delta\theta_{\mathrm{fw}}$, the phase current i_{ph} trajectory is kept closer to the optimal coenergy loop.

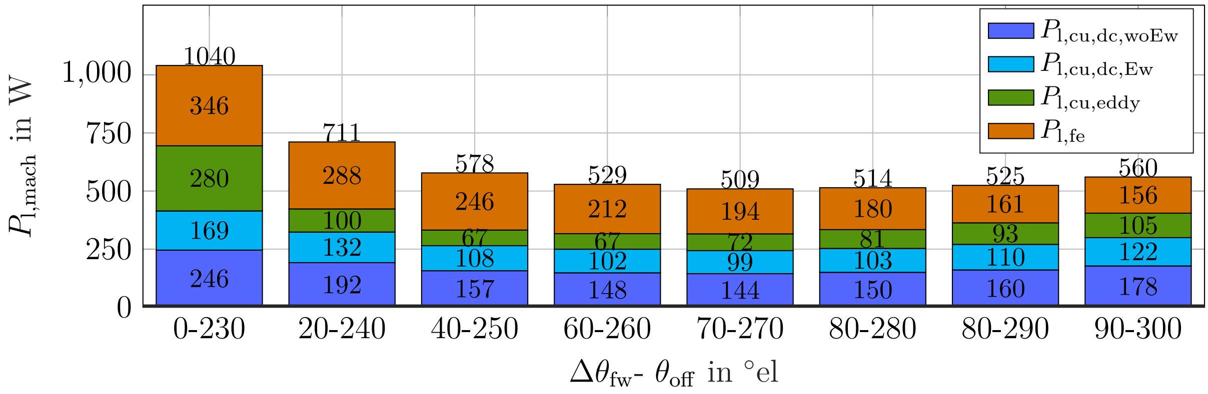

(a) operation point $PART_{\mathrm{S},40}$ (see table A.10)

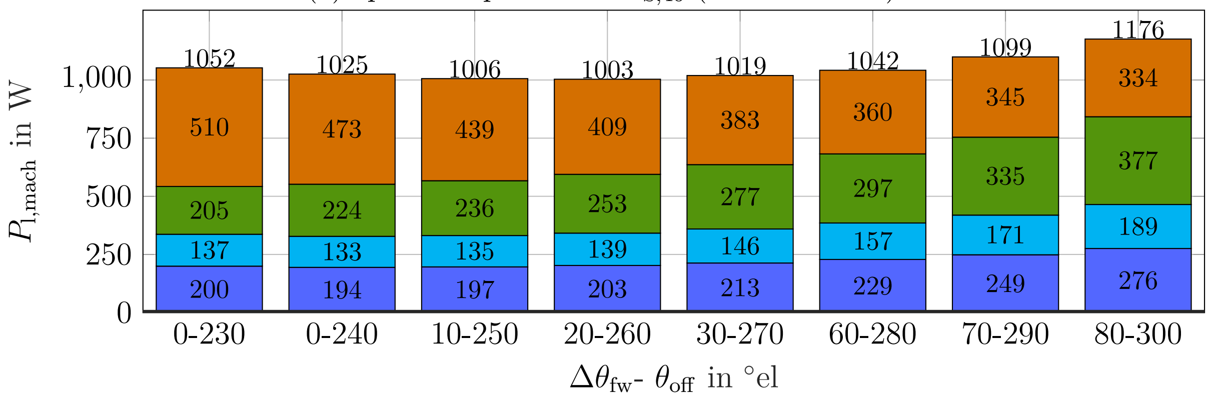

(b) operation point NOP_{S} (see table A.10)

Fig. 5.5: Machine losses $P_{\mathrm{l,mach}}$ at different operational speeds. For each turn-off angle θ_{off} the freewheeling period $\Delta\theta_{\mathrm{fw}}$ with minimal machine losses $P_{\mathrm{l,mach}}$ is depicted. Coupled FEA of HS3ph1p49N (see table A.2).

This reduces not only the phase RMS current $I_{\mathrm{ph,rms}}$ but also the frequency dependent eddy-current copper losses $P_{\mathrm{l,cu,eddy}}$ and iron core losses $P_{\mathrm{l,fe}}$. The control angle combinations $\Delta\theta_{\mathrm{fw}}$ - θ_{off} of lowest total copper losses $P_{\mathrm{l,cu,ac}}$ are found at 0 - 230 °el and 70 - 270 °el for NOP_{S} (see table A.10) and $PART_{\mathrm{S},40}$ (see table A.10), respectively. Considering the iron losses $P_{\mathrm{l,fe}}$ the minimum is shifted to 20 - 260 °el at NOP_{S} (see table A.10), while it is not affected at $PART_{\mathrm{S},40}$ (see table A.10). In the HS3ph1p49N machine a wide range of control parameter with nearly constant machine losses $P_{\mathrm{l,mach}}$ can be found at both operation points. This confirms the preliminary assumption derived from the analyzes of the HS2ph2p51N machine in [BMD16].

Analytical Prediction of Eddy-Current Copper Losses

The coupled FEA results shown before required a long simulation and exportation time as stated in section 2.3.2. To be able to quickly predict eddy-current copper losses $P_{\mathrm{l,cu,eddy}}$ at various speeds in simulation, a new empirical frequency dependent prediction method for eddy-current copper losses $P_{\mathrm{l,cu,eddy}}$ is proposed in this thesis.

Fig. 5.6 depicts the eddy-loss ratios p_{eddy} and $p_{\mathrm{eddy,woEw}}$ over a wide range of generator speeds n_{SRG} for several machines at the point of minimal machine losses $P_{\mathrm{l,mach}}$. The control angles at each simulated speed are selected from the coupled FEA results, as exemplary depicted for the HS3ph1p49N machine in fig. 5.5. It can be derived from fig. 5.6 that both parameters are linear proportional to the electric base frequency f_{el} for all considered machines. Therefore, the frequency dependency of the eddy-loss ratios p_{eddy} and $p_{\mathrm{eddy,woEw}}$ can be described by the linear relationships stated in (5.1). The required parameters are retrieved by a curve-fit to the coupled FEA results in fig. 5.6 (thick lines). The fit-parameters are listed for the four investigated machines in table 5.1, the resulting curves are shown as thin lines in fig. 5.6.

$$\begin{aligned} p_{\mathrm{eddy}}(f_{\mathrm{el}}) &= p_{\mathrm{eddy,0}} + (\alpha_{\mathrm{eddy}} \cdot f_{\mathrm{el}}) \\ p_{\mathrm{eddy,woEw}}(f_{\mathrm{el}}) &= p_{\mathrm{eddy,woEw,0}} + (\alpha_{\mathrm{eddy,woEw}} \cdot f_{\mathrm{el}}) \end{aligned} \tag{5.1}$$

Comparing the analyzed machines, the following observations can be made. In the HS3ph1p49N machine, the frequency slope $\alpha_{\mathrm{eddy,woEw}}$ is larger than in the HS2ph2p45N machine. This is caused by the smaller gap spacer d_{gsp} (see fig. 3.10) in the HS2ph2p45N compared to the HS3ph1p49N machine as listed in table 4.2. The HS3ph1p49N1 machine with

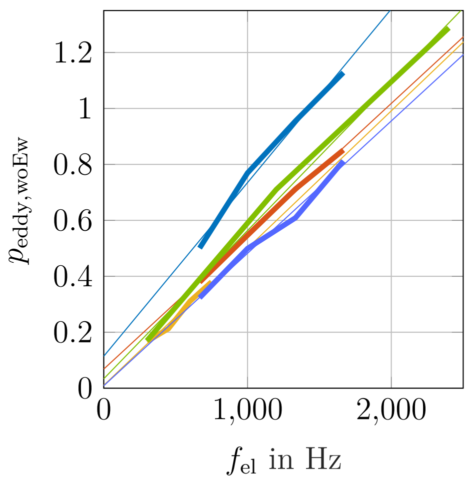

(a) eddy-loss ratio $p_{\mathrm{eddy,woEw}}$ over f_{el}

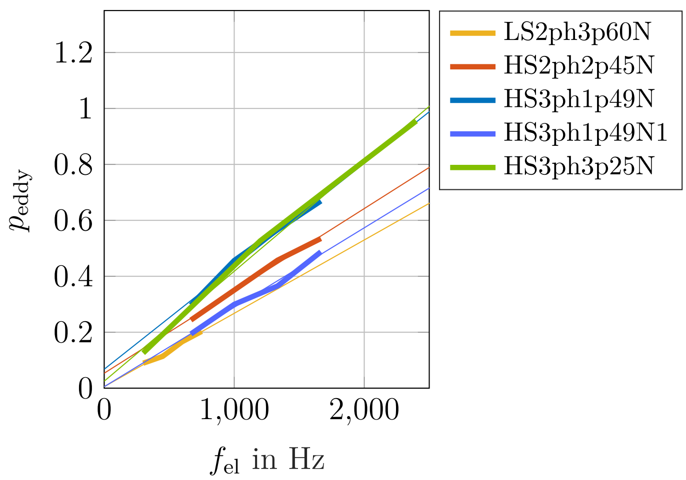

(b) eddy-loss ratio p_{eddy} over f_{el}

Fig. 5.6: Eddy-loss ratio p_{eddy} over the electric base frequency f_{el} for several machines at $\vartheta_{\mathrm{coil}} = 170\,°\mathrm{C}$. thick lines: simulated values, thin lines: fit on (5.1)

	$p_{\mathrm{eddy,woEw}}$		p_{eddy}	
	$p_{\mathrm{eddy,woEw,0}}$	$\alpha_{\mathrm{eddy,woEw}}$	$p_{\mathrm{eddy,0}}$	α_{eddy}
LS2ph3p60N	0.01	0.049 /(100 Hz)	0.005	0.026 /(100 Hz)
HS2ph2p45N	0.068	0.047 /(100 Hz)	0.053	0.029 /(100 Hz)
HS3ph1p49N	0.114	0.062 /(100 Hz)	0.068	0.037 /(100 Hz)
HS3ph1p49N1	0.009	0.047 /(100 Hz)	0.005	0.028 /(100 Hz)
HS3ph3p25N	0.034	0.053 /(100 Hz)	0.025	0.039 /(100 Hz)

Table 5.1: Frequency coefficients of (5.1) for machines listed in table A.2 - A.6.

adapted gap spacer d_{gsp} has the same frequency slope $\alpha_{\mathrm{eddy,woEw}}$ as the HS2ph2p45N machine for the eddy-loss ratio $p_{\mathrm{eddy,woEw}}$. For both HS2ph2p45N and HS3ph1p49N1 machines, the frequency slope is, with $0.002\,/(100\,\mathrm{Hz})$ or $4\,\%$, slightly lower than in the LS2ph3p60N machine. This deviation could arise from the lower dc-link voltage u_{dc}, which leads to a lower number or turns per pole $N_{\mathrm{w,pl}}$, and consequently increased wire diameter d_{w}, to achieve a energy efficient SPC (see section 4.1.1). For the frequency slopes α_{eddy}, the HS2ph2p45N and HS3ph1p49N machines show a higher value than the LS2ph3p60N machine. This change compared to $\alpha_{\mathrm{eddy,woEw}}$ is caused by the higher share of dc copper losses in the end-windings $P_{\mathrm{l,cu,dc,Ew}}$ compared to the dc copper losses without end-windings $P_{\mathrm{l,cu,dc,woEw}}$ in the LS2ph3p60N machine. Assuming no eddy-current copper losses $P_{\mathrm{l,cu,eddy}}$ in the end-windings, in pre-design it is, therefore, recommended to predict the total copper losses $P_{\mathrm{l,cu,ac}}$ with the help of $p_{\mathrm{eddy,woEw}}$ and $P_{\mathrm{l,cu,dc,woEw}}$ and to add $P_{\mathrm{l,cu,dc,Ew}}$ afterwards.

The eddy-ratio parameters listed in table 5.1 are all derived for electric base frequencies $f_{\mathrm{el}} \gg 0\,\mathrm{Hz}$. Close to electric base frequency $f_{\mathrm{el}} = 0\,\mathrm{Hz}$ the eddy-current losses $P_{\mathrm{l,cu,eddy}}$ are caused by current transients due to the inverter switching, rather than the electric base frequency f_{el}. This results in strong deviations of eddy-loss offsets $p_{\mathrm{eddy,0}}$ and $p_{\mathrm{eddy,woEw,0}}$ listed in table 5.1, even for the HS2ph2p45N and HS3ph1p49N1 machines with similar coil design. Therefore, extrapolation to very low frequencies is not recommended.

To verify, if the linearizion can be transfered to different SRG types, results of the HS3ph3p25N machine investigated in [Ral+17] are analyzed (machine parameters listed in table A.6). At 2.4 kHz and 21 Nm this automotive traction machine delivers 26 kW, close to the machines investigated in this thesis. The gap spacer d_{gsp} of 4.5 mm has a similar value than the d_{gsp} in the HS2ph2p45N, HS3ph1p49N and LS2ph3p60N machines (see table 4.2). At constant torque with a hysteresis current control (HCC), the eddy-loss ratio $p_{\mathrm{eddy,woEw}}$ rises in the HS3ph3p25N machine from 0.17 to 1.29 for an electric base frequency of 0.3 – 2.4 kHz(i) [Ral+17]. The corresponding fit of the eddy-loss ratios p_{eddy} and $p_{\mathrm{eddy,woEw}}$ are depicted in fig. 5.6. The fit parameters of (5.1) are listed in table 5.1. The HS3ph3p25N machine shows with $\alpha_{\mathrm{eddy,woEw}} = 0.053\,/(100\,\mathrm{Hz})$ a slightly higher value than the LS2ph3p60N, HS2ph2p45N and HS3ph1p49N1 machines (see table 5.1). Deviations arise from the higher power of the machine, the differing dc-link voltage u_{dc} and the chosen control at nominal operation point, as these factors strongly influence the winding design (see section 4.1.1).

From the discussed results it can be concluded that predicting the eddy-loss ratio $p_{\mathrm{eddy,woEw}}$ in pre-design by a constant $p_{\mathrm{eddy,woEw,0}}$ and $\alpha_{\mathrm{eddy,woEw}}$ is valid for machines with similar gap spacer d_{gsp}, power class and dc-link voltage u_{dc}. An extrapolation to a wide range of electric base frequencies f_{el} is a valid approach, as shown by the comparison of the high-speed machines HS2ph2p45N and HS3ph1p49N1 with the HS3ph3p25N machine [Ral+17] and the LS2ph3p60N machine. Errors can arise from the choice of control, as well as the exact wire placement and diameter d_{w} as well as the effective current density J_{eff}.

Fig. 5.7 shows a comparison of eddy-loss ratio $p_{\mathrm{eddy,woEw}}$ over electric base frequency f_{el} of the LS2ph3p60N, HS2ph2p45N and HS3ph1p49N machines (see table A.2) retrieved with coupled FEA in green (see section 2.3.2) and the analytical approach summarized in [Car08] in red (see (2.24)). For the HS2ph2p45N and HS3ph1p49N machine, the analytical

(i) This signifies a machine speed $n_{\mathrm{SRG}} = 1.5$ – $12\,\mathrm{krpm}$

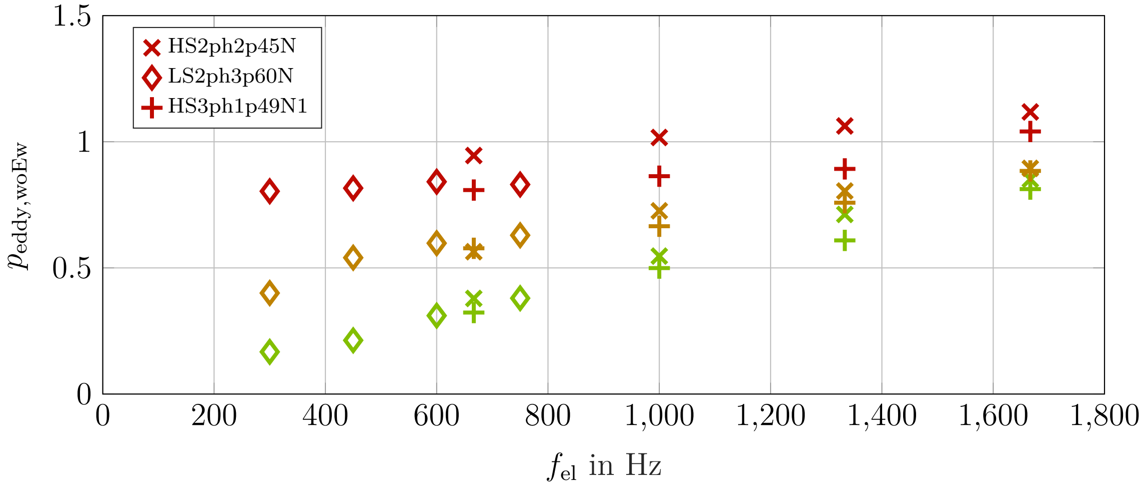

Fig. 5.7: Eddy-loss ratio $p_{\text{eddy,woEw}}$ over electric base frequency f_{el} for various calculation methods. Machines listed in table A.2. green: coupled FEA (see section 2.3.2), red: analytic results (see (2.24)) orange: analytic results (see (2.24)) considering only $k = 1{,}2$

approach shows eddy-loss ratios $p_{\text{eddy,woEw}}$ by 30 % higher than the coupled FEA at their nominal electric base frequency $f_{\text{el}} = 1.67\,\text{kHz}$. With a decrease in electric base frequency f_{el}, this deviation increases. For the LS2ph3p60N machine the relative error at its nominal electric frequency $f_{\text{el}} = 750\,\text{Hz}$ is about 224 %. This error in the LS2ph3p60N machine is very close to the error of the HS2ph2p45N machine at comparable electric base frequency f_{el} (e.g. 250 % at 667 Hz). Therefore, a fundamental error in the frequency modeling either in the employed FEA tool FLUX2D or the analytical equations is suspected. Considering only the first two harmonics ($k = 1{,}2$), as shown in fig. 5.7 in orange, the dependency on electric base frequency f_{el} is modeled much closer with the analytical approach compared to the coupled FEA. This suggests that higher frequency components are not considered in the FEA.

For further analysis, the eddy-current copper losses $P_{\text{l,cu,eddy}}$ are modeled by the frequency dependent eddy-loss ratio p_{eddy} listed in table 5.1, as this approach shows a better approximation over speed compared to the analytical approach (see (2.24)). In addition, it is closer to the modeling approach during pre-design (see section 3.3.2), as no specific winding information is required.

Assuming a constant eddy-loss ratio p_{eddy} for each machine leads to modeling errors within one operation point for a variation of control angles. Fig. 5.8a depicts a comparison of coupled FEA results (see section 2.3.2) for total copper losses $P_{\text{l,cu,ac}}$ and iron core losses $P_{\text{l,fe}}$ with results from the look-up based system simulation model (see section 2.3.1) and a constant eddy-loss ratio p_{eddy} employed in the loss post-processing at the operation point NOP_{S} (see table A.10). As can be seen in fig. 5.8b the real eddy-loss ratio p_{eddy} varies around the mean ratio at some control parameter combinations. This leads to reduced eddy-current copper losses $P_{\text{l,cu,eddy}}$ by a short freewheeling period $\Delta\theta_{\text{fw}}$ in the coupled FEA, while dc copper losses $P_{\text{l,cu,dc}}$ stay nearly constant. The point of minimal copper losses $P_{\text{l,cu,ac}}$ shifts, therefore, to a larger freewheeling period $\Delta\theta_{\text{fw}}$ compared to the look-up

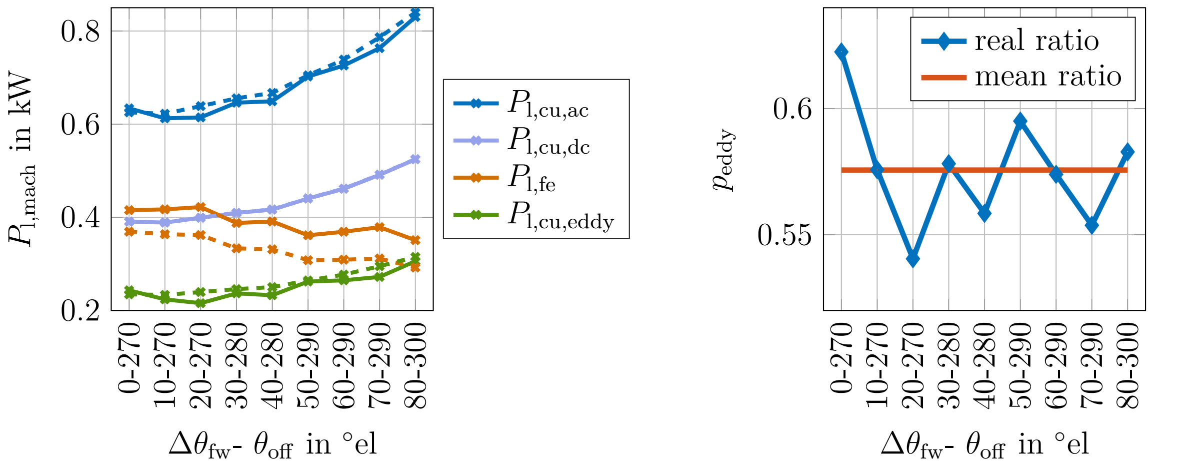

(a) look-up based system simulation model with constant p_{eddy} (dashed lines) and coupled FEA (solid lines)

(b) p_{eddy} from coupled FEA and average value for look-up based system simulation model

Fig. 5.8: Machine losses $P_{\mathrm{l,mach}}$ and eddy loss ratio p_{eddy}. For each freewheeling period $\Delta\theta_{\mathrm{fw}}$ the turn-off angle θ_{off} with minimal machine losses $P_{\mathrm{l,mach}}$ is depicted. HS2ph2p51N machine (see table A.2) at operation point NOP_{S} (see table A.10). Figure adapted from [BMD16].

based system simulation model that uses a constant eddy-loss ratio p_{eddy}.

The coupled FEA results in fig. 5.8a show a nearly constant offset in iron core losses $P_{\mathrm{l,fe}}$. A similar offset was found for the HS2ph2p45N machine with same iron core cross section but a number of turns per pole $N_{\mathrm{w,pl}} = 49$ in section 4.1.2 (see table 4.4). This offset is caused by the average flux density B_{pt} in the different machine parts considered in the iron core loss calculation method p_{Bertotti} employed in the look-up base simulation model, while the coupled FEA calculates the losses in each mesh element (see (2.29)). However, as the offset is nearly constant, the control angles of minimal losses are not affected.

5.2 Drive Losses and Efficiency

With the help of the determined eddy-loss ratio p_{eddy} parameters listed in table 5.1, the drive losses $P_{\mathrm{l,drive}}$ are analyzed at four operating points in the range of 50 – 100 % nominal input shaft power $P_{\mathrm{m,sh}}$. The power variation is performed by a variation of generator speed n_{SRG} rather than generator output torque T_{tot}, as an ICE has its best efficiency close to maximal torque [MST12]. A variation of generator output torque T_{tot} is afterwards briefly discussed and a conclusion is drawn. If not mentioned otherwise, in the next sections the system parameters listed in table 5.2 are employed.

5.2.1 Loss Distribution

Fig. 5.9 depicts the drive losses $P_{\mathrm{l,drive}}$ and its separation into the fundamental copper losses $P_{\mathrm{l,cu,ac}}$, iron core losses $P_{\mathrm{l,fe}}$ and inverter losses $P_{\mathrm{l,inv}}$ for the nominal operation point of the

Electrical system parameter	Value
source internal resistance $R_{\mathrm{i,src}}$	$100\,\mathrm{m\Omega}$
dc-link capacitance C_{dc}	$1\,\mathrm{mF}$
cable inductance L_{cab}	$3\,\mu\mathrm{H}$
cable resistance R_{cab}	$1\,\mathrm{m\Omega}$

Table 5.2: Parametrization of electric systems used within the simulations for control variation.

three built prototypes. Simulation results for the remaining operation points at variable speed and partial load can be found in section A.4.3. For all results, only the points at grid intersections were simulated. Intermediate results are linearly interpolated for better visualization. The red circles indicate the control angle combination of lowest losses.

Machine Losses

Total copper losses $P_{\mathrm{l,cu,ac}}$ (first row in fig. 5.9) rise both with freewheeling period $\Delta\theta_{\mathrm{fw}}$ and with turn-off angle θ_{off}. Beside for the HS2ph2p45N machine, the minimum is found for a freewheeling period $\Delta\theta_{\mathrm{fw}} = 0\,°\mathrm{el}$. This behavior is directly linked to a proportionality of the phase RMS current $I_{\mathrm{ph,rms}}$ to both control parameters [BMD16]. In the HS2ph2p45N machine the minimum can be found at freewheeling period $\Delta\theta_{\mathrm{fw}} = 10\,°\mathrm{el}$, however, the benefit is rather small compared to $\Delta\theta_{\mathrm{fw}} = 0\,°\mathrm{el}$. The coupled FEA results shown in fig. 5.8a confirm this. Generally, copper losses $P_{\mathrm{l,cu,ac}}$ are lowest in the HS3ph1p49N machine and highest in the LS2ph3p60N machine.

Iron core losses $P_{\mathrm{l,fe}}$ (second row in fig. 5.9) decrease with an increase in turn-off angle θ_{off} in the investigated range of the control parameters. This behavior is linked to a decrease in peak phase flux linkage $\Psi_{\mathrm{ph,pk}}$ and, consequently, lower flux densities in the core. By varying the freewheeling period $\Delta\theta_{\mathrm{fw}}$, for each turn-off angle θ_{off}, a minimum in iron core losses $P_{\mathrm{l,fe}}$ can be found (e.g. at 40 - 260 °el for the HS3ph1p49N machine). The minimum shifts to larger freewheeling periods $\Delta\theta_{\mathrm{fw}}$ with increasing turn-off angle θ_{off}. While an increase in $\Delta\theta_{\mathrm{fw}}$ decreases the peak phase flux linkage $\Psi_{\mathrm{ph,pk}}$ of each individual phase, it also widens the current pulse. The resulting phase overlap leads to increased flux density B_{pt} in the stator and rotor yokes and, consequently, increased iron core losses $P_{\mathrm{l,fe}}$. The minima of iron core losses $P_{\mathrm{l,fe}}$ can be found for all machines at the upper limit of the investigated control parameters, in contrast to the copper losses $P_{\mathrm{l,cu,ac}}$. Lowest iron core losses $P_{\mathrm{l,fe}}$ are found in the LS2ph3p60N machine, highest losses in the HS3ph1p49N machine.

Additional results for partial load operation points are depicted in section A.4.3.2 - A.4.3.4. At lower speeds, the copper loss $P_{\mathrm{l,cu,ac}}$ minima are shifted to higher values of turn-off angle θ_{off} and freewheeling period $\Delta\theta_{\mathrm{fw}}$. For the iron core losses $P_{\mathrm{l,fe}}$ this effect cannot be seen, due to the limited simulation range. The reduced back EMF e (see (2.9)) at lower speeds is responsible for an increased gradient in phase current i_{ph} and, consequently, the phase RMS current $I_{\mathrm{ph,rms}}$, to reach a constant torque. Increasing the freewheeling period $\Delta\theta_{\mathrm{fw}}$ and shifting demagnetization at lower speeds, leads to a peak phase flux linkage $\Psi_{\mathrm{ph,pk}}$ comparable to the nominal speed and more energy efficient co-energy loops W_{co} [BMD16].

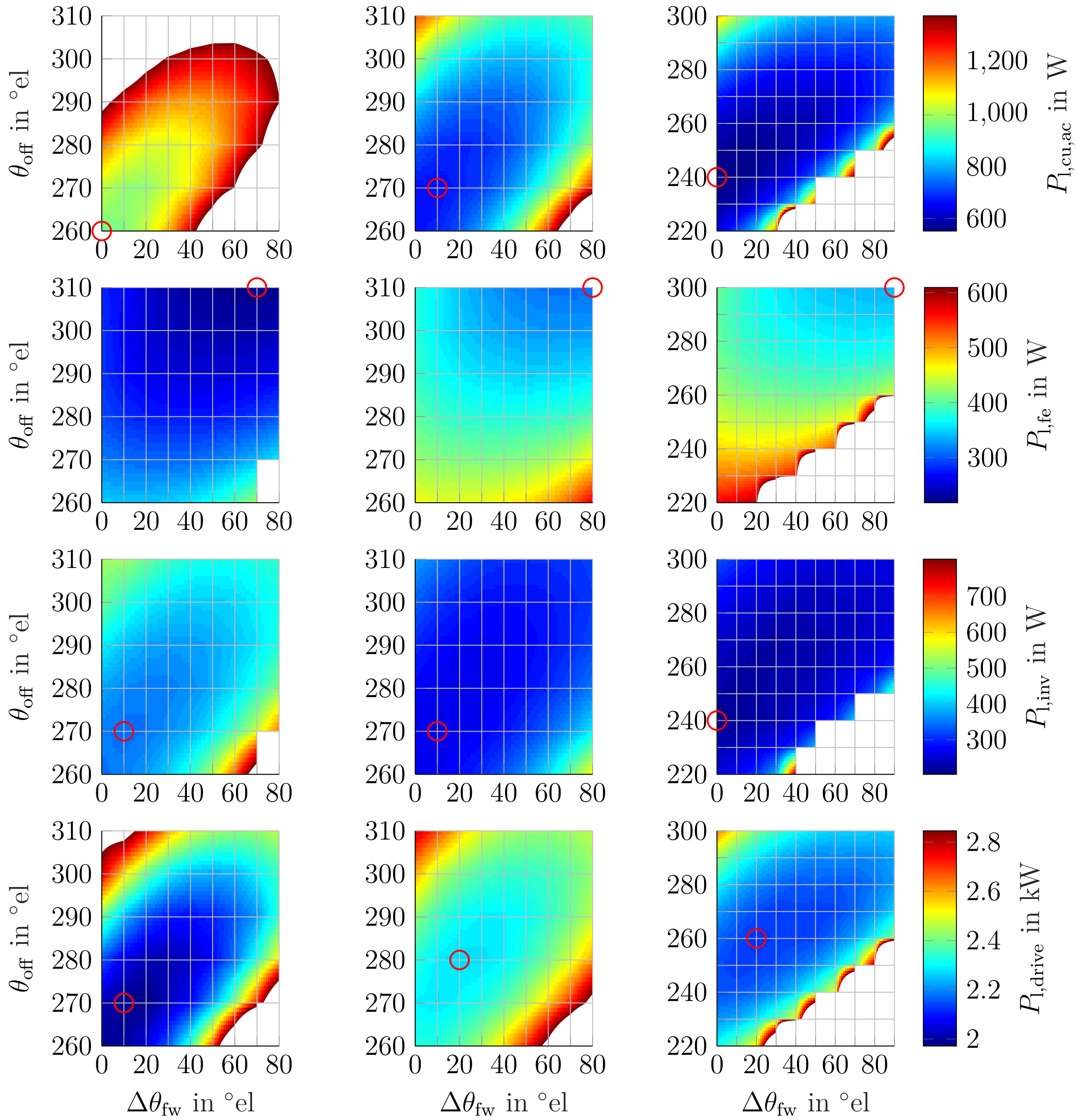

(a) LS2ph3p60N (b) HS2ph2p45N (c) HS3ph1p49N

Fig. 5.9: Simulated drive losses over switching parameters at operation point NOP_{M} (see table A.11). Turn on angle θ_{on} selected to obtain constant torque $T_{\mathrm{tot,nom}}$. Red circles mark loss minimum.

Inverter Losses

To obtain the inverter losses $P_{\mathrm{l,inv}}$ shown in fig. 5.9, all losses were simulated with the chip-characteristics of the automotive Infineon Hybrid Pack™ Light IGBT module [Inf] with three phase legs. To compare the three machines in simulation on a fair basis of equal chip area, it is assumed that the 2-phase machines employ three parallel chips per active switch, while the 3-phase machine employs only two chips per active switch[(ii)]. Compared to the module configuration with one chip per switch, the inverter losses $P_{\mathrm{l,inv}}$ can be reduced in the point of lowest losses by 25 %, 14 % and 8 % in the LS2ph3p60N, the HS2ph2p45N and die HS3ph1p49N machine, respectively. The low reduction ratios are due to the diode-like forward characteristics of IGBTs with a high initial voltage drop at zero forward current. The LS2ph3p60N machine is further disadvantaged, as the IGBTs are designed for a 705 V blocking voltage, resulting in a unnecessarily high forward voltage drop.

The inverter losses $P_{\mathrm{l,inv}}$ show a similar characteristic as the copper losses $P_{\mathrm{l,cu,ac}}$. This is caused by the employed SPC, for which the inverter losses are mainly caused by conduction losses $P_{\mathrm{l,cond}}$ [BMD16]. The small shifts are explained by the non-linearity of the conduction losses $P_{\mathrm{l,cond}}$ and the switching losses $P_{\mathrm{l,sw}}$, the latter being only dependent on switching current i_{sw}, not phase RMS current $I_{\mathrm{ph,rms}}$. This behavior can be confirmed for all three prototypes. Similar to copper losses $P_{\mathrm{l,cu,ac}}$ the lowest and highest losses can be found in the HS3ph1p49N and LS2ph3p60N machine, respectively.

Drive Losses

The combined minima of drive losses $P_{\mathrm{l,drive}}$ are in all machines close to the minima for the copper losses $P_{\mathrm{l,cu,ac}}$. The largest deviation to higher values of turn-off angle θ_{off} and freewheeling period $\Delta\theta_{\mathrm{fw}}$ can be found in the HS3ph1p49N machine, as iron core losses $P_{\mathrm{l,fe}}$ have a larger share in the drive losses $P_{\mathrm{l,drive}}$ than in the other machines. Drive losses $P_{\mathrm{l,drive}}$ are in all machines positively affected by a short freewheeling period $\Delta\theta_{\mathrm{fw}}$, however, the effect is rather small. In both high-speed machines the freewheeling period $\Delta\theta_{\mathrm{fw}}$ of minimal drive losses $P_{\mathrm{l,drive}}$ is slightly larger, due to the larger share of frequency dependent losses. Similar behavior can be found at lower speeds, the minima are only shifted to higher values of turn-off angle θ_{off} and freewheeling period $\Delta\theta_{\mathrm{fw}}$, which is in accordance to the findings in [KD17] at partial load.

5.2.2 Measurement Validation

Fig. 5.10 depicts machine, inverter and drive efficiency η_{mach}, η_{inv} and η_{drive} for measurement and simulation at the operation point NOP_{M} (see table A.11). The remaining operation points can be found in fig. A.6 to fig. A.12. The measured range of control parameters is smaller than in simulation, as it was limited by the increase in coil hot spot temperature $\vartheta_{\mathrm{coil,hs}}$ due to increased total copper losses $P_{\mathrm{l,cu,ac}}$.

At 20 kW, regarding machine efficiency η_{mach} (first row in fig. 5.10), the simulation is best matched for the HS2ph2p45N machine as already found in section 4.1.4. However, for all machines the dependence of machine efficiency η_{mach} on turn-off angle θ_{off} and freewheeling period $\Delta\theta_{\mathrm{fw}}$ found in simulation can be confirmed by the measurements. This tendency is more clearly visible for the low speed operations shown in appendix A.4.3.2 - A.4.3.4, as a larger range of control parameters could be validated on the test bench. Generally, the optima found in measurement are at slightly lower freewheeling period $\Delta\theta_{\mathrm{fw}}$ and turn-off angle θ_{off} than in simulation.

[(ii)] On the test bench both 2-phase machines only employ four chips, while the 3-phase machine employs six chips.

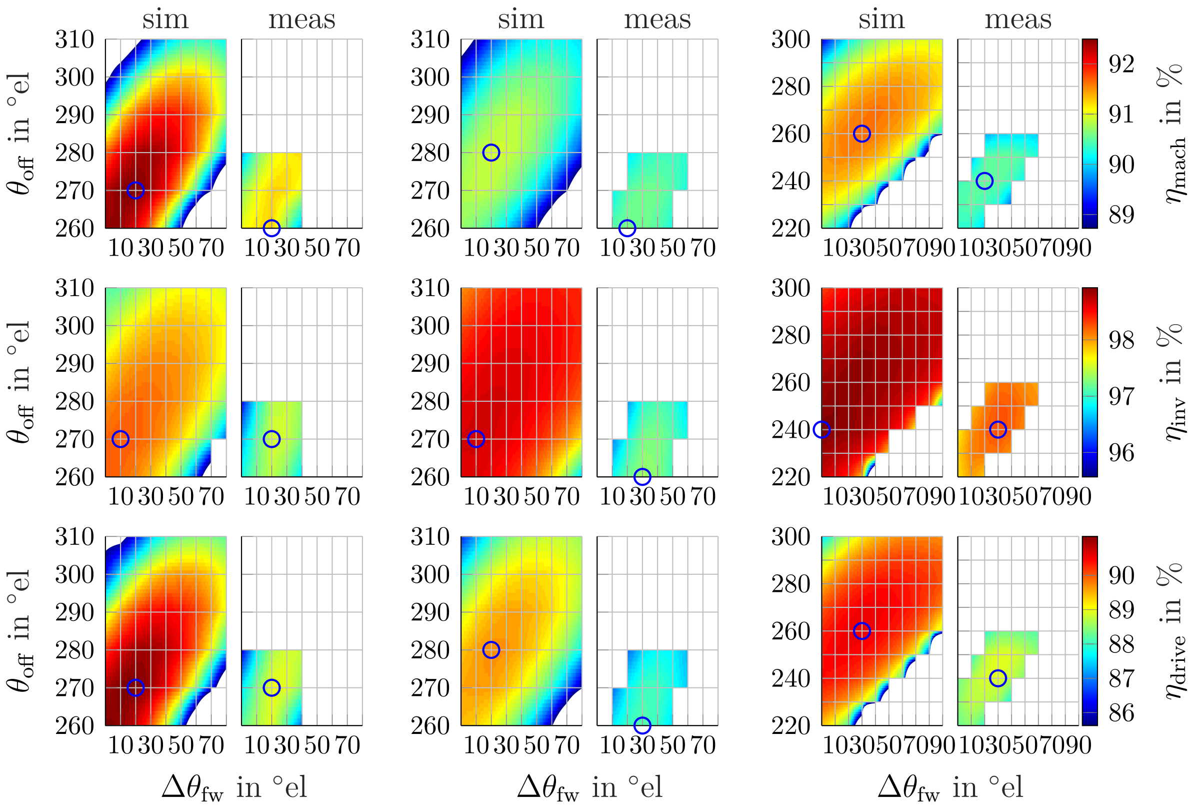

(a) LS2ph3p60N (b) HS2ph2p45N (c) HS3ph1p49N

Fig. 5.10: Comparison of simulated and measured efficiencies at operation point NOP_{M} (see table A.11). Blue circles mark efficiency maximum.

A direct comparison of inverter efficiency η_{inv} between simulation and measurement is not possible, as a different amount of chips is employed. From the results depicted in fig. 5.10 (second row) it can be summarized that inverter efficiency η_{inv} is strongly overestimated in simulation. This error is only partially explained by the higher load of the chips (see section 5.2.1). Other sources are the neglected ohmic losses in copper bars as well as the capacitor losses. Employing the same chip area per phase for both high-speed HS2ph2p45N and HS3ph1p49N machines results in an efficiency penalty of about 1 pp. The penalty is similar for the LS2ph3p60N machine. However, a different inverter, based on the Infineon Hybrid Pack™ 2, had to be employed for the measurements, due to the required phase peak current $I_{\mathrm{ph,pk}}$. Anyway, the improvement potential by a variation of freewheeling period $\Delta\theta_{\mathrm{fw}}$ and turn-off angle θ_{off} can again be confirmed for the three machines. The optima are found at slightly larger freewheeling periods $\Delta\theta_{\mathrm{fw}}$ in measurement than in simulation.

Combining both efficiencies, leads to a generally lower drive efficiency η_{drive} in measurement than in simulation. While in simulation (left columns in fig. 5.10a-5.10c), the η_{drive} optima are found at the same control angles as machine efficiency η_{mach}, in measurement (right columns in fig. 5.10a-5.10c) they are congruent with the optima of inverter efficiency η_{inv}. This indicates a stronger effect of the control angles on inverter efficiency η_{inv} in the measurements than in simulation, as a constant offset would not shift the points of maximal efficiency. As the chips are operated at a higher specific load in measurement, the increased gradient is most likely also caused by thermally increased losses.

Power Variation

The minimal measured and simulated machine losses $P_{\mathrm{l,mach}}$ and drive losses $P_{\mathrm{l,drive}}$ for the four operation points of variable speed and constant torque listed in table A.11, are depicted in fig. 5.11 at the identified maxima. For clarification, fig. 5.12 additionally visualizes the simulated individual losses at the points of maximal drive efficiency η_{drive} (η_{drive} sim in fig. 5.11).

Regarding machine efficiency η_{mach}, both high-speed HS2ph2p45N and HS3ph1p49N machines show a nearly constant efficiency over the complete power range in simulation and measurement (see fig. 5.11b and fig. 5.11c). In these two machines, the frequency dependent eddy-current copper losses $P_{\mathrm{l,cu,eddy}}$, iron core losses $P_{\mathrm{l,fe}}$ and mechanical losses $P_{\mathrm{l,m}}$ account for about 75 % of the machine losses $P_{\mathrm{l,mach}}$ (see fig. 5.12). As these losses strongly increase with generator speed (see fig. 5.12a), the effect of the nearly constant dc copper losses $P_{\mathrm{l,cu,dc}}$ is compensated. The LS2ph3p60N machine shows a higher dependence of machine efficiency η_{mach} on generator speed n_{SRG} than the HS2ph2p45N and HS3ph1p49N machines. At $P_{\mathrm{m,sh}} = 10\,\mathrm{kW}$, the measured machine efficiency η_{mach} is by 1.4 pp lower than at 20 kW. This is caused by the dc copper losses $P_{\mathrm{l,cu,dc}}$ (see fig. 5.12a), which increase only slightly with the input power $P_{\mathrm{m,sh}}$ along with the generator speed n_{SRG}. As in the LS2ph3p60N machine the dc copper losses $P_{\mathrm{l,cu,dc}}$ account for over 75 % of the machine losses $P_{\mathrm{l,mach}}$, the machine efficiency η_{mach} shows a positive correlation with speed.

For drive efficiency η_{drive}, also depicted in fig. 5.11, a similar behavior can be found in simulation, while in measurement also the HS2ph2p45N machines shows an efficiency penalty when reducing speed. This is caused by the inverter losses $P_{\mathrm{l,inv}}$, which show a stronger gradient over speed in measurement than in simulation.

Power variation can be performed by a variable speed as well as a variable torque. Due to the large share of $P_{\mathrm{l,m}}$, in the high-speed machines this is not advised. Assuming a constant electromagnetic efficiency, with linearly reduced iron core losses $P_{\mathrm{l,fe}}$ and copper

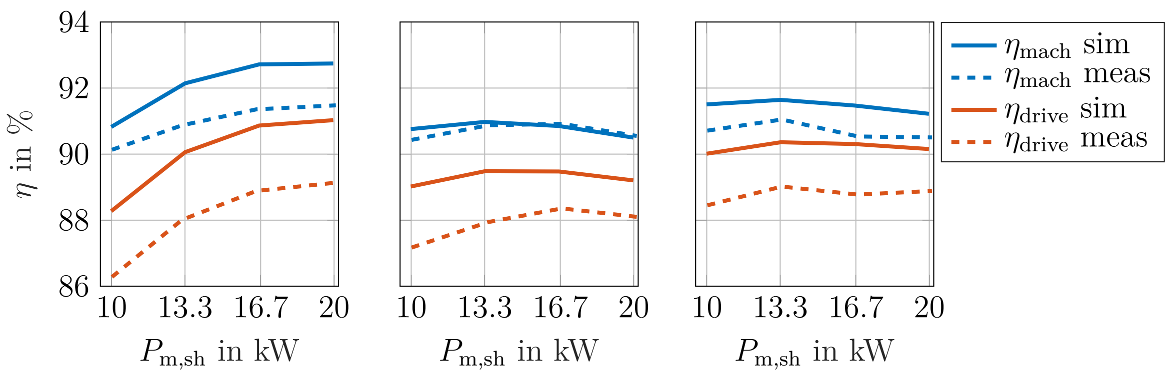

(a) LS2ph3p60N (b) HS2ph2p45N (c) HS3ph1p49N

Fig. 5.11: Simulated and measured efficiencies for variable speed and generator output torque $T_{\mathrm{tot}} = T_{\mathrm{tot,nom}}$. Operation points listed in table A.11.

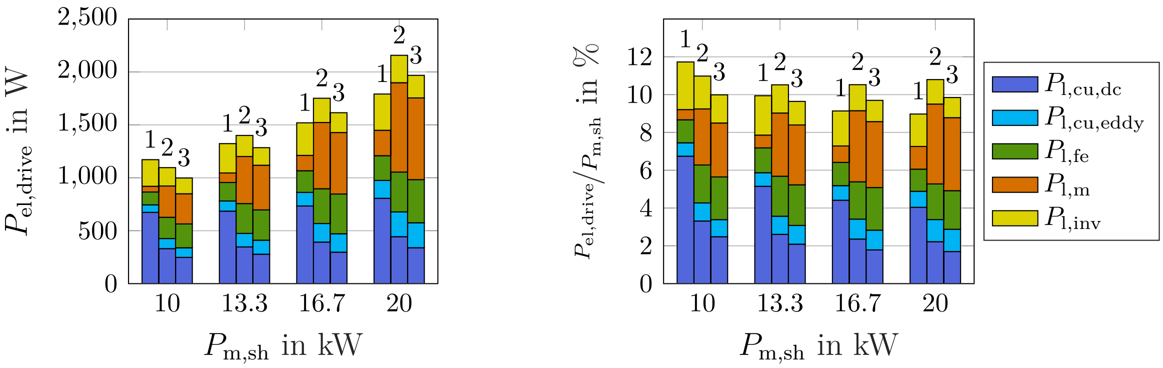

(a) absolute losses (b) relative losses

Fig. 5.12: Simulated losses for variable speed and generator output torque $T_{\mathrm{tot}} = T_{\mathrm{tot,nom}}$. Operation points listed in table A.11. 1 = LS2ph3p60N, 2 = HS2ph2p45N, 3 = HS3ph1p49N

losses $P_{\mathrm{l,cu,ac}}$, only a machine efficiency η_{mach} of $< 87\,\%$ can be reached at nominal generator speed $n_{\mathrm{SRG,nom}}$ in the HS2ph2p45N machine, if the output torque is reduced to 50 % of the nominal output torque $T_{\mathrm{tot,nom}}$. With the large share of frequency dependent losses, this assumption can be seen as best-case estimation. In [Ral+17], it was shown for the HS3ph3p25N machine that reducing the torque increases the share of eddy-current copper losses $P_{\mathrm{l,cu,eddy}}$ as well as iron core losses $P_{\mathrm{l,fe}}$, which was also confirmed by simulation at nominal speed for the HS2ph2p45N and HS3ph1p49N machine. As measurement validation at nominal generator speed $n_{\mathrm{SRG,nom}}$ was not possible, in table 5.3 a validation is performed at $0.5 \cdot n_{\mathrm{SRG,nom}}$ for the HS2ph2p45N machine. In best case, a machine efficiency η_{mach} of 87.7 % is expected, while measurement reaches 87.4 %.

In the LS2ph3p60N machine, the frequency dependent losses have a much smaller share. In best case, at nominal operation point, a reduction of machine efficiency η_{mach} by 1.2 pp by the relatively doubled mechanical losses $P_{\mathrm{l,m}}$ is expected, while measurement shows a reduction of 1.4 pp. As can be seen from fig. 5.11a, at 50 % nominal generator speed $n_{\mathrm{SRG,nom}}$ and nominal torque $T_{\mathrm{tot,nom}}$, an equal efficiency reduction was measured. Adding inverter efficiency η_{inv} to the discussion, however, the variation of torque shows a higher efficiency η_{drive} than the variation of speed by 1.6 pp at 50 % input power $P_{\mathrm{m,sh}}$.

	LS2ph3p60N		HS2ph2p45N	
n_{SRG}	$n_{\mathrm{SRG,nom}}$		$0.5 \cdot n_{\mathrm{SRG,nom}}$	
T_{tot}	$T_{\mathrm{tot,nom}}$	$0.5 \cdot T_{\mathrm{tot,nom}}$	$T_{\mathrm{tot,nom}}$	$0.5 \cdot T_{\mathrm{tot,nom}}$
η_{mach}	91.5 %	90.1 %	90.4 %	87.4 %
η_{inv}	97.4 %	97.6 %	96.5 %	96.7 %
η_{drive}	88.5 %	87.9 %	87.2 %	84.5 %

Table 5.3: Torque variation influence on measured efficiency at two constant speeds.

5.2.3 Efficiency Conclusion

Introducing a freewheeling period $\Delta\theta_{\mathrm{fw}}$, machine efficiency η_{mach} can be improved in simulation for all investigated machines. At the nominal operation point, the overall maximum of drive efficiency η_{drive} is close to the minimal copper losses $P_{\mathrm{l,cu,ac}}$. Responsible for this behavior are the large shares of dc copper losses $P_{\mathrm{l,cu,dc}}$ in the LS2ph3p60N and eddy-current copper losses $P_{\mathrm{l,cu,eddy}}$ in the high-speed HS2ph2p45N and HS3ph1p49N machines. Reducing generator speed n_{SRG}, the required freewheeling period $\Delta\theta_{\mathrm{fw}}$ to achieve maximal efficiency gets larger, compensating for the reduced back EMF e. Varying both the freewheeling period $\Delta\theta_{\mathrm{fw}}$ and the turn-off angle θ_{off} at the same time, leads at all operation points to a large area of constant efficiency. This area offers the potential to influence additional system aspects, such as acoustic behavior, without influencing the drive efficiency η_{drive}.

Measurements confirm the tendencies from simulation on machine and inverter level. For all operation points, a good match between simulated and measured machine efficiencies η_{mach} can be found. However, the areas of minimal losses are smaller, as the copper losses $P_{\mathrm{l,cu,ac}}$ are negatively influenced by the coil temperature. Inverter efficiency η_{inv} shows an offset between simulation and measurement, due to the modeling with constant chip area. Generally, inverter efficiency η_{inv} has only a small effect on the control parameters of maximal drive efficiency η_{drive}, showing a similar behavior as the copper losses $P_{\mathrm{l,cu,ac}}$.

From an efficiency point of view, for both high-speed machines the power variation is preferable by a variation of speed. For the LS2ph3p60N machine, the variation of torque and speed offer the same machine efficiency η_{mach} performance. Including the inverter, the torque variation shows an advantage of 1.6 pp over speed variation in the LS2ph3p60N machine.

5.3 Acoustic Analysis

Due to their application in a REX, the SRGs discussed in this thesis perform power variations by changing the generator speed n_{SRG} at nominal torque $T_{\mathrm{tot,nom}}$. Therefore, the fundamental electric frequency f_{el} and its harmonics of higher orders might intersect with their corresponding eigenfrequencies f_{eig}. In the following, the dynamic behavior of the three prototype machines LS2ph3p60N, HS2ph2p45N and HS3ph1p49N is analyzed in simulation and measurement. Simulation results are retrieved with the modeling approach introduced in section 2.3.4 and 4.3. Additionally, the coupling of the LS2ph3p60N machine with an ICE is presented and analyzed. Finally, improvement potential by changing control parameters (e.g. $\Delta\theta_{\mathrm{fw}}$, θ_{off}) is discussed.

High-Speed Machines

Fig. 5.13 depicts simulated and measured spectrograms from 50 − 100 % nominal generator speed $n_{\mathrm{SRG,nom}}$ at nominal generator output torque $T_{\mathrm{tot,nom}}$. In measurement, the HS2ph2p45NX machine (see section A.2.1.1) was employed. As the electromagnetic stator structure is equal to the HS2ph2p45N machine, only the mechanical background noise is influenced by this change. In section 4.3.3, a 20 dB offset was found between simulation and measurement for both the HS2ph2p45N and the HS3ph1p49N machine. As this is believed to be caused by the parametrization of the simulation model, for qualitative comparison with the measurements the colorbar amplitude of the simulation was adjusted by this offset.

In simulation, for both, the HS2ph2p45N and the HS3ph1p49N machine, the identified mode_0, mode_2 and mode_4 eigenfrequencies f_{M0}, f_{M2} and f_{M4} (see table 4.17) can be easily perceived in fig. 5.13a and fig. 5.13b. In fig. 5.13a, the 2^{nd} and 4^{th} harmonic of the HS2ph2p45N machine, exciting a mode_0 vibration, show high amplitudes over the complete speed range without intersecting with the corresponding mode_0 eigenfrequency f_{M0}. In fig. 5.13b, this behavior can be observed for the 1^{st} and 2^{nd} harmonic of the HS3ph1p49N machine, exciting a strong mode_2 vibration, without intersecting with the corresponding mode_2 eigenfrequency f_{M2}.

In the measurements shown in fig. 5.13c and 5.13d, the mechanical vibrations increase the background amplitude of the average surface velocity v_{surf} between the electromagnetic harmonics, especially below 1 kHz. These additional measured vibrations are slightly higher

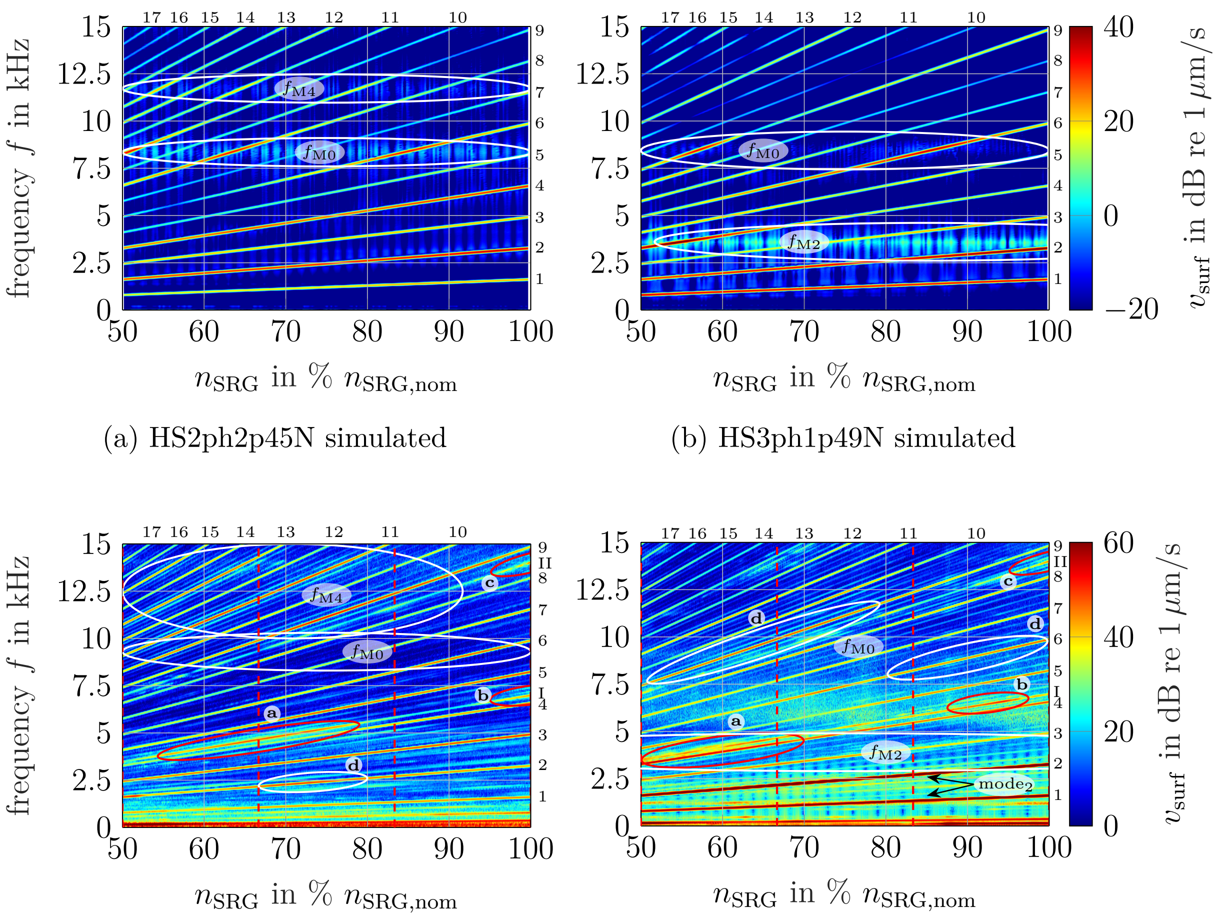

(a) HS2ph2p45N simulated

(b) HS3ph1p49N simulated

(c) HS2ph2p45NX measured

(d) HS3ph1p49N measured

Fig. 5.13: Simulated and measured surface velocities v_{surf} of high-speed machines listed in table A.2. Transition from $PART_{\text{M,50}}$ to NOP_{M} (see table A.11) at nominal generator output torque $T_{\text{tot,nom}}$.
red dashed lines: stationary comparisons in section 4.3.3 and A.4.3.5

for the HS3ph1p49N machine with the initial mechanical setup, than for the mechanically improved HS2ph2p45NX machine (see section A.2.1.1). In addition, the first two gearbox harmonics (I, II) are added to the spectrum of both machines. In the HS2ph2p45NX measurements in fig. 5.13c, the 1st gearbox harmonic completely shadows the 4th electromagnetic harmonic, which excites a mode_0 vibration, in the speed-range of 55 – 75 % $n_{\text{SRG,nom}}$ (a). In the HS3ph1p49N measurements in fig. 5.13d, in contrast the 4th harmonic overlaps with the mode_2 eigenfrequency f_{M2} in this speed range (a). Therefore, the 1st gearbox harmonic is shadowed. A 2nd distinguishable gearbox excitation can be found around 92 % and 100 % $n_{\text{SRG,nom}}$ (b) in the HS3ph1p49N and HS2ph2p45NX measurements, respectively. The difference in frequency location between the two machines, results from the changed bearing and shaft concept of the HS2ph2p45NX machine (see section A.2.1.1). The resonance excited at 6.5 kHz in the HS3ph1p49N machine ((b) in fig. 5.13d) is shifted above 7 kHz in the HS2ph2p45NX machine ((b) in fig. 5.13c), as the corresponding gearbox harmonic I just enters the area of increased amplitude in this machine. While this leads to comparable amplitudes at the nominal operation point (see stationary measurement in fig. 4.27b), for variable speed operation, it is preferable that the resonance peak is not in the considered generator speed range.

Concerning electromagnetically caused vibrations in the HS2ph2p45NX machine (see fig. 5.13c), the mode_0 eigenfrequency f_{M0} excitation can be found around 9 kHz (c), slightly higher than the 8.5 kHz expected from simulation. The amplitude increase of the 8th and 10th harmonic in the frequency range of f_{M0} is less prominent in measurement than in simulation. In case of the odd harmonics, exciting a mode_4 vibration form, the corresponding eigenfrequency f_{M4} is found roughly at the simulated frequency of 12 kHz (see fig. 5.13c). However, amplitude and frequency band of the 9th, 11th and 13th harmonic are increased compared to simulation around f_{M4}. Lower harmonics show a comparable behavior in measurement as in simulation, only the 2nd harmonic shows a peak around 2.4 kHz ((d) in fig. 5.13c), not found in simulation. In general, mode_4 and mode_0 excitation is of comparable magnitude. This is confirmed by the stationary comparisons in section A.4.3.5.

In the HS3ph1p49N measurements shown in fig. 5.13d, the mode_2 eigenfrequency f_{M2} around 3.7 kHz matches closely the value found in simulation. Generally, mode_2 vibrations of the 1st and 2nd harmonics are dominant throughout the complete operation range, even without intersecting with the corresponding mode_2 eigenfrequency f_{M2}. mode_0 vibrations of the 6th and 9th harmonic show increased amplitudes around 9 kHz ((d) in fig. 5.13d). In case of the 9th harmonic the frequency band with increased amplitudes is wider compared to simulations shown in fig. 5.13b. However, the amplitudes of mode_0 vibrations are generally much lower than the amplitudes of mode_2 vibrations (e.g. 1st and 2nd harmonic).

Low-Speed Machine

Simulations of the LS2ph3p60N machine are shown in fig. 5.14a. The even harmonics, exciting a mode_0 vibration form, clearly show a higher amplitude than the odd harmonics, exciting a mode_6 vibration form. Clear peaks can be found around $f_{\text{M0}} = 5.5\,\text{kHz}$ and $f_{\text{M6}} = 7.4\,\text{kHz}$. The high harmonic density makes it difficult to distinguish operational speeds of low structural excitation. At nominal generator speed $n_{\text{SRG,nom}}$, no harmonic directly intersects with its corresponding eigenfrequency, however, the 8th harmonic still has

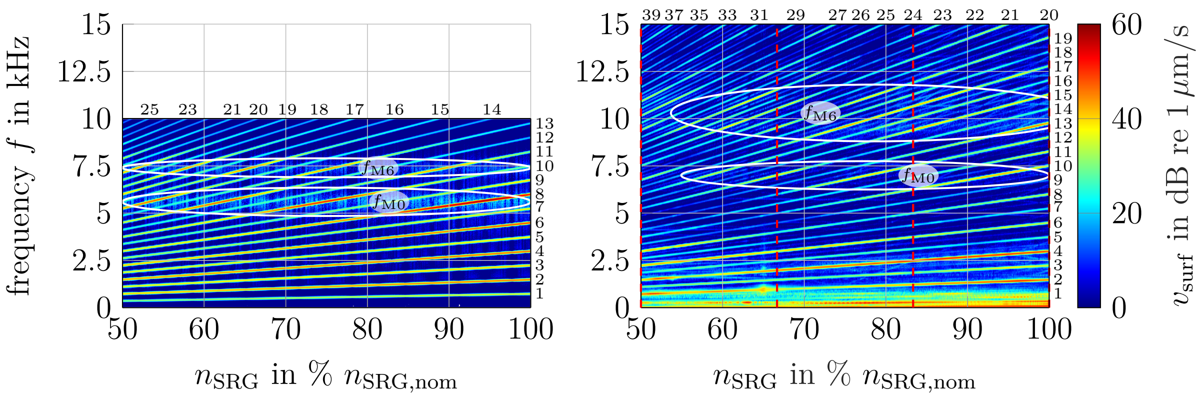

(a) simulated (b) measured

Fig. 5.14: Simulated and measured average surface velocities v_{surf} of LS2ph3p60N machine listed in table A.2. Transition from $PART_{\mathrm{M,50}}$ to NOP_{M} (see table A.11) at nominal generator output torque $T_{\mathrm{tot,nom}}$.
red dashed lines: stationary comparisons in section 4.3.3 and A.4.3.5

a strongly increased amplitude.

Comparing the simulation results shown in fig. 5.14a to measurements on an electric test bench shown in fig. 5.14b, both, the mode$_0$ and mode$_6$ eigenfrequencies f_{M0} and f_{M6} are shifted to higher frequencies, namely 7 kHz and 9.5 kHz, respectively. This is similar to the findings for the high-speed HS2ph2p45NX and HS3ph1p49N machines. These shifts are believed to be caused by the rigid connection to the test bench, increasing the stiffness of the stator structure. In addition, the amplitudes of individual harmonics in the area of the corresponding eigenfrequencies f_{M0} and f_{M6} are lower than in simulation. Due to the shift of the f_{M0} eigenfrequency to 7 kHz especially the excitation of the 8$^{\mathrm{th}}$ harmonic is reduced in measurement (see fig. 5.14b) compared to simulation (see fig. 5.14a). For the mode$_6$ vibration form, a 2$^{\mathrm{nd}}$ band of increased amplitude is found for the 17$^{\mathrm{th}}$, 19$^{\mathrm{th}}$ and 23$^{\mathrm{rd}}$ harmonic at 11 kHz. As frequency was limited to 10 kHz in simulation, these increases were not predicted. While the higher harmonics show a lower excitation in measurement compared to simulation, both the 2$^{\mathrm{nd}}$ and 4$^{\mathrm{th}}$ harmonic, which excite a mode$_0$ vibration from, show an increased amplitude. This confirms that the LS2ph3p60N machine with a pole pair number $n_{\mathrm{p}} = 3$, mainly shows a mode$_0$ vibration form.

Coupling with Internal Combustion Engine

In fig. 5.15, measurement results of the LS2ph3p60N machine in the final module combined with an ICE, as described in [Ind+16], are depicted. The machine is directly attached to the ICE housing. The combined setup is attached via rubber suspensions to a aluminum frame, realizing a much less rigid connection than the electric test bench. Only a limited speed range of 66 – 96 % $n_{\mathrm{SRG,nom}}$ was available by the ICE controller. In the investigated range, the background vibrations are increased compared to the test bench results. The general increase of vibrations, and the torque oscillations introduced by the ICE, lead to a much less distinctive perception of single harmonics. This led to a less sharp subjective noise impression of the author at the measurement site and in the final vehicle compared to the electric test bench.

Up to 2 kHz all electromagnetically induced vibrations are shadowed by the vibrations of the ICE. Only the intersection of 8^{th} and 10^{th} harmonic with the mode_0 eigenfrequency around 5.5 kHz can be clearly perceived ((a) and (b)). These peaks are located at the eigenfrequency f_{M0} expected from simulation, in contrast to the test bench measurements. The 15^{th} harmonic, which excites a mode_6, shows a minor peak around 90 % $n_{\text{SRG,nom}}$ at 10 kHz (c), corresponding to the eigenfrequencies f_{M6} found in measurements on the electrical test bench depicted in fig. 5.14.

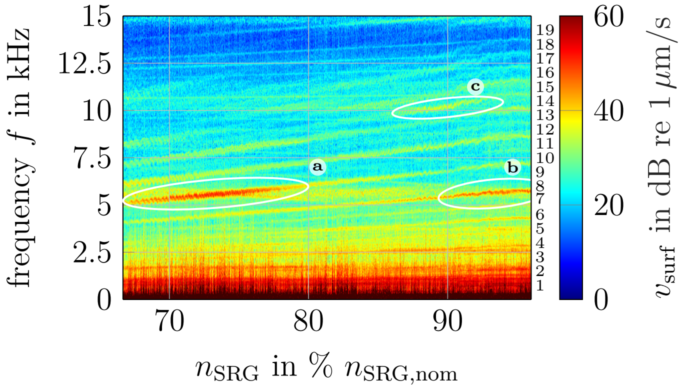

Fig. 5.15: Measured average surface velocity v_{surf} of LS2ph3p60N machine coupled with single-cylinder 4-stroke ICE.

5.3.1 Acoustic Improvements by Control

Beside structural changes, the chosen control can influence the acoustic behavior of an SRG. Sophisticated approaches, such as [Hof16], are not applicable for SRG in energy efficient SPC, as they require instantaneous controllability of the phase current. For such a controllability, a low number of turns per pole $N_{\text{w,pl}}$ is required, which has a negative effect on the machine efficiency η_{mach} (see section 4.1) and, consequently, power density (see section 4.2.4).

In SPC, the positioning of the pulse also has an influence on the acoustic behavior, as it influences the force amplitude. The early single pulse strategy from [Kas11], which was developed for the motoring mode, is transferred to SRG into a late single pulse operation for the generating mode. In [Kle+14], it was shown in simulation without application of freewheeling period $\Delta\theta_{\text{fw}}$ that a late single single pulse operation has a positive effect on the acoustic behavior of the LS2ph3p60N machine. Measurements in [Kle+14] showed a lowered surface velocity v_{surf} together with a reduced machine efficiency η_{mach}.

Adding a freewheeling period $\Delta\theta_{\text{fw}}$, offers an additional degree of freedom to influence the acoustic behavior with a lower impact on the machine efficiency η_{mach} (see section 5.2.3). Fig. 5.16 depicts the average surface velocity v_{surf} of the HS3ph1p49N machine at nominal operation point for variable control parameters close to efficiency maximum (see fig. 5.10c). Increasing the turn-off angle θ_{off} to later values and increasing the freewheeling period

$\Delta\theta_{fw}$ along with it, to keep the influence on machine efficiency η_{mach} small, has mainly an effect on vibrations around the mechanical base frequency f_m as well as around the 6^{th} electromagnetic harmonic. This harmonic excites not only a $mode_0$ vibration form. Due to the 3-phase configuration of the HS3ph1p49N machine, the torque ripple has a base frequency of $3 \cdot f_{el}$. The 6^{th} electromagnetic harmonic is, therefore, also the 2^{nd} harmonic of the torque ripple. A positive effect on $mode_2$ harmonics is only found for the 8^{th} harmonic, already > 13 kHz at nominal generator speed $n_{SRG,nom}$.

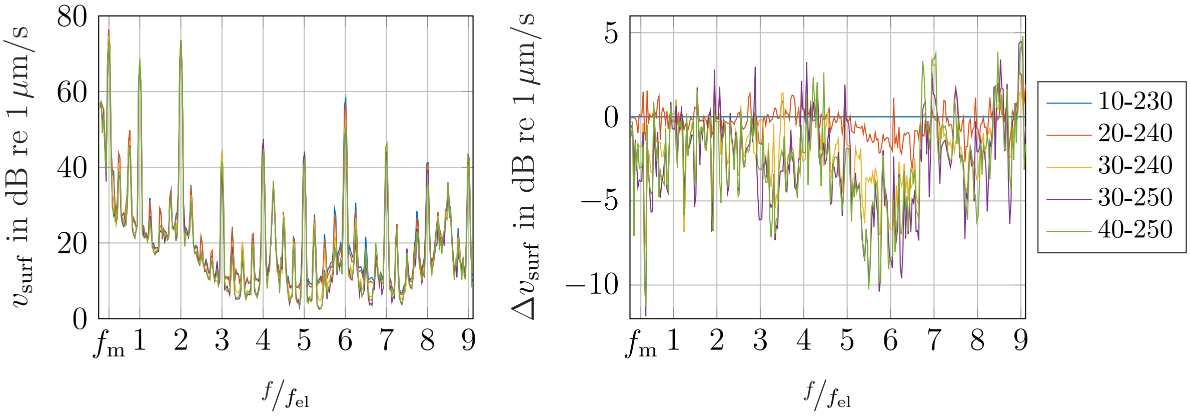

(a) absolute value

(b) absolute deviation from 10-230

Fig. 5.16: Measured surface velocity of HS3ph1p49N machine for variable control parameter $\Delta\theta_{fw}$-θ_{off} at operation point NOP_M (see table A.11).

Another known approach to improve the acoustic behavior of electrical machines, is a dithering of the pulse-width modulation (PWM) switching frequency [Bös14; BP93; CLU92]. For SRG in SPC no PWM frequency is applied. However, taking in consideration the advantage of a late turn-off angle θ_{off}, a dithering of the complete current pulse between the two extrema of maximal machine efficiency η_{mach} and minimal radial force $F_{pl,rad}$ can be implemented. In [SBD15], it was shown for various dithering approaches that the peak amplitude of individual harmonics could not be reduced in the LS2ph3p60N machine. However, the spectrum of individual harmonics was widened similar to the operation with the ICE (see fig. 5.15). As the improvement in acoustic behavior comes in hand with larger required power electronics, due to the increased phase peak current $I_{ph,pk}$ [Kle+14], it was not further analyzed in this thesis.

This brief analysis shows that the potential to improve the acoustic behavior by means of control, is rather limited in SRG operated in energy efficient SPC. The deviation from efficiency optimal control angles mainly influences mechanical vibrations (see fig. 5.16). Therefore, it is only advised if absolutely required from a mechanical point of view.

5.3.2 Acoustic Partial Load Conclusion

The initial conclusions drawn in section 4.3.4 for the nominal operation point are supported by the dynamic comparison shown in fig. 5.14 - 5.13. Throughout the complete operation range, the 1^{st} and 2^{nd} harmonic show high amplitudes for the HS3ph1p49N machine (see fig. 5.13d). Both the HS2ph2p45N (seefig. 5.13c) and the LS2ph3p60N (see fig. 5.14b) measurements show lower amplitudes of individual harmonics. Excitation of eigenfrequencies by their corresponding harmonics is mainly a problem for the 2nd harmonic of the HS3ph1p49N machine (seefig. 5.13d). As the higher torque ripple of the HS2ph2p45N machine compared to the HS3ph1p49N machine (see table 4.19) does not show a negative effect on gearbox vibrations, the HS2ph2p45N machine is clearly preferable for the high-speed scenario. The LS2ph3p60N machine measurements in fig. 5.14b show a higher harmonic density compared to the HS2ph2p45N and HS3ph1p49N measurements in fig. 5.13. While the intersection of a harmonic with its corresponding eigenfrequency f_{eig} is more likely than for the high-speed HS2ph2p45N and HS3ph1p49N machines, the LS2ph3p60N machine still shows lower amplitudes of individual harmonics. Therefore, the LS2ph3p60N machine has a preferable acoustic behavior compared to the HS2ph2p45N machine at partial load, especially as no additional gearbox noise is present, due to the direct coupling with the ICE.

From the measurements in combination with an ICE shown in fig. 5.15, it can be deduced that mechanical vibrations up to 2 kHz are covered by externally induced noise. The increased background vibration level additionally covers higher electromagnetic harmonics $> 7\,\mathrm{kHz}$. Therefore, only a cover-up of the 1st harmonic in the high-speed HS2ph2p45N and HS3ph1p49N machines is realistic. Especially, the 2nd harmonic in the HS3ph1p49N machine is expected to be still perceivable in a vehicle.

Influencing the acoustic behavior by means of control is limited in SPC. Shifting control parameter to later turn-off angle θ_{off} and simultaneously increasing the freewheeling period $\Delta\theta_{\mathrm{fw}}$ leads only to a reduced level of vibration in mode$_0$ harmonics and mechanically induced vibrations. A reduction of the prominent mode$_2$ harmonics in the HS3ph1p49N machine could not be observed. It is, therefore, only advised if absolutely required from a mechanical point of view. As the background vibration level is already increased by the ICE, no additional advantage of the angle dithering analyzed in [SBD15] is expected.

5.4 System Aspects

This section discusses the sizing of the power electronics inverter as well as the source losses $P_{\mathrm{l,src}}$ for the different machine configurations.

5.4.1 Power Electronics

The power module sizing depends on the required blocking voltage and the chip area. The former is directly linked to the dc-link voltage u_{dc}, while the latter is linked to a phase RMS current $I_{\mathrm{ph,rms}}$ and phase peak current $I_{\mathrm{ph,pk}}$ from thermal and instantaneous limitations, respectively. Table 5.4 lists the inverter apparent power $S_{\mathrm{el,inv}}$ as defined by (5.2) and phase peak current $I_{\mathrm{ph,pk}}$, for the two operation points of 10 kW and 20 kW. It can be seen, that inverter apparent power $S_{\mathrm{el,inv}}$ is nearly independent from operational speed for SPC. Comparing the machines, the HS2ph2p45N machine saves 12 % compared to the LS2ph3p60N machine, while the 3-phase HS3ph1p49N machine saves another 18 % on the 2-phase HS2ph2p45N machine.

$$S_{\mathrm{el,inv}} = u_{\mathrm{ph}} \cdot I_{\mathrm{ph,rms}} \cdot N_{\mathrm{ph}} \tag{5.2}$$

In an ideal world, inverter apparent power $S_{\mathrm{el,inv}}$ is not affected by the chosen phase voltage u_{ph}, substituting voltage by current. However, only standardized voltage steps are generally available on the market. For automotive applications of the 20 kW range a blocking voltage in the range of 600 – 700 V is common, depending on the IGBT chip generation. Therefore, reducing the system voltage below the required over-voltage safety margin has a negative effect on power module sizing, as phase RMS current $I_{\mathrm{ph,rms}}$ and peak current $I_{\mathrm{ph,pk}}$ are increased.

		$PART_{\mathrm{M,50}}$ (see table A.11)		NOP_{M} (see table A.11)	
	u_{dc} in kVA	$S_{\mathrm{el,inv}}$ in A	$I_{\mathrm{ph,pk}}$ in kVA	$S_{\mathrm{el,inv}}$ in A	$I_{\mathrm{ph,pk}}$
LS2ph3p60N	300 V	66	345	72	300
LS2ph3p60N		66	258	72	206
HS2ph2p45N	400 V	55	195	64	173
HS3ph1p49N		46	96	53	86

Table 5.4: Inverter apparent power $S_{\mathrm{el,inv}}$ and phase peak current $I_{\mathrm{ph,pk}}$ for the built prototypes.

For the sizing of the dc-link capacitor C_{dc}, two requirements are important. On the one hand, the maximal dc-link voltage deviation Δu_{dc} from the nominal dc-link voltage u_{dc} at the inverter terminals. On the other hand, to avoid extensive battery losses and potential aging, the ripple on source current i_{src} has to be limited. Table 5.5 lists the required capacitance C_{dc} for the three generator prototypes for $\Delta u_{\mathrm{dc}} = 5\,\%$ and no current reversal ($i_{\mathrm{src}} < 0\,\mathrm{A}$ in fig. 2.5) at the point of lowest battery source losses $P_{\mathrm{l,src}}$. Comparing the three machines at dc-link voltage $u_{\mathrm{dc}} = 400\,\mathrm{V}$, the requirement of dc-link voltage deviation Δu_{dc} is met with capacitances $C_{\mathrm{dc}} < 1\,\mathrm{mF}$. For the HS3ph1p49N 3-phase machine the required capacitance $C_{\mathrm{dc}} = 0.03\,\mathrm{mF}$ is also sufficient to meet the current ripple requirement. For the 2-phase LS2ph3p60N and HS2ph2p45N machines, larger capacitances C_{dc} of 3.9 mF and 1.3 mF are required at 400 V. As can be seen from the LS2ph3p60N machine at 300 V and 400 V, an increase in dc-link voltage u_{dc} has a positive effect on dc-link capacitance C_{dc} regarding voltage deviation Δu_{dc}. To avoid i_{src} reversal, however, the required dc-link capacitance C_{dc} is not reduced by the higher dc-link voltage u_{dc}.

In [KBD16b], it was found for a passive filter with a cable inductance $L_{\mathrm{cab}} = 100\,\mu\mathrm{F}$ and dc-link capacitance $C_{\mathrm{dc}} = 1\,\mathrm{mF}$ that component sizing for a dc-link voltage deviation $\Delta u_{\mathrm{dc}} = 5\,\%$ is independent of speed. To additionally avoid current reversal, however, much larger capacitances C_{dc} or inductances L_{cab} are required. To avoid excessive oversizing of the passive filter components and to decouple dc-link voltage u_{dc} from state-of-charge dependent source voltage u_{src}, [KBD16b] proposes an active filter based on a dc-dc converter.

	u_{dc}	$\Delta u_{dc} = 5\,\%$	$i_{src} < 0\,A$
LS2ph3p60N	300 V	2.40 mF	4.00 mF
LS2ph3p60N	400 V	0.80 mF	3.90 mF
HS2ph2p45N		0.44 mF	1.30 mF
HS3ph1p49N		0.03 mF	0.03 mF

Table 5.5: Required dc-link capacitor size C_{dc} to achieve 5 % Δu_{dc} or no i_{src} reversal at operation point NOP_M (see table A.11) for $R_{i,src} = 100\,m\Omega$.

5.4.2 Source Losses

The ohmic source losses $P_{l,src}$ of the three LS2ph3p60N, HS2ph2p45N and HS3ph1p49N prototypes at nominal operation point for dc-link capacitance $C_{dc} = 1\,mF$ and internal source resistance $R_{i,src} = 100\,m\Omega$ are depicted in fig. 5.17. It can be seen for all machines that a freewheeling period $\Delta\theta_{fw}$ positively affects the source losses. Introducing a freewheeling period $\Delta\theta_{fw}$ has two major benefits: Firstly, as instantaneous current reversal of phase current i_{ph} is avoided at turn-off angle θ_{off}, the current oscillations towards the battery are reduced. Secondly, the overlap of phase currents i_{ph} between adjacent phases is increased, transferring energy directly between phases rather than storing it in the dc-link capacitor C_{dc}. This has a similar effect as the switching strategies described in [Neu12], which are not applicable for SRG in SPC. It can be also seen in fig. 5.17 that control parameters for minimal source losses $P_{l,src}$ are strongly differing from minimal drive losses $P_{l,drive}$. This is in accordance with the preliminary study conducted for the HS2ph2p51N machine in [BMD16]. The absolute values in fig. 5.17 differ strongly for the three machines, due to the constant dc-link capacitance C_{dc}. As the LS2ph3p60N machine has a much lower electric base frequency f_{el} than the HS2ph2p45N and HS3ph1p49N machines, each energy pulse, described by the co-energy loop W_{co} (see fig. 2.7b) delivered to the dc-link capacitor is larger. This energy pulse leads to a higher voltage deviation Δu_{dc} in the dc-link capacitor C_{dc} and, consequently, in a higher current oscillation towards the battery.

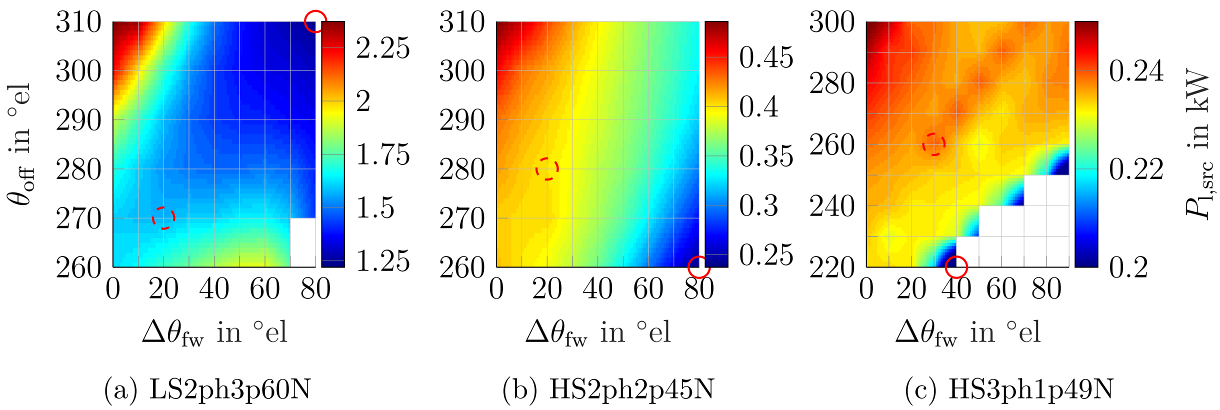

Fig. 5.17: Simulated source losses $P_{l,src}$ over switching parameters at operation point NOP_M (see table A.11). red circle: minimal $P_{l,src}$, red dashed circle: minimal drive losses $P_{l,drive}$

Employing the capacitance C_{dc} values listed in table 5.5 for no source current i_{src} reversal, leads to source losses $P_{\mathrm{l,src}}$ of 290 W, 341 W and 358 W at the point of minimal drive losses $P_{\mathrm{l,drive}}$ in case of LS2ph3p60N, HS2ph2p45N and HS3ph1p49N machine, respectively. To achieve comparable source losses $P_{\mathrm{l,src}}$, the LS2ph3p60N machine requires the largest dc-link capacitance C_{dc}. The sizing of a filter, however, needs to be performed with knowledge of the complete electric system, as cable inductance L_{cab} and battery internal resistance $R_{\mathrm{i,src}}$ as well as capacitances of additional components in the system affect the dynamic behavior. Again, a decoupling is possible by employing a dc-dc converter as suggested in [KBD16b].

From a system point of view, the high-speed machines are preferable over the low-speed machine, as the higher electric base frequency f_{el} leads to smaller additional power electronic components. Due to its 3-phase configuration, the HS3ph1p49N machine requires the smallest components of all three investigated machines.

5.5 Chapter Conclusion

In this chapter, the influence of single pulse control (SPC) parameters, including a freewheeling period $\Delta\theta_{\mathrm{fw}}$, on the system behavior of the three prototypes was analyzed in terms of efficiency and acoustic behavior.

In section 5.1 a negative effect on the ac copper losses $P_{\mathrm{l,cu,ac}}$ with an increase in turn-off angle θ_{off} in SRG was found (see fig. 5.2a). Adding a freewheeling period $\Delta\theta_{\mathrm{fw}}$ to the control parameters allows for a compensation of this effect (see fig. 5.4), as both, the peak value and the gradient around turn-off θ_{off} of pole flux linkage Ψ_{pl} are reduced. In addition, these effects positively influence the iron core losses $P_{\mathrm{l,fe}}$ (see fig. 5.5). Varying both control parameters ($\Delta\theta_{\mathrm{fw}}$, θ_{off}) together, leads at all operation points to a large area of constant efficiency (see fig. 5.10, A.7, A.10, A.12). This leads not only to a reduced sensitivity against control errors but also offers a degree of freedom to influence the system behavior.

With a large number of coupled FEA, it was found in section 5.1.1 that modeling the eddy-current copper losses $P_{\mathrm{l,cu,eddy}}$ by the frequency dependent eddy-loss ratio $p_{\mathrm{eddy,woEw}}$ (f_{el}), proposed in this thesis, is a fast approach to find preliminary control angles with good accuracy in extensive system simulations (see fig. 5.8a). The frequency dependent eddy-loss ratio $p_{\mathrm{eddy,woEw}}$ (f_{el}) can also be employed for the determination of the copper loss correction factor k_{cu} (f_{el}) (see (3.9)) instead of a constant factor in pre-design. The analysis of an additional traction machine over a wide range of electric base frequency f_{el} (see fig. 5.6) showed good transferability for machines of similar power and voltage class, as long as the winding design is comparable.

Analyzing the machines at partial load in section 5.2.2, for both high-speed machines it was found that power variation is preferable by a variation of speed rather than torque. For the low-speed machine, a variation of torque was found more advantageous if drive efficiency, including the inverter, is considered.

Regarding the acoustic behavior, the 2-phase HS2ph2p45N machine shows lower amplitudes of individual harmonics compared to the 3-phase HS3ph1p49N alternative over the complete speed range (see section 5.3). A negative influence of the higher torque ripple in the HS2ph2p45N machine was not found (see fig. 5.13c and fig. 5.13d). Together with the analysis at nominal operation point (see section 4.5) this leads to the general conclusion that 2-phase machines with a number of pole pairs $n_\mathrm{p} > 1$ are an interesting alternative compared to machines with a higher number of phases N_ph and $n_\mathrm{p} = 1$. These machines offer the same machine efficiency at improved acoustic behavior. From the exemplary coupling of the LS2ph3p60N machine with an ICE, the conclusion can be drawn that in the complete system, the individual SRG harmonics will be less distinctive, due to the high torque oscillations of the ICE. Finally, influencing the acoustic behavior by means of control mainly influences mechanical vibrations. Therefore, it should only be considered, if the machine efficiency η_mach is not negatively influenced.

From a system perspective, the oscillating energies between machine and dc-link capacitor, are directly proportional to the absolute torque ripple of the machine. The reduced electric base frequency f_el of low-speed machines leads to much larger absolute torque values and, consequently, dc-link capacitances C_dc compared to high-speed machines (see table 5.5). 3-phase machines require a smaller dc-link capacitor compared to 2-phase machines, due to their reduced absolute and relative torque ripple. Therefore, 3-phase machines are to be considered, if a configuration with a number of pole pairs $n_\mathrm{p} > 1$ reaches a sufficiently high machine efficiency.

6 Summary and Conclusion

6.1 Conclusion

Within this thesis, the suitability of SRG for a REX application was analyzed. Therefore, two drive configurations, a low-speed scenario directly coupled to the ICE and a high-speed scenario with an additional gearbox, were considered.

To chose suitable machine designs from the large amount of possible solutions, a solution space based pre-design (SSBPD) for SRGs was developed as a part of this thesis. The SSBPD decouples the geometry dependent electromagnetic torque capability (exemplary shown in fig. 3.6b) from application specific requirements, e.g. shaft power $P_{\mathrm{m,sh}}$, maximal coil temperature $\vartheta_{\mathrm{coil,max}}$ or copper fill factor f_{cu}. With the proposed approach, a FEA-verified fast overview over a solution space of several thousand machine designs can be achieved in a few seconds. From the results, the most promising designs can be further evaluated with more time consuming simulations.

With this tool and detailed analysis of the thermal behavior of the built prototypes (see table A.2), the following has been found that is also transferable to other designs. In order to find the "best" design in terms of active material volume V_{act} and, consequently, reachable torque density $\phi_{\mathrm{T,act}}$, the thermally permitted maximal current density $J_{\mathrm{th,max}}$ should be calculated separately for each design variation by a geometry dependent LPTN. Furthermore, it was found that an approximation of the eddy-current copper losses $P_{\mathrm{l,cu,eddy}}$ and the influence of end-winding related dc copper losses $P_{\mathrm{l,cu,dc,Ew}}$ is important, to correctly determine $J_{\mathrm{th,max}}$. The detailed analysis of the prototype machines, together with the comparable HS3ph3p25N machine (see table A.6), showed that a linear frequency dependent eddy-loss ratio $p_{\mathrm{eddy,woEw}}\ (f_{\mathrm{el}})$ is a viable solution to determine the total copper losses $P_{\mathrm{l,cu,ac}}$ for a wide range of electrical base frequencies f_{el} and machine configurations during pre-design.

All SRGs evaluated for the two REX speed scenarios, reached a measured machine efficiency $\eta_{\mathrm{mach}} > 91\,\%$. The low-speed machine shows an advantage of 0.4 pp compared to the high-speed machines. Therefore, it is concluded that, even if a gearbox is required, nominal generator speeds up to 25 krpm can be achieved without a significant reduction in machine efficiency. To achieve higher machine efficiencies η_{mach}, the frequency dependent eddy-current copper losses $P_{\mathrm{l,cu,eddy}}$, iron core losses $P_{\mathrm{l,fe}}$ and mechanical losses $P_{\mathrm{l,m}}$ offer further improvement potential for the high-speed machines. Employing litz wire, NO10 iron core material and a stator slot closure, simulated machine efficiencies $\eta_{\mathrm{mach}} >= 93\,\%$ are predicted for the considered machines. The highest value is reached by the 2-phase high-speed machine with 93.5 %, including the gearbox. Without a gearbox, a machine efficiency η_{mach} around 95 % is predicted for this machine. This is especially interesting for a direct attachment to gas turbines, which generally work at higher rotational speeds than ICE.

The conducted analysis have shown that in terms of dynamic REX operation, the high-speed machines are more advantageous compared to the low-speed machines, as the efficiency is constant over a wide range of generator speeds. This is beneficial, as ICEs normally offer a higher efficiency for variable speed operation, rather than variable torque. For the low-speed machine a torque variation at nominal speed is more beneficial.

Furthermore, the control strategy for SRGs was analyzed. Adding a freewheeling period $\Delta\theta_{\mathrm{fw}}$ to the SPC parameters, leads to a large area of constant machine and system efficiency, varying both freewheeling period $\Delta\theta_{\mathrm{fw}}$ and turn-off angle θ_{off} at the same time. The wide range of constant efficiency makes it possible to influence the system behavior, e.g. the source losses, without a reduction in machine efficiency. For SRG, a freewheeling period $\Delta\theta_{\mathrm{fw}}$ should, therefore, always be considered, even at nominal operation point.

Gravimetric total power densities $\xi_{\mathrm{P,tot}}$ of 1.2 kW/kg are reached for the high-speed machines, at machine efficiencies comparable to the low-speed machine. This value is 72 % higher compared to the low-speed machine, achieved by the increase in nominal generator speed $n_{\mathrm{SRG,nom}}$ from 7.5 to 25 krpm. Employing litz wire, NO10 iron core material and a stator slot closure, the predicted loss reduction in simulation leads to an increased gravimetric total power density $\xi_{\mathrm{P,tot}}$ of up to 1.7 kW/kg in the high-speed machines. This is an increase of 42 % compared to the built prototypes. In the low-speed machines only an increase by 14 % is achieved with the mentioned improvements.

The acoustic behavior of SRGs is only of secondary importance in REX, confirmed by the measurement of the low-speed 2-phase machine coupled to an ICE. However, throughout the complete investigated operation range the high-speed 2-phase machine shows lower amplitudes of individual harmonics compared to the 3-phase alternative. Therefore, as long as 3-phase machines require a number of pole-pairs $n_{\mathrm{p}} = 1$ to reach an acceptable efficiency the 2-phase machine configuration with the same electric base frequency f_{el} is preferred. Especially, as the higher torque ripple in the 2-phase machines does not result in increased gearbox induced vibrations. Finally, influencing the acoustic behavior by means of control mainly influences mechanical vibrations. Therefore, it should only be considered, if the machine efficiency η_{mach} is not negatively influenced.

For a holistic view on SRGs for REX, the material costs for the low- and high-speed machines are analyzed. Based on current market prices, about 35 % of the material costs can be saved by increasing $n_{\mathrm{SRG,nom}}$ from 7.5 to 25 krpm. The improved high-speed machines with litz wire and NO10 iron core material require a material cost increase around 20 %, which might be justified by the higher power density. This is not the case for the low-speed machine with an increase in material cost by over 60 %. Consequently, in terms of costs the high-speed machines are advantageous.

The required power electronics for SRGs for REX were compared. It was found that the torque ripple of the 2-phase machines leads to increased oscillating energies between machine and dc-link capacitor compared to 3-phase machines. This leads to very large dc-link capacitances C_{dc} for the 2-phase low-speed machine. The increased electric base frequency f_{el} in the high-speed HS2ph2p45N machine compensates this effect partially, still, the 3-phase high-speed machine requires the smallest dc-link capacitor.

Reflecting the complete analysis of the two REX speed scenarios, the most advantageous SRGs are 2-phase high-speed machines with a number of pole pairs $n_{\mathrm{p}} > 1$. Up to a generator speed of 25 krpm or an electric base frequency of 1.67 kHz, this machine configurations offer a good machine efficiency, together with an acceptable acoustic behavior. Only if the inverter sizing is of main interest, the corresponding 3-phase alternative should be considered.

6.2 Outlook

It has been shown within this thesis that the frequency dependent machine losses are key to predict hot-spot temperatures of machines with differing electrical base frequencies f_{el}. Therefore, the accurate prediction of the eddy-current copper losses $P_{\mathrm{l,cu,eddy}}$ along with the iron core losses $P_{\mathrm{l,fe}}$ and the thermal model should be further enhanced. Possible steps could be the implementation of a current profile prediction in the pre-design stage to analytically calculate the iron core losses $P_{\mathrm{l,fe}}$. In addition, the prediction of the eddy-current losses $P_{\mathrm{l,cu,eddy}}$ with the help of a constant eddy-loss ratio $p_{\mathrm{eddy,woEw}}(f_{\mathrm{el}})$ could be analyzed for machines with strongly differing input power $P_{\mathrm{m,sh}}$ and dc-link voltage u_{dc}, to derive a general prediction model. In terms of thermal modeling, the knowledge that the hot spot in SRGs is located rather on the air gap-facing coil surface than in the center of the coils could be incorporate in the employed LPTN.

For power-density sensitive applications, the efficiency improvements, by employing litz wire, NO10 iron core material and a stator slot closure, predicted in simulation should be further investigated with the help of measurements on prototypes. Especially, the reduction of the eddy-current copper losses $P_{\mathrm{l,cu,eddy}}$ by litz wire, should be analyzed and benchmarked against alternative solutions with cheaper flat wires. The thermal improvement of the stator slot closure has to be analyzed at dynamic operation, to be able to estimate the reachable power density, especially, as this measure is rather inexpensive and also reduces the windage losses $P_{\mathrm{l,wind}}$ in the air gap.

A Appendix

A.1 Derivation of Slot-to-Pole-Pitch-Ratio

The $STPR$ is a dimensionless quantity describing the stator and rotor outline of the considered SRG.

$$STPR = \frac{A_{\mathrm{slot,st}}}{A_{\mathrm{slot,st}} + A_{\mathrm{pl,st}}} = \frac{A_{\mathrm{slot,st}}}{A_{\mathrm{pitch,st}}} \tag{A.1}$$

$A_{\mathrm{pitch,st}}$ stands for the cross section area of one stator pole pitch defined by stator pole angle $\tau_{\mathrm{pl,s}}$ (fig. A.1). It is the sum of the maximally available coil cross section area in one stator slot $A_{\mathrm{slot,st}}$ and the area of one stator pole $A_{\mathrm{pl,st}}$, depicted by the blue and red areas in fig. A.1, respectively. $A_{\mathrm{pitch,st}}$ can also be expressed by (A.2) and (A.3).

$$A_{\mathrm{pitch,st}} = A_{\mathrm{pl,st}} + A_{\mathrm{slot,st}} \tag{A.2}$$

$$A_{\mathrm{pitch,st}} = \frac{\pi}{N_{\mathrm{s}}} \cdot \left({R_2}^2 - (R_1 + d_{\mathrm{g}})^2 \right) \tag{A.3}$$

The pole cross section area $A_{\mathrm{pl,st}}$ can be calculated applying an integration in the x-y-plane of fig. A.1 from $x_{\mathrm{start}} = 0$ and $x_{\mathrm{end}} = \frac{b_{\mathrm{pl,s}}}{2}$. This results in (A.4) for the cross section area $A_{\mathrm{pl,st}}$ of one pole.

$$\begin{aligned} A_{\mathrm{pl,st}} = (R_1 + d_{\mathrm{g}}) \cdot \sin({}^{\beta_{\mathrm{s}}}/_2) \cdot & \left(\sqrt{{R_2}^2 - \left((R_1 + d_{\mathrm{g}}) \cdot \sin({}^{\beta_{\mathrm{s}}}/_2) \right)^2} \right. \\ & \left. - \sqrt{(R_1 + d_{\mathrm{g}})^2 \cdot \left(1 - \sin^2({}^{\beta_{\mathrm{s}}}/_2) \right)} + \arcsin\left(\tfrac{(R_1 + d_{\mathrm{g}}) \cdot \sin({}^{\beta_{\mathrm{s}}}/_2)}{R_2} \right) \cdot \tfrac{{R_2}^2 - (R_1 + d_{\mathrm{g}})^2}{(R_1 + d_{\mathrm{g}}) \cdot \sin({}^{\beta_{\mathrm{s}}}/_2)} \right) \end{aligned} \tag{A.4}$$

With equation (A.2) the slot cross section area can be expressed by (A.5)

$$A_{\mathrm{slot,st}} = A_{\mathrm{pitch,st}} - A_{\mathrm{pl,st}} \tag{A.5}$$

Additionally, the trigonometric identity in (A.6) applies for (A.4).

$$\cos({}^{\beta_{\mathrm{s}}}/_2) = \sqrt{1 - \sin^2({}^{\beta_{\mathrm{s}}}/_2)} \tag{A.6}$$

Inserting (A.5) into (A.1), applying (A.6) and substituting $A_{\mathrm{pitch,st}}$ and $A_{\mathrm{pl,st}}$ with aid of formulae (A.3) and (A.4) yields (A.7) which allows for determining the slot-to-pole-pitch-ratio $STPR$ by means of geometric parameters.

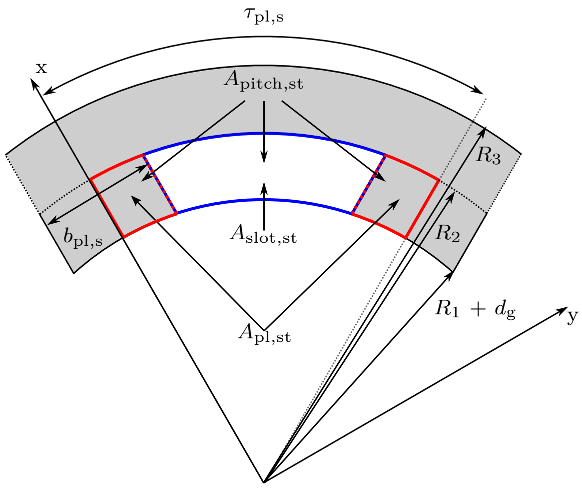

Fig. A.1: Definition of stator pole areas to calculate the $STPR$.

$$STPR = 1 - \frac{N_{\mathrm{s}} \cdot (R_1 + d_{\mathrm{g}}) \cdot \sin(\beta_{\mathrm{s}}/2)}{\pi \cdot \left({R_2}^2 - (R_1 + d_{\mathrm{g}})^2\right)} \cdot \left(\sqrt{{R_2}^2 - \left((R_1 + d_{\mathrm{g}}) \cdot \sin(\beta_{\mathrm{s}}/2)\right)^2} - (R_1 + d_{\mathrm{g}}) \cdot \cos(\beta_{\mathrm{s}}/2) + \arcsin\left(\frac{(R_1 + d_{\mathrm{g}}) \cdot \sin(\beta_{\mathrm{s}}/2)}{R_2}\right) \cdot \frac{{R_2}^2 - (R_1 + d_{\mathrm{g}})^2}{(R_1 + d_{\mathrm{g}}) \cdot \sin(\beta_{\mathrm{s}}/2)} \right) \quad \text{(A.7)}$$

In a well-designed SRG the air gap length in the aligned rotor position is small compared to the rotor tip radius $d_{\mathrm{g}} \ll R_1$. Therefore, (A.8) applies.

$$R_1 + d_{\mathrm{g}} \approx R_1 \quad \text{(A.8)}$$

Furthermore, R_1 and R_2 scale linearly with the outer machine diameter $R_{1,2} \propto D_{\mathrm{st}}$ (A.9).

$$R_1 = k_{\mathrm{R1}} \cdot D_{\mathrm{st}} \qquad \text{and} \qquad R_2 = k_{\mathrm{R2}} \cdot D_{\mathrm{st}} \quad \text{(A.9)}$$

Applying (A.8) and (A.9) to (A.7) leads to (A.10) in which the influence of the machine diameter cancels out.

$$STPR = 1 - \frac{N_{\mathrm{s}} \cdot k_{\mathrm{R1}} \cdot \sin(\beta_{\mathrm{s}}/2)}{\pi \cdot \left(k_{\mathrm{R2}}^2 - k_{\mathrm{R1}}^2\right)} \cdot \left(\sqrt{k_{\mathrm{R2}}^2 - \left(k_{\mathrm{R1}} \cdot \sin(\beta_{\mathrm{s}}/2)\right)^2} - k_{\mathrm{R1}} \cdot \cos(\beta_{\mathrm{s}}/2) + \arcsin\left(\frac{k_{\mathrm{R1}} \cdot \sin(\beta_{\mathrm{s}}/2)}{k_{\mathrm{R2}}}\right) \cdot \frac{k_{\mathrm{R2}}^2 - k_{\mathrm{R1}}^2}{k_{\mathrm{R1}} \cdot \sin(\beta_{\mathrm{s}}/2)} \right) \quad \text{(A.10)}$$

In this relation, k_{R1} and k_{R2} represent normalized quantities defining the machine outline and D_{st} is the corresponding scaling factor. For these reasons, the $STPR$ can be regarded independent of the diameter in a first order approximation. This results in visually resembling machine outlines for the same configuration and $STPR$.

A.2 Investigated Switched Reluctance Generator

A.2.1 Built Prototypes

Preliminary machines discussed in chapter 3 are defined by their design quadruple (number of phases N_{ph}, number of pole pairs n_{p}, stator outer diameter D_{st}, $STPR$). A left out parameter indicates a variable value, e.g. a (2,1,120 mm) triple defines all designs with $N_{\mathrm{ph}} = 2$, $n_{\mathrm{p}} = 1$, $D_{\mathrm{st}} = 120\,\mathrm{mm}$ and variable $STPR$.

All machines considered in detail in this thesis are named by the convention defined in table A.1. These machines have a detailed winding design. The built prototypes are listed with their characteristic parameters in table A.2. Based on the fixed iron cross-section, the permutations listed in table A.3 were built in simulation, to investigate their influence on the loss behavior. Additional to the built prototypes in this thesis, the two machines mentioned in table A.6 were considered in the detailed discussion in chapter 4 and 5. While the HS3ph3p25N machine is an actual prototype from a different project, the LS2ph2p68N only exists in simulation.

To compare the initially built prototypes LS2ph3p60N, HS2ph2p45N and HS3ph1p49N (see table A.2) at equal thermal conditions, two model variations were performed with the help of MotorCAD. For the first variation (indicated with I1) the obtained losses of the prototypes LS2ph3p60N, HS2ph2p45N and HS3ph1p49N (listed as reached in table 4.9) are kept constant and the stack length L_{stk} is increased to obtain a coil hot spot temperature of 180 °C. For the second variation the reduced losses (listed as improved in table 4.9) are applied to the MotorCAD model and the stack length L_{stk} is reduced to obtain again a coil hot spot temperature of 180 °C. The active parts length L_{act} and total machine length L_{tot} are changed in both cases by the same absolute value as the iron core stack length L_{stk}. The resulting machine lengths are listed in table A.4. All machines exist only in simulation. The machine cross sections described in table A.2 are kept constant for all variations and the influence of the changed stack length L_{stk} on dynamic phase voltage u_{ph} (see (2.9)) and, consequently, coil design and coenergy loop W_{co} are neglected.

AA	N_{ph} **ph**	n_{p} **p**	$N_{\mathrm{w,pl}}$ **N**	B
scenario identifier HS = high-speed LS = low-speed	number of phases	number of pole pairs	number of turns per coil	variation identifier defined in table A.3

Table A.1: Machine naming convention.

A.2.1.1 Mechanical Machine Variations

Due to mechanical issues, the bearing, sealing and rotor shaft concept of the HS2ph2p45N machine had to be reconsidered during the course of this thesis. Keeping the electromagnetic stator and rotor design of the HS2ph2p45N machine (see table A.2), the following mechanical changes were undertaken for the HS2ph2p45NX machine. The employed contact sealing between gearbox and generator in the HS2ph2p45N machine is replaced by a contact-less labyrinth sealing in the HS2ph2p45NX machine. The oil-lubricated grooved ball bearing B3 (see fig. 2.3b) is replaced by a cylindrical roller bearing and the grease lubricated grooved ball bearing B4 is replaced by two smaller grease lubricated grooved ball bearings. The changes result in equal electromagnetic behavior, however, the mechanical losses are changed, as discussed in section 4.1.3.

configuration (N_{ph},n_{p},D_{st},$STPR$)	(2,3,220,-)	(2,2,140,0.655)	(3,1,140,0.67)
prototype naming table A.1	LS2ph3p60N	HS2ph2p45N	HS3ph1p49N
mech. permutation	(-)	section A.2.1.1	(-)
N_{ph}	2	2	3
n_{p}	3	2	1
$STPR$	(-)	0.655	0.67
N_{s}	12	8	6
N_{r}	6	4	4
D_{st} in mm	220	140	140
D_{rot} in mm	150.7	73.6	66.3
d_{g} in mm	1.0	0.7	0.7
L_{stk} in mm	60	80	80
L_{act} in mm	90	112	118
L_{tot} in mm	140	200	200
β_{s} in $^\circ$	12	20.3	27
β_{r} in $^\circ$	12	20.3	33
electric steel material	NO30	NO20	NO20
u_{dc} in V	300	400	400
$N_{\mathrm{w,pl}}$	60	45	49
d_{gsp} in mm	4.4	5.1	4.0
d_{ins} in mm	0.1	0.1	0.1
$d_{\mathrm{ins,w}}$ in mm	0.05	0.05	0.05
d_{w} in mm	1.7	1.7	2
coil design	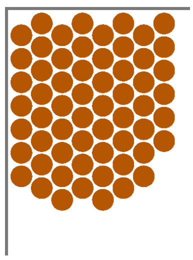	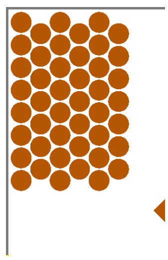	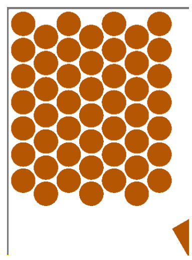
cross-section	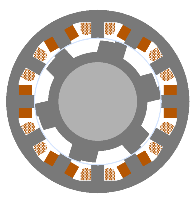	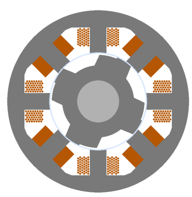	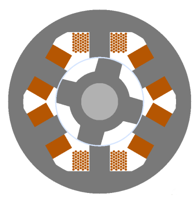
MotorCAD	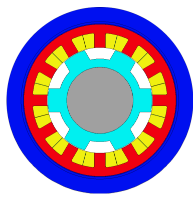	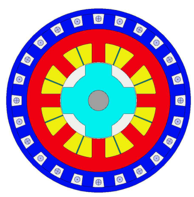	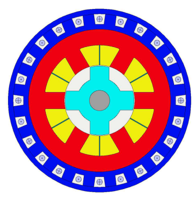

Table A.2: Main parameter of built prototypes. Cross-sections only for illustration and not to scale. Permutations of the coil design are depicted in table A.3.

	LS2ph3p60N	LS2ph3p80N	HS3ph1p49N	HS3ph1p49N1
$N_{\mathrm{w,pl}}$	60	80	49	49
d_{w} in mm	1,7	1,5	2	1,85
coil design	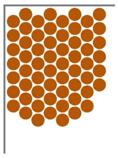	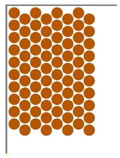	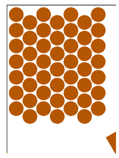	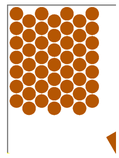

	HS2ph2p18N	HS2ph2p27N	HS2ph2p27N1	HS2ph2p33N
$N_{\mathrm{w,pl}}$	18	27	27	33
d_{w} in mm	2,7	2,2	2,2	2
coil design	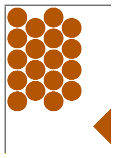	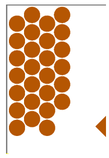	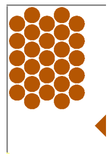	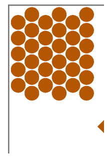

	HS2ph2p39N	HS2ph2p45N	HS2ph2p45N1	HS2ph2p45N2
$N_{\mathrm{w,pl}}$	39	45	45	45
d_{w} in mm	1,8	1,7	1,5	1,9
coil design	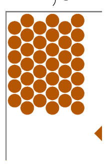	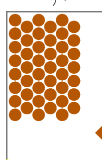	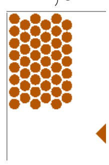	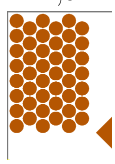

	HS2ph2p45N3	HS2ph2p45N4	HS2ph2p45N5	HS2ph2p51N
$N_{\mathrm{w,pl}}$	45	45	45	51
d_{w} in mm	2,1	2,2	1,7	1,7
coil design	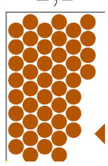	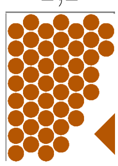	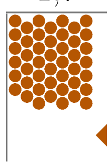	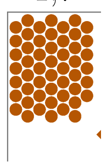

	HS2ph2p51N1	HS2ph2p57N	HS2ph2p90N	HS2ph2p90N1
$N_{\mathrm{w,pl}}$	51	57	90	90
d_{w} in mm	1,6	1,5	1,2	1,2
coil design	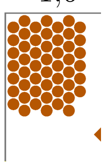	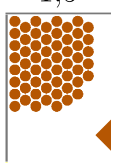	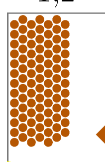	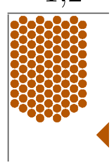

Table A.3: Permutations of prototypes in table A.2.

	machine losses $P_{\mathrm{l,mach}}$	L_{stk} in mm	L_{act} in mm	L_{tot} in mm
LS2ph3p60N	reached in table 4.9	60.0	90.0	140.0
LS2ph3p60NI1	reached in table 4.9	69.0	99.0	149.0
LS2ph3p60NI2	improved in table 4.9	54.0	84.0	134.0
HS2ph2p45N	reached in table 4.9	80.0	112.0	200.0
HS2ph2p45NI1	reached in table 4.9	81.6	113.6	201.6
HS2ph2p45NI2	improved in table 4.9	50.0	82.0	170.0
HS3ph1p49N	reached in table 4.9	80.0	118.0	200.0
HS3ph1p49NI1	reached in table 4.9	83.2	121.2	203.2
HS3ph1p49NI2	improved in table 4.9	46.0	84.0	166.0

Table A.4: Increased axial machine lengths to reach a hot spot coil temperature $\vartheta_{\mathrm{coil,hs}} = 180\,°\mathrm{C}$. Machine cross sections of corresponding prototype listed in table A.2.

	steel	aluminum	copper wires	iron core material	total weight
LS2ph3p60N	4.15 kg	9.75 kg	3.55 kg	8.69 kg	26.14 kg
LS2ph3p60NI1	4.77 kg	9.83 kg	3.83 kg	9.99 kg	28.43 kg
LS2ph3p60NI2	3.73 kg	9.70 kg	3.36 kg	7.82 kg	24.61 kg
HS2ph2p45N	1.90 kg	6.67 kg	2.08 kg	5.90 kg	16.63 kg
HS2ph2p45NI1	1.91 kg	6.81 kg	2.10 kg	6.02 kg	16.85 kg
HS2ph2p45NI2	1.59 kg	5.69 kg	1.59 kg	3.69 kg	12.55 kg
HS3ph1p49N	1.90 kg	6.76 kg	2.23 kg	5.78 kg	16.67 kg
HS3ph1p49NI1	1.93 kg	6.87 kg	2.28 kg	6.02 kg	17.10 kg
HS3ph1p49NI2	1.55 kg	5.54 kg	1.67 kg	3.33 kg	12.09 kg

Table A.5: Material weights for cost calculations in section 4.4.1.

configuration	(2,2,220,-)	(3,3,270,-)
prototype naming table A.1	LS2ph2p68N	HS3ph3p25N
N_{ph}	2	3
n_{p}	2	3
N_{s}	8	18
N_{r}	4	12
D_{st} in mm	220	270
D_{rot} in mm	144.7	110
d_{g} in mm	1.0	0.5
L_{stk} in mm	60	120
L_{act} in mm	109	-
β_{s} in °	18	10.8
β_{r} in °	18	13.3
electric steel material	NO30	NO30
u_{dc} in V	300	325
$N_{\mathrm{w,pl}}$	68	25
d_{ins} in mm	-	0.3
$d_{\mathrm{ins,w}}$ in mm	-	0.05
d_{w} in mm	-	1.6
coil design		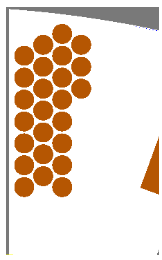
cross-section	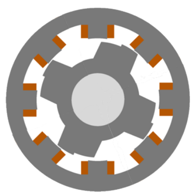	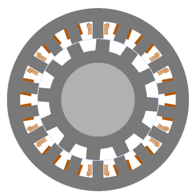

Table A.6: Main parameters of additional machines considered in this thesis. Cross-sections only for illustration and not to scale.

A.3 Simulation Model Parametrization

A.3.1 MotorCAD Base Model Parametrization

Parameter		Value
Cooling fluid water flow Q_{flow}		12 l/min
end-shaft temperature ϑ_{sh}		free
stator-housing interface		`good`
number of axial stator slices		1
Impregnation goodness ζ_{liner}		1.75
Impregnation goodness ζ_{winding}	LS2ph3p60N	1.75
	HS2ph2p45N	2
	HS3ph1p49N	1

Table A.7: MotorCAD model setup.

Machine Part	Material	Thermal Conductivity $^{W}/_{\text{m}\cdot\text{K}}$
Housing	Aluminum Alloy 1995 Cast	168
Endcap	Aluminum Alloy 1995 Cast	168
Stator Lamination	NO20 0.2 strip	27
Rotor Lamination	NO20 0.2 strip	27
Stator Inter Lamination	Default	2.72E-2
Rotor Inter Lamination	Default	2.723E-2
Winding	Copper	401
Winding Insulation	Default	0.21
Impregnation	Epoxy	0.22
Slot Liner	Nomex 410	0.14
Shaft	HS50	47
Bearing	Default	30

Table A.8: MotorCAD material parametrization.

A.4 Measurements

A.4.1 Measurement Equipment and Uncertainty

Electric Power Measurement

The phase currents i_{ph} at the phase terminals as well as the inverter input current i_{src} are measured with LEM sensors. i_{ph} is measured with 400 A (HS2ph2p45N and LS2ph3p60N) and 200 A (HS3ph1p49N) sensors, while i_{src} is measured with a 600 A sensor. All current sensors have a measurement uncertainty of 0.02 % of the measurement range. To this sensor uncertainty, the internal measurement uncertainty of the Zimmer ZES LMG500 power measurement device of up to 0.09 % of the measurement range, depending on the signal frequency, has to be added. In the frequency range of up to 3 kHz, this internal uncertainty is reduced to 0.045 %. Voltage is measured with the internal sensors of the Zimmer ZES LMG500 power measurement device. Therefore, only the measurement uncertainty has to be considered. This uncertainty is equal to the uncertainty of the current measurement.

As SRG currents are not sinusoidal but consist of a large frequency range, the exact error cannot be determined easily. Considering frequencies up to 3 kHz the total measurement error for the machine output power $P_{\mathrm{el,SRG}}$ adds up to approximately 0.75 % for the HS3ph1p49N machine and 1 % for the HS2ph2p45N and the LS2ph3p60N machine at nominal operation point NOP_{M} (see table A.11).

Mechanical Power Measurement

Mechanical power is measured with the help of a FLFM-1 torque transducer of the company GIF with integrated speed measurement. The measurement range of the torque transducer is 300 Nm, the required measurement range is defined by the large torque ripple of over 3 for the 2-phase machines (see fig. 4.19). The measurement uncertainty is 0.1 % of the measurement range or 0.3 Nm. For the high-speed machines HS2ph2p45N and HS3ph1p49N this signifies a total error of about 1 % and for the LS2ph3p60N machine a total error of 1.2 % due to the reduced $T_{\mathrm{tot,nom}}$ (see table A.11).

Combined Power Measurement Uncertainty

The before mentioned uncertainties add up to a total measurement uncertainty listed in table A.9.

machine	measurement uncertainty at NOP_{M} (see table A.11)
LS2ph3p60N	2.2 %
HS2ph2p45N	2.0 %
HS3ph1p49N	1.75 %

Table A.9: Overview of the approximate power measurement uncertainty of the employed equipment.

Temperature Measurement

Temperatures in the machines are measured with Typ-K thermocouple elements. The sensors are read by a IPEtronik M-Thermo 16 device with internal temperature compensation.

Vibration Measurement

For the vibration measurement, miniature piezo accelerometers of the type KS95B10 and KS05B100 as well as triaxial accelerometers of the type KS903.10 and KS903.100 of the company Manfred Weber Metra Meß- und Frequenztechnik in Radebeul e.K. (MMF), are employed. Due to the aluminum housings of the machines, the sensors were glued with the help of adapterpads and a ceramic methyl methacrylat glue to the machine surface. The sensors were attached to the machines in the axial center of the stator at the positions shown in fig. A.2.

The sensors are attached via sound and vibration input modules NI-9234 to a compact DAQ-chassis type cDAQ-9188 of the company National Instruments. The acceleration is sampled with a sample frequency of 51.2 kHz and the acquired data is transfered via local area network to a LabView interface.

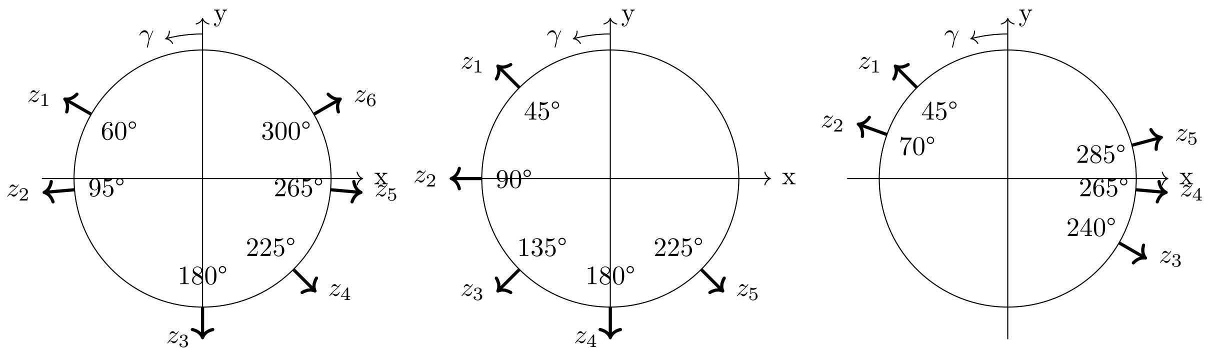

(a) LS2ph3p60N (b) HS2ph2p45N (c) HS3ph1p49N

Fig. A.2: Position of employed piezo-sensors for acoustic measurements. All sensors are positioned on the housing in the axial center of the stator iron core.

A.4.2 Electric Test Bench and Control Platform

A complete test bench setup of the HS3ph1p49N machine is depicted in fig. A.3. The test bench consists of the following components:

1. SRG (HS3ph1p49N)
2. electric prime mover (induction machine)
3. SRG control platform
4. SRG power electronics
5. dc-link capacitor bank
6. power measuring
7. accelerometer hub
8. temperature hub
9. CAN interface
10. water cooler

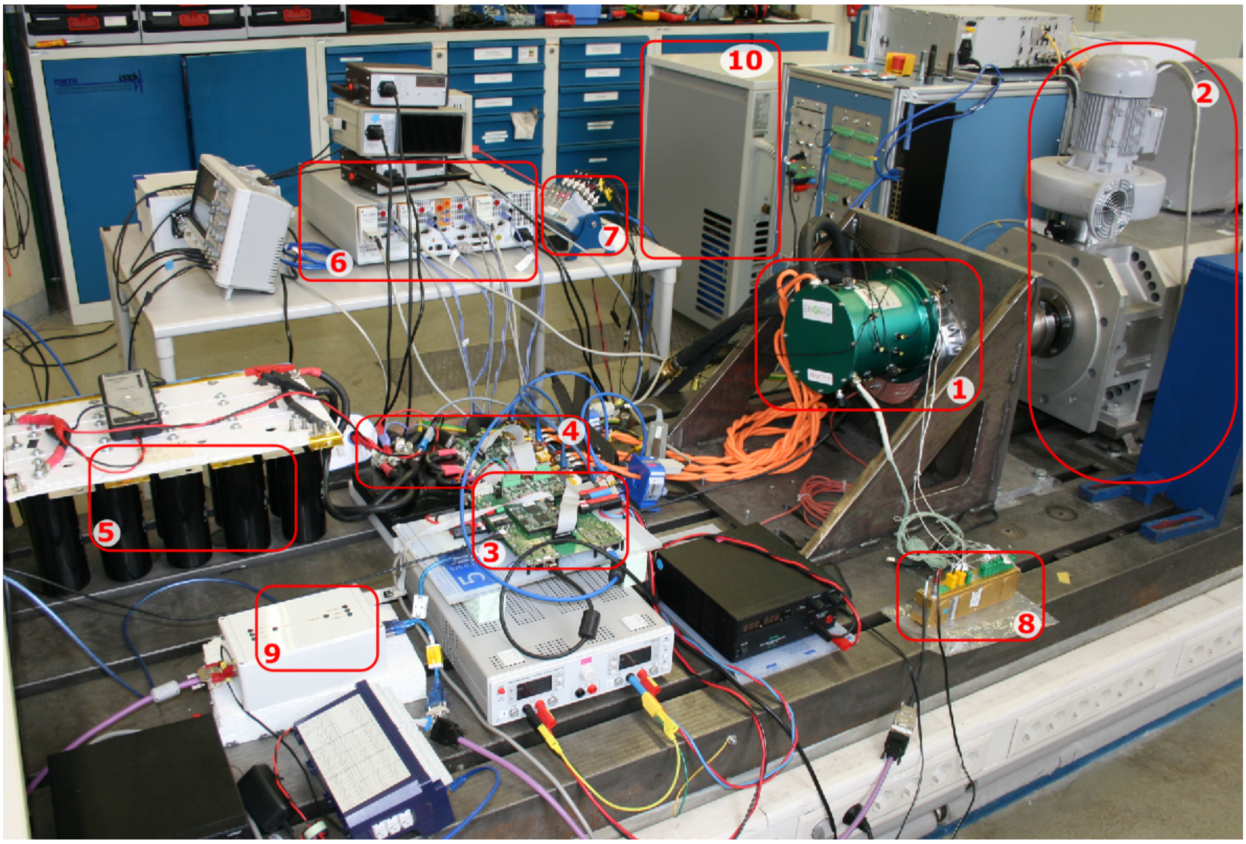

Fig. A.3: Electric test bench with components indicated above.

The inverter consists of two Infineon Hybrid Pack^{TM} Light as main power electronic component and a control platform developed at Institute for Power Electronics and Electrical Drives (ISEA). To control the machines on the test bench, a combination of a digital signal processor (DSP) and a field programmable gate array (FPGA) is employed. Time critical position sensing and current control is performed in the FPGA, while the communication with the control PC and safety functions are implemented in the DSP. More details on the control structure shown in fig. A.4 can be found in [Got+13].

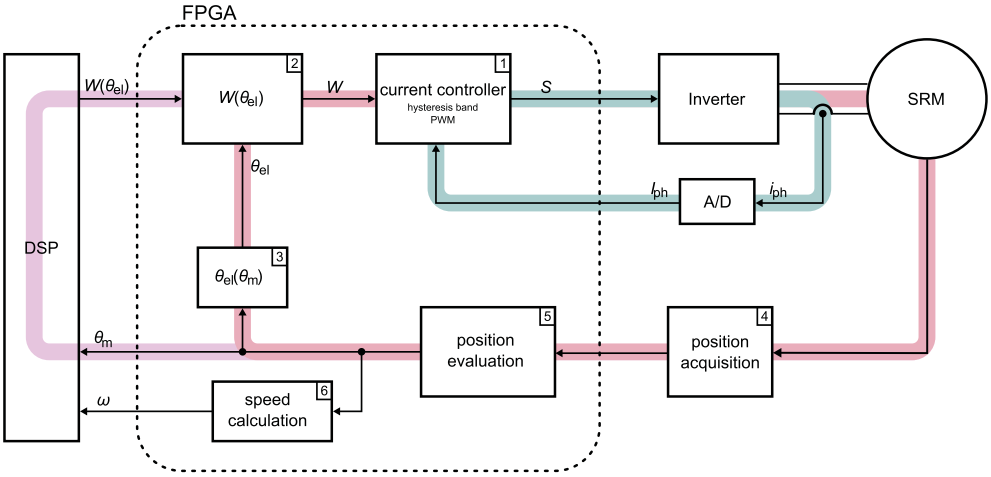

Fig. A.4: Overview of the employed SRG control structure taken from [Got+13].

A.4.3 Simulation Parameters and Measurement Results

A.4.3.1 Operation Points for Simulation and Measurement

Operation point	scenario	$P_{m,sh}$	n_{SRG}	f_{el}	T_{tot}	ϑ_{coil}
NOP_S	high-speed	20 kW	25 krpm	1667 Hz	7.64 Nm	170 °C
	low-speed	20 kW	7.5 krpm	750 Hz	25.5 Nm	170 °C
$PART_{S,40}$	high-speed	8 kW	10 krpm	667 Hz	7.64 Nm	170 °C
	low-speed	8 kW	3 krpm	300 Hz	25.5 Nm	170 °C

Table A.10: Definition of operation point NOP_S for pre-simulations for the high- and low-speed scenario.

Operation point	machine	$P_{m,sh}$	n_{SRG}	T_{tot}	$\vartheta_{coil,hs}$
NOP_M	HS2ph2p45N / HS3ph1p49N	20 kW	24 705 rpm	7.73 Nm	table A.12 - A.13
	LS2ph3p60N	20 kW	7500 rpm	25.5 Nm	table A.14
$PART_{M,83}$	HS2ph2p45N / HS3ph1p49N	16.7 kW	20 588 rpm	7.73 Nm	table A.12 - A.13
	LS2ph3p60N	16.7 kW	6250 rpm	25.5 Nm	table A.14
$PART_{M,67}$	HS2ph2p45N / HS3ph1p49N	13.3 kW	16 470 rpm	7.73 Nm	table A.12 - A.13
	LS2ph3p60N	13.3 kW	5000 rpm	25.5 Nm	table A.14
$PART_{M,50}$	HS2ph2p45N / HS3ph1p49N	10 kW	12 352 rpm	7.73 Nm	table A.12 - A.13
	LS2ph3p60N	10 kW	3750 rpm	25.5 Nm	table A.14

Table A.11: Definition of measured operation points. Parameters applied to simulation and measurement for comparison.

Simulation and Measurement Results

OP	condition	$P_{\mathrm{m,sh}}$ kW	η_{mach} %	θ_{on} in °el	θ_{fw} °el	θ_{off} °el	$I_{\mathrm{ph,rms}}$ A	$\vartheta_{\mathrm{coil,hs}}$ °C
	best meas	10.02	90.43	186.0	40	280	69.6	109
$PART_{\mathrm{M,50}}$	set sim	10.09	90.62	182.5	40	280	68.1	170
	best sim	9.98	90.76	197.6	40	290	68.4	170
	best meas	13.47	90.87	166.3	30	270	71.5	118
$PART_{\mathrm{M,67}}$	set sim	13.39	90.65	161.1	30	270	71.2	170
	best sim	13.31	90.97	177.8	30	280	70.0	170
	best meas	16.78	90.92	152.9	30	270	75.1	139
$PART_{\mathrm{M,83}}$	set sim	16.64	90.62	146.8	30	270	75.0	170
	best sim	16.64	90.85	163.9	30	280	74.5	170
	best meas	20.14	90.55	133.2	20	260	77.6	152
NOP_{M}	set sim	19.98	89.96	123.6	20	260	81.3	170
	best sim	19.98	90.50	159.8	20	280	79.2	170

Table A.12: Switching parameters, measurement and simulation results of HS2ph2p45N machine.

OP	condition	$P_{\mathrm{m,sh}}$ kW	η_{mach} %	θ_{on} in °el	θ_{fw} °el	θ_{off} °el	$I_{\mathrm{ph,rms}}$ A	$\vartheta_{\mathrm{coil,hs}}$ °C
	best meas	10.03	90.71	139.9	50	260	41.9	112
$PART_{\mathrm{M,50}}$	set sim	10.01	91.30	137.1	50	260	37.4	170
	best sim	10.01	91.51	152.4	50	270	37.6	170
	best meas	13.38	91.05	137.1	50	270	44.3	128
$PART_{\mathrm{M,83}}$	set sim	13.44	91.72	134.0	50	270	39.8	170
	best sim	13.32	91.64	152.4	40	270	39.6	170
	best meas	16.80	90.53	103.7	20	240	44.0	146
$PART_{\mathrm{M,83}}$	set sim	16.74	91.22	94.5	20	240	40.8	170
	best sim	16.65	91.47	120.0	30	260	41.0	170
	best meas	20.12	90.50	87.5	20	240	45.4	154
NOP_{M}	set sim	19.93	90.93	76.2	20	240	43.7	170
	best sim	19.98	91.22	112.0	20	260	44.0	170

Table A.13: Switching parameters, measurement and simulation results of HS3ph1p49N machine.

OP	condition	$P_{\mathrm{m,sh}}$ kW	η_{mach} %	θ_{on} in °el	θ_{fw} °el	θ_{off} °el	$I_{\mathrm{ph,rms}}$ A	$\vartheta_{\mathrm{coil,hs}}$ °C
$PART_{\mathrm{M},50}$	best meas	10.02	90.13	194.4	40	280	113.4	115
	best sim	9.99	90.48	196.3	40	280	109.4	170
$PART_{\mathrm{M},83}$	best meas	13.17	90.88	186.3	20	270	114.0	110
	best sim	13.31	91.77	188.2	20	270	110.5	170
$PART_{\mathrm{M},83}$	best meas	16.51	91.36	174.7	20	270	116.7	130
	best sim	16.63	92.36	176.5	20	270	114.3	170
NOP_{M}	best meas	20.08	91.47	161.7	20	270	122.7	140
	best sim	19.96	92.40	165.6	20	270	119.8	170

Table A.14: Switching parameters, measurement and simulation results of LS2ph3p60N machine.

Machine	material	$P_{\mathrm{l,mach}}$	$P_{\mathrm{l,cu,ac}}$	$P_{\mathrm{l,cu,eddy}}$	$P_{\mathrm{l,cu,dc}}$	$P_{\mathrm{l,fe}}$	SP	SY	RP	RY	$P_{\mathrm{l,m}}$
1	NO10	1395	975	169	806	180	35	79	24	42	240
1	NO20	1448	975	169	806	233	52	99	30	52	240
1	NO30	1517	975	169	806	302	71	126	39	66	240
2	NO10	1731	677	234	443	210	60	102	18	30	844
2	NO20	1898	677	234	443	377	112	183	31	51	844
2	NO30	2041	677	234	443	520	156	250	43	71	844
3	NO10	1576	575	236	339	229	51	118	17	43	772
3	NO20	1755	575	236	339	408	86	213	27	82	772
3	NO30	1933	575	236	339	586	121	306	38	121	772

Table A.15: Simulated losses for different iron core materials at operation point NOP_{S} (see table A.10).
1 = LS2ph3p60N, 2 = HS2ph2p45N, 3 = HS3ph1p49N, SP = stator pole, SY = stator yoke, RP = rotor pole, RP = rotor yokes

A.4.3.2 Simulation and Measurement 16.7 kW

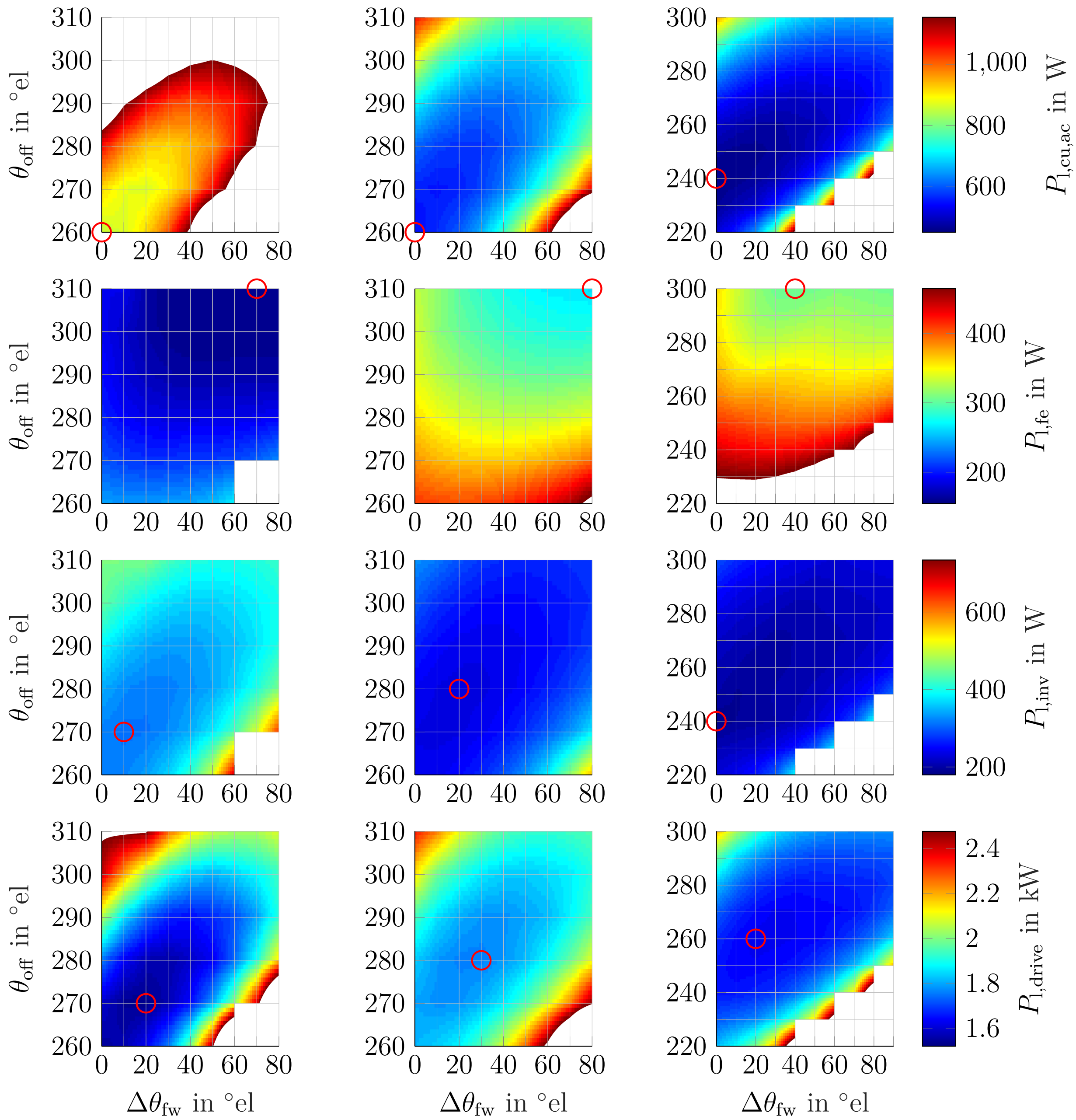

(a) LS2ph3p60N (b) HS2ph2p45N (c) HS3ph1p49N

Fig. A.5: Simulated drive losses over switching parameters at operation point $PART_{\mathrm{M},83}$ (see table A.11). Turn on angle θ_{on} selected to obtain constant torque $T_{\mathrm{tot,nom}}$. Red circles mark loss minimum.

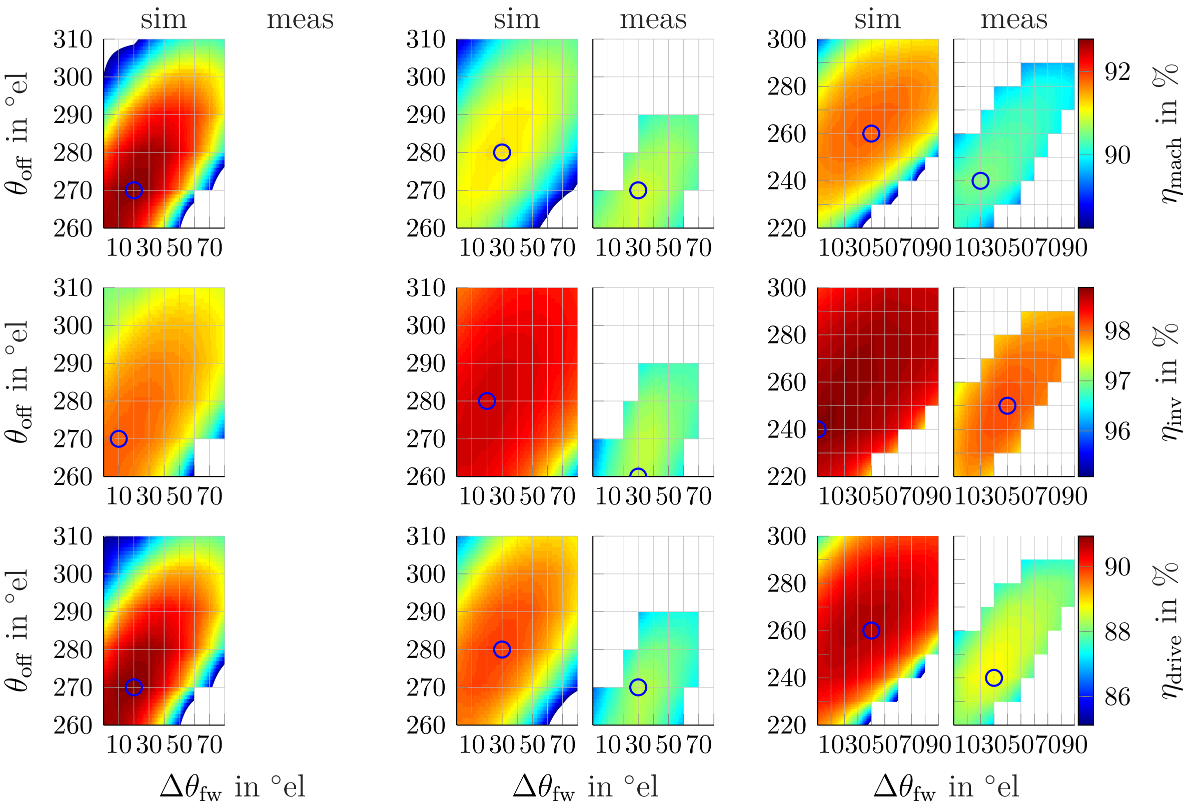

(a) LS2ph3p60N (b) HS2ph2p45N (c) HS3ph1p49N

Fig. A.6: Comparison of simulated and measured efficiencies at operation point $PART_{\mathrm{M,83}}$ (see table A.11). Blue circles mark efficiency maximum. LS2ph3p60N measurements only performed in best point (see fig. A.7).

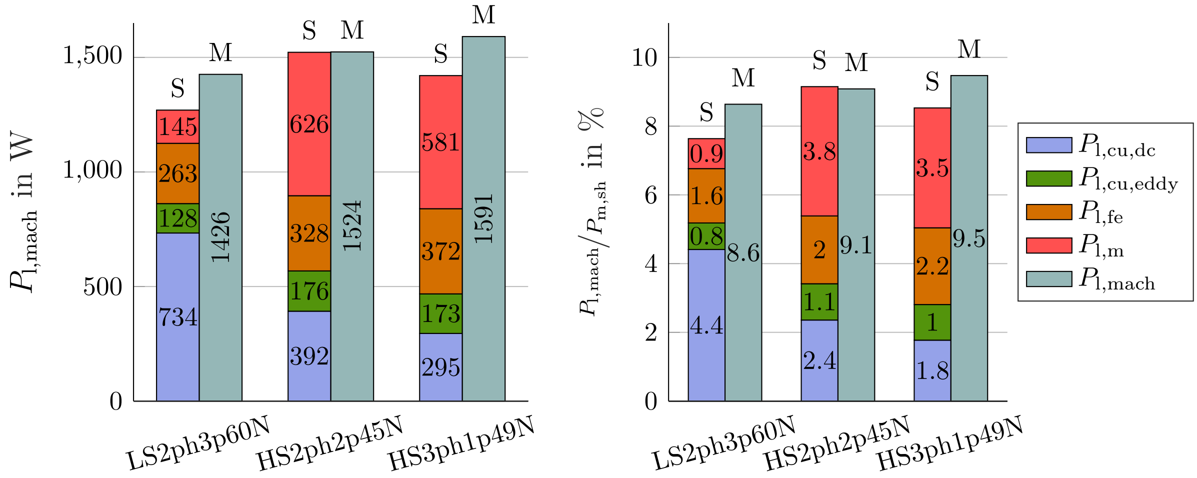

(a) absolute losses (b) losses relative to $P_{\mathrm{m,sh}}$

Fig. A.7: Comparison of simulated (S) and measured (M) machine losses $P_{\mathrm{l,mach}}$ for the built prototypes (see table A.2). operation point: $PART_{\mathrm{M,83}}$ (see table A.11)

A.4.3.3 Simulation and Measurement 13.3 kW

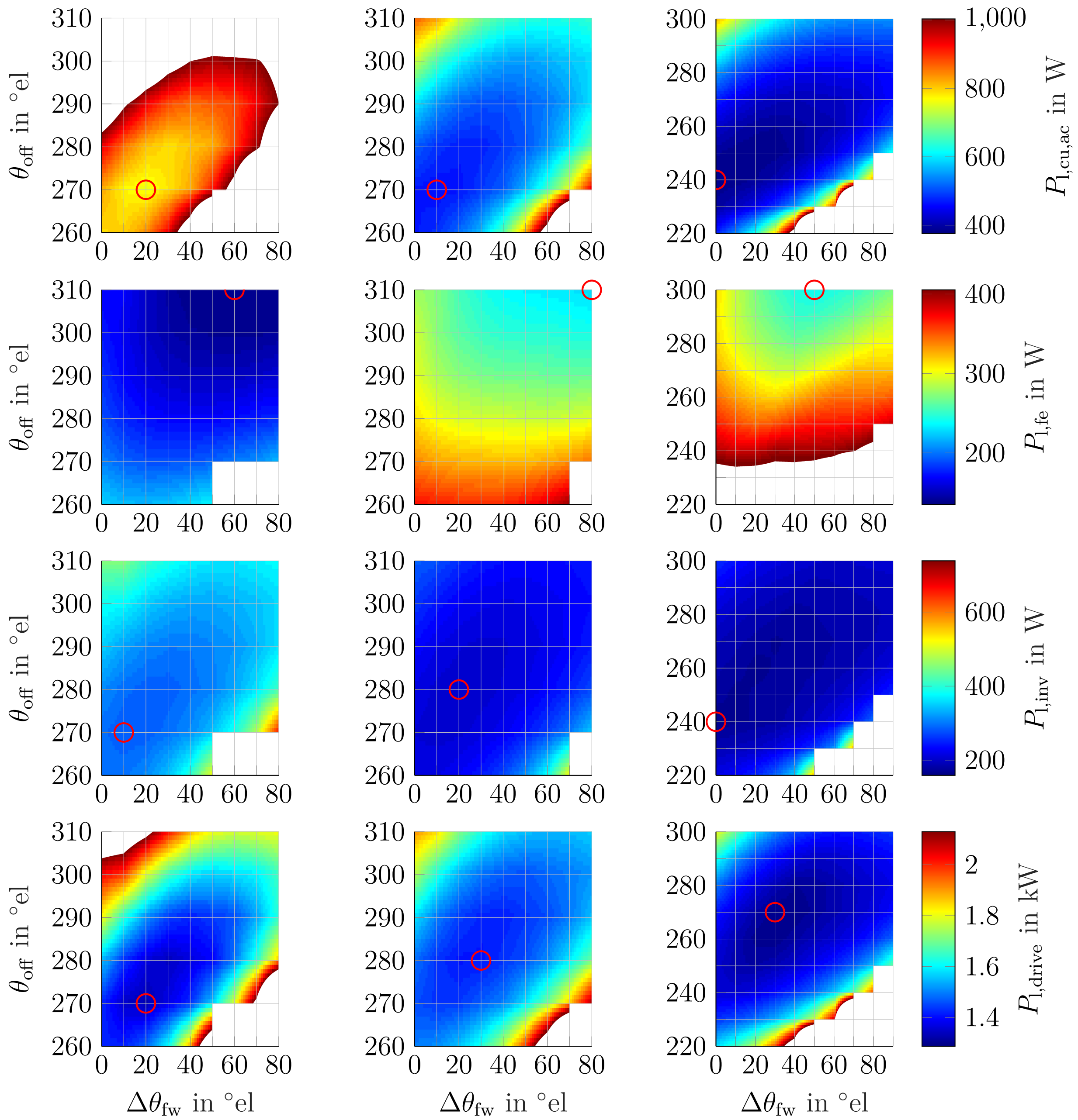

(a) LS2ph3p60N (b) HS2ph2p45N (c) HS3ph1p49N

Fig. A.8: Simulated drive losses over switching parameters at operation point $PART_{\mathrm{M,67}}$ (see table A.11). Turn on angle θ_{on} selected to obtain constant torque $T_{\mathrm{tot,nom}}$. Red circles mark loss minimum.

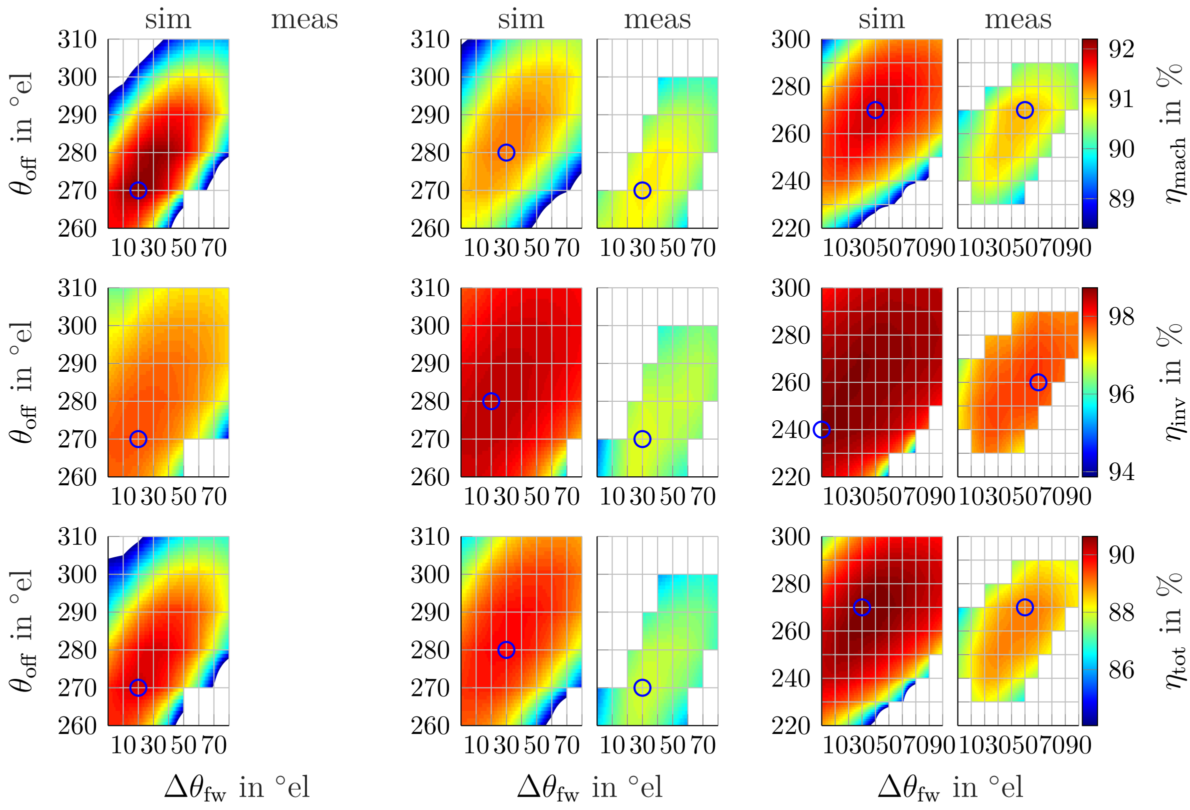

(a) LS2ph3p60N (b) HS2ph2p45N (c) HS3ph1p49N

Fig. A.9: Comparison of simulated and measured efficiencies at operation point $PART_{M,67}$ (see table A.11). Blue circles mark efficiency maximum. LS2ph3p60N measurements only performed in best point (see fig. A.10).

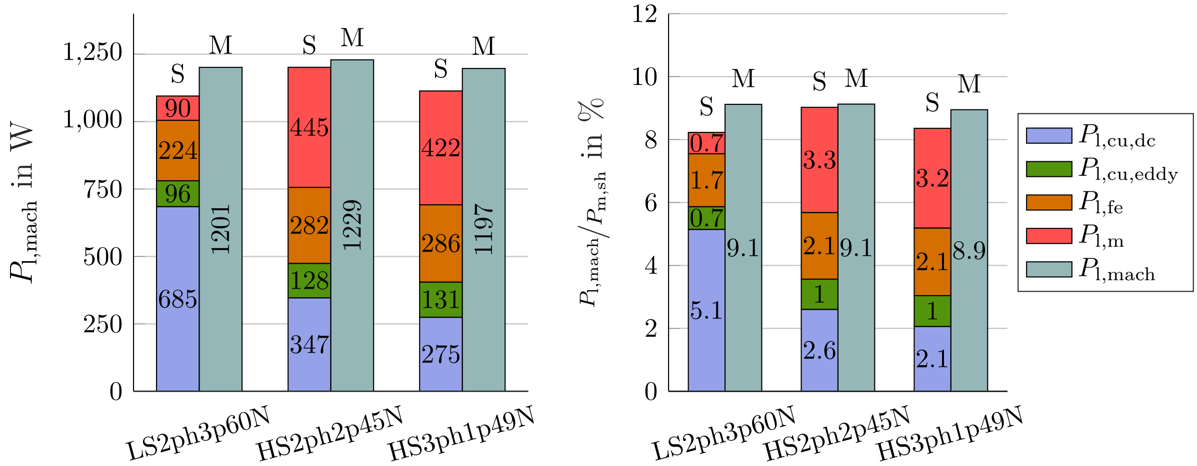

(a) absolute losses (b) losses relative to $P_{m,sh}$

Fig. A.10: Comparison of simulated (S) and measured (M) machine losses $P_{l,mach}$ for built prototypes (see table A.2). operation point: $PART_{M,67}$ (see table A.11)

A.4.3.4 Simulation and Measurement 10.0 kW

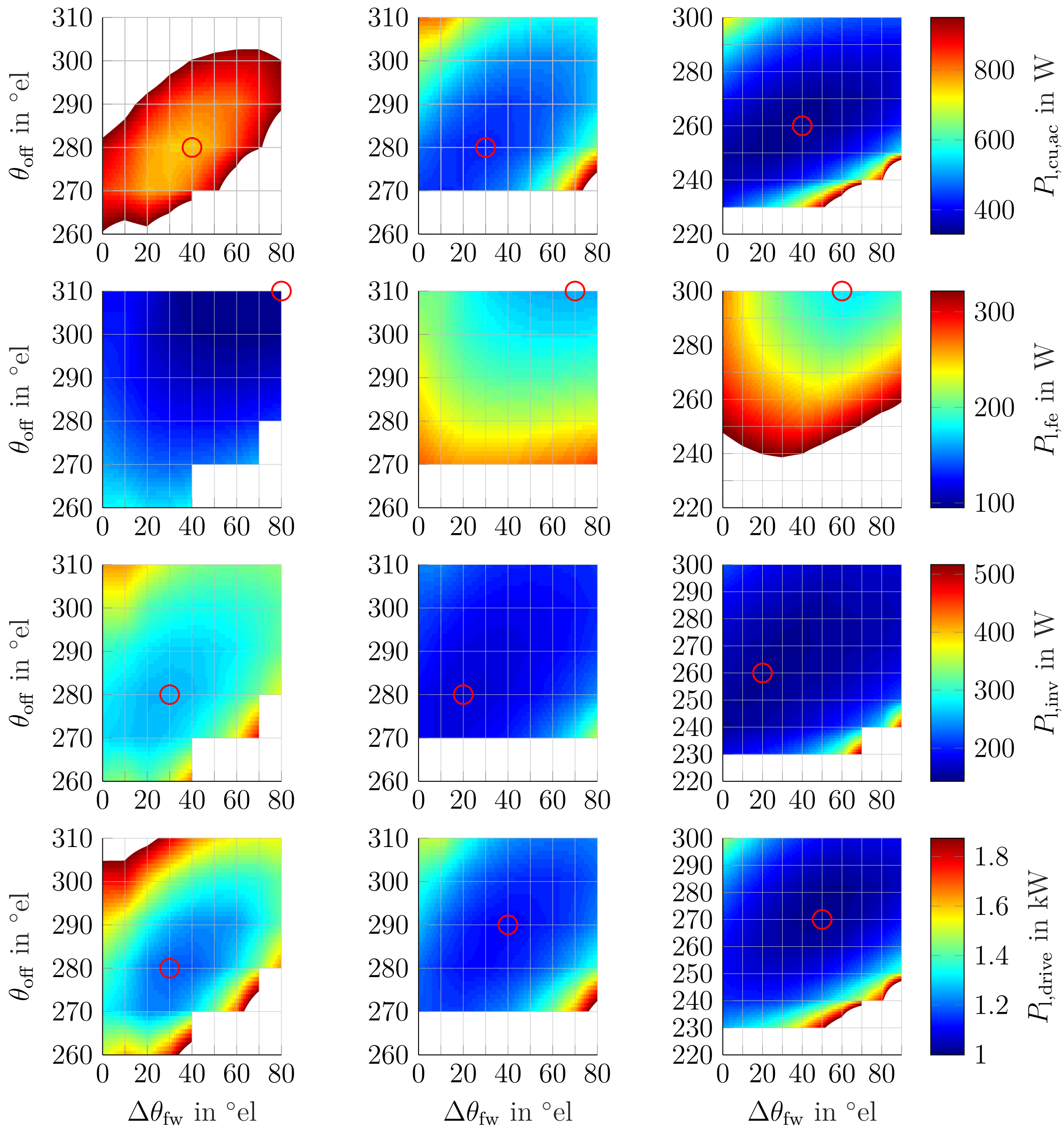

(a) LS2ph3p60N (b) HS2ph2p45N (c) HS3ph1p49N

Fig. A.11: Simulated drive losses over switching parameters at operation point $PART_{M,50}$ (see table A.11). Turn on angle θ_{on} selected to obtain constant torque $T_{tot,nom}$. Red circles mark loss minimum.

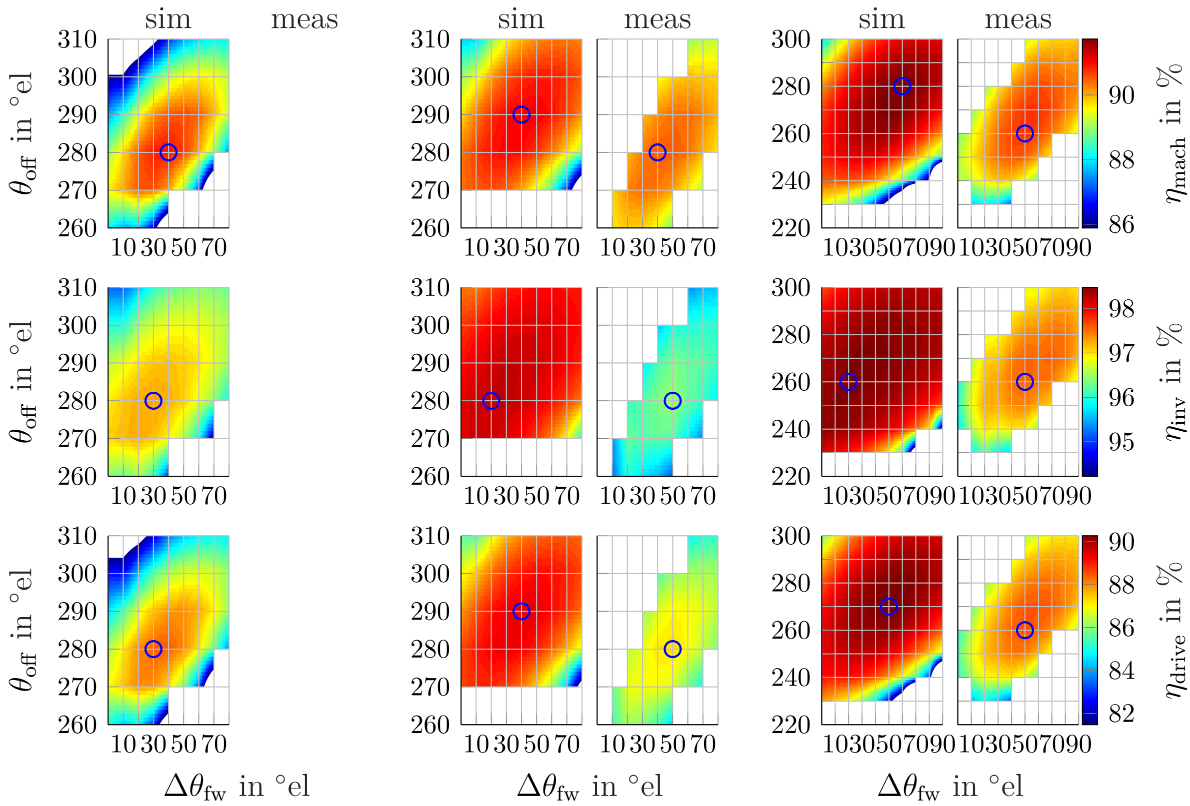

(a) LS2ph3p60N (b) HS2ph2p45N (c) HS3ph1p49N

Fig. A.12: Comparison of simulated and measured efficiencies at operation point $PART_{\mathrm{M,50}}$ (see table A.11). Blue circles mark efficiency maximum. LS2ph3p60N measurements only performed in best point (see fig. A.13).

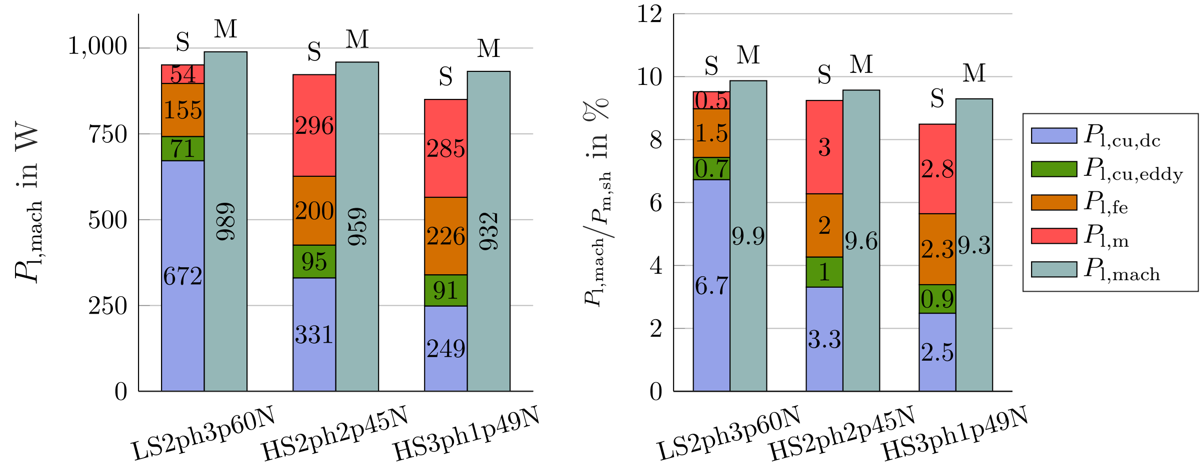

(a) absolute losses (b) losses relative to $P_{\mathrm{m,sh}}$

Fig. A.13: Comparison of simulated (S) and measured (M) machine losses $P_{\mathrm{l,mach}}$ for the built prototypes (see table A.2). operation point: $PART_{\mathrm{M,50}}$ (see table A.11)

A.4.3.5 Stationary Acoustic Comparison at Partial Load

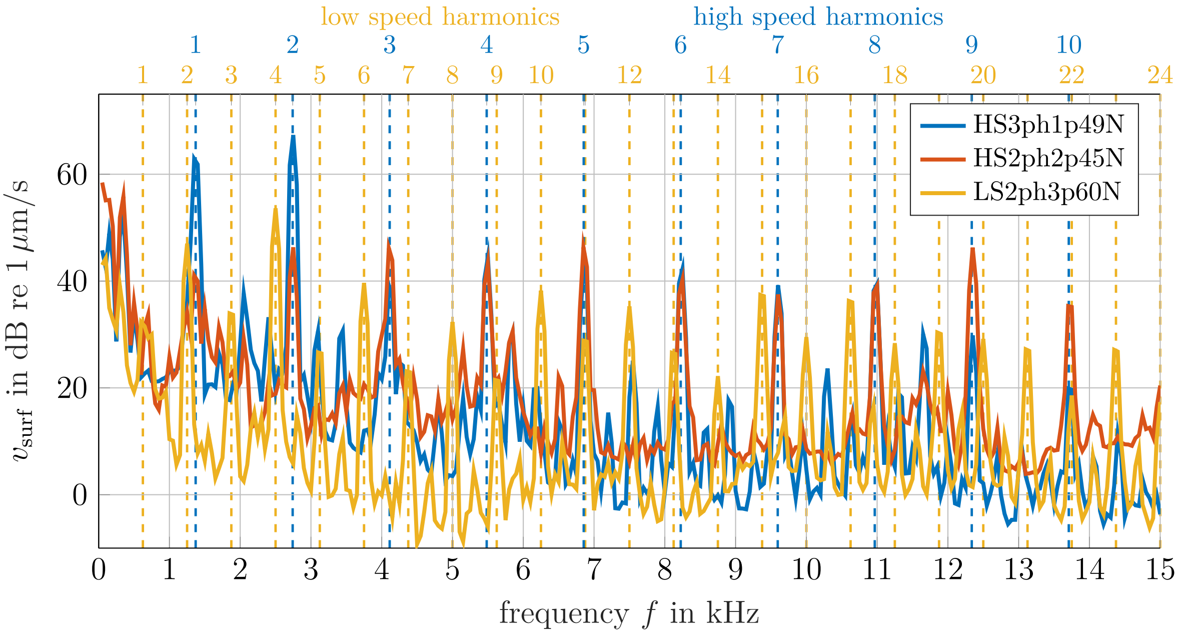

Fig. A.14: Measured average radial surface velocity v_{surf} on `Main` surface at operation point $PART_{\text{M},83}$ (see table A.11). Sensor positions specified in section A.4.1.

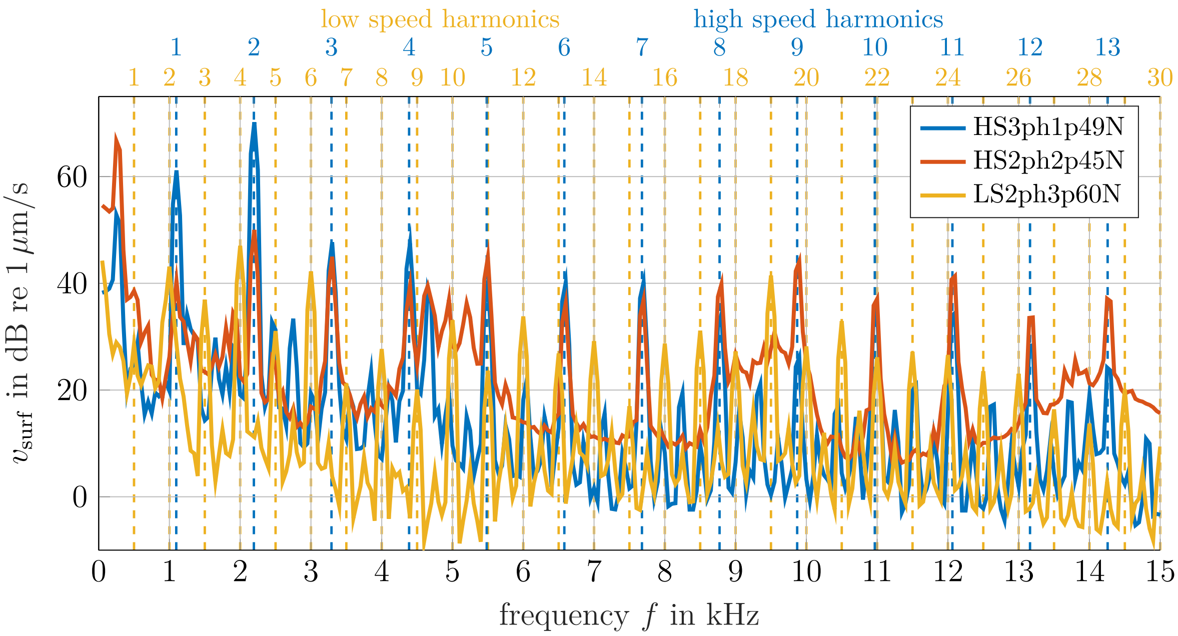

Fig. A.15: Measured average radial surface velocity v_{surf} on `Main` surface at operation point $PART_{\text{M},67}$ (see table A.11). Sensor positions specified in section A.4.1.

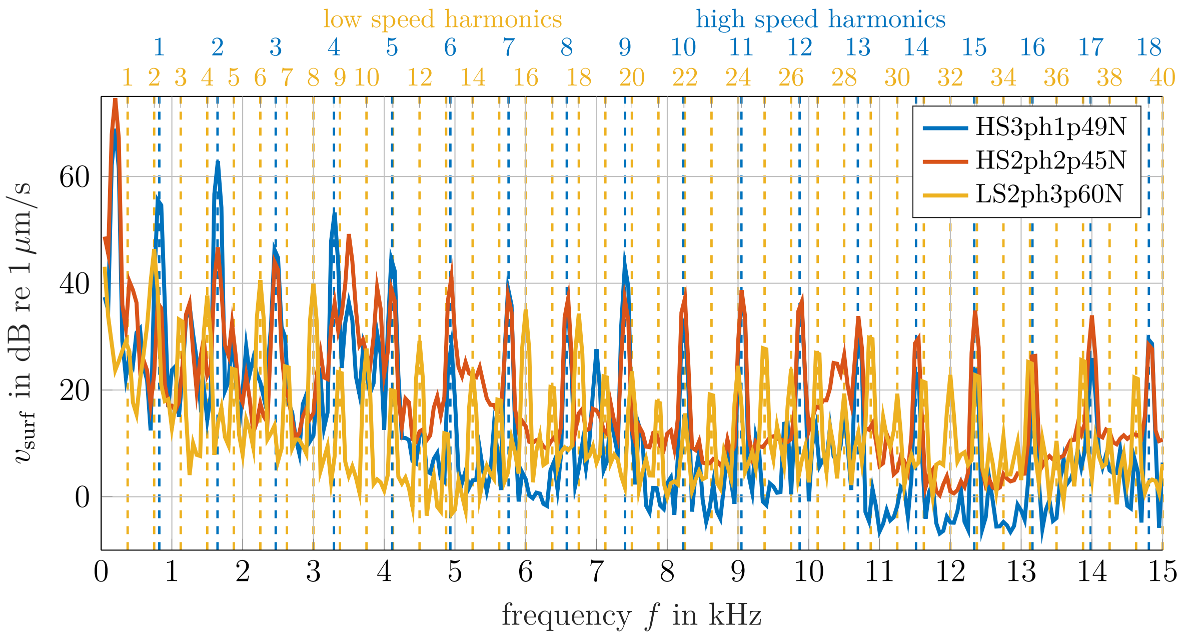

Fig. A.16: Measured average radial surface velocity v_{surf} on `Main` surface at operation point $PART_{\text{M,50}}$ (see table A.11). Sensor positions specified in section A.4.1.

Acronyms

2-D	2-dimensional
3-D	3-dimensional
AHB	asymmetric-half bridge
ANSYS	ANSYS®, (ANalysis SYStem). Finite element software employed for structural analysis in version 14
CAD	computer aided design
CCM	continuos conduction mode
CFD	computational fluid dynamics
DSP	digital signal processor
EMF	electromotive force
FEA	finite element analysis
FLUX2D	FLUX®, finite element software tool by Cedrat. Employed in version 11.2
FPGA	field programmable gate array
HCC	hysteresis current control
HEV	hybrid electric vehicle
ICE	internal combustion engine
IGBT	insulated-gate bipolar transistor
iGSE	improved generalized Steinmetz equation
ISEA	Institute for Power Electronics and Electrical Drives
LPTN	lumped parameter thermal network
LUT	lookup table
MMF	magneto motive force

MotorCAD	MotorCAD®, commercially available LPTN software to model the thermal behavior of electric machines. Employed in Version 9.3.5.1
NFLM	normalized flux linkage method
NVH	noise vibration harshness
PC	personal computer
PC-SRD	PC-SRD®, analytical design tool for switched reluctance drive by the SPEED-Consortium employed in version 8.5
PMSM	permanent magnet synchronous machine
PWM	pulse-width modulation
REX	range extender
RMS	root mean square
SE	Steinmetz equation
SPC	single pulse control
SRG	switched reluctance generator
SSBPD	solution space based pre-design
THD	total harmonic distortion
ZVL	zero-voltage-loop

Symbols

$\alpha_{\mathrm{cu,20}}$	temperature coefficient of copper for a base temperature of 20 °C
α_{eddy}	frequency coefficient of p_{eddy}
$\alpha_{\mathrm{eddy,woEw}}$	frequency coefficient of $p_{\mathrm{eddy,woEw}}$
$\alpha_{\mathrm{st,j}}$	heat transfer coefficient between stator and cooling jacket
β_{r}	rotor tooth width angle
β_{s}	stator tooth width angle
ζ_{liner}	impregnation goodness of liner
ζ_{winding}	impregnation goodness of windings
η_{drive}	efficiency of the electric drive $P_{\mathrm{el,drive}}/P_{\mathrm{m,sh}}$
η_{gear}	efficiency of the gearbox $(P_{\mathrm{m,sh}}-P_{\mathrm{l,gear}})/P_{\mathrm{m,sh}}$
η_{ICE}	efficiency of the ICE
η_{inv}	efficiency of the inverter $P_{\mathrm{el,drive}}/P_{\mathrm{el,SRG}}$
η_{mach}	efficiency of the SRG $P_{\mathrm{el,SRG}}/P_{\mathrm{m,sh}}$
η_{tot}	efficiency of the complete system $P_{\mathrm{el,src}}/P_{\mathrm{m,sh}}$
θ_{decay}	decay angle:θ_{el} at which phase current i_{ph} reaches 0 A
θ_{el}	electrical angle
θ_{fw}	freewheling angle:θ_{el} at which zero voltage is applied to generator phase
$\Delta\theta_{\mathrm{fw}}$	angle period for which zero voltage is applied to aSRG phase
θ_{m}	mechanical angle
$\Delta\theta_{\mathrm{mag}}$	angle period for which positive voltage is applied to a SRG phase
θ_{off}	turn-off angle:θ_{el} at which negative dc-link voltage is applied to generator phase
θ_{on}	turn-on angle: θ_{el} at which positive positive voltage is applied to generator phase
ϑ_{amb}	ambient temperature at the test bench
$\vartheta_{\mathrm{coil}}$	average coil temperature
$\vartheta_{\mathrm{coil,hs}}$	coil hot spot temperature
$\vartheta_{\mathrm{coil,max}}$	maximum allowed average coil temperature
$\hat{\vartheta}_{\mathrm{i}}$	measured temperatures in prototypes

ϑ_{i}	simulated temperatures in MotorCAD matched to a certain $\hat{\vartheta}_{\mathrm{i}}$
$\vartheta_{\mathrm{inlet}}$	temperature of the cooling fluid at water-jacket inlet
$\vartheta_{\mathrm{jacket}}$	average stator cooling jacket temperature
$\Delta\vartheta_{\mathrm{jacket,coil}}$	temperature rise from water jacket to coil
$\vartheta_{\mathrm{rt,bi}}$	rotor back iron temperature
$\vartheta_{\mathrm{rt,hs}}$	rotor hot spot temperature
ϑ_{sh}	temperature of the SRG shaft at rear end, cooled by gear box
$\vartheta_{\mathrm{sh,act}}$	temperature of the SRG shaft in axial center
$\vartheta_{\mathrm{st,bi}}$	stator back iron temperature
$\vartheta_{\mathrm{st,hs}}$	stator hot spot temperature
λ_{coil}	thermal conductivity of copper resin compound in the coil
λ_{ins}	thermal conductivity of insulation slot liner
λ_{resin}	thermal conductivity of insulating resin
λ_{st}	thermal conductivity of stack lamination
$\xi_{\mathrm{P,act}}$	input power $P_{\mathrm{m,sh}}$ to active parts weight m_{act} ratio
$\xi_{\mathrm{P,tot}}$	input power $P_{\mathrm{m,sh}}$ to machine weight m_{SRG} ratio; gravimetric power density
$\xi_{\mathrm{T,act}}$	total torque T_{tot} to active parts weight m_{act} ratio
$\xi_{\mathrm{T,tot}}$	total torque T_{tot} to machine weight m_{SRG} ratio; gravimetric torque density
ρ_{fl}	air gap fluid density
$\varrho_{\mathrm{sp,cu}}$	specific copper resistivity
$\tau_{\mathrm{pl,s}}$	stator pole segment angle
$\phi_{\mathrm{P,act}}$	input power $P_{\mathrm{m,sh}}$ to active parts volume V_{act} ratio
$\phi_{\mathrm{P,tot}}$	input power $P_{\mathrm{m,sh}}$ to machine volume V_{SRG} ratio; volumetric power density
$\phi_{\mathrm{T,act}}$	total torque T_{tot} to active parts volume V_{act} ratio
$\phi_{\mathrm{T,act,pl}}$	pole torque T_{pl} to active parts volume V_{act} ratio
$\phi_{\mathrm{T,tot}}$	total torque T_{tot} to machine volume V_{SRG} ratio; volumetric torque density
ω_{SRG}	angular frequency of SRG shaft
$\dot{\omega}_{\mathrm{SRG}}$	derivative angular frequency of SRG shaft
Θ_{pl}	magnetomotive force in one pole
$\Theta_{\mathrm{pl,pk}}$	peak magnetomotive force during one electric period in one pole
Φ_{pl}	pole flux
Ψ_{ph}	phase flux linkage

$\Psi_{\mathrm{ph,pk}}$	peak value of the phase flux linkage
Ψ_{pl}	pole flux linkage
$b_{\mathrm{pl,r}}$	rotor pole width
$b_{\mathrm{pl,s}}$	stator pole width
c_{Al}	specific cost of aluminum
c_{Cu}	specific cost of Typ-H isolated copper wire
c_{litz}	specific cost of litz wire
c_{NO10}	specific cost for NO10 electrical steel
c_{NO20}	specific cost for NO20 electrical steel
c_{NO30}	specific cost for NO30 electrical steel
c_{steel}	specific cost of steel
d_{csp}	minimal distance between two adjacent coils in one slot
d_{derate}	deviation from the maximum of the $T_{\mathrm{pl}}/\Theta_{\mathrm{pl_{pk}}}$ for design comparison
d_{g}	air gap length between rotor and stator pole tips
d_{gsp}	minimal radial distance between coil and stator pole tip
$d_{\mathrm{g,step}}$	additional air gap length for asymmetric step
d_{ins}	insulation slot liner thickness
$d_{\mathrm{ins,w}}$	thickness of copper wire insulation
$d_{\mathrm{sh,fe}}$	iron steel sheet thickness
d_{t}	relation between exploitable and maximal available torque at a certain $\Theta_{\mathrm{pl,pk}}$
d_{w}	diameter of one copper wire
e	back EMF
f_{cu}	ratio between A_{cu} and A_{w}
f_{eig}	eigenfrequency
f_{el}	electrical base frequency
f_{m}	mechanical base frequency of SRG shaft
f_{M0}	mode$_0$ eigenfrequency
f_{M2}	mode$_2$ eigenfrequency
f_{M4}	mode$_4$ eigenfrequency
f_{M6}	mode$_6$ eigenfrequency
f_{slot}	ratio between A_{w} and $A_{\mathrm{slot,st}}$
f_{trans}	excitation frequency of the transmission
$h_{\mathrm{pl,r}}$	rotor pole height

$h_{\mathrm{pl,s}}$	stator pole height
i_{dev}	instantaneous current through one power electronic component
i_{ph}	current in one phase
i_{src}	instantaneous current towards the electric power source (e.g. battery)
i_{srg}	sum of all phase currents
i_{sw}	switching current
$k_{\mathrm{arc,s}}$	stator tooth width adjustment factor
k_{cu}	correction factor for frequency dependent copper losses
k_{d}	duty cycle; relation between phase peak $I_{\mathrm{ph,pk}}$ and rms current $I_{\mathrm{ph,pk}}$
$k_{\mathrm{d,cor}}$	duty-cycle correction factor to account for deviation from idealized rectangular current shapes
$k_{\mathrm{R,dc}}$	correction factor between real $R_{\mathrm{dc,ph}}$ and estimated $R_{\mathrm{dc,ph,est}}$
k_{trq}	torque output parameter
m_{act}	mass of machine iron and copper
m_{gear}	mass of gearbox
m_{SRG}	mass of complete machine including gearbox
n_{ICE}	rotational speed of internal combustion engine
n_{m}	order of a certain structural mode shape
n_{p}	number of pole pairs
n_{sh}	shaft rotational speed
n_{SRG}	rotational generator speed
$n_{\mathrm{SRG,nom}}$	nominal rotational generator speed
p_{Bertotti}	specific iron losses calculated by Bertotti formula
p_{eddy}	ratio between $P_{\mathrm{l,cu,eddy}}$ and $P_{\mathrm{l,cu,dc}}$
$p_{\mathrm{eddy,0}}$	p_{eddy} at $0\,\mathrm{Hz}$
$p_{\mathrm{eddy,woEw}}$	ratio between $P_{\mathrm{l,cu,eddy}}$ and $P_{\mathrm{l,cu,dc,woEw}}$
$p_{\mathrm{eddy,woEw,0}}$	$p_{\mathrm{eddy,woEw}}$ at $0\,\mathrm{Hz}$
p_{fe}	specific core loss of a certain iron core material
p_{FLUX}	specific iron loss formula implemented in FLUX2D
p_{IEM5}	specific iron losses calculated by IEM5 formula
pp	percent points
p_{SE}	specific iron losses calculated by SE
u_{dc}	dc-link capacitor voltage at power electronic switch terminals
Δu_{dc}	dynamic deviation from u_{dc}

u_{dev}	instantaneous voltage across one power electronic component
u_{ph}	voltage at machine terminals
u_{src}	power source voltage
v_{surf}	average surface velocity
$w_{\mathrm{y,r}}$	rotor yoke thickness
$w_{\mathrm{y,s}}$	stator yoke thickness
A_{cu}	effective copper cross section of one stator pole
$A_{\mathrm{pitch,st}}$	cross section area of one stator pole pitch
$A_{\mathrm{pl,st}}$	cross section of one stator pole
$A_{\mathrm{slot,st}}$	maximally available coil cross section area in one stator slot
A_{w}	cross section are of one stator pole which can be filled by copper
B_{m}	maximum flux density
B_{pt}	magnetic flux density in a specific iron core section
B_{pk}	peak flux density in the iron core
B_{s}	saturation flux density
C_{d}	skin friction coefficient
C_{dc}	dc-link capacitor to filter source current
D_{rot}	rotor tip surface diameter
D_{st}	stator outer diameter
$E_{\mathrm{off,dev}}$	current dependent power electronic device turn-off energy
$E_{\mathrm{on,dev}}$	current dependent power electronic device turn-on energy
$F_{\mathrm{pl,rad}}$	pole radial force
$I_{\mathrm{ph,pk}}$	maximum phase current
$I_{\mathrm{ph,rms}}$	phase RMS current
J_{eff}	effectively applied current density during operation
J_{rot}	rotor inertia
$J_{\mathrm{th,max}}$	thermally permitted maximal current density
K_{sal}	saliency factor
L_{cab}	cable inductance between source and inverter
L_{tot}	total machine length including the housing
L_{ph}	inductance of one machine phase
$L_{\mathrm{pl,1}}$	inductance of one pole with number of turns per pole $N_{\mathrm{w,pl}} = 1$
L_{stk}	iron core stack length
L_{act}	active parts length including the end-winding overhangs

N_{dev}	total number of power electronic devices in the inverter
N_{ph}	number of electrical machine phases
N_{pt}	number of iron core sections to calculate iron core losses $P_{\text{l,fe}}$
N_{r}	number of rotor poles
N_{s}	number of stator poles
$N_{\text{teeth,pinion}}$	number of teeth on pinion in transmission
$N_{\text{w,pl}}$	number of windings on one pole
$P_{\text{el,drive}}$	electric output power at power electronic inverter
$P_{\text{el,src}}$	power stored in electric source: $P_{\text{m,sh}}$- $P_{\text{l,tot}}$
$P_{\text{el,SRG}}$	electric output power of SRG
$P_{\text{l,bear}}$	mechanical bearing losses in the generator
$P'_{\text{l,coil,hpl}}$	$P_{\text{l,cu,ac}}$ of half a stator pole related to L_{stk}
$P_{\text{l,cond}}$	conduction losses in power electronics inverter
$P_{\text{l,cu,ac}}$	sum of frequency dependent and independent copper losses in stator coils
$P_{\text{l,cu,dc}}$	frequency independent dc-copper losses in stator coils
$P_{\text{l,cu,dc,Ew}}$	frequency independent dc-copper losses in the end-windings
$P'_{\text{l,cu,dc,hpl}}$	$P_{\text{l,cu,dc}}$ of half a stator pole related to L_{stk}
$P_{\text{l,cu,dc,woEw}}$	frequency independent dc-copper losses in the stator coils without end-windings
$P'_{\text{l,cu,dc,woEw,hpl}}$	$P_{\text{l,cu,dc,woEw}}$ of half a stator pole related to L_{stk}
$P_{\text{l,cu,eddy}}$	frequency dependent copper losses in stator coils
$P_{\text{l,drive}}$	sum of losses $P_{\text{l,inv}}$ and $P_{\text{l,mach}}$
$P_{\text{l,fe}}$	core iron losses
$P_{\text{l,gear}}$	mechanical gearbox losses (including bearing)
$P_{\text{l,inv}}$	sum of switching and conduction losses in power electronics inverter
$P_{\text{l,m}}$	mechanical losses
$P_{\text{l,mach}}$	machine losses, sum of $P_{\text{l,cu,ac}}$ and $P_{\text{l,fe}}$ and $P_{\text{l,m}}$
$P_{\text{l,src}}$	ohmic power source losses
$P_{\text{l,sw}}$	switching losses in power electronics inverter
$P_{\text{l,tot}}$	sum of all losses $P_{\text{l,src}}$, $P_{\text{l,inv}}$ and $P_{\text{l,mach}}$
$P_{\text{l,wind}}$	windage losses in the air gap
$P_{\text{m,sh}}$	mechanical input power at shaft
Q_{flow}	volumetric flow rate of coolant

R_1	rotor tip surface radius $^{D_{\mathrm{rot}}}/_{2}$
R_2	stator pole ground radius $= R_3$- $w_{\mathrm{y,s}}$
R_3	stator outer radius $^{D_{\mathrm{st}}}/_{2}$
$R_{\mathrm{ac,pl,1}}$	ac copper resistance of one pole with number of turns per pole $N_{\mathrm{w,pl}} = 1$
$R_{\mathrm{ac,ph}}$	ac copper resistance of one machine phase
R_{cab}	cable resistance between source and inverter
$R_{\mathrm{dc,ph}}$	dc copper resistance of one machine phase
$R_{\mathrm{dc,ph,est}}$	estimated dc copper resistance of one machine phase
$R_{\mathrm{dc,ph,Ew}}$	dc copper resistance of the end-windings of one phase
$R_{\mathrm{dc,ph,woEw}}$	dc copper resistance of one phase without end-windings
$R_{\mathrm{eddy,ph}}$	estimated eddy-current copper resistance of one machine phase
$R_{\mathrm{i,src}}$	source internal resistance
$RMSE$	root mean square error
R_{sh}	shaft radius
$R'_{\mathrm{th,c}}$	stack length L_{stk} related thermal coil resistance
$R'_{\mathrm{th,j}}$	stack length L_{stk} related thermal stator to frame contact resistance
$R'_{\mathrm{th,st}}$	stack length L_{stk} related thermal stator resistance
$R'_{\mathrm{th,st,hpl}}$	stack length L_{stk} related thermal resistance of a half stator pole
$R'_{\mathrm{th,y}}$	stack length L_{stk} related thermal stator yoke resistance
R_0	rotor pole ground radius
$S_{\mathrm{el,inv}}$	inverter apparent power
$STPR$	slot-to-pole-pitch-ratio, This ratio was initially introduced as $CTSR$ in [BBD12] and renamed to r_{NG} in [Bra13].
T_{bear}	drag torque caused by bearings
T_{el}	duration of one electric period $^{1}/_{f_{\mathrm{el}}}$
T_{gear}	drag torque caused by gearbox
T_{m}	drag torque caused by mechanical losses $P_{\mathrm{l,m}}$
T_{pl}	torque produced by one stator pole
T_{tot}	average total machine output torque
$T_{\mathrm{tot,nom}}$	nominal total machine output torque
$T_{\mathrm{tot,pk}}$	dynamic peak total machine output torque
$U_{\mathrm{src,nom}}$	nominal power source voltage in no-load condition
V_{act}	volume of machine iron and copper

V_{fe}	volume of machine iron core
V_{gear}	volume of gearbox
V_{pt}	volume of a specific machine section to calculate iron core losses $P_{\mathrm{l,fe}}$
V_{SRG}	volume of complete machine including gearbox
W_{co}	coenergy loop
$W_{\mathrm{co,max}}$	maximal available magnetic co-energy loop
W_{mag}	stored field energy
${}^{T_{\mathrm{pl}}}/_{\Theta_{\mathrm{pl}}}$	pole torque T_{pl} to pole MMF Θ_{pl} ratio
${}^{T_{\mathrm{pl}}}/_{\Theta_{\mathrm{pl}}}{}_{\mathrm{pk}}$	peak value of pole torque T_{pl} to pole MMF Θ_{pl} ratio

List of Figures

List of Tables

Bibliography

[AK11] Aharon, I. and Kuperman, A. 'Topological Overview of Powertrains for Battery-Powered Vehicles With Range Extenders'. In: *IEEE Transactions on Power Electronics* 26.3 (2011), pp. 868–876. ISSN: 0885-8993. DOI: 10.1109/TPEL.2011.2107037 (cit. on p. 3).

[AG15] Altenrath, T. and Gassmann, T. 'GKN Two Speed Electric Front Axle for the BMW i8: The first two speed eAxle on the market'. In: *Hybrid and Electric Drivetrains*. 2015, pp. 72–80 (cit. on p. 16).

[And+17] Andert, J.; Herold, K.; Savelsberg, R., and Pischinger, M. 'NVH Optimization of Range Extender Engines by Electric Torque Profile Shaping'. In: *IEEE Transactions on Control Systems Technology* 25.4 (2017), pp. 1465–1472. ISSN: 1063-6536. DOI: 10.1109/TCST.2016.2601286 (cit. on p. 104).

[And+12] Andert, J.; Köhler, E.; Niehues, J., and Schürmann, G. 'KSPG Range Extendera New Pathfinder to Electromobility'. In: *ATZautotechnology* 12.2 (2012), pp. 26–33. ISSN: 1616-8216. DOI: 10.1365/s35595-012-0105-0 (cit. on pp. 3, 4).

[AHR01] Anwar, M. N.; Husain, I., and Radun, A. V. 'A comprehensive design methodology for switched reluctance machines'. In: *IEEE Transactions on Industry Applications* 37.6 (2001), pp. 1684–1692. ISSN: 0093-9994. DOI: 10.1109/28.968179 (cit. on pp. 21, 22).

[BP98] Barnes, M. and Pollock, C. 'Power electronic converters for switched reluctance drives'. In: *IEEE Transactions on Power Electronics* 13.6 (1998), pp. 1100–1111. ISSN: 0885-8993. DOI: 10.1109/63.728337 (cit. on p. 9).

[Ben13] Benini, E. *Progress in gas turbine performance*. Rijeka: InTech, 2013. ISBN: 978-953-51-1166-5 (cit. on p. 4).

[Ber88] Bertotti, G. 'General properties of power losses in soft ferromagnetic materials'. In: *IEEE Transactions on Magnetics* 24.1 (1988), pp. 621–630. ISSN: 0018-9464. DOI: 10.1109/20.43994 (cit. on p. 14).

[BP93] Blaabjerg, F. and Pedersen, J. K. 'Digital implemented random modulation strategies for AC and switched reluctance drives'. In: *IECON '93 - 19th Annual Conference of IEEE Industrial Electronics*. 1993, pp. 676–682. DOI: 10.1109/IECON.1993.338999 (cit. on p. 127).

[BMW17] BMW. *Technische Daten - Der neue BMW i3*. 2017. URL: https://www.press.bmwgroup.com/deutschland/article/attachment/T0273661DE/392973 (visited on Mar. 14, 2018) (cit. on p. 4).

[Bog+09] Boglietti, A.; Cavagnino, A.; Staton, D.; Shanel, M.; Mueller, M., and Mejuto, C. 'Evolution and Modern Approaches for Thermal Analysis of Electrical Machines'. In: *IEEE Transactions on Industrial Electronics* 56.3 (2009), pp. 871–882. ISSN: 0278-0046. DOI: `10.1109/TIE.2008.2011622` (cit. on pp. 18, 19).

[Bös14] Bösing, M. *Acoustic modeling of electrical drives: Noise and vibration synthesis based on force response superposition: Zugl.: Aachen, Techn. Hochsch., Diss., 2013*. Vol. 71. Aachener Beiträge des ISEA. Aachen: Shaker, 2014. ISBN: 978-3-8440-2752-5 (cit. on pp. 19, 94, 97, 127).

[Bra13] Brauer, H. J. *Schnelldrehender geschalteter Reluktanzantrieb mit extremem Längendurchmesserverhältnis: Zugl.: Aachen, Techn. Hochsch., Diss., 2013*. Vol. 68. Aachener Beiträge des ISEA. Aachen: Shaker, 2013. ISBN: 9783844023459 (cit. on pp. 10, 11, 19, 21–26, 30, 40, 42–44, 48, 53, 54, 75, 76, 169).

[BBD12] Brauer, H. J.; Burkhart, B., and De Doncker, R. W. 'Comprehensive electromagnetic design procedure for switched reluctance machines'. In: *6th IET International Conference on Power Electronics, Machines and Drives (PEMD 2012)*. 2012, pp. 1–6. DOI: `10.1049/cp.2012.0259` (cit. on pp. 21, 24, 34, 37, 38, 42–45, 169).

[BD15] Brauer, H. J. and De Doncker, R. W. 'Thermal Modeling of a High-Speed Switched Reluctance Machine with Axial Air-gap Flow for Vacuum Cleaners'. In: *EPE Journal* 22.2 (2015), pp. 22–29. ISSN: 0939-8368. DOI: `10.1080/09398368.2012.11463820` (cit. on p. 18).

[Bur+16] Burkhart, B.; Klein-Hessling, A.; Hafeez, S. A., and De Doncker, R. W. 'Influence of Freewheeling on Single Pulse Operation of a Switched Reluctance Generator'. In: *19th International Conference on Electrical Machines and Systems (ICEMS)*. 2016 (cit. on pp. 26, 27, 30).

[Bur+17] Burkhart, B.; Klein-Hessling, A.; Ralev, I.; Weiss, C. P., and De Doncker, R. W. 'Technology, Research and Applications of Switched Reluctance Drives'. In: *CPSS Transaction on Power Electronics and Applications* 2 (2017), pp. 12–27 (cit. on pp. 5, 7, 10).

[BMD16] Burkhart, B.; Mittelstedt, A., and De Doncker, R. W. 'Solution space based pre-design approach to compare and select configurations of switched reluctance machines'. In: *8th IET International Conference on Power Electronics, Machines and Drives (PEMD)*. 2016, pp. 1–6. DOI: `10.1049/cp.2016.0178` (cit. on pp. 23, 63, 111, 115, 116, 118, 130).

[CJS00] Calverley, S. D.; Jewell, G. W., and Saunders, R. J. 'Aerodynamic losses in switched reluctance machines'. In: *IEE Proceedings - Electric Power Applications* 147.6 (2000), pp. 443–448. ISSN: 1350-2352. DOI: `10.1049/ip-epa:20000719` (cit. on pp. 15, 16).

[CLU92] Cameron, D. E.; Lang, J. H., and Umans, S. D. 'The origin and reduction of acoustic noise in doubly salient variable-reluctance motors'. In: *IEEE Transactions on Industry Applications* 28.6 (1992), pp. 1250–1255. ISSN: 0093-9994. DOI: `10.1109/28.175275` (cit. on p. 127).

[cap18] capstone. *C30*. 2018. URL: `https://www.capstoneturbine.com/products/c30` (visited on Mar. 13, 2018) (cit. on p. 4).

[Car08] Carstensen, C. E. *Eddy currents in windings of switched reluctance machines: Zugl.: Aachen, Techn. Hochsch., Diss., 2007*. Vol. 48. Aachener Beiträge des ISEA. Aachen: Shaker, 2008. ISBN: 978-3-8322-7118-3 (cit. on pp. 10, 14, 35, 40, 43, 48, 52, 54, 56, 61, 113).

[DPV11] De Doncker, R. W.; Pulle, D. W., and Veltman, A. *Advanced Electrical Drives: Analysis, Modeling, Control*. Power Systems. Dordrecht: Springer Science+Business Media B.V, 2011. ISBN: 978-94-007-0181-6. DOI: `10.1007/978-94-007-0181-6` (cit. on p. 7).

[Dow66] Dowell, P. L. 'Effects of eddy currents in transformer windings'. In: *Electrical Engineers, Proceedings of the Institution of* 113.8 (1966), pp. 1387–1394. ISSN: 0020-3270. DOI: `10.1049/piee.1966.0236` (cit. on pp. 13, 14, 54, 60).

[ESH12] Eggers, D.; Steentjes, S., and Hameyer, K. 'Advanced Iron-Loss Estimation for Nonlinear Material Behavior'. In: *IEEE Transactions on Magnetics* 48.11 (2012), pp. 3021–3024. ISSN: 0018-9464. DOI: `10.1109/TMAG.2012.2208944` (cit. on p. 14).

[Ema+05] Emadi, A.; Rajashekara, K.; Williamson, S. S., and Lukic, S. M. 'Topological Overview of Hybrid Electric and Fuel Cell Vehicular Power System Architectures and Configurations'. In: *IEEE Transactions on Vehicular Technology* 54.3 (2005), pp. 763–770. ISSN: 0018-9545. DOI: `10.1109/TVT.2005.847445` (cit. on p. 3).

[Eng18] Engiro. *RE20-3*. 2018. URL: `http://www.engiro.de/de/produkte/range-extender/alle-range-extender/re-20-3/` (visited on Mar. 13, 2018) (cit. on p. 4).

[Fah02] Fahimi, B. 'On the suitability of switched reluctance drives for starter/generator application'. In: *Vehicular Technology Conference. IEEE 55th Vehicular Technology Conference. VTC Spring 2002*. 2002, pp. 2070–2075. DOI: `10.1109/VTC.2002.1002988` (cit. on p. 16).

[FBE15] Fairall, E. W.; Bilgin, B., and Emadi, A. 'State-of-the-art high-speed switched reluctance machines'. In: *IEEE International Electric Machines & Drives Conference (IEMDC)*. 2015, pp. 1621–1627. DOI: `10.1109/IEMDC.2015.7409280` (cit. on p. 16).

[Fai+09] Faiz, J.; Ganji, B.; Carstensen, C. E.; Kasper, K. A., and De Doncker, R. W. 'Temperature Rise Analysis of Switched Reluctance Motors Due to Electromagnetic Losses'. In: *IEEE Transactions on Magnetics* 45.7 (2009), pp. 2927–2934. ISSN: 0018-9464. DOI: `10.1109/TMAG.2009.2015755` (cit. on p. 22).

[Fer+12] Ferrari, C. et al. *Studie zu Range Extender Konzepten für den Einsatz in einem batterieelektrischen Fahrzeug – REXEL*. Ed. by Deutsches Zentrum für Luft- und Raumfahrt e.V. and Ministerium für Finanzen und Wirtschaft. 2012 (cit. on pp. 4, 5).

[Fer+95] Ferreira, C. A.; Jones, S. R.; Heglund, W. S., and Jones, W. D. 'Detailed design of a 30-kW switched reluctance starter/generator system for a gas turbine engine application'. In: *IEEE Transactions on Industry Applications* 31.3 (1995), pp. 553–561. ISSN: 0093-9994. DOI: 10.1109/28.382116 (cit. on pp. 16, 17, 73, 92).

[Fie07] Fiedler, J. O. *Design of low noise switched reluctance drives: Zugl.: Aachen, Techn. Hochsch., Diss., 2006*. Vol. 44. Aachener Beiträge des ISEA. Aachen: Shaker, 2007. ISBN: 978-3-8322-5864-1 (cit. on pp. 26, 44, 94, 97, 101).

[Fis+09] Fischer, R.; Fraidl, G. K.; Hubmann, C.; Kapus, P. E.; Kunzemann, R.; Sifferlinger, B., and Beste, F. 'Range Extender Module'. In: *ATZautotechnology* 9.5 (2009), pp. 40–46. ISSN: 2192-886X. DOI: 10.1007/BF03247140 (cit. on p. 4).

[FNP16] Fuchs, A.; Nijman, E., and Priebsch, H.-H., eds. *Automotive NVH Technology*. 1st ed. 2016. SpringerBriefs in Applied Sciences and Technology. Cham: Springer, 2016. ISBN: 9783319240558. DOI: 10.1007/978-3-319-24055-8 (cit. on p. 6).

[Fue+05] Fuengwarodsakul, N. H.; Fiedler, J. O.; Bauer, S. E., and De Doncker, R. W. 'New methodology in sizing and predesign of switched reluctance machines using normalized flux-linkage diagram'. In: *European Conference on Power Electronics and Applications*. Vol. 4. 2005, pp. 2704–2711. DOI: 10.1109/IAS.2005.1518842 (cit. on pp. 21, 24).

[Gv15] Gebrehiwot, M. and van den Bossche, A. 'Starting requirements of a range extender for electric vehicles: Based on a small size 4-stroke engine'. In: *International Journal of Automotive Technology* 16.4 (2015), pp. 707–713. ISSN: 1229-9138. DOI: 10.1007/s12239-015-0071-9 (cit. on p. 6).

[Gis+15] Gissing, J.; Lichius, T.; Baltzer, S.; Hemkemeyer, D., and Eckstein, L. 'Predictive Energy Management of Range-Extended Electric Vehicles Considering Cabin Heat Demand and Acoustics'. In: *IFAC-PapersOnLine* 48.15 (2015), pp. 209–216. ISSN: 24058963. DOI: 10.1016/j.ifacol.2015.10.030 (cit. on p. 3).

[GWG16] Goh, S. Y.; Wale, J., and Greenwood, D. 'Thermal analysis for stator slot of permanent magnet machine'. In: *2016 XXII International Conference on Electrical Machines (ICEM)*. 2016, pp. 2093–2098. DOI: 10.1109/ICELMACH.2016.7732811 (cit. on p. 79).

[Got+13] Gottschlich, J.; Burkhart, B.; Coenen, C., and De Doncker, R. W. 'Fully digital FPGA-based current controller for switched reluctance machines'. In: *IEEE International Symposium on Sensorless Control for Electrical Drives and Predictive Control of Electrical Drives and Power Electronics (SLED/PRECEDE)*.

2013, pp. 1–7. DOI: 10.1109/SLED-PRECEDE.2013.6684481 (cit. on pp. 148, 149).

[GN11] Grebe, U. D. and Nitz, L. T. 'Voltec – Das Antriebssystem für Chevrolet Volt und Opel Ampera'. In: *MTZ - Motortechnische Zeitschrift* 72.5 (2011), pp. 342–351. ISSN: 0024-8525. DOI: 10.1365/s35146-011-0084-5 (cit. on p. 3).

[gre10] greencarcongress. *Jaguar Introduces C-X75 Gas Micro-turbine Extended Range Electric Vehicle Concept*. 2010. URL: http://www.greencarcongress.com/2010/09/cx75-20100930.html (visited on Mar. 13, 2018) (cit. on pp. 4, 5).

[gre18] greencarcongress. *Techrules unveils production design of series-hybrid Ren RS with micro-turbine range extender; 330 km/h*. 2018. URL: http://www.greencarcongress.com/2018/03/20180306-techrules.html (visited on Mar. 13, 2018) (cit. on p. 4).

[GF07] Grote, K.-H. and Feldhusen, J. *Dubbel: Taschenbuch für den Maschinenbau*. 22. Aufl. s.l.: Springer-Verlag, 2007. ISBN: 978-3-540-49714-1 (cit. on p. 16).

[HHM11] Hannoun, H.; Hilairet, M., and Marchand, C. 'Experimental Validation of a Switched Reluctance Machine Operating in Continuous-Conduction Mode'. In: *IEEE Transactions on Vehicular Technology* 60.4 (2011), pp. 1453–1460. ISSN: 0018-9545. DOI: 10.1109/TVT.2011.2124478 (cit. on p. 11).

[HM94] Hendershot, J. and Miller, T. J. E. *Design of brushless permanent magnet motors*. Vol. 37. Monographs in Electrical and Electronic Engineering. Magna Physics Pub, 1994. ISBN: 978-1881855033 (cit. on pp. 21, 30, 34).

[Hen+11] Hennen, M. D.; De Doncker, R. W.; Fuengwarodsakul, N. H., and Fiedler, J. O. 'Single-Phase Switched Reluctance Drive With Saturation-Based Starting Method'. In: *IEEE Transactions on Power Electronics* 26.5 (2011), pp. 1337–1343. ISSN: 0885-8993. DOI: 10.1109/TPEL.2010.2076366 (cit. on p. 6).

[Hof16] Hofmann, A. *Direct Instantaneous Force Control: Key to Low-Noise Switched Reluctance Traction Drives*. 1. Auflage. Vol. 83. Aachener Beiträge des ISEA. Aachen: Shaker, 2016. ISBN: 978-3-8440-4715-8 (cit. on p. 126).

[HQD14] Hofmann, A.; Qi, F., and De Doncker, R. W. 'Developing the concept for an automotive high-speed SRM drive with focus on acoustics'. In: *7th IET International Conference on Power Electronics, Machines and Drives (PEMD)*. 2014, pp. 1–5. DOI: 10.1049/cp.2014.0353 (cit. on p. 4).

[Hof14] Hofmann, P. *Hybridfahrzeuge: Ein alternatives Antriebssystem für die Zukunft*. 2. Aufl. Wien: Springer, 2014. ISBN: 978-3-7091-1779-8. DOI: 10.1007/978-3-7091-1780-4 (cit. on pp. 3, 16, 94).

[HL16] Hung, N. B. and Lim, O. 'A review of free-piston linear engines'. In: *Applied Energy* 178 (2016), pp. 78–97. ISSN: 03062619. DOI: 10.1016/j.apenergy.2016.06.038 (cit. on p. 4).

[Ida17] Idaho National Laboratory. *Acvanced Vehicles*. 2017. URL: https://avt.inl.gov/vehicle-type/all-powertrain-architecture (visited on Oct. 8, 2017) (cit. on pp. 4, 5).

[Ind+16] Inderka, R. B.; von Malottki, S.; Nizzola, C.; Burkhart, B.; Klein-Hessling, A., and De Doncker, R. W. 'Cost Efficient Switched Reluctance Generator for Range Extension Unit'. In: *25th Aachen Colloquium Automobile and Engine Technology*. 2016, pp. 1–14 (cit. on pp. 3, 4, 6, 104, 125).

[Inf] Infineon. *HybridPACK^{TM} FS200R07A5E3_S6 Light* (cit. on p. 117).

[Jun+12] Jungreuthmayer, C.; Bauml, T.; Winter, O.; Ganchev, M.; Kapeller, H.; Haumer, A., and Kral, C. 'A Detailed Heat and Fluid Flow Analysis of an Internal Permanent Magnet Synchronous Machine by Means of Computational Fluid Dynamics'. In: *IEEE Transactions on Industrial Electronics* 59.12 (2012), pp. 4568–4578. ISSN: 0278-0046. DOI: 10.1109/TIE.2011.2176696 (cit. on p. 81).

[Kas11] Kasper, K. A. *Analysis and control of the acoustic behavior of switched reluctance drives: Zugl.: Aachen, Techn. Hochsch., Diss., 2010*. Vol. 57. Aachener Beiträge des ISEA. Aachen: Shaker, 2011. ISBN: 978-3-8322-9869-2 (cit. on pp. 94, 95, 97, 126).

[KF17] Kerdsup, B. and Fuengwarodsakul, N. H. 'Performance and cost comparison of reluctance motors used for electric bicycles'. In: *Electrical Engineering* 99.2 (2017), pp. 475–486. ISSN: 0948-7921. DOI: 10.1007/s00202-016-0373-6 (cit. on p. 5).

[KM06] Kioskeridis, I. and Mademlis, C. 'Optimal efficiency control of switched reluctance generators'. In: *IEEE Transactions on Power Electronics* 21.4 (2006), pp. 1062–1071. ISSN: 0885-8993. DOI: 10.1109/TPEL.2006.876827 (cit. on p. 107).

[KKC14] Kiyota, K.; Kakishima, T., and Chiba, A. 'Estimation and comparison of the windage loss of a 60 kW Switched Reluctance Motor for hybrid electric vehicles'. In: *International Power Electronics Conference (IPEC-Hiroshima - ECCE-ASIA)*. 2014, pp. 3513–3518. DOI: 10.1109/IPEC.2014.6870001 (cit. on p. 15).

[Kiy+16] Kiyota, K.; Kakishima, T.; Chiba, A., and Rahman, M. A. 'Cylindrical Rotor Design for Acoustic Noise and Windage Loss Reduction in Switched Reluctance Motor for HEV Applications'. In: *IEEE Transactions on Industry Applications* 52.1 (2016), pp. 154–162. ISSN: 0093-9994. DOI: 10.1109/TIA.2015.2466558 (cit. on p. 15).

[Kle18] Klein-Hessling, A. *Active DC-Power Filters for Switched Reluctance Drives during Single-Pulse Operation: to be published*. RWTH Aachen University, 2018 (cit. on p. 71).

[KBD16a] Klein-Hessling, A.; Burkhart, B., and De Doncker, R. W. 'Active source current filtering to minimize the DC-link capacitor in switched reluctance drives'. In: *IEEE 2nd Annual Southern Power Electronics Conference (SPEC)*. 2016, pp. 1–7. DOI: 10.1109/SPEC.2016.7846034 (cit. on p. 59).

[KBD16b] Klein-Hessling, A.; Burkhart, B., and De Doncker, R. W. 'Iron loss redistribution in Switched Reluctance Machines using bidirectional phase currents'. In: *8th IET International Conference on Power Electronics, Machines and Drives (PEMD)*. 2016, pp. 1–6. DOI: `10.1049/cp.2016.0219` (cit. on pp. 14, 63, 129, 131).

[Kle+14] Klein-Hessling, A.; Burkhart, B.; Scharfenstein, D., and De Doncker, R. W. 'The effect of excitation angles in single-pulse controlled switched reluctance machines on acoustics and efficiency'. In: *17th International Conference on Electrical Machines and Systems (ICEMS)*. 2014, pp. 2661–2666. DOI: `10.1109/ICEMS.2014.7013950` (cit. on pp. 107, 126, 127).

[KD15] Kojima, T. and De Doncker, R. W. 'Impact of zero-volt loop on efficiency of switched reluctance motors'. In: *18th International Conference on Electrical Machines and Systems (ICEMS)*. 2015, pp. 677–681. DOI: `10.1109/ICEMS.2015.7385120` (cit. on p. 107).

[KD17] Kojima, T. and De Doncker, R. W. 'Impact of Zero-Volt Loop Control on Efficiency of Switched Reluctance Motors'. In: *IEEE Transactions on Industry Applications* PP.99 (2017), p. 1. ISSN: 0093-9994. DOI: `10.1109/TIA.2017.2679684` (cit. on pp. 107, 118).

[KMV13] Kosmatin, P.; Miljavec, D., and Vončina, D. 'Increasing efficiency of the switched reluctance generator at low-speed operation'. In: *8th International Conference on Compatibility and Power Electronics (CPE), 2013*. 2013, pp. 197–202. ISBN: 978-1-4673-4911-6. DOI: `10.1109/CPE.2013.6601154` (cit. on p. 107).

[Kra18] Kraftfahrtbundesamt. *Jahresbilanz des Fahrzeugbestandes am 1. Januar 2018*. 2018. URL: `https://www.kba.de/DE/Statistik/Fahrzeuge/Bestand/b_jahresbilanz.html` (visited on Apr. 25, 2018) (cit. on p. 1).

[Kri14] Krings, A. *Iron losses in electrical machines: Influence of material properties, manufacturing processes, and inverter operation: Zugl.: Stockholm, Kungliga Tekniska Högskolan, Diss., 2014*. Vol. 2014,19. Trita-EE. Stockholm, 2014. ISBN: 978-91-7595-099-0 (cit. on pp. 14, 63).

[KAL88] Krishnan, R.; Arumugan, R., and Lindsay, J. F. 'Design procedure for switched-reluctance motors'. In: *IEEE Transactions on Industry Applications* 24.3 (1988), pp. 456–461. ISSN: 0093-9994. DOI: `10.1109/28.2896` (cit. on pp. 21, 22, 34).

[Kri01] Krishnan, R. *Switched reluctance motor drives: Modeling, simulation, analysis, design, and applications*. Industrial electronics series. Boca Raton, Fl: CRC Press, 2001. ISBN: 0-8493-0838-0 (cit. on pp. 25, 26).

[Law+80] Lawrenson, P. J.; Stephenson, J. M.; Blenkinsop, P. T.; Corda, J., and Fulton, N. N. 'Variable-speed switched reluctance motors'. In: *IEE Proceedings B - Electric Power Applications* 127.4 (1980), pp. 253–265. ISSN: 0143-7038. DOI: `10.1049/ip-b:19800034` (cit. on pp. 7, 22).

[Liu+16] Liu, C.; Zheng, X.; Yin, M., and Cheng, X. 'Design of high thermal conductivity insulation adhesive (H-class) for low voltage motor'. In: *IEEE Transactions on Dielectrics and Electrical Insulation* 23.4 (2016), pp. 1907–1914. ISSN: 1070-9878. DOI: 10.1109/TDEI.2016.7556461 (cit. on p. 79).

[Lon+03] Long, S. A.; Schofield, N.; Howe, D.; Piron, M., and McClelland, M. 'Design of a switched reluctance machine for extended speed operation'. In: *International Electric Machines & Drives Conference*. 2003, pp. 235–240. DOI: 10.1109/IEMDC.2003.1211269 (cit. on p. 17).

[MJ89] MacMinn, S. R. and Jones, W. D. 'A very high speed switched-reluctance starter-generator for aircraft engine applications'. In: *IEEE National Aerospace and Electronics Conference*. 1989, pp. 1758–1764. DOI: 10.1109/NAECON.1989.40453 (cit. on pp. 16, 17, 92).

[MRT91] Mellor, P. H.; Roberts, D., and Turner, D. R. 'Lumped parameter thermal model for electrical machines of TEFC design'. In: *IEE Proceedings B - Electric Power Applications* 138.5 (1991), pp. 205–218. ISSN: 0143-7038. DOI: 10.1049/ip-b.1991.0025 (cit. on p. 30).

[MST12] Merker, G. P.; Schwarz, C., and Teichmann, R. *Grundlagen Verbrennungsmotoren: Funktionsweise, Simulation, Messtechnik*. 5., vollständig überarbeitete, aktualisierte und erweiterte Auflage, 2011. ATZ/MTZ-Fachbuch. Wiesbaden: Vieweg+Teubner Verlag / Springer Fachmedien Wiesbaden GmbH Wiesbaden, 2012. ISBN: 9783834813930. DOI: 10.1007/978-3-8348-8306-3 (cit. on pp. 3, 5, 6, 104, 115).

[MCA12] Michon, M.; Calverley, S. D., and Atallah, K. 'Operating Strategies of Switched Reluctance Machines for Exhaust Gas Energy Recovery Systems'. In: *IEEE Transactions on Industry Applications* 48.5 (2012), pp. 1478–1486. ISSN: 0093-9994. DOI: 10.1109/TIA.2012.2210010 (cit. on p. 16).

[Mil93] Miller, T. J. E. *Switched Reluctance Motors and Their Control*. Vol. 31. Monographs in Electrical and Electronic Engineering. Clarendon Press, 1993. ISBN: 978-0198593874 (cit. on pp. 7, 8, 21, 25, 26, 28).

[Mül10] Müller, S. *Der Startvorgang von hybridisierten Ottomotoren - Untersuchung, Bewertung, Optimierung*. Darmstadt, 2010 (cit. on p. 6).

[Nat+14] Nategh, S.; Krings, A.; Wallmark, O., and Leksell, M. 'Evaluation of Impregnation Materials for Thermal Management of Liquid-Cooled Electric Machines'. In: *IEEE Transactions on Industrial Electronics* 61.11 (2014), pp. 5956–5965. ISSN: 0278-0046. DOI: 10.1109/TIE.2014.2308151 (cit. on p. 75).

[Neu12] Neuhaus, C. R. *Schaltstrategien für geschaltete Reluktanzantriebe mit kleinem Zwischenkreis: Zugl.: Aachen, Techn. Hochsch., Diss., 2011*. Vol. 64. Aachener Beiträge des ISEA. Aachen: Shaker, 2012. ISBN: 384401487X (cit. on p. 130).

[NW03] Niemann, G. and Winter, H. *Maschinenelemente: Band 2: Getriebe allgemein, Zahnradgetriebe - Grundlagen, Stirnradgetriebe*. Zweite, völlig neubearbeitete Auflage. Berlin, Heidelberg and s.l.: Springer Berlin Heidelberg, 2003. ISBN: 978-3-662-11874-0. DOI: 10.1007/978-3-662-11873-3 (cit. on p. 16).

[NB13] Nuwantha Fernando, W. U. and Barnes, M. 'Electromagnetic Energy Conversion Efficiency Enhancement of Switched Reluctance Motors With Zero-Voltage Loop Current Commutation'. In: *IEEE Transactions on Energy Conversion* 28.3 (2013), pp. 482–492. ISSN: 0885-8969. DOI: 10.1109/TEC.2013.2272638 (cit. on p. 107).

[Pis+12] Pischinger, M.; Tomazic, D.; Wittek, K.; Esch, H.-J.; Köhler, E., and Baehr, M. 'A Low NVH Range-Extender Application with a Small V-2 Engine - Based on a New Vibration Compensation System'. In: *2012 Small Engine Technology Conference & Exhibition*. SAE Technical Paper Series. SAE International400 Commonwealth Drive, Warrendale, PA, United States, 2012. DOI: 10.4271/2012-32-0081 (cit. on p. 4).

[Pis14] Pistoia, G. *Lithium-ion batteries: Advances and applications*. First edition. Amsterdam, Boston, and Heidelberg: Elsevier, 2014. ISBN: 978-0-444-59513-3 (cit. on p. 4).

[Qi+16] Qi, F.; Ralev, I.; Stippich, A., and De Doncker, R. W., eds. *Model predictive overload control of an automotive switched reluctance motor for frequent rapid accelerations: 2016 19th International Conference on Electrical Machines and Systems (ICEMS)*. 2016 (cit. on p. 80).

[QSD14] Qi, F.; Schenk, M., and De Doncker, R. W. 'Discussing details of lumped parameter thermal modeling in electrical machines'. In: *7th IET International Conference on Power Electronics, Machines and Drives (PEMD)*. 2014, pp. 1–6. DOI: 10.1049/cp.2014.0479 (cit. on pp. 18, 30).

[Rad92] Radun, A. V. 'High-power density switched reluctance motor drive for aerospace applications'. In: *IEEE Transactions on Industry Applications* 28.1 (1992), pp. 113–119. ISSN: 0093-9994. DOI: 10.1109/28.120219 (cit. on p. 16).

[Rad95] Radun, A. V. 'Design considerations for the switched reluctance motor'. In: *IEEE Transactions on Industry Applications* 31.5 (1995), pp. 1079–1087. ISSN: 0093-9994. DOI: 10.1109/28.464522 (cit. on pp. 16, 26).

[RFR98] Radun, A. V.; Ferreira, C. A., and Richter, E. 'Two-channel switched reluctance starter/generator results'. In: *IEEE Transactions on Industry Applications* 34.5 (1998), pp. 1026–1034. ISSN: 0093-9994. DOI: 10.1109/28.720442 (cit. on p. 16).

[Ral+17] Ralev, I.; Qi, F.; Burkhart, B.; Klein-Hessling, A., and De Doncker, R. W. 'Impact of Smooth Torque Control on the Efficiency of a High-Speed Automotive Switched Reluctance Drive'. In: *IEEE Transactions on Industry Applications* 53.6 (2017), pp. 5509–5517. ISSN: 0093-9994. DOI: 10.1109/TIA.2017.2743680 (cit. on pp. 5, 35, 52, 53, 71, 113, 121).

[RJ10] Reddy, P. B. and Jahns, T. M. 'Analysis of bundle losses in high speed machines'. In: *2010 International Power Electronics Conference (IPEC - Sapporo)*. 2010, pp. 2181–2188. DOI: 10.1109/IPEC.2010.5542354 (cit. on p. 61).

[RF95] Richter, E. and Ferreira, C. 'Performance evaluation of a 250 kW switched reluctance starter generator'. In: *IAS '95. Conference Record of the 1995 IEEE Industry Applications Conference Thirtieth IAS Annual Meeting*. 1995, pp. 434–440. DOI: 10.1109/IAS.1995.530332 (cit. on p. 16).

[SBD15] Scharfenstein, D.; Burkhart, B., and De Doncker, R. W. 'Influence of an FPGA-based switching angle dithering on acoustics in single-pulse controlled switched reluctance machines'. In: *IEEE 11th International Conference on Power Electronics and Drive Systems*. 2015, pp. 754–761. DOI: 10.1109/PEDS.2015.7203471 (cit. on pp. 127, 128).

[Sch15] Schenk, M. *Simulative Untersuchung der Wicklungsverluste in Geschalteten Reluktanzmaschinen: Dissertation*. Vol. Band 78. Aachener Beiträge des ISEA. 2015. ISBN: 978-3-8440-4282-5 (cit. on pp. 14, 18, 52, 56, 59, 61, 77, 107).

[Sch17] Schmalstieg, J. *Physico-electrochemical simulation of lithium-ion batteries - Implementation, parametrization and application*. RWTH Aachen University, 2017. DOI: 10.18154/RWTH-2017-04693 (cit. on p. 12).

[SL09] Schofield, N. and Long, S. 'Generator Operation of a Switched Reluctance Starter/Generator at Extended Speeds'. In: *IEEE Transactions on Vehicular Technology* 58.1 (2009), pp. 48–56. ISSN: 0018-9545. DOI: 10.1109/TVT.2008.924981 (cit. on pp. 16, 17, 73, 92).

[SC03] Shaukatullah, H. and Claassen, A. 'Effect of thermocouple wire size and attachment method on measurement of thermal characteristics of electronic packages'. In: *Nineteenth Annual IEEE Semiconductor Thermal Measurement and Management Symposium*. 2003, pp. 97–105. DOI: 10.1109/STHERM.2003.1194345 (cit. on p. 80).

[Sho+10] Shoujun, S.; Weiguo, L.; Peitsch, D., and Schaefer, U. 'Detailed Design of a High Speed Switched Reluctance Starter/Generator for More/All Electric Aircraft'. In: *Chinese Journal of Aeronautics* 23.2 (2010), pp. 216–226. ISSN: 10009361. DOI: 10.1016/S1000-9361(09)60208-9 (cit. on p. 16).

[Sig18] Sigler, D. *e-Genius Extends Its Range*. 2018. URL: http://sustainableskies.org/e-genius-extends-range/ (visited on Mar. 13, 2018) (cit. on p. 4).

[ST04] Sozer, Y. and Torrey, D. A. 'Closed loop control of excitation parameters for high speed switched-reluctance generators'. In: *IEEE Transactions on Power Electronics* 19.2 (2004), pp. 355–362. ISSN: 0885-8993. DOI: 10.1109/TPEL.2003.823178 (cit. on p. 107).

[SPE08] SPEED Consortium. *PC-SRD*. 2008 (cit. on p. 22).

[SBC05] Staton, D.; Boglietti, A., and Cavagnino, A. 'Solving the More Difficult Aspects of Electric Motor Thermal Analysis in Small and Medium Size Industrial Induction Motors'. In: *IEEE Transactions on Energy Conversion* 20.3 (2005), pp. 620–628. ISSN: 0885-8969. DOI: 10.1109/TEC.2005.847979 (cit. on p. 18).

[Ste92] Steinmetz, C. P. ‘On the Law of Hysteresis’. In: *Transactions of the American Institute of Electrical Engineers* IX.1 (1892), pp. 1–64. ISSN: 0096-3860. DOI: 10.1109/T-AIEE.1892.5570437 (cit. on p. 14).

[Tak+12] Takeno, M.; Chiba, A.; Hoshi, N.; Ogasawara, S.; Takemoto, M., and Rahman, M. A. ‘Test Results and Torque Improvement of the 50-kW Switched Reluctance Motor Designed for Hybrid Electric Vehicles’. In: *IEEE Transactions on Industry Applications* 48.4 (2012), pp. 1327–1334. ISSN: 0093-9994. DOI: 10.1109/TIA.2012.2199952 (cit. on pp. 5, 16).

[TS03] Tang, X. and Sullivan, C. R. ‘Stranded wire with uninsulated strands as a low-cost alternative to litz wire’. In: *PESC 2003 - Power Electronics Specialist Conference*. 2003, pp. 289–295. DOI: 10.1109/PESC.2003.1218308 (cit. on p. 61).

[TS04] Tang, X. and Sullivan, C. R. ‘Optimization of stranded-wire windings and comparison with litz wire on the basis of cost and loss’. In: *2004 IEEE 35th Annual Power Electronics Specialists Conference*. 2004, pp. 854–860. DOI: 10.1109/PESC.2004.1355530 (cit. on p. 61).

[Tay] Taylor, W. H. ‘Improvements in Obtaining Power by means of Electro-Magnetism’. 8255 (cit. on p. 7).

[Umw18] Umweltbundesamt. *Klimabilanz 2017: Emissionen gehen leicht zurück: Niedrigere Emissionen im Energiebereich, höhere im Verkehrssektor*. 2018. URL: https://www.umweltbundesamt.de/daten/klima/treibhausgas-emissionen-in-deutschland#textpart-1 (visited on Apr. 25, 2018) (cit. on p. 1).

[van12] van Treek, D. *Position sensorless torque control of switched reluctance machines: Zugl.: Aachen, Techn. Hochsch., Diss., 2011*. Vol. 61. Aachener Beiträge des ISEA. Aachen: Shaker, 2012. ISBN: 9783844010145 (cit. on p. 26).

[Ven+02] Venkatachalam, K.; Sullivan, C. R.; Abdallah, T., and Tacca, H. ‘Accurate prediction of ferrite core loss with nonsinusoidal waveforms using only Steinmetz parameters’. In: *2002 IEEE Workshop on Computers in Power Electronics, 2002. Proceedings*. 2002, pp. 36–41. DOI: 10.1109/CIPE.2002.1196712 (cit. on p. 14).

[Vra68] Vrancik, J. *Prediction of Windage Power Loss in Alternators*. 1968 (cit. on pp. 15, 36, 64, 65, 68–70).

[WMM15] Widmer, J. D.; Martin, R., and Mecrow, B. C. ‘Optimization of an 80-kW Segmental Rotor Switched Reluctance Machine for Automotive Traction’. In: *IEEE Transactions on Industry Applications* 51.4 (2015), pp. 2990–2999. ISSN: 0093-9994. DOI: 10.1109/TIA.2015.2405051 (cit. on p. 16).

[Yat17] Yatsu, M. *Revisiting Rare Earths: The Ongoing Efforts to Challenge China’s Monopoly*. 2017. URL: https://thediplomat.com/2017/08/revisiting-rare-earths-the-ongoing-efforts-to-challenge-chinas-monopoly/ (visited on Mar. 14, 2018) (cit. on p. 5).

Aachener Beiträge des ISEA

ABISEA Band 1
Eßer, A.
Berührungslose, kombinierte Energie- und Informations-übertragung für bewegliche Systeme
1. Auflage 1992, 130 Seiten
ISBN 3-86073-046-0

ABISEA Band 2
Vogel, U.
Entwurf und Beurteilung von Verfahren zur Hochausnutzung des Rad-Schiene-Kraftschlusses durch Triebfahrzeuge
1. Auflage 1992, 130 Seiten
ISBN 3-86073-060-6

ABISEA Band 3
Redehorn, Th.
Stromeinprägendes Antriebssystem mit fremderregter Synchron-maschine
1. Auflage 1992, 130 Seiten
ISBN 3-86073-061-4

ABISEA Band 4
Ackva, A.
Spannungseinprägendes Antriebssystem mit Synchron-maschine und direkter Stromregelung
1. Auflage 1992, 135 Seiten
ISBN 3-86073-062-2

ABISEA Band 5
Mertens, A.
Analyse des Oberschwingungsverhaltens von taktsynchronen Delta - Modulationsverfahren zur Steuerung von Pulsstromrichtern bei hoher Taktzahl
1. Auflage 1992, 170 Seiten
ISBN 3-86073-069-X

ABISEA Band 6
Geuer, W.
Untersuchungen über das Alterungsverhalten von Bleiakkumulatoren
1. Auflage 1993, 100 Seiten
ISBN 3-86073-097-5

ABISEA Band 7
Langheim, J.
Einzelradantrieb für Elektrostraßenfahrzeuge
1. Auflage 1993, 215 Seiten
ISBN 3-86073-123-8
(vergriffen)

ABISEA Band 8
Fetz, J.
Fehlertolerante Regelung eines Asynchron-Doppelantriebes für ein Elektrospeicherfahrzeug
1. Auflage 1993, 136 Seiten
ISBN 3-86073-124-6
(vergriffen)

ABISEA Band 9
Schülting, L.
Optimierte Auslegung induktiver Bauelemente für den Mittelfrequenzbereich
1. Auflage 1993, 136 Seiten
ISBN 3-86073-174-2
(vergriffen)

ABISEA Band 10
Skudelny, H.-Ch.
Stromrichtertechnik
4. Auflage 1997, 259 Seiten
ISBN 3-86073-189-0

ABISEA Band 11
Skudelny, Ch.
Elektrische Antriebe
3. Auflage 1997, 124 Seiten
ISBN 3-86073-231-5

ABISEA Band 12
Schöpe, F.
Batterie-Management für Nickel-Cadmium Akkumulatoren
1. Auflage 1994, 156 Seiten
ISBN 3-86073-232-3
(vergriffen)

ABISEA Band 13
v. d. Weem, J.
Schmalbandige aktive Filter für Schienentriebfahrzeuge am Gleichspannungs-fahrdraht
1. Auflage 1995, 125 Seiten
ISBN 3-86073-233-1

ABISEA Band 14
Backhaus, K.
Spannungseinprägendes Direktantriebssystem mit schnelllaufender geschalteter Reluktanzmaschine
1. Auflage 1995, 156 Seiten
ISBN 3-86073-234-X
(vergriffen)

ABISEA Band 15
Reinold, H.
Optimierung dreiphasiger Pulsdauermodulations-verfahren
1. Auflage 1996, 116 Seiten
ISBN 3-86073-235-8

ABISEA Band 16
Köpken, H.-G.
Regelverfahren für Parallelschwingkreis-umrichter
1. Auflage 1996, 125 Seiten
ISBN 3-86073-236-6

ABISEA Band 17
Mauracher, P.
Modellbildung und Verbundoptimierung bei Elektrostraßenfahrzeugen
1. Auflage 1996, 192 Seiten
ISBN 3-86073-237-4

ABISEA Band 18
Protiwa, F.-F.
Vergleich dreiphasiger Resonanz-Wechselrichter in Simulation und Messung
1. Auflage 1997, 178 Seiten
ISBN 3-86073-238-2

ABISEA Band 19
Brockmeyer, A.
Dimensionierungswerkzeug für magnetische Bau-elemente in Stromrichter-anwendungen
1. Auflage 1997, 182 Seiten
ISBN 3-86073-239-0

Aachener Beiträge des ISEA

ABISEA Band 20
Apeldoorn, 0.
Simulationsgestützte Bewertung von Steuerverfahren für netzgeführte Stromrichter mit verringerter Netzrückwirkung
1. Auflage 1997, 132 Seiten
ISBN 3-86073-680-9

ABISEA Band 21
Lohner, A.
Batteriemanagement für verschlossene Blei-Batterien am Beispiel von Unterbrechungsfreien Stromversorgungen
1. Auflage 1998, 144 Seiten
ISBN 3-86073-681-7

ABISEA Band 22
Reinert, J.
Optimierung der Betriebseigenschaften von Antrieben mit geschalteter Reluktanzmaschine
1. Auflage 1998, 168 Seiten
ISBN 3-86073-682-5

ABISEA Band 23
Nagel, A.
Leitungsgebundene Störungen in der Leistungselektronik: Entstehung, Ausbreitung und Filterung
1. Auflage 1999, 160 Seiten
ISBN 3-86073-683-3

ABISEA Band 24
Menne, M.
Drehschwingungen im Antriebsstrang von Elektrostraßenfahrzeugen - Analyse und aktive Dämpfung
1. Auflage 2001, 192 Seiten
ISBN 3-86073-684-1

ABISEA Band 25
von Bloh, J.
Multilevel-Umrichter zum Einsatz in Mittelspannungs-Gleichspannungs-Übertragungen
1. Auflage 2001, 152 Seiten
ISBN 3-86073-685-X

ABISEA Band 26
Karden, E.
Using low-frequency impedance spectroscopy for characterization, monitoring, and modeling of industrial batteries
1. Auflage 2002, 154 Seiten
ISBN 3-8265-9766-4

ABISEA Band 27
Karipidis, C.-U.
A Versatile DSP/ FPGA Structure optimized for Rapid Prototyping and Digital Real-Time Simulation of Power Electronic and Electrical Drive Systems
1. Auflage 2001, 164 Seiten
ISBN 3-8265-9738-9

ABISEA Band 28
Kahlen, K.
Regelungsstrategien für permanentmagnetische Direktantriebe mit mehreren Freiheitsgraden
1. Auflage 2003, 158 Seiten
ISBN 3-8322-1222-1

ABISEA Band 29
Inderka, R.
Direkte Drehmomentregelung Geschalteter Reluktanzantriebe
1. Auflage 2003, 190 Seiten
ISBN 3-8322-1175-6

ABISEA Band 30
Schröder, S.
Circuit-Simulation Models of High-Power Devices Based on Semiconductor Physics
1. Auflage 2003, 124 Seiten
ISBN 3-8322-1250-7

ABISEA Band 31
Buller, S.
Impedance-Based Simulation Models for Energy Storage Devices in Advanced Automotive Power Systems
1. Auflage 2003, 136 Seiten
ISBN 3-8322-1225-6

ABISEA Band 32
Schönknecht, A.
Topologien und Regelungsstrategien für das induktive Erwärmen mit hohen Frequenz-Leistungsprodukten
1. Auflage 2004, 170 Seiten
ISBN 3-8322-2408-4

ABISEA Band 33
Tolle, T.
Konvertertopologien für ein aufwandsarmes, zweistufiges Schaltnetzteil zum Laden von Batterien aus dem Netz
1. Auflage 2004, 150 Seiten
ISBN 3-8322-2676-1

ABISEA Band 34
Götting, G.
Dynamische Antriebsregelung von Elektrostraßenfahrzeugen unter Berücksichtigung eines schwingungsfähigen Antriebsstrangs
1. Auflage 2004, 166 Seiten
ISBN 3-8322-2804-7

ABISEA Band 35
Dieckerhoff, S.
Transformatorlose Stromrichterschaltungen für Bahnfahrzeuge am 16 2/3Hz Netz
1. Auflage 2004, 158 Seiten
ISBN 3-8322-3094-7

ABISEA Band 36
Hu, J.
Bewertung von DC-DC-Topologien und Optimierung eines DC-DC-Leistungsmoduls für das 42-V-Kfz-Bordnetz
1. Auflage 2004, 156 Seiten
ISBN 3-8322-3201-X

ABISEA Band 37
Detjen, D.-0.
Characterization and Modeling of Si-Si Bonded Hydrophobie Interfaces for Novel High-Power BIMOS Devices
1. Auflage 2004, 146 Seiten
ISBN 3-8322-2963-9

ABISEA Band 38
Walter, J.
Simulationsbasierte Zuverlässigkeitsanalyse in der modernen Leistungselektronik
1. Auflage 2004, 134 Seiten
ISBN 3-8322-3481-0

ABISEA Band 39
Schwarzer, U.
IGBT versus GCT in der Mittelspannungsanwendung - ein experimenteller und simulativer Vergleich
1. Auflage 2005, 184 Seiten
ISBN 3-8322-4489-1

ABISEA Band 40
Bartram, M.
IGBT-Umrichtersysteme für Windkraftanlagen: Analyse der Zyklenbelastung, Modellbildung, Optimierung und Lebensdauervorhersage
1. Auflage 2006, 195 Seiten
ISBN 3-8322-5039-5

ABISEA Band 41
Ponnaluri, S.
Generalized Design, Analysis and Control of Grid side converters with integrated UPS or Islanding functionality
1. Auflage 2006, 163 Seiten
ISBN 3-8322-5281-9

ABISEA Band 42
Jacobs, J.
Multi-Phase Series Resonant DC-to-DC Converters
1. Auflage 2006, 185 Seiten
ISBN 3-8322-5532-X

ABISEA Band 43
Linzen, D.
Impedance-Based Loss Calculation and Thermal Modeling of Electrochemical Energy Storage Devices for Design Considerations of Automotive Power Systems
1. Auflage 2006, 150 Seiten
ISBN 3-8322-5706-3

ABISEA Band 44
Fiedler, J.
Design of Low-Noise Switched Reluctance Drives
1. Auflage 2007, 183 Seiten
ISBN 978-3-8322-5864-l

ABISEA Band 45
Fuengwarodsakul, N.
Predictive PWM-based Direct Instantaneous Torque Control for Switched Reluctance Machines
1. Auflage 2007, 150 Seiten
ISBN 978-3-8322-6210-5

ABISEA Band 46
Meyer, C.
Key Components for Future Offshore DC Grids
1. Auflage 2007, 196 Seiten
ISBN 978-3-8322-6571-7

ABISEA Band 47
Fujii, K.
Characterization and Optimization of Soft-Switched Multi-Level Converters for STATCOMs
1. Auflage 2008, 206 Seiten
ISBN 978-3-8322-6981-4

ABISEA Band 48
Carstensen, C.
Eddy Currents in Windings of Switched Reluctance Machines
1. Auflage 2008, 190 Seiten
ISBN 978-3-8322-7118-3

ABISEA Band 49
Bohlen, 0.
Impedance-based battery monitoring
1. Auflage 2008, 200 Seiten
ISBN 978-3-8322-7606-5

ABISEA Band 50
Thele, M.
A contribution to the modelling of the charge acceptance of lead-acid batteries - using frequency and time domain based concepts
1. Auflage 2008, 168 Seiten
ISBN 978-3-8322-7659-1

ABISEA Band 51
König, A.
High Temperature DC-to-DC Converters for Downhole Applications
1. Auflage 2009, 160 Seiten
ISBN 978-3-8322-8489-3

ABISEA Band 52
Dick, C. P.
Multi-Resonant Converters as Photovoltaic Module-Integrated Maximum Power Point Tracker
1. Auflage 2010, 192 Seiten
ISBN 978-3-8322-9199-0

ABISEA Band 53
Kowal, J.
Spatially-resolved impedance of nonlinear inhomogeneous devices - using the example of lead-acid batteries -
1. Auflage 2010, 214 Seiten
ISBN 978-3-8322-9483-0

ABISEA Band 54
Roscher, M.
Zustandserkennung von LiFeP04-Batterien für Hybrid- und Elektrofahrzeuge
1. Auflage 2011, 194 Seiten
ISBN 978-3-8322-9738-l

ABISEA Band 55
Hirschmann, D.
Highly Dynamic Piezoelectric Positioning
1. Auflage 2011, 156 Seiten
ISBN 978-3-8322-9746-6

Aachener Beiträge des ISEA

ABISEA Band 56
Rigbers, K.
Highly Efficient Inverter Architectures for Three-Phase Grid Connection of Photovoltaic Generators
1. Auflage 2011, 254 Seiten
ISBN 978-3-8322-9816-9

ABISEA Band 57
Kasper, K.
Analysis and Control of the Acoustic Behavior of Switched Reluctance Drives
1. Auflage 2011, 214 Seiten
ISBN 978-3-8322-9869-2

ABISEA Band 58
Köllensperger, P.
The Internally Commutated Thyristor - Concept, Design and Application
1. Auflage 201 J, 212 Seiten
ISBN 978-3-8322-9909-5

ABISEA Band 59
Schoenen, T.
Einsatz eines DC/DC-Wandlers zur Spannungsanpassung zwischen Antrieb und Energiespeicher in Elektro-und Hybridfahrzeugen
1. Auflage 2011, 138 Seiten
ISBN 978-3-8440-0622-3

ABISEA Band 60
Hennen, M.
Switched Reluctance Direct Drive with Integrated Distributed Inverter
1. Auflage 2012, 150 Seiten
ISBN 978-3-8440-0731-2

ABISEA Band 61
van Treek, D.
Position Sensorless Torque Control of Switched Reluctance Machines
1. Auflage 2012, 144 Seiten
ISBN 978-3-8440-IO 14-5

ABISEA Band 62
Bragard, M.
Tue Integrated Emitter Turn-Off Thyristor. An Innovative MOS-Gated High-Power Device
1. Auflage 2012, 172 Seiten
ISBN 978-3-8440-1152-4

ABISEA Band 63
Gerschler, J. B.
Ortsaufgelöste Modellbildung von Lithium-Ionen-Systemen unter spezieller Berücksichtigung der Batteriealterung
1. Auflage 2012, 350 Seiten
ISBN 978-3-8440-1307-8

ABISEA Band 64
Neuhaus, C.
Schaltstrategien für Geschaltete Reluktanzantriebe mit kleinem Zwischenkreis
1. Auflage 2012, 144 Seiten
ISBN 978-3-8440-1487-7

ABISEA Band 65
Butschen, T.
Dual-ICT- A Clever Way to Unite Conduction and Switching Optimized Properties in a Single Wafer
1. Auflage 2012, 178 Seiten
ISBN 978-3-8440-1771-7

ABISEA Band 66
Plum, T.
Design and Realization of High-Power MOS Turn-Off Thyristors
1. Auflage 2013, 130 Seiten
ISBN 978-3-8440-1884-4

ABISEA Band 67
Kiel, M.
Impedanzspektroskopie an Batterien unter besonderer Berücksichtigung von Batteriesensoren für den Feldeinsatz
1. Auflage 2013, 232 Seiten
ISBN 978-3-8440-1973-5

ABISEA Band 68
Brauer, H.
Schnelldrehender Geschalteter Reluktanzantrieb mit extremem Längendurchmesserverhältnis
1. Auflage 2013, 202 Seiten
ISBN 978-3-8440-2345-9

ABISEA Band 69
Thomas, S.
A Medium-Voltage Multi-Level DC/DC Converter with High Voltage Transformation Ratio
1. Auflage 2014, 236 Seiten
ISBN 978-3-8440-2605-4

ABISEA Band 70
Richter, S.
Digitale Regelung von PWM Wechselrichtern mit niedrigen Trägerfrequenzen
1. Auflage 2014, 134 Seiten
ISBN 978-3-8440-2641-2

ABISEA Band 71
Bösing, M.
Acoustic Modeling of Electrical Drives - Noise and Vibration Synthesis based on Force Response Superposition
1. Auflage 2014, 208 Seiten
ISBN 978-3-8440-2752-5

ABISEA Band 72
Waag, W.
Adaptive algorithms for monitoring of lithium-ion batteries in electric vehicles
1. Auflage 2014, 242 Seiten
ISBN 978-3-8440-2976-5

ABISEA Band 73
Sanders, T.
Spatially Resolved Electrical In-Situ Measurement Techniques for Fuel Cells
1. Auflage 2014, 138 Seiten
ISBN 978-3-8440-3121-8

Aachener Beiträge des ISEA

ABISEA Band 74
Baumhöfer, T.
Statistische Betrachtung experimenteller Alterungsuntersuchungen an Lithium-Ionen Batterien
1. Auflage 2015, 174 Seiten
ISBN 978-3-8440-3423-3

ABISEA Band 75
Andre, D.
Systematic Characterization of Ageing Factors for High-Energy Lithium-Ion Cells and Approaches for Lifetime Modelling Regarding an Optimized Operating Strategy in Automotive Applications
1. Auflage 2015, 210 Seiten
ISBN 978-3-8440-3587-2

ABISEA Band 76
Merei, G.
Optimization of off-grid hybrid PV-wind-diesel power supplies with multi-technology battery systems taking into account battery aging
1. Auflage 2015, 194 Seiten
ISBN 978-3-8440-4148-4

ABISEA Band 77
Schulte, D.
Modellierung und experimentelle Validierung der Alterung von Blei-Säure Batterien durch inhomogene Stromverteilung und Säureschichtung
1. Auflage 2016, 168 Seiten
ISBN 978-3-8440-4216-0

ABISEA Band 78
Schenk, M.
Simulative Untersuchung der Wicklungsverluste in Geschalteten Reluktanzmaschinen
1. Auflage 2016, 142 Seiten
ISBN 978-3-8440-4282-5

ABISEA Band 79
Wang, Y.
Development of Dynamic Models with Spatial Resolution for Electrochemical Energy Converters as Basis for Control and Management Strategies
1. Auflage 2016, 198 Seiten
ISBN 978-3-8440-4303-7

ABISEA Band 80
Ecker, M.
Lithium Plating in Lithium-Ion Batteries: An Experimental and Simulation Approach
1. Auflage 2016, 170 Seiten
ISBN 978-3-8440-4525-3

ABISEA Band 81
Zhou, W.
Modellbasierte Auslegungsmethode von Temperierungssystemen für Hochvolt-Batterien in Personenkraftfahrzeugen
1. Auflage 2016, 192 Seiten
ISBN 978-3-8440-4589-5

ABISEA Band 82
Lunz, B.
Deutschlands Stromversorgung im Jahr 2050
Ein szenariobasiertes Verfahren zur vergleichenden Bewertung von Systemvarianten und Flexibilitätsoptionen
1. Auflage 2016, 196 Seiten
ISBN 978-3-8440-4627-4

ABISEA Band 83
Hofmann, A.
Direct Instantaneous Force Control Key to Low-Noise Switched Reluctance Traction Drives
1. Auflage 2016, 244 Seiten
ISBN 978-3-8440-4715-8

ABISEA Band 84
Budde-Meiwes, H.
Dynamic Charge Acceptance of Lead-Acid Batteries for Micro-Hybrid Automotive Applications
1. Auflage 2016, 168 Seiten
ISBN 978-3-8440-4733-2

ABISEA Band 85
Engel, S. P.
Thyristor-Based High-Power On-Load Tap Changers Control under Harsh Load Conditions
1. Auflage 2016, 170 Seiten
ISBN 978-3-8440-4986-2

ABISEA Band 86
VanHoek, H.
Design and Operation Considerations of Three-Phase Dual Active Bridge Converters for Low-Power Applications with Wide Voltage Ranges
1. Auflage 2017, 242 Seiten
ISBN 978-3-8440-5011-0

ABISEA Band 87
Diekhans, T.
Wireless Charging of Electric Vehicles - a Pareto-Based Comparison of Power Electronic Topologies
1. Auflage 2017, 156 Seiten
ISBN 978-3-8440-5048-6

ABISEA Band 88
Lehner, S.
Reliability Assessment of Lithium-Ion Battery Systems with Special Emphasis on Cell Performance Distribution
1. Auflage 2017, 202 Seiten
ISBN 978-3-8440-5090-5

ABISEA Band 89
Käbitz, S.
Untersuchung der Alterung von Lithium-Ionen-Batterien mittels Elektroanalytik und elektrochemischer Impedanzspektroskopie
1. Auflage 2016, 258 Seiten
DOI: 10.18154/RWTH-2016-12094

ABISEA Band 90
Witzenhausen, H.
Elektrische Batteriespeichermodelle: Modellbildung, Parameteridentifikation und Modellreduktion
1. Auflage 2017, 286 Seiten
DOI: 10.18154/RWTH-2017-03437

ABISEA Band 91
Münnix, J.
Einfluss von Stromstärke und Zyklentiefe auf graphitische Anoden
1. Auflage 2017, 178 Seiten
DOI: 10.18154/RWTH-2017-01915

ABISEA Band 92
Pilatowicz, G.
Failure Detection and Battery Management Systems of Lead-Acid Batteries for Micro-Hybrid Vehicles
1. Auflage 2017, 212 Seiten
DOI: 10.18154/RWTH-2017-09156

ABISEA Band 93
Drillkens, J.
Aging in Electrochemical Double Layer Capacitors: An Experimental and Modeling Approach
1. Aufl. 2017, 179 Seiten
DOI: 10.18154/RWTH-2018-223434

ABISEA Band 94
Magnor, D.
Globale Optimierung netzgekoppelter PV-Batteriesysteme unter besonderer Berücksichtigung der Batteriealterung
1. Auflage 2017, 210 Seiten
DOI: 10.18154/RWTH-2017-06592

ABISEA Band 95
Iliksu, M.
Elucidation and Comparison of the Effects of Lithium Salts on Discharge Chemistry of Nonaqueous Li-O_2 Batteries
1. Aufl. 2018, 160 Seiten
DOI: 10.18154/RWTH-2018-223782

ABISEA Band 96
Schmalstieg, J.
Physikalisch-elektrochemische Simulation von Lithium-Ionen-Batterien: Implementierung, Parametrierung und Anwendung
1. Aufl. 2017, 176 Seiten
DOI: 10.18154/RWTH-2017-04693

ABISEA Band 97
Soltau, N.
High-Power Medium-Voltage DC-DC Converters: Design, Control and Demonstration
1. Aufl. 2017, 176 Seiten
DOI: 10.18154/RWTH-2017-04084

ABISEA Band 98
Stieneker, M.
Analysis of Medium-Voltage Direct-Current Collector Grids in Offshore Wind Parks
1. Aufl. 2017, 144 Seiten
DOI: 10.18154/RWTH-2017-04667

ABISEA Band 99
Masomtob, M.
A New Conceptual Design of Battery Cell with an Internal Cooling Channel
1. Aufl. 2017, 167 Seiten
DOI: 10.18154/RWTH-2018-223281

ABISEA Band 100
Marongiu, A.
Performance and Aging Diagnostic on Lithium Iron Phosphate Batteries for Electric Vehicles and Vehicle-to-Grid Strategies
1. Aufl. 2017, 222 Seiten
DOI: 10.18154/RWTH-2017-09944

ABISEA Band 101
Gitis, A.
Flaw detection in the coating process of lithium-ion battery electrodes with acoustic guided waves
1. Aufl. 2017, 132 Seiten
DOI: 10.18154/RWTH-2017-099519

ABISEA Band 102
Neeb, C.
Packaging Technologies for Power Electronics in Automotive Applications
1. Aufl. 2017, 132 Seiten
DOI: 10.18154/RWTH-2018-224569

ABISEA Band 103
Adler, F. S.
A Digital Hardware Platform for Distributed Real-Time Simulation of Power Electronic Systems
1. Aufl. 2017, 156 Seiten
DOI: 10.18154/RWTH-2017-10761

Aachener Beiträge des ISEA

ABISEA Band 104
Becker, J.
Flexible Dimensionierung und Optimierung hybrider Lithium-Ionenbatteriespeichersysteme mit verschiedenen Auslegungszielen
1. Aufl., 2017, 157 Seiten
DOI: 10.18154/RWTH-2017-09278

ABISEA Band 105
Warnecke, A.
Degradation Mechanisms in NMC Based Lithium-Ion Batteries
1. Aufl. 2017, 158 Seiten
DOI: 10.18154/RWTH-2017-09646

ABISEA Band 106
Taraborrelli, S.
Bidirectional Dual Active Bridge Converter using a Tap Changer for Extended Voltage Ranges
1. Aufl. 2017

ABISEA Band 107
Sarriegi, G.
SiC and GaN Semiconductors – The Future Enablers of Compact and Efficient Converters for Electromobility
1. Aufl. 2017

ABISEA Band 108
Senol, M.
Drivetrain Integrated Dc-Dc Converters utilizing Zero Sequence Currents
1. Aufl. 2017

ABISEA Band 109
Koijma, T.
Efficiency Optimized Control of Switched Reluctance Machines
1. Aufl. 2017

ABISEA Band 110
Lewerenz, M.
Dissection and Quantitative Description of Aging of Lithium-Ion Batteries Using Non-Destructive Methods Validated by Post-Mortem-Analyses
1. Aufl. 2018

ABISEA Band 111
Büngeler, J.
Optimierung der Verfügbarkeit und der Lebensdauer von Traktionsbatterien für den Einsatz in Flurförderfahrzeugen
1. Aufl. 2018

ABISEA Band 112
Wegmann, R.
Betriebsstrategien und Potentialbewertung hybrider Batteriespeichersysteme in Elektrofahrzeugen
1. Auflage 2018

ABISEA Band 113
Nordmann, H.
Batteriemanagementsysteme unter besonderer Berücksichtigung von Fehlererkennung und Peripherieanalyse
1. Aufl. 2018

ABISEA Band 114
Engelmann, G.
Reducing Device Stress and Switching Losses Using Active Gate Drivers and Improved Switching Cell Design
1. Aufl. 2018

ABISEA Band 115
Klein-Heßling, A.
Active DC-Power Filters for Switched Reluctance Drives during Single-Pulse Operation
1. Aufl. 2018

Range Extender with a combustion engine and a generator offer a high energy density to electrify vehicles. To be competitive, Range Extender need to be cost effective, compact and very reliable, thus the switched reluctance generator is one potential solution. To assess the switched reluctance generator technology, two speed scenarios are considered and analyzed in this work. A new design approach is introduced to compare a vast number of potential machine configurations in a very short time. The machine performance is then analyzed with the help of simulation results and prototype measurements. From the analysis, a recommendation on the most suitable machine configuration is derived. Finally, the influence of the control parameter and power variation on the machine efficiency and the acoustic behavior is analyzed. The work offers guidance in the choice of an appropriate switched reluctance generator configuration as well as its operational speed for Range Extender applications.

ISSN 1437-675X